Synthesis, magnetism and reactivity of graphene nanoribbons

Alejandro Berdonces Layunta

Tutor: Dimas García de Oteyza

May, 2023

Synthesis, magnetism and reactivity of graphene nanoribbons

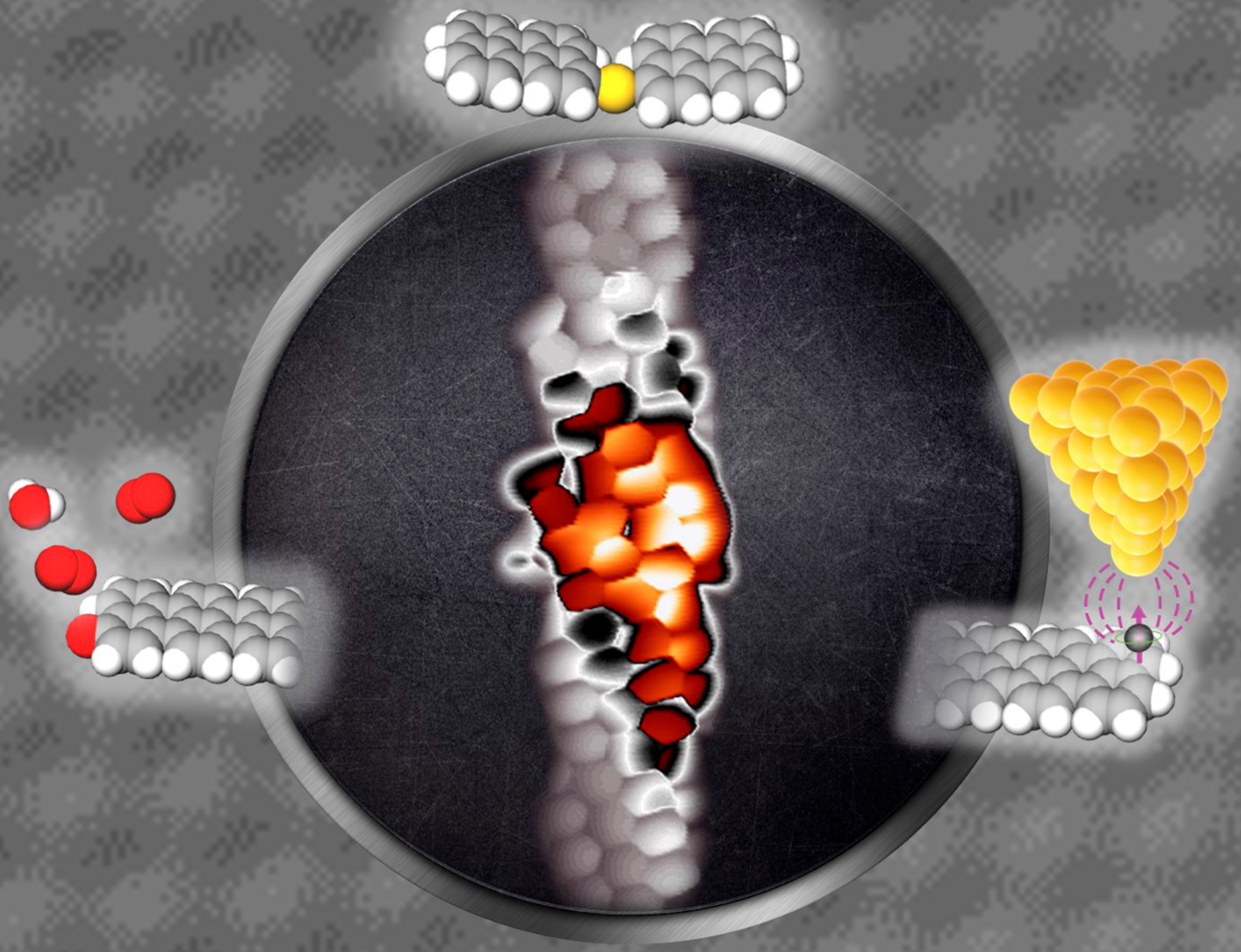

Alejandro Berdonces Layunta

Tutor: Dimas García de Oteyza

eman ta zabal zazu

Universidad del País Vasco

Euskal Herriko Unibertsitatea

May, 2023

Agradecimientos

Durante estos cuatro años he tenido la suerte de cruzarme con mucha gente que ha hecho que todo el tiempo y el esfuerzo invertido valgan la pena. Tanto en lo académico como en lo personal, ellos son los que han marcado este doctorado y me siento afortunado de haber podido conocerlos. Le estoy muy agradecido a mi director, Dimas. Desde aquella primera reunión improvisada en la que le conté mi TFG y que no sé cómo le llevo a apostar por mí. Durante estos años ha sido más un tutor que un jefe, y me ha enseñado a investigar y a escribir. Tu fuiste el primer ejemplo de que se puede tener principios en la ciencia, y que nosotros estamos aquí para aprender, más que para publicar. Te deseo lo mejor por Gijón. También quiero mencionar a Martina, por ser mi cotutora en la sombra, y con la que ha sido un gusto trabajar. Next, I want to thank all the postdocs and lab mates that taught me all I know about STM: James, you showed me that patience is key to be a good spectroscopist. You are the best even if you like boring color scales. I miss your English lessons in the lab. Sabri, who taught me about being methodic, what was crucial during my year as a junior PhD. Tao Wang, the best mate in the lab, you always knew the exact reference, and you showed me that the best Chinese food is not so well known. I will have to go to your city and try the best lamb in Asia. Patrick, the latino philipino, who taught me the relation between hospitality and good food and made the lab a little bit funnier every day. Néstor, my antecessor, I hope you find your path in Switzerland; and Paula, who has to keep the level high now in the lab while I learn to surf in order to be

able to beat her. You all were part of a small lab that made huge advances, see you all soon. Quiero mencionar a todo el grupo de física de nanoestructuras del CFM. Hacéis una gran comunidad, donde siempre hay alguien dispuesto a echar una mano si se necesita. A Max, que siempre tenía la herramienta necesaria, a Celia, A Sara, a Miguel, y a Enrique Ortega. También quiero agradecer a Martin Švec y a Pavel Jelínek que me mostraran Praga y los encantos de su gastronomía día a día durante tres meses, en los que aprendí como si hubiesen sido tres años; así como a toda la gente de Praga que espero volver a ver. Una parte esencial de esta tesis han sido personas dedicadas al lado computacional de la ciencia. Sin ellos avanzaríamos a oscuras en cada nuevo experimento. También quiero agradecer a todas las que forman el DIPC la ayuda prestada. En concreto a Marimar, Bea y Olatz, que han aguantado mis preguntas, me han solucionado problemas y siempre con el mejor humor. Os echaré de menos. Pero no sólo tengo le estoy agradecido a la gente de la ciencia. Fuera del ambiente académico también ha habido mucha gente que han hecho de apoyo en estos años, haciendo emocionantes los (no muchos) ratos libres que había, apoyándome siempre o simplemente estando ahí: Primero de todo van mis padres, claro. Quiero agradecer a mi padre el haberme dicho que siguiera mi camino, sino hubiese sido por su insistencia no me habría lanzado a la piscina en un momento tan duro. De mi madre qué voy a decir, es mi madre. Hemos capeado muchos temporales juntos, y ella siempre está ahí, apoyando a todos sin dudar. Te quiero. También quiero agradecérselo al resto de mi familia, tíos y primos, sois de lo mejorcito. A Marta, porque siempre ha estado ahí, a capa y espada. Ella tiene el chute de energía que a veces me falta. Es la compañera de viaje ideal, y es capaz de hacerme parecer puntual. En estos años hemos llegado al círculo polar, hemos regateado por una chilaba, hemos recorrido mil sitios por tierra y por aire, pero lo importante es lo

bien que lo hemos pasado juntos, donde fuera. Muchas gracias. Al Krustycamp y todos los que han estado alistados en nuestro campamento. A Aarón y Mateo como socios fundadores durante aquellos primeros caóticos meses. Las recetas con extra de picante a las dos de la mañana, las charletas en el balcón y las sesiones de cine en casa. Durante nuestro tiempo juntos me acostumbré a llegar a casa al final del día y encontrar un grupo de gente nueva, de cualquier punto del mundo, tomando algo en nuestro salón. A Pablo, por ser tan Pablo. Porque nos entendemos perfectamente, porque sé que me llevo una amistad que va a durar. Porque los maños nos tenemos que apoyar cuando salimos a explorar. A Jose, Carmelo y Bastian; todos formaron parte del club que montamos en pandemia y fueron habituales huéspedes en nuestro salón. En nuestra casa ya no erais turristos sino locales. También a las Irenes, que nos enseñaron las fiestas locales. Y por supuesto al nuevo campamento, con Toni y Raúl. ¡A todos, nos vemos pronto! También quiero acordarme de Álvaro e Iker, por haber empezado el club del bocata. Sois gente maravillosa y con una actitud increíble, como el resto de los fotónicos, Jon, Martin, Mikel, Antxon, Bruno, Fernando, Carlos, María y todos los demás... También me acuerdo ahora de mis químicos, Marta, Juan, Quique, María, David, etcétera. Porque sigamos encontrando un lugar para encontrarnos. Y a todos los demás que me estoy dejando, que seguro que se merecen más que una dedicatoria. Y a todo el que le dedique el tiempo necesario a leer esta tesis.

Contents

Resumen

El Microscopio de Efecto Túnel (STM por sus siglas en inglés) fue desarrollado por Gerd Binnig y Heinrich Rohrer en 1981, en IBM Zürich. [1, 2] Su logro fue único: En sólo dos años lograron minimizar el ruido y lograr la estabilidad térmica necesaria para alcanzar resolución subnanométrica en un cristal de oro.[1]

Años antes existió un precursor del cual Binning y Rohrer no estaban al tanto: el "topographiner".[3] Este instrumento operaba en el rango de decenas de voltios, utilizando la emisión por efecto de campo para escanear la topografía de superficies con una resolución de micras. Sin embargo, el STM lo superó en varios órdenes de magnitud, siendo capaz de obtener resolución atómica en superficies.

Los avances técnicos logrados a partir de ese primer microscopio son inconmensurables. Las microscopías de sonda local (SPM, por sus siglas en inglés) han hecho posible la observación directa de la estructura molecular a nivel atómico. No solo eso: ahora podemos medir las consecuencias tangibles de una función de onda de una sola molécula, su densidad de estados, para comprender sus propiedades. En combinación con la síntesis de superficies, las SPM permitieron el desarrollo de nuevos materiales con propiedades únicas. Y entre todos ellos, las cintas de grafeno (GNRs) han atraído una gran parte de la atención de los últimos años debido a sus propiedades únicas, muy prometedoras para la electrónica molecular.

Las GNRs son polímeros altamente conjugados que difuminan las fronteras con

los cristales 1-D. Se introdujeron al mundo como un derivado del grafeno, que unos años antes había supuesto una revolución para la ciencia, entre otras cosas, por los conos de Dirac de su estructura electrónica. [4, 5, 6, 7] Las nanocintas están confinadas lateralmente, lo que secciona el cono de dirac en bandas que pueden o no cruzar el nivel de Fermi. Esto origina la existencia de nanocintas semiconductoras, cuyo bandgap puede ser alterado modificando su longitud, anchura, el perfil de sus bordes o mediante la adición de heteroátomos u otros grupos funcionales. [8, 5] En consecuencia, las GNRs se presentan como una alternativa prometedora al silicio semiconductor para la fabricación de procesadores a escala nanométrica.[6, 9, 10]

Al margen de su aplicación directa, las GNR representan una fuente increíble de nueva física, ya que pueden albergar electrones π desapareados.[7, 11, 12] Es un concepto contraintuitivo: ¿cómo se puede explicar, en términos termodinámicos, que un par de estados desapareados se mantengan independientes dentro de la misma red π? Para un químico orgánico sería una pesadilla, acostumbrado a huir de los radicales libres por su alta inestabilidad. Para nosotros, sin embargo, un polímero orgánico con actividad magnética y espínes localizados es una oportunidad muy enriquecedora. Trabajamos en ultra alto vacío, con superficies atómicamente limpias, lo cual protege las cintas del ataque de reactantes atmosféricos. Tanto es así que, a día de hoy, la reactividad de las cintas ha pasado prácticamente desapercibida para la ciencia de superficies.

Un requisito para poder abarcar todas las alternativas electronicas de las cintas de grafeno, es la capacidad de sintetizarlas con precisión atómica. Las estrategias bottom-up abrieron esta posibilidad, sintetizando las cintas en la superficie a partir de monómeros

precursores. El acoplamiento de Ullmann, la estrategia más extendida, emplea una polimerización guiada por radicales.[13] El precursor se deposita en una superficie catalítica, comúnmente metálica, que a continuación se calienta para promover la ruptura homolítica de los enlaces carbono-halógeno del precursor. Los radicales resultantes guían la formación de enlaces carbono-carbono hacia una polimerización controlada, seguida de reacciones de ciclo deshidrogenación (CDH) que planarizan las cintas. Sin embargo, hay particularidades de esta estrategia que siguen inexploradas para la mayoría de los precursores no convencionales.

A lo largo de esta tesis estudiaremos las nanocintas de grafeno. Exploraremos algunos mecanismos de síntesis, su magnetismo y reactividad. Buscaremos correlaciones entre todo lo anterior y qué estrategias podemos utilizar para proteger las nanocintas del ataque químico del entorno. La estructura de la tesis será la siguiente:

-**Primer capítulo**: Aquí plantearemos el contexto de esta tesis. Cómo se construye la comprensión actual de las GNRs a través de la aromaticidad, los modelos tight binding y la topología, y su relación con el magnetismo del carbono. Nos enfocaremos en dos clases de nanocintas, las 3,1-chGNRs quirales y la familia 3p+2 de bordes armchair, que serán protagonistas en el resto del trabajo.

-**Segundo capítulo**: Esta segunda parte de la introducción describe las técnicas empleadas en nuestra investigación. Desarrollaremos en profundidad temas como el sistema de vacío, las microscopías de sonda local, la espectroscopía de rayos X (XPS, por sus siglas en inglés) y la síntesis en superficie.

-**Tercer capítulo**: Tras estudiar un protocolo de síntesis para los 5-aGNR, parte de la familia 3p+2, descubrimos un mecanismo de reacción nunca antes visto. Mediante SPM y XPS, desentrañamos los detalles de la reacción que llevan a la obtención de ribbons de gran calidad.

--**Cuarto capítulo**: Con la ayuda de cálculos de teoría del funcional de la densidad electrónica (DFT) y del STM, nos propusimos cuantificar el bandgap de los 5-aGNR. Durante la caracterización, identificamos en ellas la presencia de orbitales desapareados magnéticos mediante medidas de transporte de carga, y los relacionamos con su alta reactividad frente al oxígeno molecular (O_2).

--**Quínto capítulo**: Exploramos la reactividad de las cintas quirales 3,1,4-chGNR cuando son expuestas a condiciones ambientales. A pesar de que en ellas no residen orbitales desapareados, se mostraron reactivas frente a componentes atmosféricos específicos, como O_2 y H_2O.

--**Sexto capítulo**: Estudiamos dos estrategias de proteccion para las 3,1,4-chGNR. A través de la hidrogenación y la funcionalización de los bordes zigzag con grupos protectores, se lograron cintas estables a las condiciones atmosféricas, que pudieron ser regeneradas una vez de vuelta en la campana de vacío. Con esto, se abre una puerta para su aplicación en dispositivos electrónicos.

--**Séptimo capítulo**: Ciertos tipos de defectos generados en las 3,1,4-chGNR durante la protección fueron capaces de estabilizar orbitales π desaparejados en el-

las, los cuales se acoplaron magnéticamente bajo ciertas condiciones. Probamos el efecto de la distancia, la quiralidad y la funcionalización en la intensidad del acoplamiento, y desarrollamos un modelo de Hückel para entender los efectos independientes de cada variable.

--**Octavo capítulo**: Aquí se incluyen las conclusiones, perspectivas futuras, y una relación de los artículos publicados durante la tesis.

Abstract

Gerd Binnig and Heinrich Rohrer developed the Scanning Tunnelling Microscope (STM) in 1981, at IBM Zürich. [1, 2] They reached a major milestone only two years after its first conception: They were able to minimize the noise and reach the thermal stability necessary for sub-nanometric resolution.[1] There is a precursor of which Binning and Rohrer were unaware: the topographiner.[3] This instrument operated in the range of tens of Volts, using the field effect emission to scan the topography of surfaces with a resolution of microns. Nonetheless, the STM overcame that by orders of magnitude, being able to obtain atomic resolution on a gold surface.

The progress achieved from those first experiments is incommensurate. Scanning probe microscopies (SPMs) have made possible to reach atomic resolution in molecules. Not only that: We are now able to measure the tangible consequences of a single molecule wavefunction, its density of states, in order to understand its properties. In combination with surface synthesis, SPMs allowed the discovery of new materials with unique physics. And among them, graphene nanoribbons (GNRs) have attracted a significant attention due to their promising properties for molecular electronics.

GNRs are highly conjugated polymers that blur the boundaries with 1-D crystals. They were presented to the world as a derivative of graphene, which had revolutionized the scientific world a few years earlier due to its unique electronics characterized by its Dirac cones.[4, 6, 7, 5] GNRs are quantized by their lateral confinement, and as a result, their bands exhibit "slices" of graphene's electronic structure, either crossing the Fermi level or

showing a semiconductor bandgap. Their electronic structure can be altered by adjusting their length, width, edge shape, and by adding heteroatoms or other functional groups [8, 5], making them a promising alternative to silicon in nanometer-scale processors [6, 9, 10].

In addition, GNRs are an incredible source of new physics, as they can host unpaired π electrons [7, 11, 12]. It is a counterintuitive concept: How is it thermodynamically possible for a pair of single states to remain unpaired within the same π lattice? Apart from the purely causal explanation, an organic molecule with magnetically active states and local spin moment is an enriching opportunity for solid-state physics, even if it frightens organic synthesis researchers, for whom unpaired electrons are a source of instability. Nevertheless, our working conditions - ultra-high vacuum and atomically clean surfaces - allowed us to ignore their reactivity, even though it may hinder their future applicability.

The study of GNRs electronics requires from atomically precise ribbons, synthesized from monomers through bottom-up strategies. The most extended strategy is the Ullmann coupling[13] The precursor is deposited on a catalitic surface, followed by an annealing of the surface to promote the homolitic splitting of carbon-halogen bonds. Resulting radicals from this reaction guide a polymerization, which is catalized by the surface, followed by cyclodehydrogenation (CDH) reactions that planarize the ribbons. However, the detailed insights of this strategy remain unexplored for some unorthodox precursors.

This thesis will explore the synthesis of graphene nanoribbons, studying their magnetism and reactivity, which remains largely unexplored by our field. We will examine the causes of the latter and identify strategies that we can use to protect the nanoribbons.

The dissertation will follow this structure:

-**First chapter**: Here we will explore the scientific perspective of this thesis. How we built the actual understanding of GNRs through aromaticity, tight binding models and topology, and its relation with the magnetism of carbon. We will focus on two classes of ribbons, the 3,1-chiral GNR and the 3p+2 armchair family, that will be protagonist in the rest of the work.

-**Second chapter**: This second part of the introduction refers to the techniques employed during the thesis. Details about the vacuum system, the scanning probe methodologies, X-ray Photoelectron Spectroscopy (XPS) and surface syntesis will be developed in depth.

-**Third chapter**: The study performed of a synthesis strategy for a member of the 3p+2 family, the 5-armchair GNR, revealed a novel and unreported reaction mechanism. By means of AFM and XPS, we explored the reaction details that result in the obtention of such high yields.

--**Fourth chapter**: With the help of Density Functional Theory (DFT) calculations and STM, we adressed the bandgap of 5-armchair GNR. The characterization included the magnetic identification of single states in them through transport measurements and their relation with the ribbon reactivity to O_2.

--**Fifth chapter**: We explored the reactivity of 3,1,4-chiral graphene nanorib-

bons (GNRs) when exposed to atmospheric conditions. Despite lacking unpaired orbitals, the ribbons showed sensitivity to atmospheric reactives (O_2 and H_2O).

--**Sixth chapter**: We designed and tested two different protection strategies for the 3,1,4-chiral GNRs. Through hydrogenation and edge functionalization, we were able to turn them stable in atmospheric conditions and regenerate them afterwards, making them feasible for their application in devices.

--**Seventh chapter**: The point defects in the 3,1,4-chiral GNRs stabilized unpaired π orbitals, that couple magnetically under certain conditions. We tested the effect of the distance, chiralities, and functionalization in the exchange interaction energy, and developed a Hückel model to understand single variable effects.

--**Eigth chapter**: Includes the conclusions, outlook and a relation of the articles published during the thesis period.

CHAPTER 1

Introduction: Scientific context

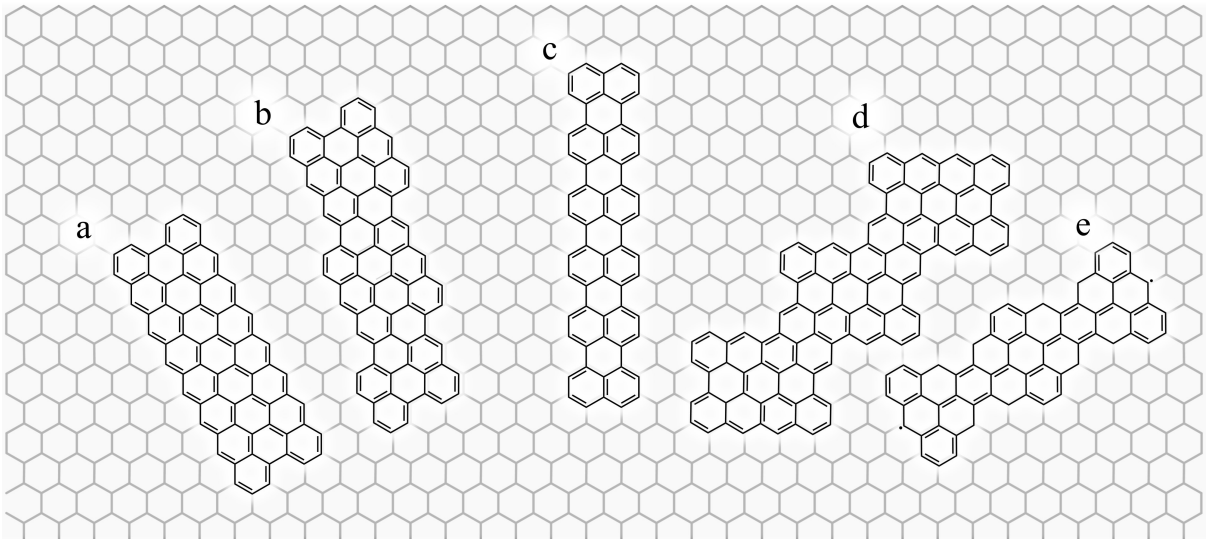

Figure 1.1: from left to right: a) Zigzag, b) 3,1-chiral and c) armchair graphene nanoribbons. The rest are non-yet synthesized d) 2,2-chiral and e) bay-edged GNR.

Graphene nanoribbons are highly conjugated polymers that blur the boundaries with 1-D crystals. They were presented to the world as a derivative of graphene, which had revolutionized the scientific world a few years earlier due to its unique electronics.[4, 6, 7, 5] GNRs can be divided into different groups depending on the shape of their edges. Three types of ribbons come from a parallel slicing of the graphene lattice: armchair and zigzag edged ribbons, and a periodic alternation of them named chiral graphene nanoribbons, shown in Figure 1.1 (a-c), left and center. More complex classes of edges have been proposed, and in some cases, synthesized: stepper chiral ribbons, they do not follow the close-packed configuration for its edge orientation and thus display longer segments of either the zigzag or armchair edges, giving them that "sharper" look shown in Figure 1.1 (d);[12] cove-edge ribbons from Figure 1.1 (e),[14, 15] which resemble the zigzag in their relative alignment with the graphene lattice, but with one edge atom missing from every two; barbed ribbons, which again are parallel to the zigzag ones but miss a row, with edges decorated with CH_2

atoms.[16] They are predictably reactive, and probably never synthesized for that reason; ear-like ribbons, with an armchair backbone with extra rings attached, either hexagonal or non-benzenoic;[15] and the list keeps going.[8] Although these non-conventional ribbons will not be adressed within this thesis, this is a sight of the vast landscape of possibilities.

For understanding their electronic structure, a common departure point is a well known (by solid-state physicists) tight-binding model. This method employs a small number of parameters, such as the orbital overlap (defined by the hopping constant for each bond) and the energy of an electron in an atomic orbital (called on-site energy), to define a material and predict its underlying properties. Its simpler version only accounts for the interaction between neighboring atoms, but it can predict the quasi-metallic electronic structure of graphene.[17, 18] When you chop it in one dimension, as is the case for GNRs, graphene's Dirac cone becomes quantized in specific energy bands, shown in Figure 1.2 (a).[19] Depending on the angle in which you cut the ribbon out of graphene, you will get a 1D structure with different slices.[20]

This quantization is easier to visualize focusing on the reciprocal space. For the armchair GNR, the resulting structure will be semiconductor (but for the 3p+2 family of Figure 1.2(b), which we will adress in depth later). In the case of the zigzag GNR, one of those slices goes through the K point, resulting in Fermi-level states. [21, 18] Referring this to molecular orbital theory, they are defined as non-bonding states:[22] Even though they reside in a conjugated p-lattice, they are equivalent to unpaired p orbitals, half occupied, that don't take part in a bonding-antibonding system.

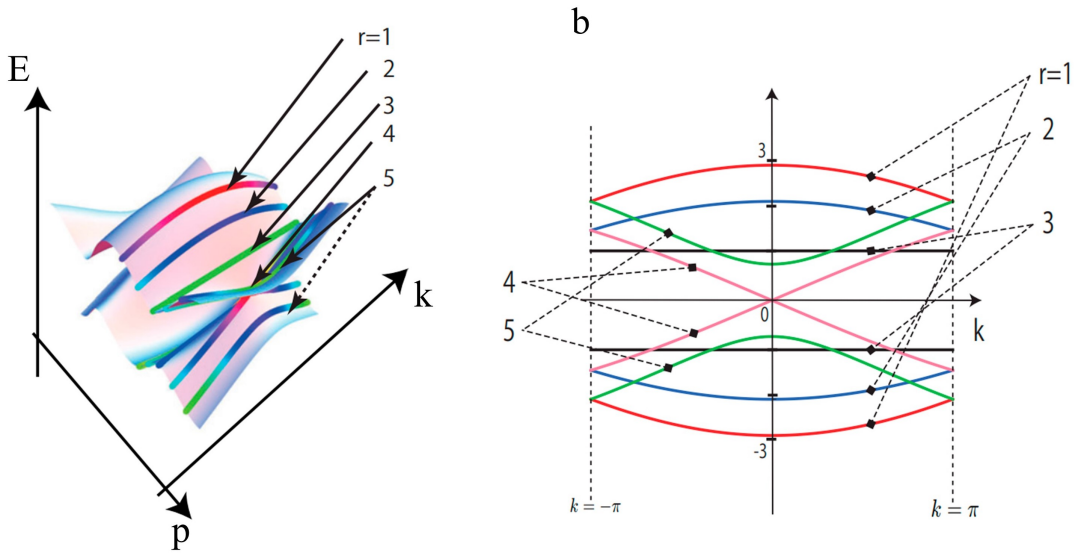

Figure 1.2: a) 3D plot of bulk graphene band structure. The bold lines are the 5-armchair GNR bands caused by its lateral confinement. b) The slices (bands) taken from a), with subband indexes, proyected onto the E-k plane, result in its electronic structure. From [18].

The solid-state physics perspective is general, well-justified and universal for every graphene nanoribbon. However, it lacks a "bottom-up" explanation: How a finite-size molecule with no topological frustration[23] or lattice imbalance[24] ends up with a first-level prediction including unpaired p electrons. Let's analyze the apparent paradox:

Before studying the subject, one might expect that each type of graphene nanoribbons would have almost identical properties. They are quasi-ideal hydrocarbons in which every atom has a similar environment to the rest. Could the edge hydrogens make the difference? If considering just each C sp^2 atom by itself, the difference is not remarkable. Between a three-carbon bonded and a two-carbon+hydrogen the difference seems minimal, a slight change in the partial charge caused by inductive effect.[25] The difference we are referring here causes individual 3 eV bandgap unit-cells to form metallic, gapless ribbons.

This long-range emergence[26, 27] of bands is caused by the fundamentals of π conjugation.

The nature of a π lattice departs from its σ-stabilized scaffold: The orbitals involved 'only' have planar directionality.[28, 29, 30] Let's make a comparison between the two types of bonds. Obviating the exception of diatomic hydrogen, a σ bond is always formed by an hybridization of s and p orbitals, sometimes even d. The resulting hybrids point in the direction of the bond, one for each bonding atom. Without getting into the deep waters of quantum interaction, two σ neighbouring bonds relate with each other exclusively through inductive effects.[25] In contrast, π bonds are formed by p_z orbitals (at least for the first row of the periodic table). The π symmetry of the p_z orbital is characterized by a C_∞ vertical axis. It is not directional in a first instance, thus able to hybridize with any nearby orbital without preference. For polyaromatic hydrocarbons (PAH), there is a single p orbital for each atom, which means, it is exclusionary.

Let's imagin a carbon atom from a PAH with its three neighbouring carbons (a,b and c): Strengthening the bond with "a" and "b" atoms, weakens the bond with "c". Therefore, it will require a stronger bonding with their farther neighbours (d and e) to get a full stabilization of their four valences. This alternation in the bonding can be translated as alternating hopping constants in the tight-binding model. The effects are long-range modulations, convoluted like Bloch's functions, which fade the frontiers of molecular bond order theory with solid-state electronic bands.[31] Those simple rules give birth to conjugation, aromaticity, π radicals, or graphene's electronic structure.

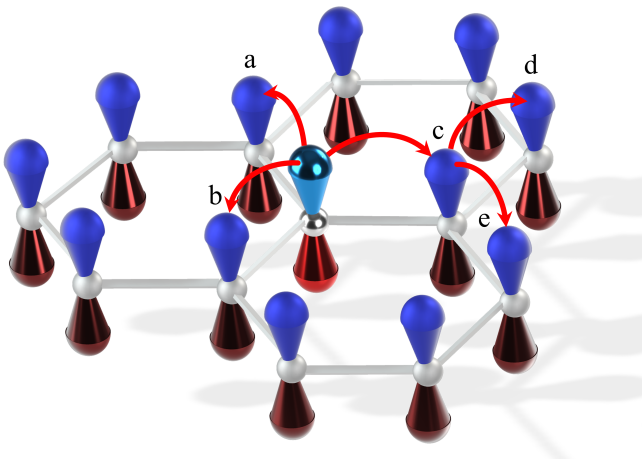

Figure 1.3: Graphene detail. The p_z orbital of the central carbon is forming π bonds with a,b and c p_z. The total π character of $a+b+c=1$ stabilized valence. The same rule is applied to the b atom π bonds, it means, $a+d+e=1$. As a result, the strength of b and c bonds affects d and e even though they comprehend different atoms.

1.1 Reductionism, Reasoning and Emergence

The whole landscape of the properties related with PAHs roots into the same causes: The nature of π bonds. However, it was impossible deducing a priori all the related physics observed in GNR in the last decade. As it is written in "Roald Hoffman on the Philosophy, Art, and Science of Chemistry":[32]

"Simplistic reductionism is alive and well whitin science. (...) There are theoretical chemists who really think that all the concepts of chemistry would be clarified by rigorous definitions, of course based on physics. (...) Here is what I believe: In dealing with the complexity of this world, human beings adduce explanations in two modes. Vertical understanding is the classical reductionist kind. Horizontal understanding is expressed in the

concepts, definitions and symbolic structures at the same level of complexity as the object to be understood. Horizontal explanations, like dictionary definitions, but richer, are quasi-circular. My stronger claim is that most concepts in chemistry that have proven productive in the design of new experiments are not reducible to physics. To be specific, I'm thinking of aromaticity, (...)

Reductionist claim that they labor to reach the roots. And once the elementary particles are understood, and all the forces too, then one could move upscale, and with the workings of those building blocks and forces, a bit of the aleatory thrown in, the macroscopic would emerge. At any level. I'm skeptical; I've hardly ever seen a soul move upscale.

I think chemistry does move upscale, climb ladders of complexity, creates new molecules and emergent phenomena. It does so by alternating small riggs of reductionist analysis with lots of intuitive thinking on the horizontal level."

On this book Hoffman defends horizontal vs vertical reasoning; of intuition vs formal reasoning; and chemistry vs physics (not in vain he earned his Nobel prize in chemistry). Apart from the ruthless teasing that he enjoys to perform against physicists, let's emphasize an idea that has been explicited: He refers to "emergent" phenomena. "Emergence" is the association of individual, simple units into a collective entity whose properties are different to the sum of its parts.[27, 26]

This is an ambiguous definition, and it looks for that so. Emergence has been identified as such at the hexagonal shapes in ice crystals, the formation of nations, or

biological evolution. Any of those phenomena have a common factor: When considering the single unit that brought them (a water molecule, a citizen, or a monkey) you cannot predict the outcome of their aggregation.

Emergent phenomena can be measurable. For example, natural selection is well known. Sometimes to the point of being tuned at will, like the artistic sculpting of snowflakes.[33] However, from a single individual it would be impossible to predict what was going to happen. This matches with Hoffmann's idea of horizontal vs vertical reasoning. The conceptualization of what particles do compose a system (let's say, a GNR formed by carbon atoms) does not summarize the whole story. You may be able to obtain something close to its electronic structure from a tight-binding model, but is not until you understand what is really stabilizing its electrons (let's say, a Clar sextets rule) that you start to comprehend the presence of π radicals in it. You require the observation of many structures with similar phenomenology to trace a tendency. Its later abstraction will result in concepts like aromaticity, Hückel or Clar's rule. Those are trends which come from the observation of similar structures, and allow to predict the characteristics of yet-unexplored ones.

We left an open question behind: How a finite-size molecule with no topological frustration[34] or lattice imbalance[35, 36] ends up with a first-level prediction of unpaired p orbitals. Its origin has been connected previously with the nature of π conjugation. Along this chapter, we will summarize the already known concepts about polyaromatic hydrocarbon (PAH) conjugation in order to get closer to an answer. Let's start by the simplest phenomena and move towards more complex physics. That way, we can get to the roots of graphene nanoribbon theory through the same paths that explain aromaticity. An exercise

of horizontal reasoning.

1.2 History of aromaticity

The uniqueness of carbon was perceived from the earliest start of chemical science. Not in vain its diverse reactivity caused the scientist of the 18th century to defend the "vitalism": theory that describes organic compounds as embedded with a "vital force" impossible to replicate from inert sources. [37] This idea survived the formal proposal of elemental carbon in 1789, and even reached the XX century.[38, 39] August Kekulé discovered carbon tetravalency in 1857,[40] almost simultaneously to Archibald Scott Couper. There is a sorrowful story here: Due to a confusion of his superior, Archibald's work was published few months later than expected, and the rage and frustration for the delay costed him the position and mental health for life.[41, 42] Kekulé's fast development of carbon comprehension continued inexorably, and seven years later he proposed the cyclic arrangement of benzene.[43]

From that point, the field progressed in huge steps. Armstrong proposed the "uniformly distributed affinity" of the cycle, a primitive concept for the delocalization.[44] Bambeberg proposed the pentavalency of nitrogen in unsaturated heterocycles, referring to the lone pair of electrons it can give to a π system, years before the discovery of those subatomic particles in 1897.[45] After Armit and Robinson coined the term "aromatic sextet",[46] Pauling and Wheland developed, finally, a mature theory for aromaticity in 1935.[47, 48]

1.3 Aromaticity in graphene nanoribbons

Aromatic molecules are characterized by having delocalized molecular orbitals around their Fermi level. However, all conjugated molecules hold this characteristic, regardless of their stability. Hückel's rule (1931-1937)[49, 50, 51] discerns the conjugated monocyclic rings with 4n+2 electrons as the most stable ones, those defined as 'aromatic' due to the pleasant smell of the first that were studied (back when smelling your creations was a common practice by synthetic chemists). They show a higher thermodynamical stability compared to what could be expected from their elementary composition, also more stable than analogous linear molecules.[52] The ones with 4n electrons suffer from the opposite, they lack any aromatic stabilization and undergo distortions that break their conjugation. [53, 54]

Aromaticity is considered an open topic by some authors, which keep digging in its origin and building bigger, more exotic structures.[52, 56] However, we can get an intuitive idea of the origin of the additional stability by simple modellization. The resulting molecular orbital energies calculated from a first order tight-binding model are drawn in the figure 1.4.

The origin of Hückel's rule is so fundamental that it roots in rules of symmetry, geometry and group theory. A first insight shows that rings with an even number of carbons have two orbitals, fully bonding-antibonding as the most/least stables, marked in Figure 1.4 in blue. Discarding these two, the rest of the orbitals are degenerated in couples. If

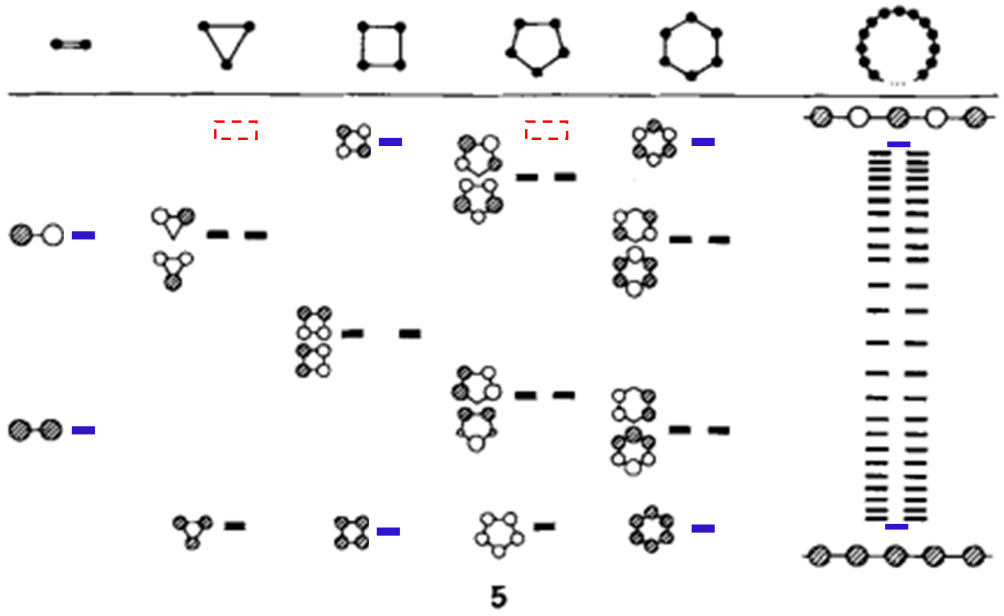

Figure 1.4: Conjugated rings series, with orbital energies and wavefunction phase sketched. Adapted from [55]. Fully bonding-antibonding pairs have been marked in blue, only present in the even structures. Uneven structures lack from a fully antibonding orbital, marked as red, dashed squares.

our system has 4n+2n orbitals (ethene, benzene) they will be symmetrically distant from Fermi level. Rings with an odd number of carbons (C_3H_3, C_5H_5) cannot generate a fully antibonding orbital, as they cannot have a perfect alternancy of the wavefunction phase (figure 1.4, red squares). Those rings with 4n atoms (C_4H_4, C_8H_8, $C_{12}H_{12}$, $C_{16}H_{16}$, Figure 1.5) host two molecular orbitals at Fermi with alternating bonding-antibonding character in their bonds, shifted by one carbon, which will be non-bonding in the net count, (Figure 1.5).

From this simple Hückel model we can already see how you can develop an intuitive vision of the unique stability of 4n+2 cyclic systems. This configuration splits symmetrically in energy, occupying every stabilized state and emptying the rest. In the case of the 4n systems, like the cyclobutadiene, you end up with two non-bonding orthogonal

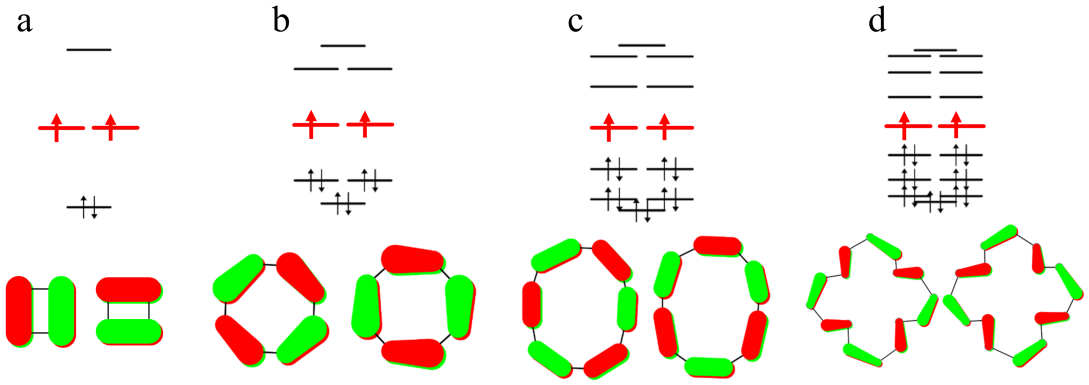

Figure 1.5: Members of the antiaromatic ring family with c=4n. a)c=4 b)c=8 c)c=12 d)c=16. The non-bonding states are plotted in the bottom.

states, half filled. In order to maximize stability, the system goes through a Jahn-Teller distortion in order to break the symmetry and stabilize one of them at the expense of the other. The stabilized one will will become fully occupied and the unstabilized one fully unoccupied, resulting in a net stabilization of the system.

Hückel's rule is accurate in the prediction of the stability of aromatic rings. However, it is just a first-order approximation that makes some assumptions: For it, every bond is identical in strength, and physical deformations or misalignments of the molecule cannot be predicted. The antiaromatic family shows the limitations of the method: It is able to predict the origin of its notable unstability compared to the rest of the cycles. Nevertheless, it misses the prediction of its consequences, which constists on a Jahn-Teller distortion that affects every member of the family. For the case of the cyclobutadiene, this rupture from D_4h to D_2h only affects to the bond order and atomic distance. For the cyclooctatetraene, figure 1.5 (b), the molecule escapes from the planar conformation to a D_2d. The distorted ring has a lower conjugation, therefore it is considered "non-aromatic" rather than purely

antiaromatic.

Hückel's rule only refers to monocyclic rings, so it didn't help to predict the distribution of aromaticity in poly aromatic hydrocarbons (PAH). Even tough a naive interpretation would consider every ring identical in aromatic character, experiments showed a different reactivity for each carbon. For that reason new empiric rules had to be developed for extended systems. Inspired by Armit and Robinson "aromatic sextet", Clar developed his sextet rule (1972).[57]

1.3.1 Clar' sextets rule

In a PAH, a Clar sextet is that benzenoid cycle in which the three double bonds are placed within it, resembling benzene (figure 1.6(a)). In order to make it easier to identify, it is often drawn as a circle in the middle of the benzene ring, as in figure 1.6(b). The higher the number of sextets, the higher the stability, considering that the rest of the factors (number of paired electrons, compensation of the nuclear charge) remain the same. Clar's rule states that for a given benzenoid PAH, the Kekulé's structure with the highest number of sextets will be the most influential one for its properties.[58] The presence of a Clar sextet in a specific ring is exclusionary for its nearest rings. If a structure can be drawn with two contiguous sextets sharing a double bond, it counts as a single one that oscillates between them, often signalled with arrows as in figure 1.6(c). It is considered a qualitative method of analysis, even tough it has physical implications (those rings holding a sextet in the most stable structure show a higher electronic density). [59, 58, 60, 61]

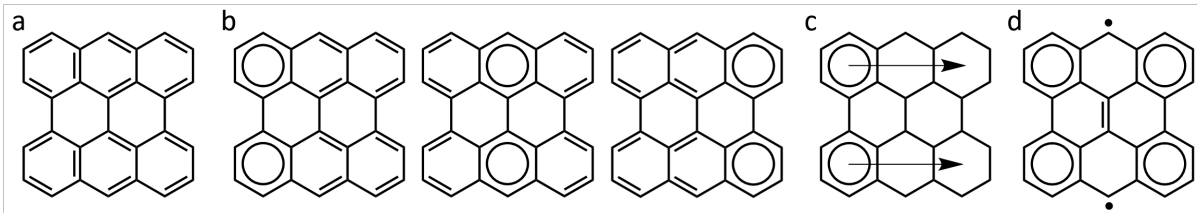

Figure 1.6: Different interpretations of a bysanthene aromaticity pattern. a) A Close shell bond distribution. b) Following "a" bond pattern, we can draw two Clar sextets in this structure. However, those could be placed in any ring. c)If the Clar sextets can be placed in different positions of the moiety, it can be represented by arrows along their path. In this case we see the typical "acene" bond configuration for both sextets. d) The open-shell way of drawing the structure allows to draw two extra sextets, in exchange for the presence of two radicals.

There are several attempts to quantitatively determine the stability given by a Clar sextet. [58, 62, 63] The resulting stabilization is unexpectedly high: The formation of three Clar sextets is close to the formation energy of a double bond.[63, 64] From here, we can start to glimpse the reason of π radical formation. Sometimes, the structure of a molecule that reaches the highest number of Clar sextets is unable to stabilize all of its p_z electrons though π bond formation (figure 1.6(d)), which we often refer as an open-shell structure, in opposition to the close-shell structure without unpaired electrons. The leftover single electrons are not stabilized, but the total stabilization caused by the higher number of sextets compensates. Trinquier and Malrieu looked for the limits of π radical character caused by Clar sextets: a reduced radicalary character can still be observed for structures where the open-shell form exceeds the close-shell by one single Clar sextet.[62] It is a matter of thermodynamic stability: there is an exponential relation between the total stability of a resonant structure (a Clar resonator) and its weight for the net electronic configuration of the molecule. [58] For the specific example employed along this explanation, which is

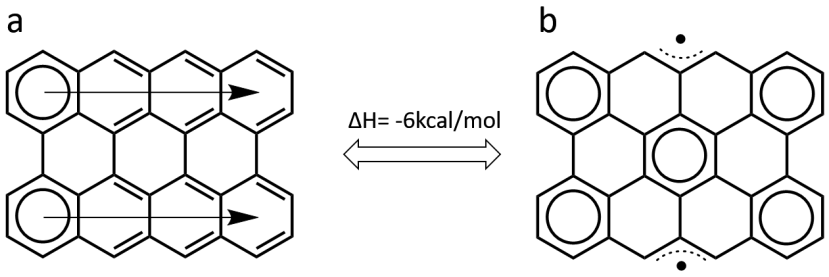

Figure 1.7: Different resonant structures for peritetracene. The close shell structure a) has two Clar sextets against the five of the open-shell structure b). Following the prediction of Trinquier, the b) structure is more stable.

bisanthene, it has been calculated a mainly close-shell character.[65]

1.3.2 Zigzag edges in graphene nanoribbons

We can transport the Clar sextet method to periodic graphene nanostructures (GNR): How many Clar sextets we have by unit cell in exchange of how many radicals. For the case of the zigzag edged graphene nanoribbons (like the short peritetracene from figure 1.7), Clar's rule drives us directly to their edge state magnetism. Due to their topology, they can be drawn with a fixed amount of Clar sextets, no matter their total length. The total amount of sextets is defined by their width, as figure 1.7(a) shows. The arrows there run along the positions where that same Clar sextet can be drawn, keeping their number constant regardless of their length. Characteristic acene-like double bond arrangements can be appreciated in this PAH, see figure 1.6(b), 1.7(a). In order to maximize the number of Clar sextets, we can draw them as figure 1.7(b) shows. It is the only configuration with the highest amount of sextets. The reason is simple: Clar sextets cannot share bonds; they have to be

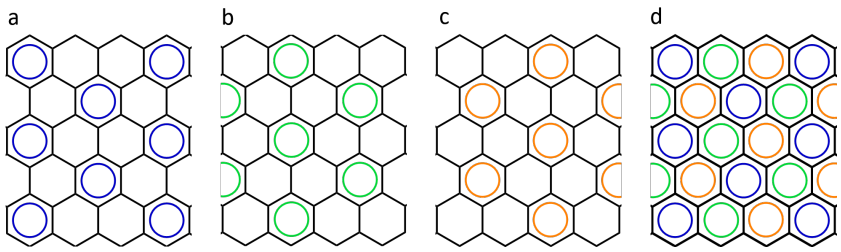

Figure 1.8: The three different sublattices of a graphene sheet.

isolated from each other. As a result, the graphene pattern can be divided into three ring sublattices, drawn in figure 1.8. For peritetracene 1.7(b), all Clar sextets place in one of the sublattices.

For the rest of zigzag GNRs, the majoritarian sublattice depends on their edges. However, any wider/longer than peritetracene with regular edges is going to have a major Clar resonator with unpaired orbitals at its edges. Peritetracene itself has three extra sextets in exchange for two unpaired electrons. Those electrons are not in specific carbon atoms, but delocalized in "magnetic islands along the edges".[66, 62] The unpaired states can develop periodically for longer zigzag GNRs on each edge.

The acenes, as the narrowest zigzag GNRs, resemble in behaviour to the zigzag ribbons. When they grow 7-rings or longer (heptacene), they become predominantly open-shell. [67] However, conventional Clar sextet's theory does not justify it. The presence of unpaired electrons only creates one sextet, not enough to justify their open-shell character in thermodynamic terms. Yeh et. al[63] argued it in terms of Kekulé structures: While the number of close-shell structures increases linearly with the length, the abundance of open-shell resonant forms grows exponentially. the combined weight of all open-shell structures

(which are ten times more abundant) surpasses that of the stable close-shell structure. This trend holds for longer acenes: around the 14-acene, resonant structures with four unpaired electrons become ten times more abundant than those with two unpaired electrons, making them the predominant structure.

Chiral graphene nanoribbons (ch-GNRs) are the result of a periodic combination of zigzag and armchair edges. The most accurate definition would be “prochiral”, as their chirality is positional: each isomer could be turned into the other by flipping.[68] However that process has never been observed on the surface, it would be highly energy demanding, so we can claim that surface really causes a symmetry breaking factor with practical consequences. The "chiral" term is justified by the chirality of the original precursor and polymer which take part in the ribbon synthesis. The chiral precursor selectively binds to form homopolymers, which are polymers composed of a single enantiomer, preserving its chirality. After planarization, this leads to the formation of a specific prochiral isomer on the surface. This process exhibits total efficiency, as synthesizing ribbons from an enantiopure sample results in a pure sample of the prochirality derived from it.[68, 21, 69]

The aromaticity of ch-GNRs depends on their width and length, and the characteristic length of each edge segment as well. In the figure 1.9 we can see the intrinsic dependence with their width. The wider (3,1,8)-chGNR, schemed in figure 1.9(a) are strictly open-shell.[12] Its zigzag edges are far enough to generate four Clar sextets per broken bond. As a result, each edge hosts metallic states coupled magnetically to the opposite edge states. For narrower (3,1)-chGNR, the number of Clar sextets per unit cell (UC) decreases and the edge states of both sides hybridize until reaching the predominantly close-shell structure,

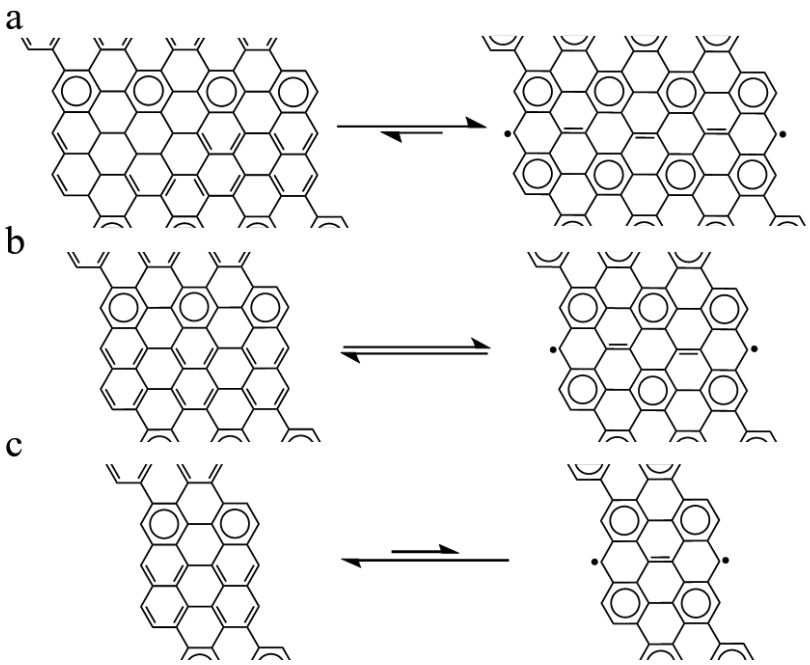

Figure 1.9: The family of (3,1)-chiral graphene nanoribbons. The numbers define the (zigzag, armchair) ratio. An additional number defines the width, like a) (3,1,8)-chGNR b) (3,1,6)-chGNR c) (3,1,4)-chGNR. Longer arrows mark the predominant structures.

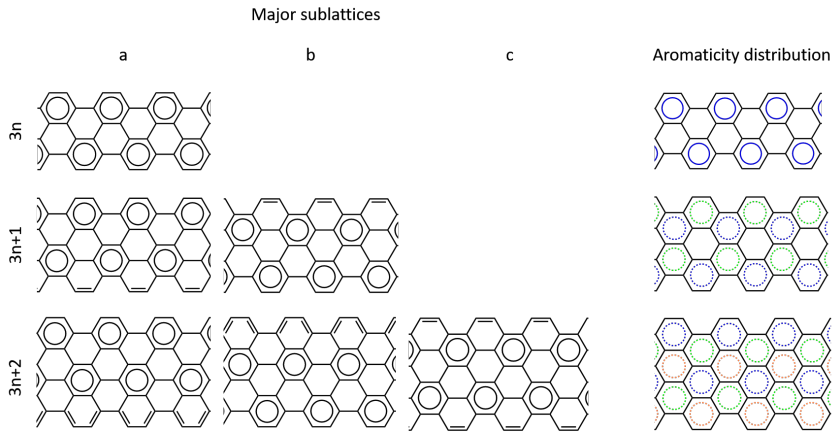

Figure 1.10: The differences in aromaticity between the three families of armchair ribbons. The major sublattices are those with the highest amount of Clar sextets per unit cell, for each ribbon.

figure 1.9(c).[12]

1.3.3 The armchair graphene nanoribbons' family tree

Armchair graphene nanoribbons (aGNRs) share specific similarities. Due to their orientation with respect to the graphene lattice, their zigzag edges just appear at the terminations of the ribbon. For them, unpaired orbitals are not periodic but punctual at both ends (if present at all). This is not a premise, but the natural result of drawing the maximum number of Clar sextets in the ribbons. The presence of radicals is variable whatsoever, and depends on different factors, such as the specific width of the ribbon or the atom row in which it is terminated.

Let's develop the armchair GNR families in relation with their aromaticity. We can start by the easiest case, the 6-aGNR, shown in figure 1.10(top). The number defines the

amount of transversal atom rows of the ribbon. For 6-aGNR, we can draw the maximum number of Clar sextets by placing them in in the external rings of the ribbon, in a fixed configuration. The reason is simple: For this specific graphene ribbon, one of the hexagonal sublattices is more abundant than the other two, containing more rings. As a result, the Clar resonator located on that sublattice plays a major role, defining the electronic properties of the ribbon.

Adding three extra rows of carbons to the armchair edge is equivalent of adding one row of hexagons to each sublattice. For that reason the 6, the 9, the 12-aGNR will have a similar aromaticity distribution. In consequence, they are conventionally grouped into the 3n-aGNR family. This family is characterized by having a semiconductor character, with over 1 eV bandgaps on Au(111).[70]

While adding three rows of carbon atoms translates into analogous aromaticity, adding a single row results in a completely different behavior. The 7-aGNR, figure 1.10 (mid) was the first ribbon synthesized on surface and that one whose end states (unpaired electronic states present in its ends) were first characterized.[7] Its hexagonal lattice has two majoritarian sublattices, figure 1.10 mid (a,b), so there are two different structures that match in amount of Clar sextets. The end result will be a combination of both, with the remaining hexagonal sublattice deficient in electronic density compared to the other two. The presence of radicals at its ends is not trivial (no pun intended): Anthracene-wide ends on a 7-aGNR carry an open-shell character with them, while adding half a unit cell on each end would result in a close-shell structure.[71] This aromaticity distribution is common for any aGNR with 3n+1 rows.[72]

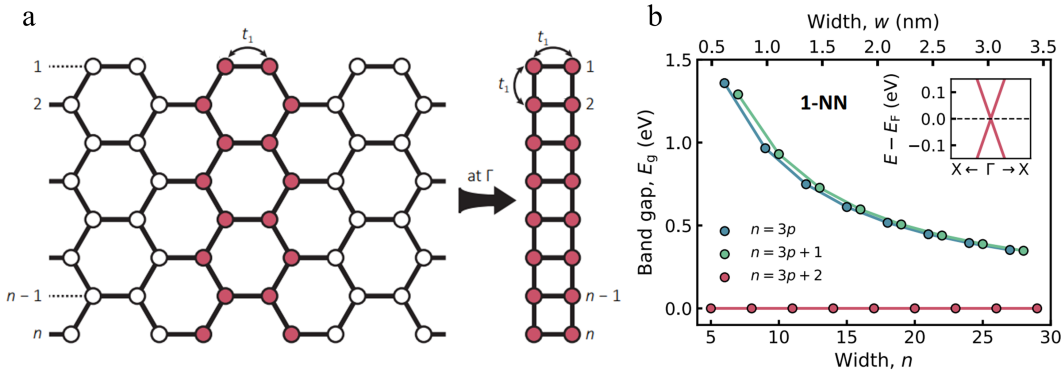

Figure 1.11: a) 8-aGNR, with drawings of the first-hopping constants for the tight binding model. It shows the transformation of the periodic ribbon in a ladder diagram that Tepliakov employs to find hidden symmetries at Γ. *b) Evolution of the energy bandgap,* E_g *first-neighbour tight-binding calculated bandgaps for armchair GNR. Width (n) refers to the number of rows of the ribbon. The inset shows the band structures in the vicinity of the* Γ *point for the 3p+2 ribbon with n = 8. From [73].*

The 3n+2 family is problematic for Clar's theory: The periodic ribbons hold the same number of rings on every hexagon sublattice. This causes the three sublattices to have identical aromaticity in the final electronic structure, as each Clar resonator has the same weight.[58] The implications of this absolute bond equivalency are not straightforward. However, a Hückel model can help with its interpretation.

1.3.4 Hückel modelling of armchair graphene nanoribbons

A rigorous simulation of a GNR should have an infinite number of unit cells, resulting in a band structure like the one of Figure 1.2 (b). An alternative modelling method consist of "cyclying" few unit cells as if we were dealing with a circular ribbon:[74, 73] The ribbons are periodic, so each carbon of the contiguous unit cells has an identical twin within

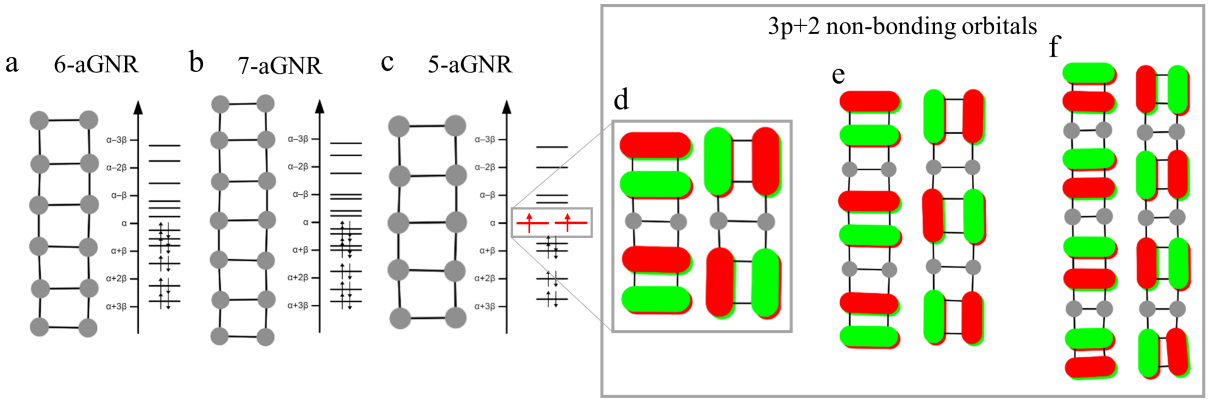

Figure 1.12: Example of the tight-binding model for each of the three families. a)3p b)3p+1 c)3p+2. Every 3p+2 develop non-bonding Fermi level states with the same pattern, characterized by the cyclobutadiene moieties isolated by non participating rows. Here we can observe the non-bonding states for the d)5-aGNR e)8-aGNR f)11-aGNR

our unit cell. The solution for a finite model is to replicate this intercell bonds with fictional, intra-cell conections which will emulate their hoppings, as in figure 1.11 (a). [74, 73]

The result is a ladder scheme of cyclobutadienes fused together, with as many rows as the modelled ribbon had. Due to the simplification of the model, states don't disperse as bands,so we get a "frame" of what the states look like at the Γ point. In spite of its similarity with cyclobutadiene, the ladder distribution shows a bandgap for both 3n and 3n+1 rows, figure 1.11 (a,b). For the 3n+2 whatsoever, it estimates two non-bonding Fermi level states shown in Figure 1.12(c). If we take a look at those two non-bonding states in figure 1.12 (d-f), we can see how their distribution resembles a stacked pile of the cyclobutadiene non-bonding states of figure 1.5(a) separated by rows of carbons with no DOS.[73] It is an interesting coincidence: the structures with fully delocalized aromaticity (3n+2-aGNR) are predicted to have non-bonding states. One way of understanding it is that highly conjugated

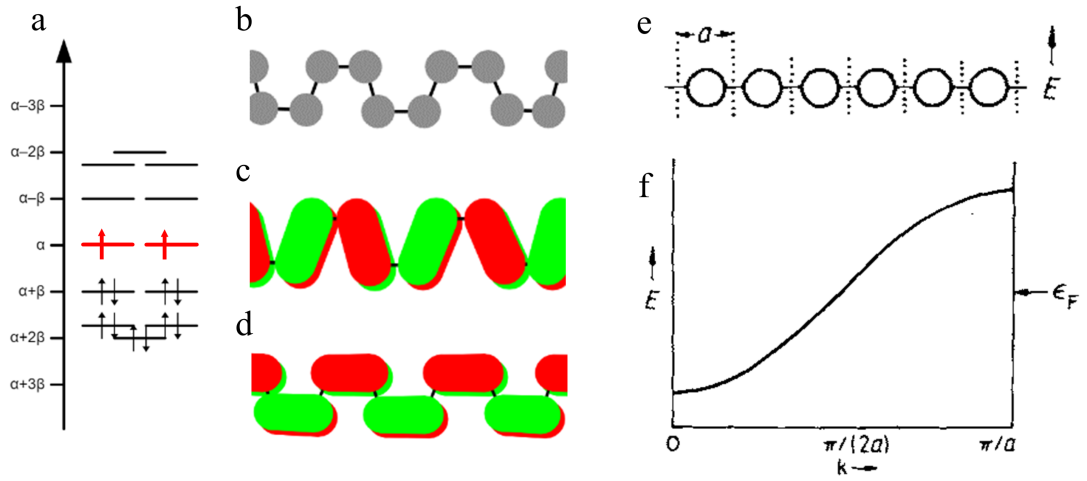

Figure 1.13: a) Molecular orbital energy diagram of six cell cis-polyacetylene, where we can see the two quantized non-bonding states. b) Molecular structure. c) and d) Non-bonding states, with complimentary wavefunctions. e) Simple modelling of a periodic linear polyacetylene with one atom per unit cell. f) Its energy diagram for the continuous π band, crossing the fermi level (ϵ_F). All the calculations are performed a first neighbour tight-binding model.

molecules have lower bandgaps. For the 3n+2 family, as the epitome of delocalization, tight-binding predicts a metallic ribbon.

By comparison with antiaromatic rings, we know that the molecule shown in Figure 1.12 (c) would undergo a Jahn-Teller distortion, similar to cyclobutadiene. However, the 3n+2 ribbons depart from the antiaromatic rings in the periodicity of their structure. In the same way, the distortion should be periodic as well.

1.4 π radicals

In that way, the polyacetylene may be a closer comparison to the 3n+2 family and will shed some light about the mechanisms determining their electronics. Its cis configuration (Figure 1.13 (b)) can be discretized by connecting its first atom to the last. That way we get the same result: Two non-bonding states (Figure 1.13 (a)) with alternating DOS (Figure 1.13 (c, d)). Their distribution is analogous to the non-bonding states along the edges of the 5-aGNR (Figure 1.12 (d)) or the antibonding cycles. However, as we increase the number of atoms , the discrete orbitals form a continuous π band, shown in figure 1.13 (f).[55]

1.4.1 The Shu-Schrieffer-Heeger model

The model consists of a chain of C sp^2 atoms. We can understand it as a one-dimensional chain of p_z orbitals, where each atom binds to its two neighbours. Prior to chemical distortions caused by the sigma bonds, they result in a single atom unit cell, of length=a, with identical hopping constants, figure 1.13 (e).

The model predicts for this system to be metallic. However, measurements of undoped polyacetylene found a semiconductor with a 1.5 eV bandgap.[75] The reason behind resembles the cyclobutadiene-case: a periodic distortion keeps the system from having semioccupied states at Fermi.

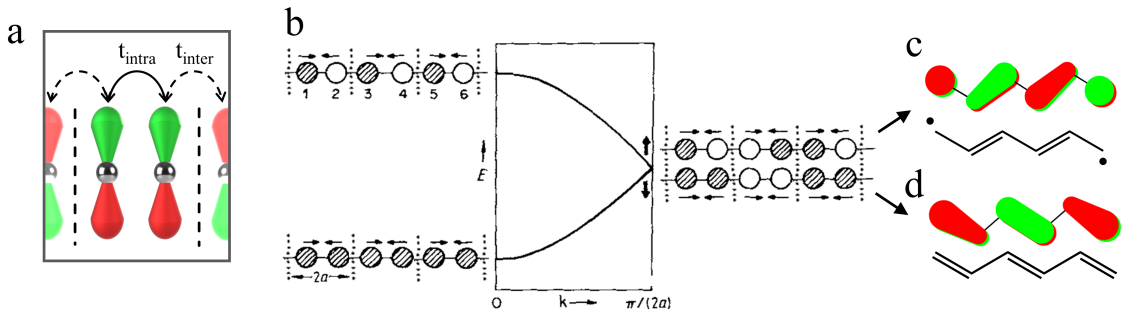

Figure 1.14: a) A two-atom unit cell of polyacetylene including the hopping constants. The orbital configuration represented relates with the d) state. b) Energy graph of its π band folded. Each circle represents a π orbital, with color-coded phase. The arrows show the effect of Peierls distortion for increasing $r = t_{intra}/t_{inter} > 1$. *As a result, the band splits to open a bandgap, filling (d) and emptying (c), otherwise half-filled. The opposite distortion* ($r < 1$) *would populate the topological state (c) with solitons at positions 1 and 6. Figure b) from [55]*

The C sp^2 chain breaks its symmetry by grouping the orbital sites in pairs (Figure 1.14 (a)). In consequence, the π band folds in two fully filled/empty bands. This phenomenon can be modelled by defining different hoping constants for the intra (t_{intra}) and intercell (t_{inter}) spaces. As the ratio r=t_{intra}/t_{inter} increases, a bandgap opens at the Fermi level, as it is sketched by the arrows in figure 1.14(b). We can conceptually translate this as distributing the atoms in alternating double-single bonds. This effect is called Peierls distortion.[76, 77]

Since we have an even number of carbon atoms, they can be divided into pairs without any leftovers when $r > 1$, as shown in Figure 1.14 (d). However, an interesting phenomenon occurs when $r < 1$. If the intercell hopping exceeds the intracell hopping, the onset of the empty band crosses Fermi and the orbital depicted in Figure 1.14 (c) becomes

populated. This leaves the terminal π atomic orbitals unpaired as neutral solitons without another electron to couple with.[78, 79] For $r < 1$, the system stabilizes unpaired electrons in the π-network, creating single states that are protected by the topology of the material.

However, the modelling doesn't imply that this phenomenology is going to be the most stable, spontaneous behaviour. The pure polymer exhibits a semiconductor bandgap and does not display magnetic properties. For the n-doped polyacetylene, however, the c state gets filled, and it is possible to detect the presence of solitons.[78, 80, 81, 82]

Similarly, in the case of the 3n+2 family, we find a situation analogous to that of the undistorted model, with two bands intersecting at the Fermi level, making a stabilizing distortion likely. However, due to the more complex nature of this system, intricate distortions may arise, requiring the use of more advanced analytical tools to understand it.

1.4.2 What is topology?

Formally, topology is "the branch of mathematics dealing with those properties of a geometrical object (of arbitrary dimensionality) that are unchanged by continuous deformations".[83] It has been implemented in multitude of applications outside its theoretical field, such as biology,[84], computer science,[85] and condensed matter physics.[86, 87] Here, topology can predict the appearance of electronic states of lower dimensionality at the edges of the system studied. A material that gives origin to topological states is referred to as topologically non-trivial. Those states appear as the result of abruptly ending a periodic

band of the bulk with significant weight at the transition with the vacuum or another trivial phase.

The magnitude that defines the topological character of a band is its Zak phase (γ), which is obtained from the integral of the Berry connection.[88] The mathematical definition of this entity goes out of the scope of this thesis. However, a concise summary of its application to graphene nanoribbons, as systems with inversion/mirror symmetries centered around the origin of the unit cell, reads like this:

The topological character of a GNR is defined by the Zak phase of its occupied bands. For those, (γ_{total}) = ($\gamma_{intercell}$) = π for topological bands, and γ_{total}=0 for trivial ones. The underlying reason is that vacuum is considered to have γ_{vacuum}=0. It is at the transition between two different topological regimes where the topologically protected states emerge, as a border effect.[89, 71] The topological invariant ($\mathbb{Z}_2$) summarizes the topology for every band of a GNR, resulting in $\mathbb{Z}_2$=1 for the topologically active ribbons and $\mathbb{Z}_2$=0 for trivial ones. For reference, r>1 polyacetylene would be $\mathbb{Z}_2$=0, while r<1 polyacetylene is $\mathbb{Z}_2$=1, topologically non-trivial.

Topology is a powerful analytical tool for understanding the electronic properties of solids. It allows us to relate the presence of an single state with the filling of a specific non-trivial band.[91] When a modification is made to the material causing the highest occupied band (trivial) and the lowest unoccupied band (topological) to cross at the Fermi level, a topological transition occurs. This is illustrated in Figure 1.15.[92]

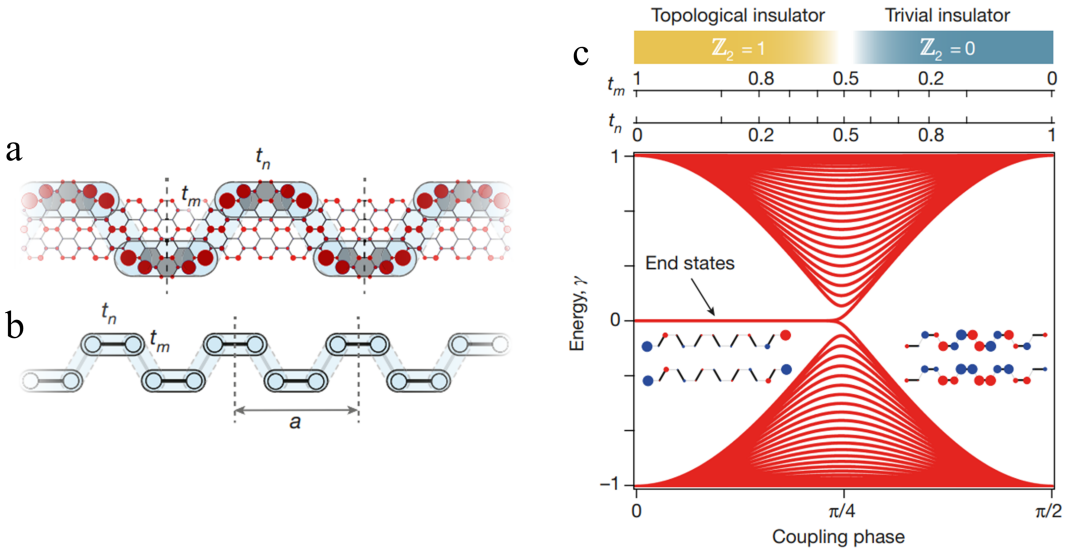

Figure 1.15: Topological analysis of a) ribbon electronic structure. a) Molecular structure of the ribbons, with four zigzag segments per unit cell. b) Tight-binding model of the ribbon, with t_n as the intra-edge hopping constant and t_m as the inter-edge. c) Electronic structure of a 25-dimer chain as a function of the phase, related with $t_n + t_m = 1$. As $t_m > t_n$ (from right to left), the bands cross and topological end states appear at Fermi level. From [90].

The ribbon hosts single states at its zigzag edges, which couple through different hopping constants depending on their relative configuration, enabling its bandgap to be modelled at will. The transition from a trivial to a topological regime is illustrated in Figure 1.15(c) as the bands cross, which is experimentally referred to as "gap-closing" [93, 94] followed by a "reopening" [95, 96]. To induce a topological transition in the ribbon, the bands involved should have different symmetries, which is indicative of opposite Zak phases [93].

All of these phenomena are well understood by mathematical theory. However, the terminology inherited can be confusing: the "topologically protected states" are by definition shielded against deformations on the phase edge, as shortening or extension would only displace the topological state. This transformation can be translated, while maintaining the model, as subtracting or adding whole unit cells to the ribbon. However, deviating from the prescribed rules of this protective mechanism, such as by introducing an additional atom at the termination of certain ribbons, would inevitably lead to the quenching of their single states, as will be elucidated in detail within this thesis [97]. Similarly, adding half a unit cell to each ribbon end would produce a similar effect: a punctual chemical modification in real space but a global shift of the unit cell for reciprocal space, resulting in a ribbon with the opposite topology [71, 98]

1.4.3 Ovchinnikov's rule and topologic frustration

We have described how the aromatic stabilization or the molecular relaxation can lead to topologically non-trivial magnetic states. However, other principles can lead to unpaired orbitals in a more direct way, linked to the intrinsic topology of some structures.

It is possible to simplify our understanding of atoms by reducing them to "punctual particles that pair". By doing so, we can focus on their fundamental behavior without getting bogged down by their individual properties. We can start from any given benzenoid PAH. In this lattice, each atom binds to its three-closest neighbours, and no other. Due to the symmetry of the material, this divides the honeycomb lattice in two trigonal carbon sublattices, in which each carbon only binds to the opposite sublattice carbon atoms (red and blue in figure 1.16). This simmetry principle is what causes the graphene unit cell to host two atoms, one for each sublattice.

The two sublattices stabilize and cancel out each other's free valences. Therefore, it is necessary for both sublattices to match in the number of carbon atoms in order to form a close-shell structure. If there is a mismatch in the size of the sublattices, it can induce a net magnetic moment in the system, resulting in unpaired states that align ferromagnetically, as illustrated in figure 1.16(a). This phenomenon is known as Ovchinnikov's rule, and it is described by $S_{GS} = |n_b - n_r| + 1$ representing the spin multiplicity of the system, and n_b, n_r being the number of atoms in each lattice. [35, 36]

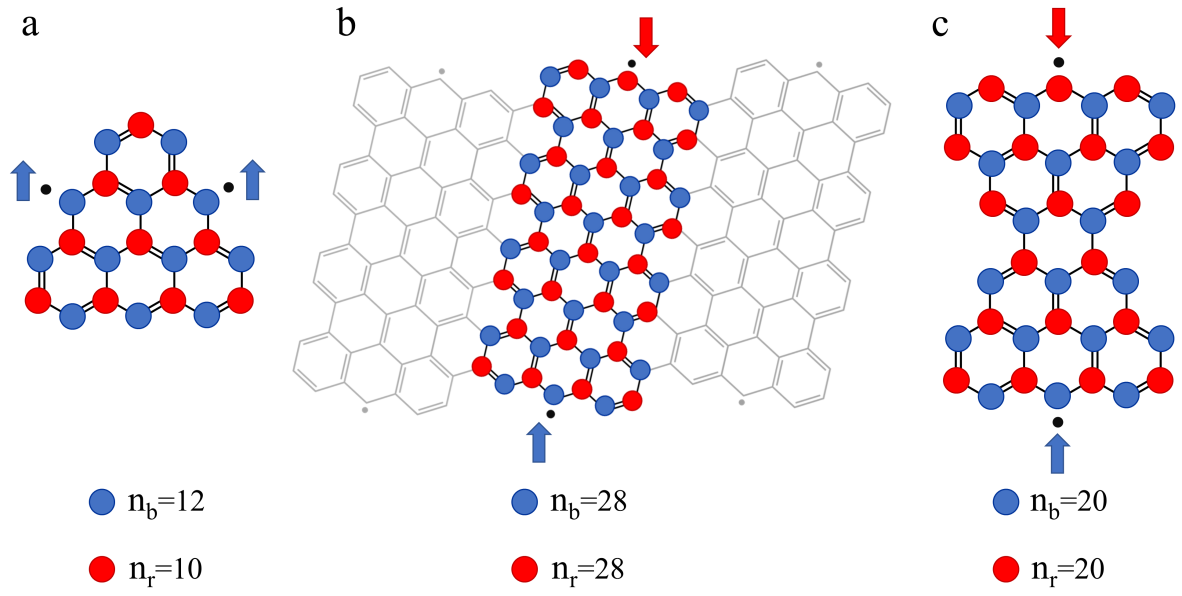

Figure 1.16: Different consequences of the Ovchinnikov's rule. a)Sublattice imbalance in 3-triangulene led to ferromagnetic spin coupling. S=1 b)Metallic 3,1,8-chGNR, with its aromatically induced spin-polarized states antiferromagnetically coupled. c) Clar's Goblet with unpaired orbitals due to its topological frustration.

This rule, which is referred to as Lieb's theorem by many current authors, has implications that extend further. Empirical observations have revealed a trend in the ordering of magnetism, where unpaired states residing in the same sublattice align ferromagnetically (and vice versa), irrespective of the principle that originally promoted their appearance in the first place. [36, 99, 100, 101, 102, 103, 104]

Another case in which a material can exhibit magnetic activity is known as "topological frustration." Similar to the way Clar sextets can prevent single states from coupling in open-shell molecules, structures lacking sufficient π bonds between their two sublattices show single states. Consequently, instead of containing magnetic islands where the unpaired orbitals are located in one sublattice, these molecules have structural islands separated by insufficient connections,[62] wherein the majority sublattice determines the net spin.[34] Other phenomena, like substitutional heteroatoms or non-benzenoid arrangements, can lead also to magnetically active nanographenes.[103, 102, 105]

After this introduction, we can get an insight to the real nature of 5-aGNR: What happens to the bands matching at Fermi when we trascend the model, and how previous works adressed their bandgap from experimental and theoretical results.

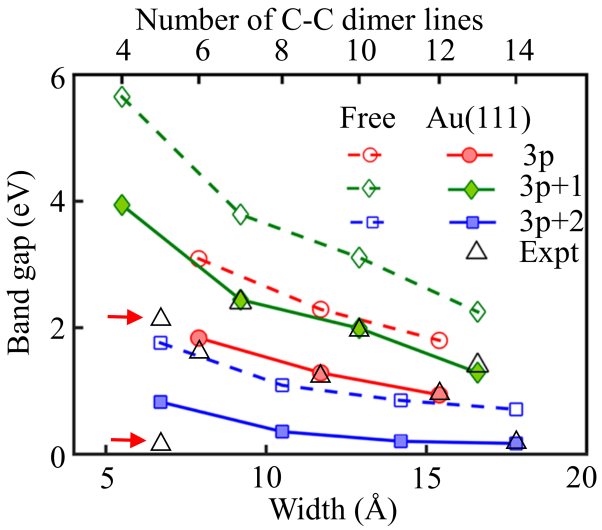

Figure 1.17: Theoretical prediction for aGNR bandgap free standing (Free) and on Au(111). The use of Local Spin Density Approximation (LDA) + GW predicted most of the experimental results (Expt), but for the 5-aGNR (red arrows). Theoretical data from [108]. Experimental data from: 5-aGNR[106, 107]. 7 from [109, 7]. 6,9,12 [70]. 10 from [72]. 13 from [110]. Original graph from [111].

1.5 First characterizations of the 5-aGNR

The 5-aGNR were synthesized for the first time in 2015 by two different groups, months apart.[106, 107] Both of them employed brominated precursors on a Au surface for the synthesis. Zhang employed a tetrabrominated one, while Kimouche bet for a dibrominated one that required extra hydrogens to cleave. This process generates an excess of hydrogen that neutralizes some termini, yielding finite ribbons. By contrast, the lack of atomic hydrogen on the surface of Zhang's samples resulted in long, kinked 5-aGNR stripes.

Despite the different pathways employed, the resulting ribbons must have similar electronic properties. Zhang proposed a bandgap of 2.1 eV, but Kimouche contradicted him,

showing states around the Fermi level, and framed the 5-aGNR as quasi-metallic structures with a 100 meV HOMO-LUMO gap.

To this point, we haven't seen evidence against the idea of metallic 5-aGNR. However, all the simulations of ribbons presented were Hückel-like models. Those relate with some advantages, like the direct addressing of the properties observed as electronic or aromatic effects. The cost for this is falling into some simplifications. As this models do not relax to an energy minimum, they naively consider every hopping constant equal, which is, every bond equivalent. For that reason, they are not as representative of real systems as other simulations. State-of-the-art simulations of graphene nanoribbons done by Kharche et al. estimated the bandgaps of 5-aGNR free-standing and on Au(111) using a GW model complemented with a phenomenological addition of screening potentials, resulting in a 0.88 eV gap for infinite 5-aGNR on the metallic surface and 1.1 eV gap for free standing ribbons, in stark contrast to the experiments. [111]

Previous experimental evidence and theory contradict each other. Still, there are differences between them which could be causing the discrepancies: the calculations simulated infinite ribbons while the measurements were done on short graphene nanoribbons. That is some phenomena related with the border effects could be causing the difference between the two. All in all, based on this premise, we decided to give another look to the 5-aGNR.

CHAPTER 2

Introduction: Techniques

The instrumentation used in research is a critical aspect of our work. Some scholars have even proposed that technological advances are the main driving force behind the advancement of knowledge.[112] However, it would be a drastic oversimplification to neglect the contribution of experimentalists, which however, depend crucially on his/her instruments to work. In this chapter, the different resources utilized to develop our research will be outlined.

2.1 The vacuum system

It is responsible for the ideal conditions in which our experiments take place. Even tough it is a combination of many independent components, they have to be perfectly assembled to maintain an appropriate environment for the sample preparation and scanning. If one piece leaks, the whole instrument needs to be shut down until the air-tight seal recovers. That collective dependence is responsible for the idea of a single system.

The experiments were performed inside a Scienta-Omicron commercial equipment capable of reaching pressures around 1^{-10} mbar, in the range of ultra high vacuum, shown in figure 2.1. Such an inert environment allows us to synthesize highly reactive species, which otherwise would be degraded by the atmospheric reactants, (as we will demonstrate afterwards).

The system consist in three independent chambers, and a transfer bar to move

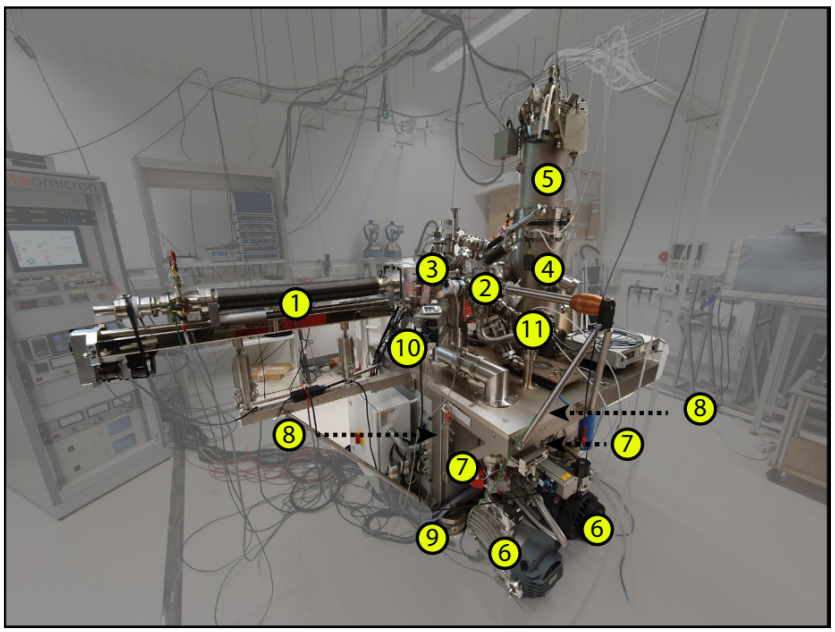

Figure 2.1: . Picture of the vacuum system. To point out, the manipulator (1), the fast-entry chamber (2), the preparation (3) and the STM chambers (4) under the cryostat (5). Two rough pumps (6) as secondary pumps for the turbo pumps (7) lower the pressure. Additional ion pumps (8). There are also pneumatic damping legs (9), mass spectrometer (10) and evaporators (11). Adapted from [113].

samples in between (1): One purely dedicated to host the LT-STM and the storage of clean samples (4); a preparation chamber in which the sample cleaning and preparation take place (3), and a load-lock with a reduced size (2) and its own turbo-pump (7) solely dedicated to the transfer of samples from the atmosphere to the insides of the system. Another turbo-pump is connected directly to the preparation chamber (7). It allows the transition from the low-vacuum regime to the ultra high vacuum after the system was vented for rutinary maintenance, and sustains the ultra-high vacuum when specially hard degassings or ion sputtering need to be done. When there are no "dirty processes" happening inside, the vacuum can be maintained with two independent ion pumps in both STM and preparation chambers (8). Extra Titanium Sublimation Pumps (TSPs) are attached to both chambers (10). They are specifically good for the pumping of hydrogen, with which the rest of the pumps struggle. For measuring the pressure, two hot cathode gauges (model) are attached to the main chambers, plus an extra full-range sensor for the loadlock.

2.2 Scanning Tunnelling Microscopy

It is fundamentally based on the quantum tunnelling of electrons through a vacuum barrier. The classical mathematical description for this system would be:

$$\frac{p^2}{2me} + U_0 = E \tag{2.1}$$

where U_0 is the potential energy of the barrier, and the electron momentum, mass and energy are represented by p, m_e and E respectively. In this purely classical, non-

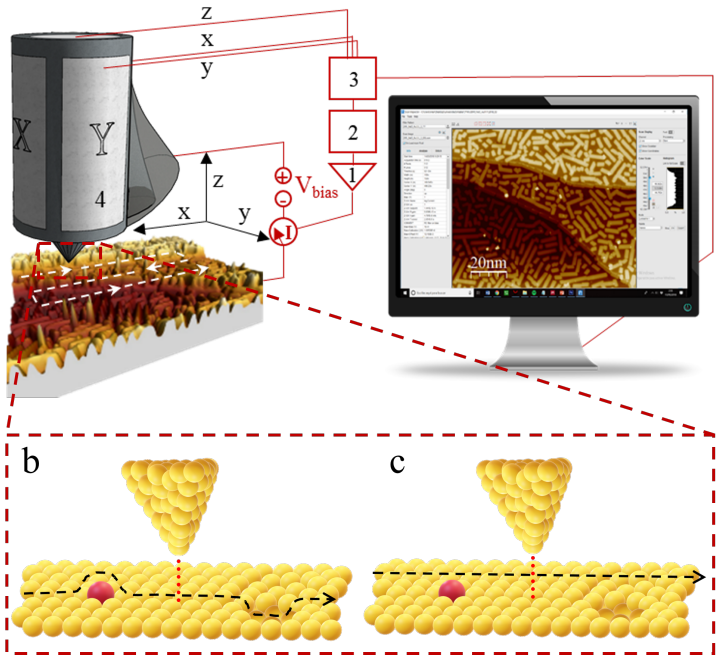

Figure 2.2: a) Infogram of the working mechanism of a single-tube STM. 3-Control unit. b)STM in constant current mode. The tip compensates the height changes, with z as the signal. c) STM in constant height mode. The tunnel current is the signal for the imaging.

relativistic interpretation, the outcome is univocally predicted: If $E > U_0$, the electron will leap through the potential barrier, otherwise reflected. In the more realistic approximation of quantum mechanics, the electron displays a wavelike nature. This property is the origin of a non-negligible probability of propagating through a barrier with $E < U_0$. In this frame the electron wavefunction is described by the one-dimensional stationary Schrödinger equation:

$$-\frac{\hbar}{2m_e}\frac{\partial^2}{\partial x^2}\Psi(x) + V(x)\Psi(x) = E\Psi(x) \tag{2.2}$$

The solution for an electron with energy lower than the potential barrier ($E < U_0$) is composed by different parts depending on the region:

I) For the incident and reflected wavefunction at the left side of the barrier ($x < 0$) the equation acquires a sinusoidal shape. A_1 is the incident wavefunction amplitude and A_2 for the reflected:

$$\psi_I(x) = A_1 e^{ikx} + A_2 e^{-ikx} \ \textit{with}\ k = \frac{\sqrt{2mE}}{\hbar} \tag{2.3}$$

II) Within the barrier ($0 < x < d$), the solutions have an evanescent[114] character with the form:

$$\psi_{II}(x) = B_1 e^{-\chi x} + B_2 e^{\chi x} \ \textit{with}\ \chi = \frac{\sqrt{2m(U_0 - E)}}{\hbar} \tag{2.4}$$

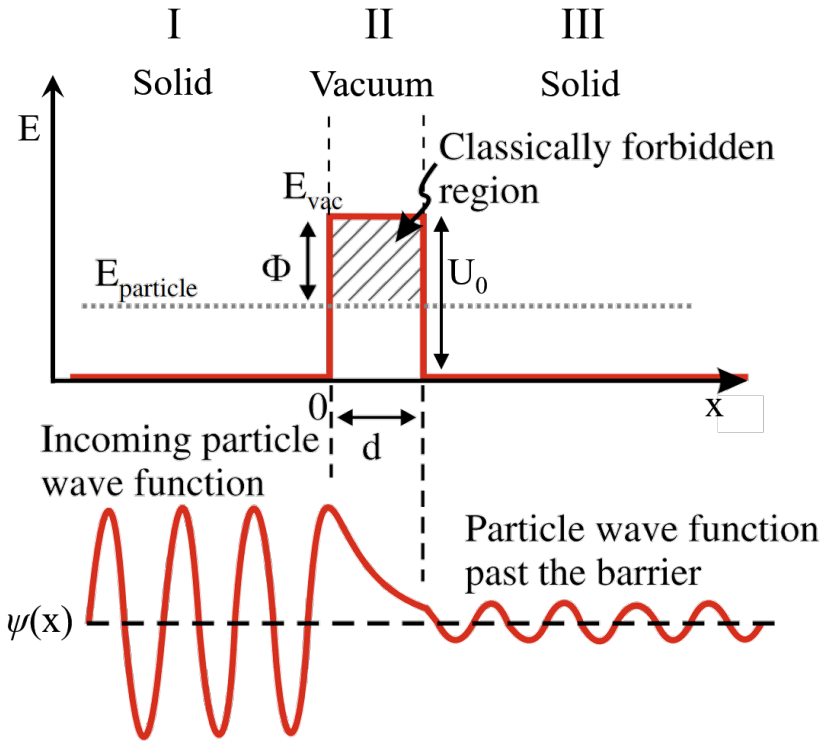

Figure 2.3: Model of an electron tunnelling through a barrier of height U_0 and thickness d. The initial position of the particle is at the left, moving to the right. Taken from [115]

III) The transmitted electron wavefunction at the right side ($x > d$), sinusoidal as well, with an amplitude equal to C_1:

$$\psi_{III}(x) = C_1 e^{ikx} \tag{2.5}$$

χ and k are the characteristic wavevectors on their regions. The probability density for the particle position is defined by $|\psi_i^2(x)|$ in the $x + \partial x$ region. It is noteworthy to say that the probability for the tunneling, called transmittance (T), decays exponentially with the barrier thickness (d) and the square root of $U_0 - E$.:

$$I \propto T = \frac{\psi(transmitted)^2}{\psi(incident)^2} \propto e^{-2\chi d} \tag{2.6}$$

Considering $E << U_0$, and that a typical value of the work function for metals is $\Phi = U_0 = 5eV$, the decay constant $\chi \approx 11.4nm^{-1}$. This translates into a current decay by an order of magnitude every 2 Å increase in the tip-sample distance, which provides the excellent vertical resolution of the STM.[116]

Bardeen developed an inceptive theory of the tunneling current from an STM tip in 1961.[117, 118] It was based on Fermi's Golden rule, a formula representing the transition rate from an occupied state to a continuum of empty states consequence of a perturbation:[119, 120, 121, 118]

Let's suppose that we have a system in an eigenstate $|\psi_i\rangle$ of an unperturbed Hamiltonian H_0 with energy E_i. Besides $|\psi_i\rangle$, H_0 has a quasi-continuum of eigenstates $|\psi_n\rangle$ with eigenenergies $\{E_n\}$. E_n are non-degenerate states that increase with n in the interval [a,c] that comprehends E_i. Initially $|\psi_i\rangle$ lives unaffected by $|\psi_n\rangle$, until it is perturbed at t=0 by H, which is constant for t≥0. H is an undefined perturbation that couples $|\psi_i\rangle$ to $|\psi_n\rangle$ with strength $M = \langle\psi_n|V|\psi_i\rangle$. It is necessary that $(H_0 + H)|\psi_i\rangle = E_\alpha$, by words, H must not affect the eigenenergy of the initial state, and ψ_i, ψ_n must remain orthogonal for every n as well after perturbation.[106, 121] Fermi defined P_n as the probability of finding the system in the quasicontinuum ψ_n, and its transition rate ($W_{i\longrightarrow n}$) for $t \to \infty$ as:

$$W_{i\longrightarrow n} = \frac{dP_n}{dt} = \frac{2\pi}{\hbar}|M|^2\rho_n(E_i) \; for \; M = \langle\psi_n|H|\psi_i\rangle \tag{2.7}$$

Here $\rho_n(E_i)$ is the density of states of the quasi-continuum at the energy of the initial state. To this extent Fermi's golden rule defines the transition rate $W_{I\longrightarrow\alpha}$ for a localized system. Bardeen extended it to the case where ψ_i and ψ_n are spatially separated, as it's the case for the tunnel effect. It inherited two main assumptions from Fermi's rule:

-Tunnelling is weak enough that a first-order approximation is valid.

-Tip/sample wavefunctions are separated of each other, and do not overlap. This is a reasonable assumption for the bound states of the system.

Plus, further assumptions which were required for its application:[118, 120]

-Electron-electron interactions are ignored, allowing the use of single-electron Hamiltonians.

-The potential of the tip and sample are independent of each other.

-Occupation probabilities for tip and sample are independent of each other. It is justified considering both as infinite reservoirs of electrons.

-Both tip and sample are electrochemically stable.

Bardeen considers the potential of the tip, U_t, as a perturbation for the sample and viceversa. For that reason it is a requisite that $U_t\psi_{s,n} = 0$ and $U_s\psi_{t,m} = 0$. As tip and sample wavefunctions can be considered orthogonal, $\langle\psi_{s,n}|\psi_{t,m}\rangle \approx 0$, the conditions for Fermi's Golden rule are fulfilled by the system. The resulting expression is:[117]

$$W_{t\to s} = \frac{2\pi}{\hbar}|M_{n,m}|^2\rho_s(E_t) \; for \; M_{n,m} = \langle\psi_{s,n}|H|\psi_{t,m}\rangle \tag{2.8}$$

where $\rho_s(E_t)$ is the sample DOS at the energy E_t. The tunnelling matrix $M_{n,m}$ can be written as the flux integral through the surface A that splits through the tunnelling junction, by the direction of its normal vector, n:[117, 118]

$$M_{n,m} = \langle\psi_{s,n}|H|\psi_{t,m}\rangle = -\frac{\hbar^2}{2m}\int_{\partial A}[\psi_{t,m}\nabla\psi_{s,n} - \psi_{s,n}\nabla\psi_{t,m}]\cdot dn \tag{2.9}$$

Then, resembling first-order perturbation theory, current in Bardeen's formalism is given by:

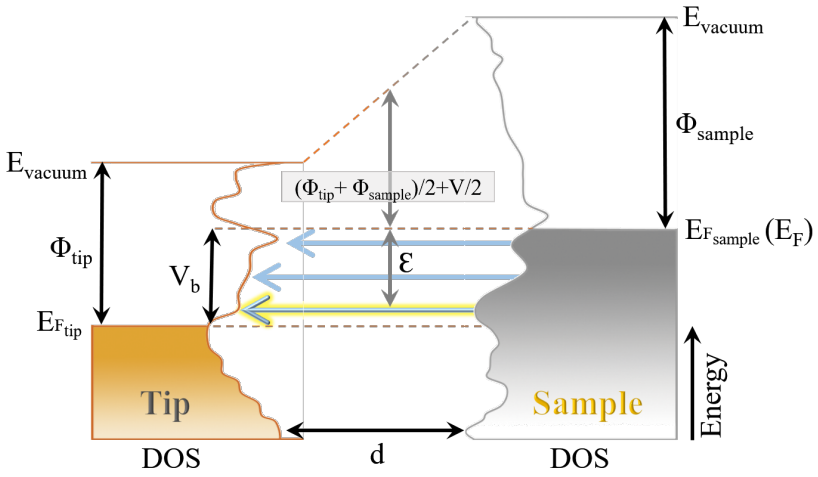

Figure 2.4: Tunneling between the tip and the sample. The vertical axis defines the Energy distribution, while the horizontal represents the DOS at a given energy. When V_b is applied to the tip sample junction, the electrons within the defined energy range tunnel from the occupied levels to the unoccupied. The average potential energy barrier is defined for the highlighted transition.

$$I = \frac{2\pi e}{\hbar} \sum_{n,m} f(E_m, T)[1 - f(E_n + V_b, T)]|M_{n,m}|^2 \delta(E_m - E_n) \tag{2.10}$$

where $f(E_F, T)$ and $f(E_F + V_b, T)$ are the Fermi-Dirac distributions of the tip and sample at temperature T and V_b is the bias applied to the tip-sample junction. For high temperatures, it must include a term for reverse tunnelling, while for low kT the Fermi-Dirac level distribution resembles as a step function. C.J.Chen expressed it as an integral for the continuum of states:

$$I = \frac{4\pi e}{\hbar} \int_0^{V_b} |M(\epsilon)|^2 \rho_t(E_F - V + \epsilon)\rho_B(E_F + \epsilon) d\epsilon. \tag{2.11}$$

For small tunneling voltages where the work function (Φ) is not surpassed ($V_b << \Phi$) and the tunnelling matrix element does not vary $M(\epsilon) = M(0)$, the convolution of tip and sample DOS determines the tunnelling current:[116]

$$I \propto \int_0^{V_b} \rho_s(E_F - V_b + \epsilon)\rho_t(E_F + \epsilon)\, d\epsilon \tag{2.12}$$

From that expression we can deduce that the STM is sensible to textures in the density of states of both tip and sample. This is the doubled edged sword of the STM: It allows to explore changes in the electronic structure of atomically similar structures (otherwise we would see GNR as homogeneous stripes with null interest for physicists); however, it can be problematic for molecules with huge DOS near the Fermi level that saturate the instrument. This states appear in magnetically active molecules, and imply dealing with massive currents in order to obtain similar resolutions to other systems.

The range of states scanned depends on both the value and the polarity of the bias applied to the junction. The convention rules that a negative bias lowers the tip's Fermi level relative to the sample's Fermi level, and viceversa. Following this consensus, a negative bias means $E_{Ftip} < E_{Fsample}$, as in Figure 2.4. Hence electrons will tunnel from sample's filled states to tip's empty ones, in terms of energy. Referring to the local nature of the measurements, Tersoff and Hamann calculated the tunnelling current for an σ wavelike tip with a uniform DOS:

$$I \propto \sum_n |\psi_n(r_0)|^2 \delta(E_n - E_F) \tag{2.13}$$

The tip's regular shape "averages away" its contribution to the tunneling conductance. Now the current is proportional to the unperturbed sample wavefunction localized under the tip ($\psi(r_0)$), proof that STM is spatially sensitive to the local density of states (LDOS). [122]

2.2.1 Scanning Tunneling Spectroscopy

Our current arises of the quantum nature of the electrons. The alignment of the tip and sample occupancy levels opens the window to tunnel from the occupied states at one side to the empty ones on the opposite. Thus, it allows to detect the presence of states at specific energies: The derivative of the current with the bias is related with the presence of states at that specific energy. Assuming a constant transmission coefficient (T), the main contribution to the current change with V_b is:

$$\frac{dI}{dV} \approx \rho_s(E_F + V_b)\rho_t(E_F) \tag{2.14}$$

Apart from the T and tip DOS, which for the ideal case are constant, the differential conductance ($\frac{dI}{dV}$) is proportional to the sample density of states (ρ_s) at the chosen bias (V_b).

A lot of information about the LDOS can be extracted from the derivative of the current signal, in which Scanning tunnelling spectroscopy (STS) is based. We employ a lock-in amplifier that introduces a sinusoidal AC voltage in the milivolt (mV) range. The frequency of oscillation is chosen in order to avoid electronic noise sources (thus, multiples of 50 Hz) or any other noise. To detect those, the direct way implies to measure a power spectrum of the DC current with the tip relatively close to the surface. The feedback has to be turned off to avoid recording its response as a noise, and select an oscillation frequency far from external noises. Once chosen, by measuring the current signal caused by the lock-in AC-voltage while the tip remains far from the surface, we can discard the capacitative contribution. The measured signal in these conditions is an "artifact" and must be relegated to the virtual, discarded coordinate of the lock-in. After sweeping across the desired range of bias and deconvoluting the signal, the resulting curve is a dI/dV vs bias curve. A profile of the DOS sliced by energy relative to the substrate's Fermi level. Of the molecule underneath the tip, in our case. It is possible to perform an scan employing the dI/dV as signal, and obtain information of the spatial distribution of the DOS at that specific energy, as shown in figure 2.5. This results in a crucial tool for studying the electronic structure of our samples.

There are multiple factors that affect the measurement. The amplitude of the AC voltage. The bigger the oscillation, the better our signal to noise ratio. However, this increase implies a reduced energy resolution. A lower signal-to-noise can be compensated with higher tunnelling currents for the cost of risking the tip-sample junction integrity. Another way could be increasing the acquisition time in expenses of a more time-consuming measurement. The precision of the measurement increases with the square root of the ac-

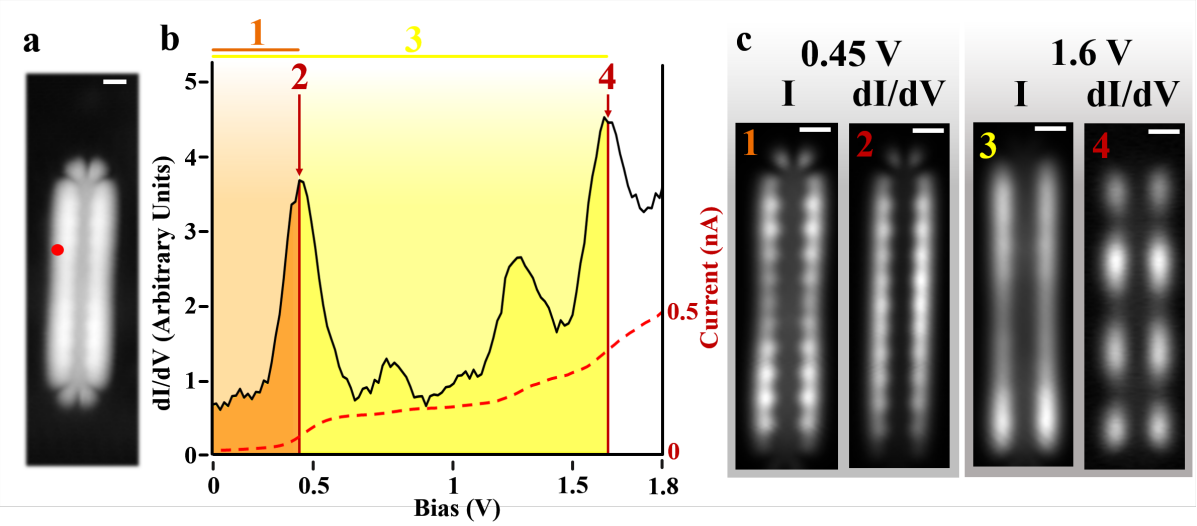

Figure 2.5: Comparison between the current and the differential conductance. a) Topography of a graphene nanoribbon. b) STS taken at the red dot. c) Constant height scans taken at the energies of two states. At 0.45 V, the current (1) and differential conductance (2) signals look similar, as we are scanning at LUMO energy. At 1.6 V, electrons tunnel through all the states from Fermi to the bias, so the current resembles a convolution of the whole band (3), whereas the differential conductance (4) is able to resolve the modulation of the band at that specific energy.

quisition time, so the range in which this is cost-effective is limited. Multiple sweeps of the V_b have the same effect on the signal-to-noise ratio.

2.2.2 On-surface magnetism

Along this thesis, other phenomena out of molecular states will leave an imprint in the spectroscopy. One is the surface state, caused by the drastic transition between the bulk of the metal and the vacuum. Others are a Kondo peak at Fermi and inelastic electronic excitations, hints of magnetic states on the sample.[123, 124, 125]

The Kondo excitation is characteristic of magnetic impurities with a single unpaired electron (S=1/2).[125, 126, 127, 128] The magnetic moment is screened by forming a correlated electron system with the surrounding non-magnetic electrons from the surface. Impurity and surface together form a collective singlet whose electrons can exchange elastically without energy loss. That opens a magnetic electron transfer channel that appears as a sharp peak at bias $V_b = 0V$, shown in figure 2.6(a,d).[128, 125]

However, not every peak at Fermi has to be considered a Kondo. Some half-filled states can be pinned at Fermi due to the interplay between the surface work function and the molecule ionization energy, which results in a phenomenon with a similar fingerprint.[70] There are different criteria to confirm the magnetic nature of a Fermi level peak: First, checking its broadening with the temperature. Additional to the thermal broadening of spectroscopy, the electron-electron scattering cause Kondo peaks to broaden quadratically with the temperature resembling a Fermi-liquid behaviour.[129] The second method consists on applying a magnetic field to the sample. A Kondo peak splits by Zeeman effect into two peaks, one for each opposite spin level, simmetrically to the Fermi level.[127] An adittional method will be proposed and tested in chapter 4: Thanks to the tuning of the work function effect, we can gate the S=1/2 state. That way it is possible to relate the Kondo peak with the electron filling of the unpaired state. We will explain this experiment in depth later.

More complex spin systems have different footprints. Two unpaired electrons antiferromagnetically coupled produce two symmetric steps around the Fermi level, shown in Figure 2.6 (c,f). Their separation is twice the excitation energy necessary for flipping one spin, from S=0 to S=1. [131] For a ferromagnetically aligned triplet, with ground state

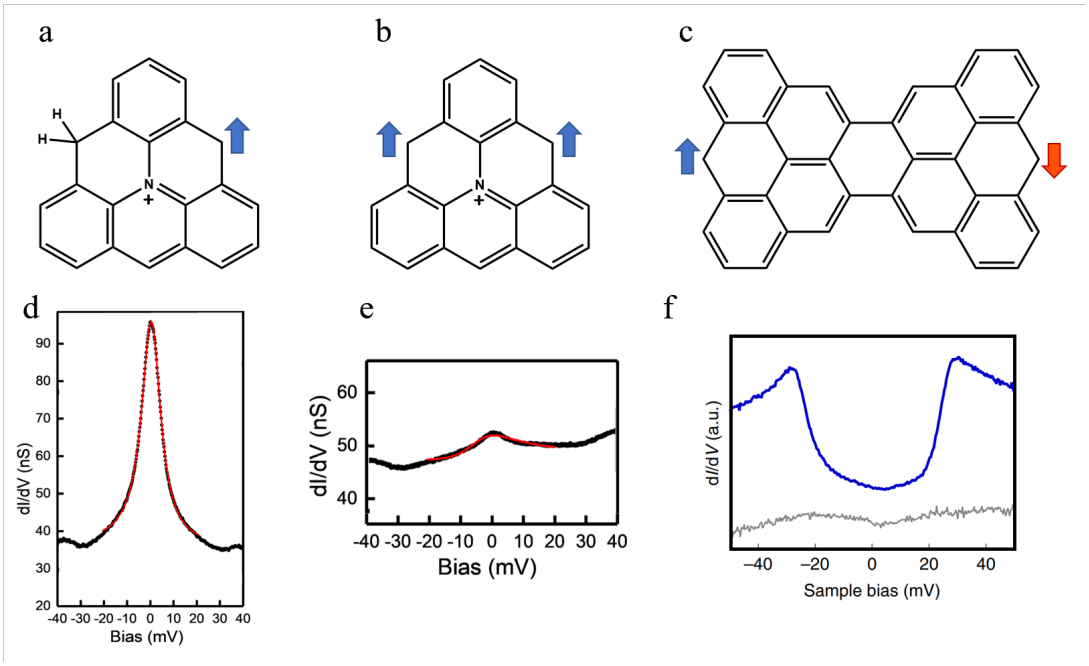

Figure 2.6: Magnetically active and their spectroscopic fingerprint. a) S=1/2 and its Kondo peak d). b) S=1 and a partially screened Kondo e). c) S=0 open-shell and its inelastic excitation steps f). d,e from [130]. f from [34].

S=1, the spectroscopy usually have weak or absent spin-flip steps. Instead, they can show an underscreened Kondo, weaker than a S=1/2, shown in Figure 2.6 (b,e).[132, 130, 131]

2.2.3 Tip preparation

The model presented above describes to a great extent how the ideal tip of an STM is modelled, with constant DOS at every bias. However, that idea is excruciatingly far from the real world. There are many techniques in order to sharpen our tip from scratch to something close to an atomically sharp-regular DOS tip. The starting material commonly is a metallic wire: Electrochemical etching, ion bombardment, field emission, scissor slicing...[133] Different resources are employed to sharpen it atomically. The fitness of the resulting tips for STM and STS, however, is not 100% reproducible. The ideal tip for the STM has been depicted as an infinitely sharp filament, trigonometrically fated to terminate in one single atom. Tips like that have been fabricated with atomic precision by ion beam etching.[134] Although some worked, others didn't. Sharp tips that we have tried worked better after a generous poking into the surface, which left them crippled, but fully functional.

What is the lecture? The phenomenology that concerns STM operates at atomic scale. The part influential for the result of the measure comprehends no more than the last few nanometers of the tip (other techniques, as the light-mediated ones, lack from this freedom).[135] In consequence, the tip construction is a stochastic process (when it is done correctly; as there are infinite ways of making a useless tip). Almost any shape of material

can terminate in a single atom after a few pokings against the surface. In this principle relies the tip-sharpening process: A combination of mild indents on the surface with bias pulses which reshapes the last few atoms. This procedure can build completely new tip shapes and discard whole chunks of material, or coat our tip in the material that forms the surface. All that until we get the desired probe.

It is not trivial to discern what are the requirements for a good tip. First, obviously, sharpness. When scanning for resolving the states of a molecule, we aim for the single atom tip which can reach the highest resolution. For atomic manipulation, however, symmetric blunt (always metallic) tips showed to do a better job. For performing STS, we would like the tip to have a homogeneous distribution of states along the range of energies (typically $\pm$ 2 V), as every feature it has will appear in the spectroscopy, mixed with the sample's signal. The only way of probing the states of the tip is to measure the LDOS in a well-known surface, and compare with the bibliographic examples to identify the tip contribution. The ultimate goal is to obtain a featureless tip that provides representative data of the sample.

2.2.4 Functionalized tips

Having mastered the basics of tip formation and scanning, there are extraordinary techniques that push the limits of scanning probe technologies one step further. There is a wide variety of atoms and molecules that we can pick with our probe, so their different spatial conformation and valence orbitals will affect our sensitivity in unexpected ways.

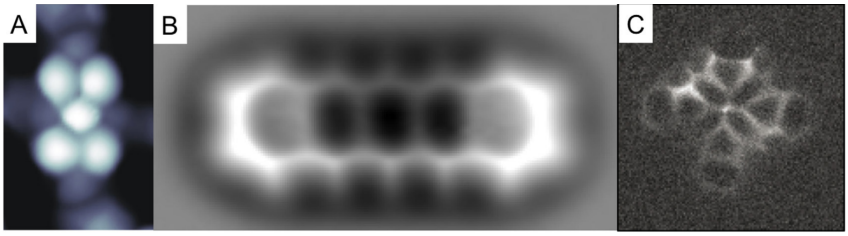

Figure 2.7: FIGURE 2.5: Functionalized STM tips. a) Bond-resolving STM image of PTCDA molecule by Temirov et. al. with an hydrogen-functionalized tip[136] b) NC-AFM bond resolution of pentacene using a CO tip by Leo Gross et. al.[137] c) Constant height IETS-STM image of CoPc molecule with CO-functionalized tip, by Chian et. al.[138] Figure taken from [139]

Atoms from the halogen group, specifically chlorine, can get a higher resolution for orbital imaging. Heavier halogens like Br and I have more diffuse orbitals, while Cl frontier states are the p orbitals of the first layer. Cl-functionalized tips resolve isotropic σ-like images, which obtain the same type of contrast as a metallic s-wavefunction tip. However, its directionality gets sharper scans of the electronic levels of the molecule. Another argument in favor of its use is the simplicity of the functionalization. After depositing NaCl on the surface, picking the Cl atom is as easy as adjusting the feedback to 100 mV, 100 mA over the ionic islands and descent the tip 300 pm forth and back. The vacancy left proves the functionalized tip, together with an enhancement of the resolution.

For the imaging of molecules, there is little option sharper than what a $1p$ orbital can obtain without extra phenomenology happening under the tip. However, some molecular tips can overtake the orbital resolution and resolve the atomic structure underneath. In 2008, Temirov and coworkers resolved the hexagonal patron of a PTCDA molecule thanks to a STM tip functionalized with hydrogen.[136] Shortly after, Leo Gross and his team got a similar result on NC-AFM measurements of pentacene using a tip attached to a

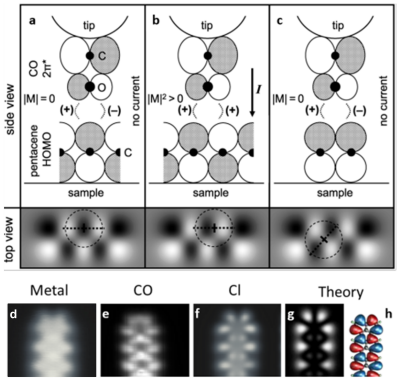

Figure 2.8: a-c) Effective overlap between the $2\pi*$ orbital of CO and pentacene HOMO. The color scale represents the alternating wavefunction sign, and the dotted line in the "top view" indicates the orientation of the CO orthogonal cut plane. Configurations a,c result in a transmission matrix $|M| = 0$, equivalent to no zero signal, while b results in an effective transmission. Taken from ref[140]. (d-f) Experimental CH dI/dV maps of a 12-UC 5-aGNR end with different tips, compared to the g) simulated s-wave tip dI/dV and h) wavefunction. The opposite sign of the CO lobes causes it to be gradient-sensitive (b). The overlap of a purely p-wave tip with a constant wavefunction underneath gives no net signal (a and c). The CO imaging results in a combination of p and s-wave tips (e), while a Cl tip (f) is a sharp, close to the purely s-wave tip (g).

CO molecule.[137] Posterior results got comparable images by IETS-STM and STS.[138, 141] These molecules act as an electrical transducer, turning the short-range molecular forces into a modulated signal of the junction conductance. For the case of the AFM, it is a direct transmission of the intermolecular forces to the cantilever. The molecular tip is atracted by Van-der-Waals forces, but repelled by Pauli's forces.[142] In the working conditions, low bias and constant height imaging, the lateral torsion modes deflect the molecule, what reflects in the signal. The sharp relaxations occur everytime the tip crosses a covalent bond.

Both techniques have been employed for the resolution of the internal structure of molecules and the study of on-surface chemical reactions.[143, 144] Combined with KPFM, they were able to determine the elements conforming a surface (from a limited pool of candidates),[145] as well as the change in the bond order depending on the charge state of the molecule.[146] Some authors have proposed the possibility to image intermolecular bonds with it.[147, 148] However, models proved that the sharp signal considered indicative of a bond appears between atoms which are close enough, regardless there is an attractive interaction between them.[149]

We tipically apply two different protocols for CO funcionalization. Their alternative use depends whether it is the final stage of the sample or it requires further annealing: If it is not necessary, we first deposited NaCl islands and then leaked CO through the preparation chamber in the cold STM head. With the sample inside, we opened the STM door to let those molecules adsorb in the cold surface.The molecules are easily observable on the ionic islands, and can be picked up by tip pulsing -2V on them. The second method is used when we are going to anneal the sample afterwards and avoids deposition NaCl, as

it aggregates in three dimensional crystals with temperature. For picking the CO from the gold surface, the protocol consisted in scanning the surface at -100 mV, 1 nA until a carbon monoxide molecule eventually attaches to the tip.

2.2.5 Atomic Force Microscopy

Despite the great success that the STM supposed to the surface science community, it still relayed on what is basically a disadvantage: Only conductive layers could be scanned correctly, with an efficient drainage of the injected electrons. For that reason, Binnig developed an instrument in which the signal measured was the deflection of a flexible cantilever against the surface, the Atomic Force Microscope (AFM).[150] It was introduced to the community in 1985. [151] The initial prototype oscillated a cantilever attached to a piezo, which at one side had the sample to scan while at the opposite had an STM tip as the detection unit for the deflection. Two different feedback loops kept the system in a sutile equilibrium; one regulated the amplitude of the oscillation whereas another took care of the resonance frequency and phase. This type of oscillating cantilever, referred as "dynamic", is the best one towards a non-agressive scanning of the surface, so it was quickly combined with the STM in order to measure molecular samples. The force resolution of a setup like that can reach $2{\cdot}10^{-16}N$, which is sensible enough for detecting inter-atomic forces in the range of $10^{-9}N$. This instrument was capable of obtaining atomic-size surface rugosities of an insulating sample just one year after its invention.[152, 153]

There are two main mechanisms to acquire information from the sample: One

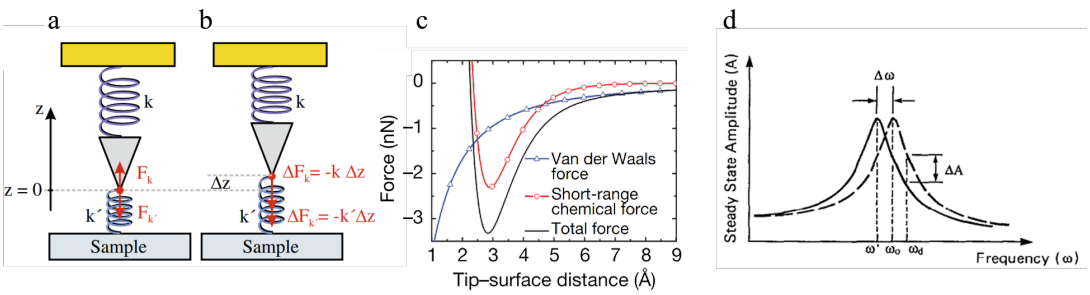

Figure 2.9: a,b) modellization of an AFM tip and the spring-like cantilever behaviour, from [115]. c) Force relation of the FM-AFM tip following a Lennard-Jones model, from [154]. d) Changes in amplitude and frequency of the oscillation when working in AM and FM, from [155]

based on the variation of the total amplitude at the initial resonance frequency, named Amplitude Modulated (AM)-AFM and one which employs the shift in the maximum resonance frequency as the signal, called Frequency Modulated (FM)-AFM. The second method produces the highest lateral resolution and is the basis of what we call henceforth non-contact AFM (NC-AFM); nevertheless, the conversion from the interaction forces to $\Delta\omega$ is not trivial from a theoretical perspective. For an unperturbed harmonic oscillator with mass m and spring constant/coupling (k_0) the resonance frequency is:

$$\omega_0 = \frac{1}{2\pi}\sqrt{\frac{k_0}{m}} \tag{2.15}$$

For the dynamic case, we can implement the external force of the sample in the k as $k = k_0 + k_t$ in the limit of $k_0 >> k_t$, the Taylor expansion of the square root yields:

$$\Delta\omega = \omega - \omega_0 \approxeq -\omega_0 \frac{k_t}{2k_0} \tag{2.16}$$

ω is the modified resonance frequency of the cantilever under the effect of the surface forces. Considering that $k_t = \frac{\partial F}{\partial z}$, the relation between the force and frequency shift results as:

$$\Delta\omega \approxeq -\frac{\omega_0}{2k_0}\frac{\partial F}{\partial z} = \frac{\omega_0}{2k_0}\frac{\partial^2 P}{\partial z^2} \tag{2.17}$$

where P represents the tip-sample interaction potential. There are two lessons about this formula which tell about the FM/NC-AFM:

We can see how the frequency shift employed by the FM-AFM is directly proportional on the gradient of the force with respect to the z ($\Delta\omega \propto \frac{\Delta F}{\Delta z}$). In contrast, the signal measured in AM-AFM (the amplitude) is proportional to the force through Hooke's law ($\Delta A \propto \frac{F}{k}$), figure 2.9(a).[156]

When the tip is close to the surface, $\frac{\partial F}{\partial z}$ is dominated by the Lennard-Jones interaction of the front-most tip atom with the atom directly below it (see figure 2.9 (b)). Conversely, the long-distance contribution of tip-sample interactions governs the behavior of F. For that reason surface science employs the $\Delta\omega$ as signal, as it offers the highest spatial resolution to the very last atoms of the tip-surface junction. Just to puntualize, it was experimentally observed that $\Delta\omega$ equals the force gradient averaged over the entire amplitude of the oscillation (weighed to a semicircular function). Therefore, FM-AFM loses sensitivity when the tip oscillates at large amplitudes.[157]

Even though the initial design of the AFM included an STM tip, it was a mere operator for the cantilever. The team already suggested that a combination of both techniques could be born from installing the STM tip directly at the cantilever.[151] The construction of our equipment is few iterations forward from the original design but it still relays on the same conceptual design. It consists of a Scienta-Omicron head 'single-tube' type[158] attached to a double shield (N2+He) cryostat. A Nanonis control unit with an integrated lock-in amplifier operates the instrument. The main head of the microscope is insulated from vibrations and other mechanical noises by a system of three springs which hold it while it is measuring. For further external noise reduction, four pneumatic legs can lift the whole machine together with the preparation chamber to dampen ground noises. However, it remained unnecesary during the experimentation, as the laboratory lays over a block of concrete insulated from the rest of the ground. The head itself can run both STM and AFM measurements , the latter being based on a tuning fork design.[159]

2.3 X-ray Photoelectron Spectroscopy

Photoemision spectroscopy consists in the study of electrons emitted by a solid due to light excitation. This effect was discovered by Heinrich Hertz[160] and Wilhelm Hallwachs[161] in 1887/1888, and later explained by Einstein.[162] When a photon source impinges the surface, it excites the electrons from the occupied levels of the solid. Those electrons which absorb enough hv energy escape the potential well of the atom, with the energy surplus transformed into the kinetic energy of the runaway electron. There, the

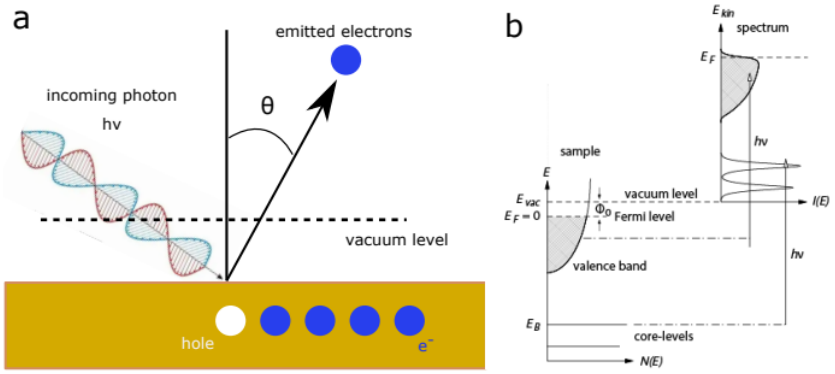

Figure 2.10: Schematic ilustration from XPS working principle. a)As the X-ray incides in the surface, an electron is scattered away from the surface. b)Schematic view of the photoemission process in the single-particle picture. Electrons with binding energy E_B can be excited above the vacuum level E_{vac} by photons with energy $h > E_B + \Phi_0$. The photoelectron energy distribution E_{kin} can be measured by the analyser and is an spectra of the occupied density of electronic statesd in the sample. from [164]

experimentalist finds their yield: the electrons escaped carry information about the source atom in their energy, providing elemental and chemical information about the surface.

The electrons extracted from the surface go through different processes. X-rays can penetrate through few microns of solid material. After escaping the source atom, they scatter through the crystal due to the interaction with other electrons and atomic nucleus. Depending on their initial kinetic energy and the material, the distance they can travel varies, a factor referred as the mean free path. For XPS, this distance goes from 0.5nm to 10 nm for the highest energies. This means that even tough the X-rays have a high penetrative capacity, the detected electrons come only from the last few layers, providing the technique a high surface sensitivity. Just for our specific case with Au and the 100-500 eV energy range, the mean free path is around 0.4-1nm.[163]

The energies of the peaks for most elements have been listed, enabling identification of surface atoms by XPS. Other system electrons can affect the signal by screening of the nucleus attractive, causing a relative shift compared to the reference peaks. Higher binding energies indicate an electrodeficient system with a positive charge, which may be due to an electronegative substituent in the molecule or the surface work function, providing valuable chemical information about the atom environment.

Using Temperature Dependent (TD) XPS, multiple scans of a sample can be performed during annealing to track the shift and abundance of different atomic signals at various temperatures. This technique allows for monitoring the shifts caused by chemical evolution of surface molecules, enabling real-time tracking of surface reactions.

2.4 Sample preparation

There is a bunch of instruments solely dedicated to the correct conditioning of the crystals and the posterior sample preparation.

First of all, the surface of the metallic crystal is bombarded by accelerated Argon ions in a process named "sputtering". Two different sputtering guns have been employed along this thesis, one based on a hot filament as source of ions,[165] and another that extracts electrons from the gas with a strong static magnetic field originated by a magnetron.[166] The resulting positively charged Argon gets shot to the sample through an electric field generated

by a high voltage.[167] The argon ions tear off nanometric chunks of matter from the surface of the crystal; what results in an irregular, but chemically pristine surface. By annealing it we recover its crystaline structure, now free from contaminants. Multiple cycles of this process may be necessary to get the optimal surface. Despite the previous protocol is the mainstream recipe, our trials towards a simultaneous sputtering plus annealing concluded in cleaner samples.

To introduce precursors we use three different protocols. The simplest one only requires from a silicon wafer mounter on a special sample holder. A spatula stained with the molecules to measure is faintly rubbed in the surface of the silicon, so it leaves a barely visible trace. Then, the evaporator sample is pumped down in the loadlock to desorb any contamination and transferred to the preparation chamber as the pressure reaches $4 \cdot 10^{-6}$ mbar. The stage has specifically designed contacts for both sides of the silicon, so when a current passes through it, the wafer rapidly heats to red hot. A burst of sublimated molecules from the crystal comes from the surface, and land on a metallic sample, placed previously close to the sample. This method is referred to as "flash evaporation" in the literature. [168]

The second method is more laborious, as it involves adding external components to the machine. However, it allows for the regulation of the temperature reached by the molecules, and thus the generation of a stable sublimation rate. First, a solid sample of molecules is placed in a Knudsen cell, which is located inside a retractable bellow that is connected to a concentric inlet of the preparation chamber. The sample is then pumped down to a pressure below $1 \cdot 10^{-5}$ mbar and baked below the sublimation temperature to remove any environmental contamination. Once it reaches an optimal pressure, the valve

between the chambers is opened, and the bellow is retracted to approach the Knudsen cell to the chamber. The equipment is now ready to calibrate the sublimation rate using a quartz microbalance and deposit a flow of molecules. While the crucible can achieve a stable sublimation rate of intact, small molecules, heavier compounds may have a degradation temperature lower than their sublimation temperature, requiring flash annealing to sublime a fraction of intact molecules.

The third protocol is case-specific for gases, liquids, or solids with low sublimation temperatures. For gases such as O_2 or Ar, only a gas/vacuum pipeline system connected to the chamber through a leak valve is required. For liquids and solids whose high vapor pressures do not allow them to be placed under high vacuum, they are placed in a glass bulb. The atmosphere inside the glass bulb is purged by performing several pumping/argon cycles. The glass bulb containing the compound can be cooled by immersing it in liquid nitrogen to avoid boiling. Once the purity of the line atmosphere is verified by mass spectrometry, the leak valve can be used to deposit the sublimated molecules onto the sample. If the flow is not high enough, the glass bulb can be heated to increase the compound's vapor pressure.

The quartz microbalance is a vital component of the evaporation process. It consists of an oscillator made from a thin crystal of quartz. When the appropriate alternating voltage is applied to the crystal, it resonates at a frequency of approximately 5 MHz in our case. When matter is deposited on the crystal, its resonance frequency decreases. The system is capable of detecting this shift and converting it into mass or layers. The quartz microbalance has outstanding sensitivity, capable of detecting coverages as low as 1/1000 of a monolayer of hydrogen.[169].

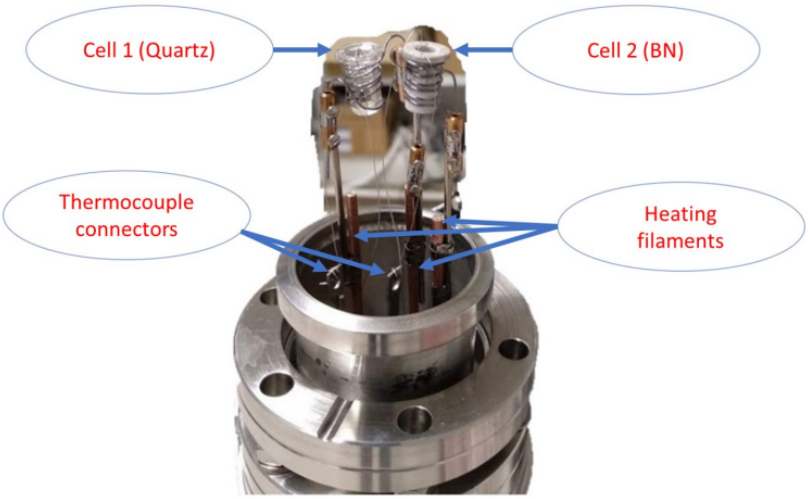

Figure 2.11: from sabri

2.5 Insights of the surface synthesis

On-surface synthesis of GNR was inspired by Grill's 2007 work about on surface polymerization by Ullmann coupling. [170] The first atomically-precise on-surface synthesis of armchair/chevron GNR succeeded in 2010. [171] Two years later, the hierarchical reaction mechanism was demonstrated by the use of different halogens functionalizing the same precursor. [172, 173] In 2013, Bronner functionalized the ribbons with heteroatoms by modification of the precursor [174] and formed ribbon heterojunctions. [175] It was after its prediction in 2017 [71] that topological bands started being studied in GNR and it nowadays remain as an open topic.[90, 176]

On-surface synthesis is a snowflake within the chemical discipline. The field of synthesis has a vast amount of resources to get the desired products done: pressure, solvents, state of matter, catalyzers, atmosphere, temperature are the most conventionals. From this

repertory, surface synthesis is limited, in most of them, to a single alternative, with potential advantages:

By definition, the playground is some type of surface. Due to their advantageous properties, the main surfaces employed are the faces of single crystals of Cu, Ag and Au. Those metals are the most common catalyzers since the birth of the discipline in 1999.[177] Their reactivity decreases in the presented order, so reactions in Au are conventionally more energy demanding than in Ag or Cu. Common flat crystal orientations are (111) and (100). Other crystals employed are (110), having a reduced two-fold symmetry which may favour a linear alignment of the molecules, and conditions the reaction pathways.[178]

The presence of the surface as support for the reaction relegates the solvent from its main task on conventional chemistry. So it is, that its presence is not necessary anymore, better said, counterproductive as a source of contaminations and side reactions. For that reason it is not employed in most of the cases. The precursor is deposited by sublimation, and no liquid takes part in the whole process eliminating other source of contamination as well.

Different activation methods are possible: Thermal activation by annealing of the crystal; photoactivation is an option as well, even though its working principle on metals is under discussion; tip activation is another way for exciting the molecules over their activation energy in a controlled way, with spatial control (giving up the scalability in the way).

Those sound like advantages for the reactivity. However, there are some inher-

ent limitations. First, the posibility to purify the reaction product fades with the absence of solvent. Thanks to the STM characteristics, we can choose the desired product while scanning, nevertheless, a significative amount of contaminations can hinder the scanning and make the search for the product unbearable. The sublimation strategy limits us to molecules light enough to change phase before the molecular lysis, but big enough so they adsorb to the surface. The topology of the surface also affects the products: Its shape stabilizes the molecules on top of them depending on their total contact area. This means, molecules with a larger planar surface exposed to the crystal surface will be more favourable, and more likely to be generated. It is a lucky coincidence, as the STM bond-resolving CO tips need from planar products to resolve the molecular structures.

A generic synthesis of GNR would be like this: It begins with an Ullmann reaction, where an halogenated precursor is deposited on the surface. It does not need to be planar but must not be so bulky that the halogen cannot reach the surface. The metal catalyst initiates the C-X bond cleavage and stabilizes the radicals generated. These reactive products are thermodynamically stabilized by coordination with the metallic atoms. Nevertheless, metal-organic complexes are considered to be reaction intermediates, sometimes observable, sometimes virtual. Then, they combine to form a C-C bond, neutralizing both radicals and coupling their carbon skeletal structures at the previously halogenated positions. This way, halogen acts as a tool to direct the reaction towards the desired product. However, this method is not infallible; sometimes steric hindrance or overly reactive surfaces can cause a side-reaction to become the major product. Following the carbon-carbon bond formation, the obtained polymers after the first step may be non-planar. The flattening ef-

fect of the surface then comes into play: hydrogens cleave and leave the surface, sometimes combining with the halogen leftovers. If the precursor was designed correctly, the carbons will accommodate a flat conformation, maybe benzenoic, maybe not, but conjugated in a π lattice useful for our study.

2.5.1 The design of the precursor molecules

Designing a synthesis strategy is more of an art than a science, as it requires a lot of intuition, and even the most favored reactions can fail at times. Similar to traditional chemistry, on-surface chemistry follows a reverse engineering strategy. We begin with the desired product and break it down into manageable fragments using the known surface tools. These fragments can then be synthesized by solution chemistry and deposited by sublimation. We can divide the desired structure into identical fragments whose carbon backbone will be analogous to that of our precursor. On surface, carbon cleaving or changing positions is unlikely, so we can assume the carbon backbone is invariant a priori. Each of these units binds to one another through specific positions, which are potential halogenation sites. Ullmann coupling is symmetric, meaning both sides of the coupling are identical with no selection rules. Since we cannot choose where the resulting radical binds, a good option is to place the halogens in analogous positions comparable due to symmetry rules, to avoid side-reactivity.

However, there are other factors to consider in the synthesis process. Large planar PAHs often lack solubility, what can make the synthesis of the precursor itself im-

possible. Bulky groups are useful avoid $\pi - \pi$ stacking and increase solubility but they are unfavorable for surface synthesis. An alternative is to partially break the π conjugation by splitting some bonds to create a three-dimensional precursor. Due to the hierarchical reactivity, these precursors will first form a three-dimensional polymer by bonding through the halogen positions on the surface (assuming the steric hindrance allows this bond formation) and then undergo cyclodehydrogenation (CDH). If the units have an odd number of carbons, some may be kept as C sp^3 to maintain a closed-shell structure before surface deposition, as a "protective" measure before dehydrogenation by annealing. [24, 179]

CHAPTER 3

5-aGNR growth

We have chosen to adopt the synthetic pathway developed by Kimouche et al. for the synthesis of 5-aGNR.[107] We employed commercial dibromoperylene (DBP), which Peter Liljeroth kindly shared with us. Dibromoperylene is a unique case for the Ullmann coupling: It is planar prior to the reaction, even though the conventional reaction pathway would include to form a three-dimensional polymer on the surface. The reason behind is that, unlike tetrabromonaphtalene,[106] it has hydrogens in positions that will require from a CDH to form the ribbon.

The expected mechanism consists of a metal-catalyzed polymerization reaction guided by the halogens in the reactant.[180, 173] As we anneal the surface, the homolytic cleavage of the carbon-halogen bond develops due to the catalytic effect of the surface. With few exceptions[181] in the reported Ullmann-coupling experiments on Au(111), the halogen abstraction is directly followed by the formation of C-C bonds[182, 183, 183] without a measurable metal-organic intermediate. It results in a three-dimensional polymer. However, neither the metal-organic or the polymer have been previously observed for this reaction pathway.

The precursor employed is a mixture of structural isomers, Figure 3.1 (a,b).[107] We decided to perform a minucious study of the reaction pathway to disentangle its mechanism. For that aim we used bond-resolving SPM to determine the species involved and TD-XPS to identify the reaction window and the abundance of each intermediate.

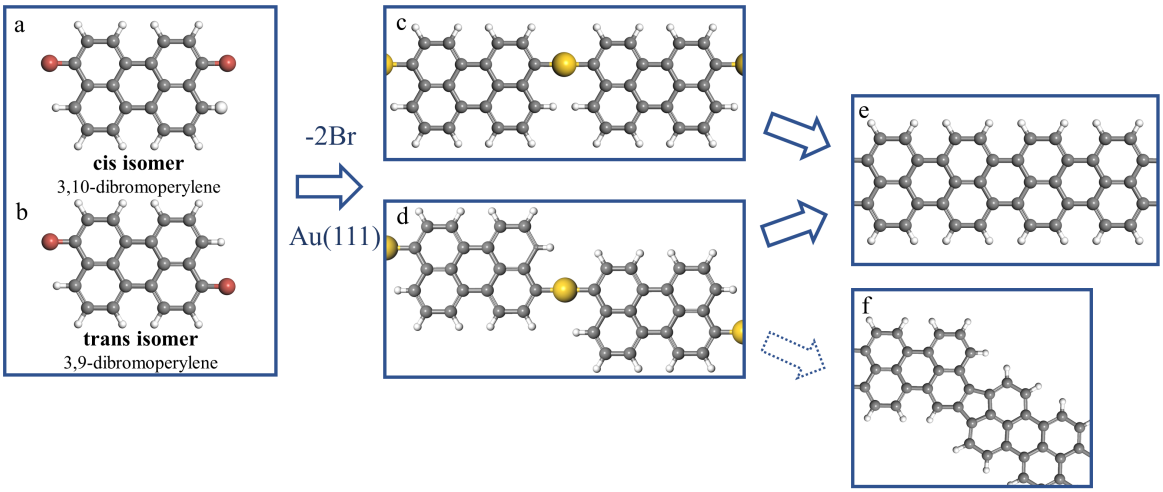

Figure 3.1: Figure 1. Illustrative scheme of the steps in the 5-AGNR formation pathway. (a, b) Carbon-halogen bonds of 3,9- or 3,10-dibromoperylene are cleaved when the molecule is annealed on Au(111). (c, d) The resulting diradical is stabilized by forming metal-organic chains. (e, f) In the same step, graphene nanoribbons are also formed, which suggests that dehydrogenation/C-C addition occurs simultaneously or is mediated by an unstable short-lived intermediate

3.1 SPM identification of the species involved

We deposited a sub-monolayer coverage of DBP onto a clean Au(111) surface slightly under room temperature, followed by a stepwise annealing to increasing temperatures. After each annealing step, the sample was cooled to 5 K for characterization, shown in Figure 3.2. We used a combination of BR-STM and NC-AFM with CO-functionalized tips for resolving the carbon backbone of the surface species.[137]

The figure 3.2(a) shows a constant-current STM image of the as-deposited reactants. The molecules self-assemble into porous networks with short-range ordering. Typical

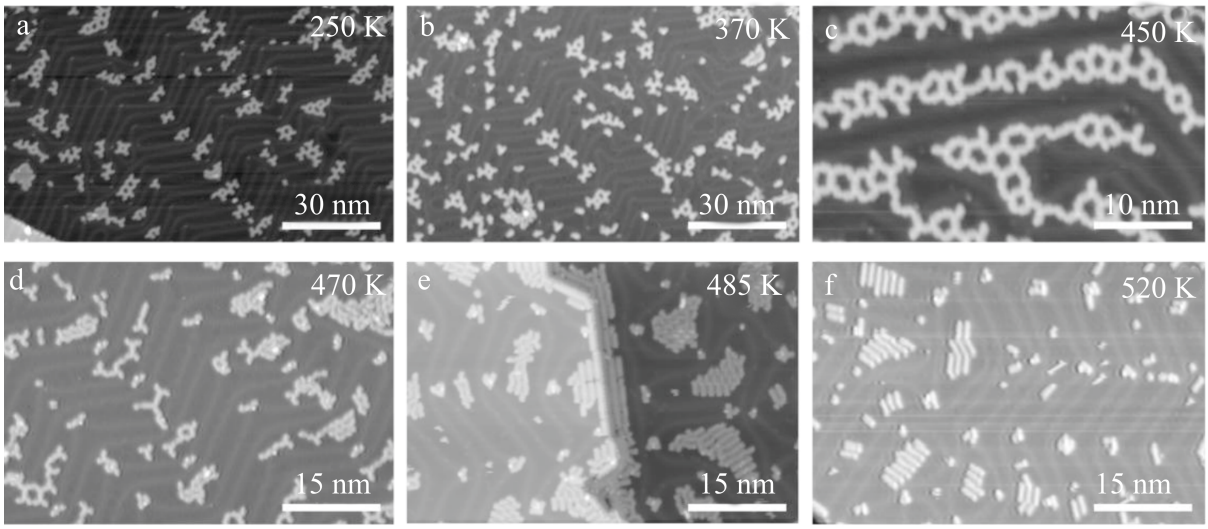

Figure 3.2: STM overview images of the DBP/Au(111) sample after annealing to various temperatures. STM set points as indicated. (a) Low coverage of DBP on Au(111) as-deposited at 250 K (-1.05 V, 0.1 nA). (b) The sample of Fig. S1a in the main manuscript after annealing to 100 °C (0.30 V, 0.20 nA). (c) The sample of Fig. 2a in the main manuscript after annealing to 175 °C (-0.78 V, 0.12 nA). (d) After annealing to 200 °C (0.48 V, 0.33 nA). (e) After annealing to 215 °C (-0.95 V, 0.05 nA). (f) After annealing to 250 °C (-0.58 V, 0.07 nA).

motifs are formed by clusters of four and six molecules. As can be seen in the BR-STM images in the Figure 3.3(a), the Br atoms are still attached to the molecule and stabilize the self-assembled structures *via* halogen bonds. Interestingly, we find that the *cis* isomer (Figure 3.3(b)) tends to form 90° angles, which led to square formations in *cis* aggregations. In the meanwhile, *trans* aggrupations form 120° angles and hexagonal closed structures (Figure 3.3(c)). Mixed aggregations of *cis* and *trans* result in irregular shapes. We adscribe this behaviour to the steric hindrance caused by the hydrogenated edges near to the Br atoms. *cis* isomers can be approached to both Br from the same side, allowing sharper corners, while the *trans* have alternating favourable assembling sides, which goes for wider approaching angles. This sample's look is identical to the result of evaporating DBP onto cooled 250K Au(111), or 175°C, both hot-deposited or annealed afterwards.

After further annealing, the situation gradually starts to evolve. Figure 3.3(d) is an AFM image highlighting the different kinds of molecules that were typically found after annealing the sample to 200°C (see Figure 3.2(d) for an overview image). There we can observe an intact DBP molecule (blue arrow) coexisting with molecules presenting either one or two lost bromines. The debrominated sides of molecules appear comparatively darker in the AFM image, suggesting a lower adsorption height, which we assign to the stronger interaction that the radical has with the surface. The Au(111) atoms can bond to stabilize the radical forming a metal-organic species. Some of these intermediates form chains, with the radicals of adjacent molecules pointing toward each other, connected to an intermediate Au adatom. The Laplace-filtered AFM image of such a chain in figure 3.3 (e) enables a closer inspection of the bonding region between adjacent molecules. The apparent

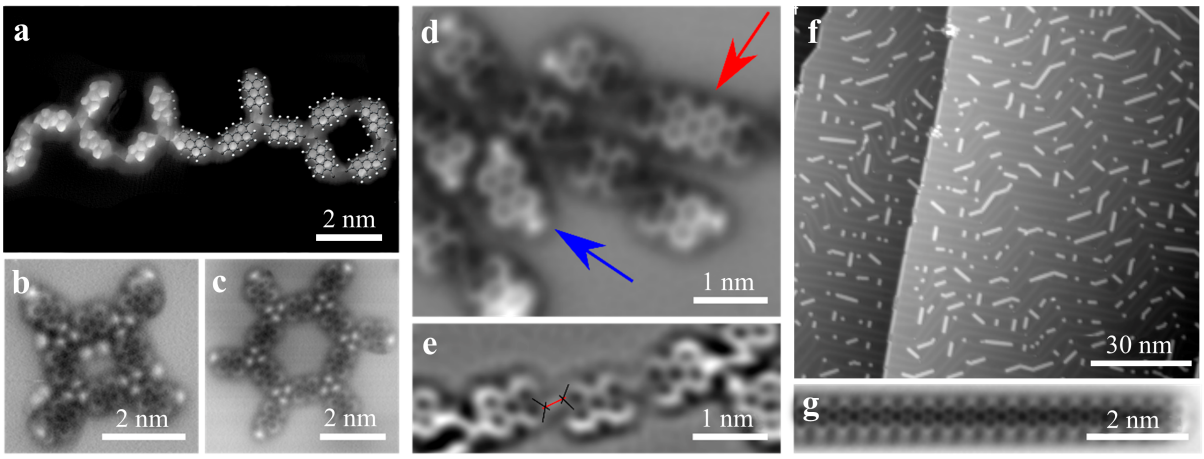

Figure 3.3: Figure 2. SPM characterization of 5-AGNR formation from DBP on Au(111). STM and AFM set points as indicated. (a) BR-STM image of the sample after deposition of DBP molecules (-0.05 V, 0.1 nA). (b, c) AFM images of self-assembled structures (b: 0.29 V, 0.05 nA, z = -0.4 Å; c: 0.31 V, 0.2 nA, z = 0.2 Å). (d) AFM image after annealing to 200 °C (-0.22 V, 0.1 nA, z = 0.0 Å). The blue arrow marks an intact DBP molecule, and the red arrow a molecular dimer. (e) Laplace-filtered AFM image (0.2 V, 0.1 nA, z = 0.2 Å). The red line marks the apparent bond connecting two DBP radicals. (f) Overview STM image after annealing to 330 °C (-0.73 V, 0.1 nA). (g) AFM image of a single 5-AGNR (-0.2 V, 0.1 nA, z = -0.15 Å).

bond[184, 142, 149] between two monomers is around 3-4Å, too long for a covalent bond. In addition, STM images of the same connection present a circular feature at certain bias where the Au is proposed to be, supporting the identification of the species as a metal-organic intermediate. It is hard to discern whether it is an actual adatom or a surface adatom that is partially lifted out of the surface plane.

The AFM image in figure 3.3(d) also reveals the presence of a molecule with a carbon backbone twice the length of the DBP monomer (red arrow). It is a dimer of precursors, after debromination C-C formation and cyclodehydrogenation (CDH). It suggests that the final reaction is already possible at temperatures with partial debromination efficiency. The coexistence of brominated precursor with the final product is a unique result never observed before, as the rest of the GNR studied show well separated temperature thresholds for polymerization upon radical formation by debromination and the subsequent formation of GNRs by CDH.[171, 182, 185] However, it is not solid enough proof to corroborate the co-existance of all three species in the same temperature window: If the annealing+cooling was fast enough, the partial debromination could be a kinetic result, rather than a metastable temperature plateau.

Annealing the sample above 250°C leads to the formation of well-defined, mostly straight 5-aGNRs, as the images in figure 3.3 (e,g) evidence. The overview STM image agrees with previous reports of synthesis of these ribbons from DBP.[186, 107]

3.2 XPS evolution with the temperature

To get a precise insight about the temperature dependence of the reaction we performed a series of synchrotron radiation XPS measurements at the Pearl beamline in the Swiss Light Source, SLS. The TD-XPS could be capable as well of evidencing the coexistence of the three reaction stages. We prepared a coverage of DBP around 80% of a monolayer on a resistively heated stage. The XPS data at room temperature for the Br 3d doublet arising from the $j = 3/2$ and $j = 5/2$ components[187] (in the figure 3.4 (a,b)) relate to molecular Br.

At around 150°C these peaks start decreasing and another doublet associated with atomic Br shows up at lower binding energy (figure 3.4 (c)), maintaining the total Br 3d intensity unchanged (figure 3.4 (d)). Instead, the integration of the total carbon signal starts decreasing along with the halogen activation onset (figure 3.4 (d)). The carbon reduction relates to a partial desorption of the debrominated molecules, lighter and more volatile than the heavier precursor. These combined signatures mark the onset for the C-Br bond cleavage and the corresponding metal-organic formation. The total Br signal for the sum of molecular and atomic species remains constant until the temperature reaches around 190°C (figure 3.4 (b,d)). The halogen desorption is known to be promoted by the presence of atomic hydrogen.[188, 189] The Br and H combine in the metallic surface to form $HBr_{(g)}$, which desorbs from the surface. As the only source of hydrogen is the last step of the ribbon formation, we asociate 190°C with the CDH onset. However, the dehalogenation of the reaction is not completed until 200°C. Therefore, in this temperature range there is coexistence of all reaction species (DBP, metal-organic intermediates and GNRs) on the surface, which

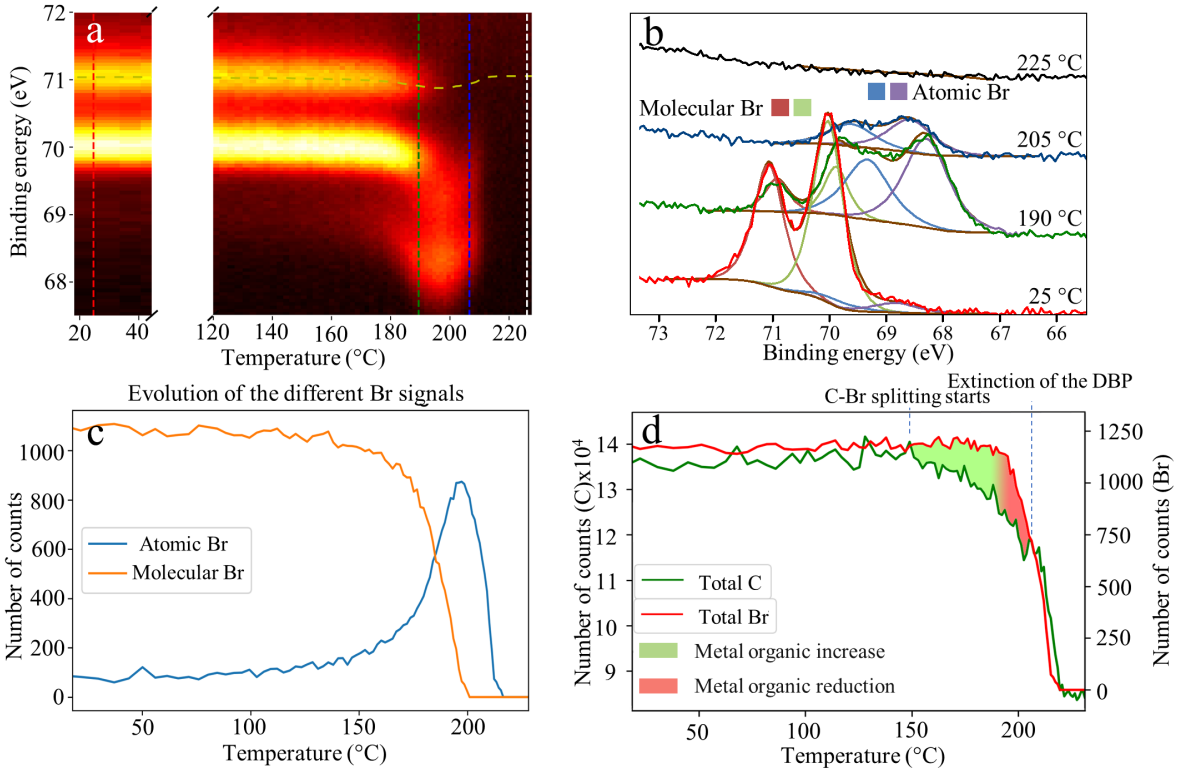

Figure 3.4: Figure 3. Core-level temperature dependence of DBP on Au(111) acquired at the SLS synchrotron. (a) Photoemission evolution with increasing temperature at the Br 3d energy window. Dashed yellow line represents the calculated shift in the signal caused by the change in the surface work function (explained in SI1). (b) Selected XPS spectra of the Br 3d indicated by the dashed lines in panel (a). In the red spectrum there is a pair of peaks assigned to molecular Br. The blue spectrum shows the complete transformation into atomic Br and its progressive desorption from the surface, which is complete in the black spectrum. (c) Br peak intensity evolution extracted from the spectral fitting of the temperature ramp. (d) Comparison of the integrated C 1s and Br 3d signals with increasing temperature. While C desorption is linked to C-Br splitting, Br desorption is associated with the presence of H caused by cyclodehydrogenation (ribbon formation). All the XPS measurements were taken with 420 eV photon energy.

matches our SPM experiments. The difference with respect to the SPM experiments is that in this case, the sample was ramping the temperature overnight at around 2min/°C. It is a pretty slow rate which would allow the sample to reach its chemical equilibrium, discarding flash annealing effects as the origin of the mixture of species.

To understand the evolution of the C 1s signal we required a more elaborate fitting than the Br 3d. After some fruitless analysis with constant work function (developed in Appendix A), we decided to calibrate the workfunction shift caused due to the accumulation of atomic Br at the surface. Figure 3.5(a) shows the rigid shift of the DBP Br doublet during the temperature ramp that pointed in that direction. Its correlation with the atomic Br concentration is shown in figure 3.5 (b). Using molecular Br as reference has multiple advantages: molecular Br is associated with unchanged molecules and can therefore be associated to work function modifications, it can be followed univocally along the reaction and, being bound to the molecular carbon backbone, the effect on the carbon atoms can be assumed to be similar. With this correlation at hand, we can use the atomic Br signal to calibrate the workfunction shift (Figure 3.5 (c)), drawn in figure 3.4(a) as the yellow dashed line. The C temperature-dependent spectra of figure 3.6 includes this calibration.

After this, we put forward a DFT model that provides the binding energies of each of the carbon atoms present in the reactants, metal-organic intermediates and cyclodehydrogenated ribbons (figure 3.6 (c,d)), which is then used for the experimental C 1s fitting (figure 3.6(a)). In the reactant, the calculations reveal three groups of carbon atoms related by their similar XPS shifts (coloured in figure 3.6(b)), equal for both isomers. As the intuition would tell, the group with the largest binding energy corresponds to C atoms bound to the

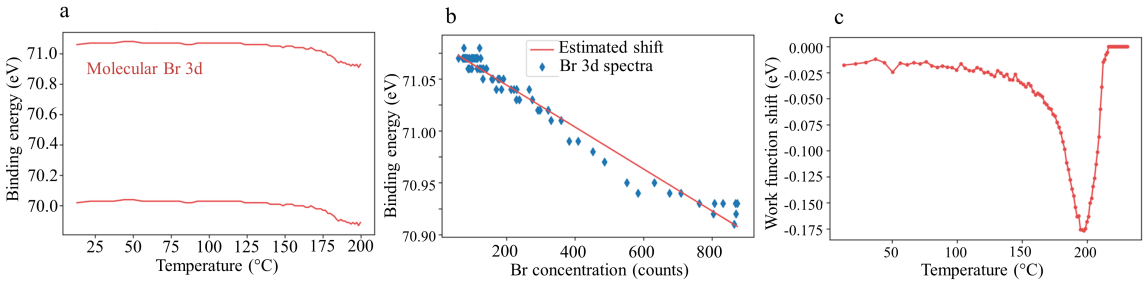

Figure 3.5:) a) Position of the pairs of bromine peaks with the temperature. Although the atomic Br peak shifts dramatically, the effect is also observed in the molecular Br. It has been proposed previously that the presence of atomic Br in the surface can change the average work function. b) Linear correlation between the Br concentration and the binding energy shift of the molecular Br. c) Estimated shift of the carbon XPS, as extracted from applying the function of b) to the atomic Br concentration.

more electronegative Br atoms, followed by the C-C species, and C-H as the lowest binding energy (H being less electronegative). The calculated energy spread within each group is largest for the latter, which justifies the use of a substantially larger width for this component (figure 3.6(b), green), while still maintaining the intensity ratio dictated by the group's stoichiometry.

The calculations for the graphene nanoribbons reveal two groups of carbon atoms by their shift, corresponding to the edge carbons bronded to hydrogen and those bonded only to other carbon atoms (figure 3.6(c,d)). For the fitting, the CC/CH ratio was left free, since it varies as the ribbons grow longer. Such ratio evolution validates the adequateness of the proposed fitting and simultaneously provides complementary information about the GNRs growth dynamics, as we will show later.

For the metal-organic intermediates DFT finds binding energies at values be-

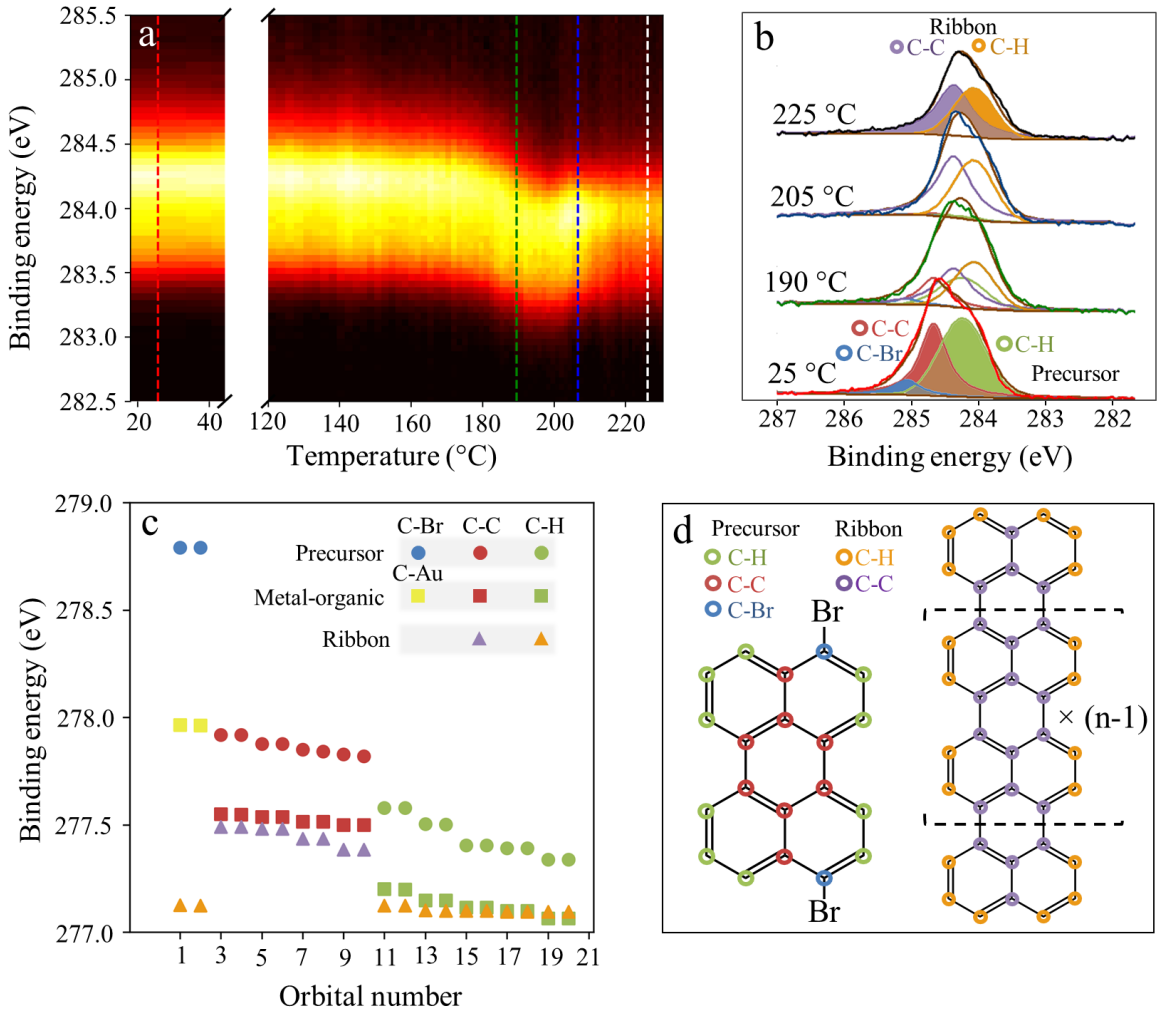

Figure 3.6: Synchrotron XPS analysis of the annealing of DBP on Au(111) for the C 1s. (a) XPS temperature evolution. (b) Selected XPS spectra of the C 1s indicated by the dashed lines in (a). (c) Core-level binding energy simulations for each of the carbon atoms within the precursor molecule, metal-organic intermediates, and a two-unit-cell-long ribbon. (d) Color-coded representation of the different categories into which the carbon atoms are grouped according to their core-level binding energies of (c).

tween those of the precursor and the ribbon (figure 3.6 (c)) Such energy positions enormously complicate the experimental fittings since multiple reaction species coexist on the surface at these temperatures (figure 3.4 (d)), each contributing with a variety of carbon signals and all squeezed in the spectra within less than 2 eV. Moreover, this combined with a predictably low ratio of metal-organic in the surface and the small temperature window, and the absence of previous XPS measurements that can help with the assignment made hard to find its XPS signal. Trying to guess their position from the DFT simulations could be an option. However, due to the high interaction between the metal-organic and the surface, its shift could vary compared to the rest of the species. With this hopeless landscape we decided to keep its signal out of our fitted models. In essence, we avoid overfitting and refrain from blind guessing this low-concentration species in the XPS data (figure 3.6(a)). Further attemps of fitting the MO shown in Appendix A.

Contrarily, we can trust the fitting results from the components asociated with pristine reactants and components asociated with the GNRs, both of which can be nicely fitted independently of one another at the low and high temperature ends of Figure 3.6(b).

After the workfunction shift and carbon fitting, the C-C/C-H ratio in the XPS fits on the GNRs allow us to extract the average ribbon length for the relevant temperature window (figure 3.7 (a)). It reveals three different phases in the GNR growth (figure 3.7 (b,c)). In a first stage, when the reaction is actively fed by the product of the dehalogenation, the GNRs maintain a constant average length around 3 monomeric units. Accordingly, the reaction does not proceed like a nucleation mechanism, where the initially formed GNRs are more likely to grow. Instead, the reaction is likely to happend between single dehalogenated

units that encounter each other on the surface. We rationalize this scenario by a larger mobility of the monomeric or dimeric units, which are thus more likely to encounter each other and react than the already formed longer ribbons.

A second phase sets in once almost all the DBP has been fully dehalogenated, whereby the source of metal-organic units and Br is exhausted, and short active chains start decreasing in concentration. The average lenght of the GNRs suddenly grows over a relatively small temperature window for three reasons: (i) the steric hindrance of the Br on the surface is reduced by desorption, accelerating the reaction; (ii) the lighter short GNRs/MO monomeric and dimeric species desorb from the surface (as supported by the still decreasing C signal, leaving room for the formation of longer GNRs (figure 3.7(c), shadowed area); and (iii) the scarcity of DBP in the surface supposes a lack of sources of short ribbon fragments. In the last phase, the average GNR length remains again relatively constant since the more volatile GNRs have already fused or desorbed, and the terminal units left are neutralized with hydrogen. There are no residual MO structures, and the only possible reaction is the uncontrolled dehydrogenation + fussion of mature GNRs, whose yield is very low at the maximum probed temperatures, justifying the absence of changes in the XPS spectra.

The resulting sample after the XPS measurements was characterized by STM at the end of the experiment (see inset of figure 3.6(d)), allowing for the determination of the statistical GNR length distribution after reaching the highest temperatures. The average GNR length extracted from the XPS analysis is around 7 monomers(figure 3.6(c)). To be comparable with the STM histogram it needs to be appropriately weighted, since the signal measured by XPS is directly proportional to the number of atoms, so that longer ribbons

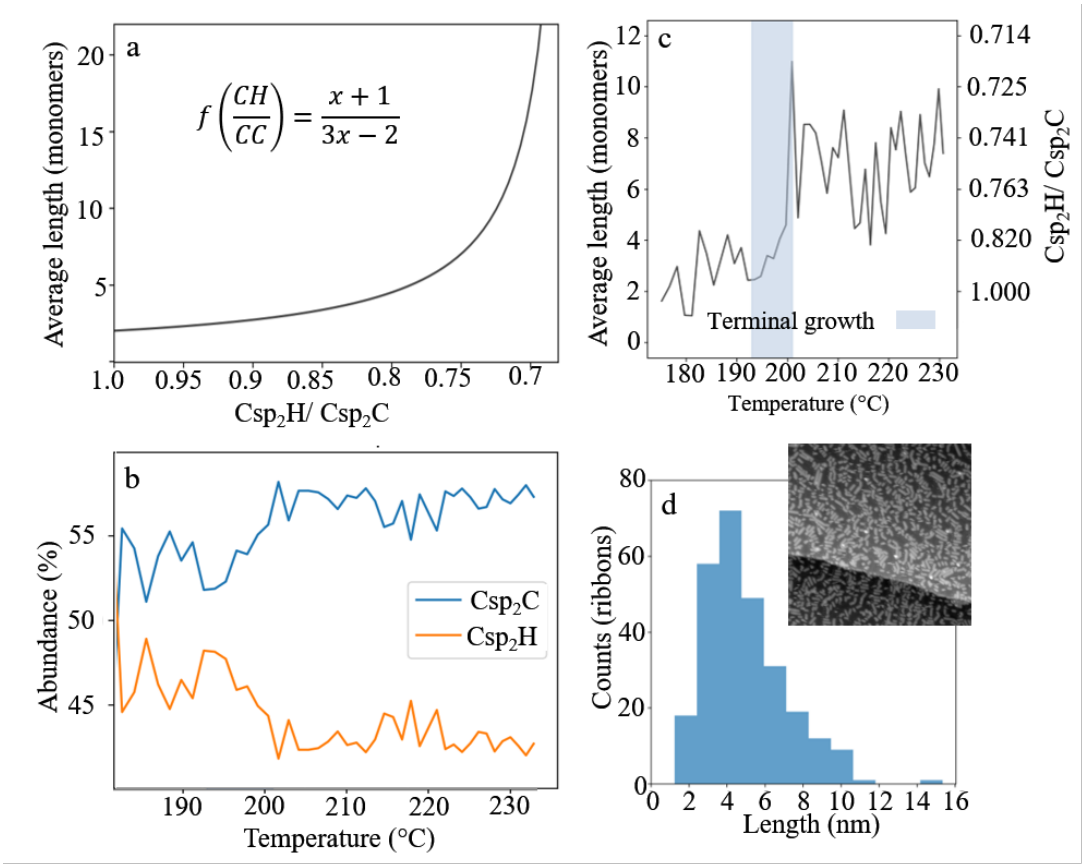

Figure 3.7: a) Relation between the CH/CC ratio and the average length of the ribbons. b) Relative abundance of the carbon peaks over the ribbon formation window. c) Average length of the ribbons during the XPS temperature ramp, extracted from the CH/CC intensity ratio. The C-C/C-H signal ratio of the GNR (right scale) increases with monomer length from 1 to 1.33. The shaded area demarks a window of significative growth in length. (d) Average length histogram extracted from STM images recorded after the temperature ramp, as the one shown.

provide a larger signal contribution than shorter ones. Taking this into consideration, we find an excellent match in the average ribbon length between both techniques, validating the previous interpretation of the growth dynamics.

At this point we draw attention on the notable and rather unexpected tendency of the studied reactants to fuse in a collinear manner that results in straight 5-aGNRs (figure 3.1(e)) rather than at an angle (figure 3.1(f)).[186, 107] Although the GNR growth process and the ultimate quality of the ribbons are known to be often affected by the precursor's concentration, these findings apply to all the coverages studied within this work, which range from very low amounts up to 80% of a monolayer. This is particularly noteworthy given the mixture of both *cis* and *trans* reactives, as well as the coexistence of parallel (figure 3.1 (c)) and staggered (figure 3.1 (d)) alignments in the metal-organic intermediates (figure 3.3 (e)). In this regard, however, note that whereas the SPM analysis can only identify the metastable structure of the reaction intermediates upon cooling to SPM imaging temperatures (5 K in our case), at high temperatures the molecules are very mobile and can explore a wider region of the potential energy surface. For example, the weak bonding of MO structures allows the bonds to split and re-form in a dynamic equilibrium,[190] in a similar way as metal organic complexes do in solution chemistry.[191] For that reason, the metal-organic intermediates are expected to go through both staggered and parallel configurations, as reflectedin figure 3.8. We can therefore discard the initial metal-organic configuration as a factor that modifies the outcome of the reaction. Hydrogen migrations display relatively low activation barriers as well (especially in the presence of radicals)[144, 192] potentially allowing the reactants to switch between the *cis* and *trans* configurations at the temperatures employed.

3.3 An alternative mechanism

The prevalence for the linear bonding motif and straight 5-aGNR may be expected from thermodynamic arguments. It involves the formation of a six-membered ring after the CDH step, in contrast to a five-membered ring for the kinked junction. The thermodynamic preference for the former relates to the lower strain of the structure involving exclusively hexagonal rings, as well as to the tendency to avoid spin frustration caused by odd-membered rings in carbon sp^2-bonded carbon networks,[193] which reduces the stability of such structures and is typically mirrored in lower HOMO-LUMO gap values.[193, 194] Indeed, we have confirmed this by DFT calculations of molecular dimers, which reveal their linear coupling product to be 0.46 eV more stable in the Gibbs free energy than the kinked one.[195] Nevertheless, the regioselectivity toward the benzenoid product is univocally related with the halogen activation of the precursor. In its absence, with comparable sub-monolayer precursor coverage regime, there is a clear prevalence of the kinked junctions instead, as observed in Zeying Cai's work with nonhalogenated quaterrylene (four unit cell long 5-aGNR).[196] They rationalized this scenario as an effect of a kinetically driven reaction, conclusion we absolutely agree with. For further explanation, see appendix A.5. We theorized the following as the reaction mechanism: in the absence of radicals, the intermolecular coupling proceeds preferentially *via* an initial covalent bonding of the two molecules through the more reactive zigzag edge carbon atoms, but in a staggered configuration to minimize the steric hindrance (figure 3.8(b)). Thereafter, a CDH reaction in the resting adjacent C sites will necessarily form a five-membered ring and a kinked junction. Likewise, starting from

the halogenated reactants, if a single covalent bond were directly formed after dehalogenation or after the formation of a metal-organic complex, following a conventional Ullmann coupling scenario, the parallel alignment would be disfavored because of steric hindrancefor the same reason (figure 3.8(a)). In contrast, molecules binding with a staggered alignment would share the structure with the intermediate assumed for the quaterrylene case and thus continue the reaction toward the kinked product (figure 3.8(b)).

Instead, we propose that the bonding mechanism at work here derives from a concerted bond formation at the two zigzag sites by activation of two C-H bonds that is facilitated by the radicals generated at the dehalogenation sites (figure 3.8(c,d)). Upon abstraction of two hydrogens from the intermediate's zigzag ends, the two monomers are univocally bound to form the thermodynamically favored product, promoting the formation of fully benzenoid, straight GNRs. An alternative activation of a lateral carbon in staggered MO intermediates (figure 3.8(e)) is comparatively unfavorable due to the lower stability of the end products, but may still be responsible for the non-negligible presence of kinked junctions. Although the latter may also stem from a conventional Ullmann coupling sequence, this seems unlikely because the intermediate with a single covalent bond has not been observed in our experiments. Note that mechanism like the one we propose is unfavourable for the fully hydrogenated ends case of Zeying Cai. It would require the simultaneous activation of four C-H bonds per fusion, which would have a huge energy barrier and a specific alignment of the molecules in the surface.[197] The unfavored Ullmann coupling with DBP molecules contrasts with the reaction mechanism followed by the majority of other GNR precursors. We associate this with the steric hindrance between dehalogenated DBP molecules, which

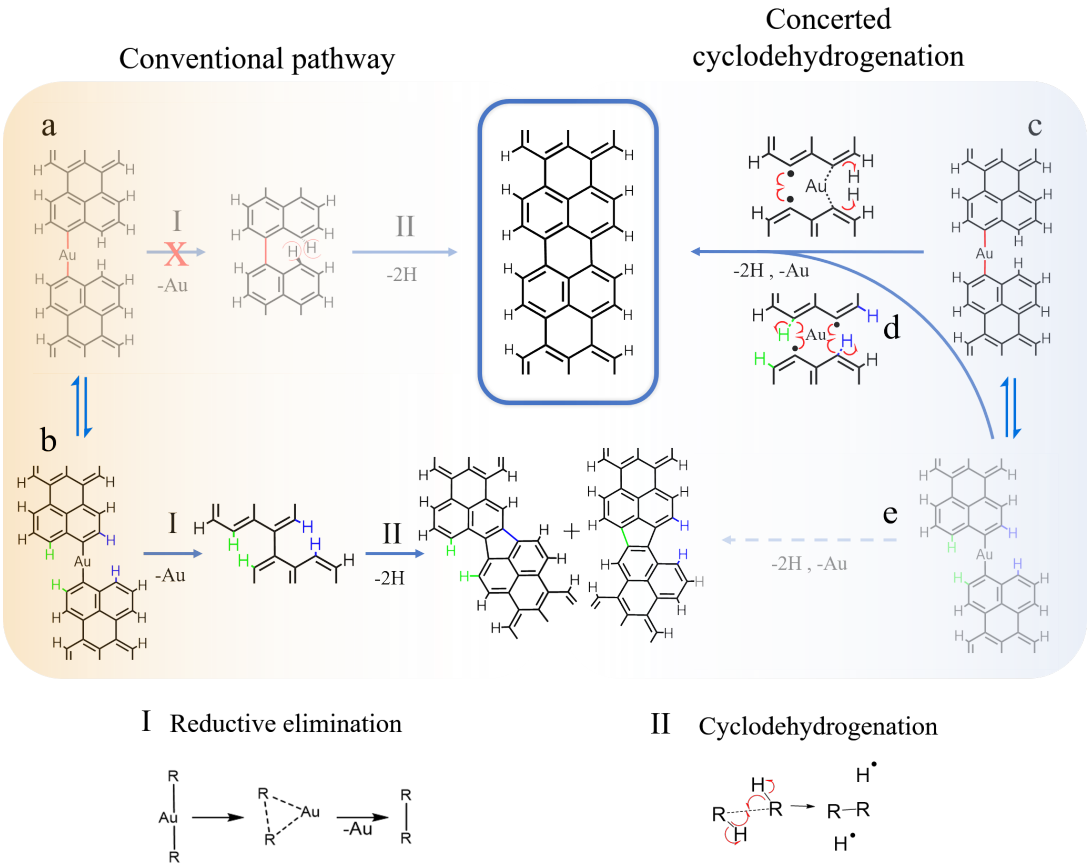

Figure 3.8: Figure 5. Diverse combinations of reaction pathways and their products. The conventional pathway for DBP is sterically impeded for collinear reactants (a) and would lead to the formation of kinked ribbons for staggered reactants (b). Instead, a concerted cyclodehydrogenation process starting from both collinear (c) and staggered (d) intermediates results in straight ribbons. (e) A similar concerted cyclodehydrogenation but with activation of lateral carbon atoms would form kinked junctions.

is amplified by their flat structure. This forces the molecules to be coplanar on the Au(111) surface, leaving no room to avoid steric hindrance, as seen in more flexible three-dimensional assemblies.

As a result, a metal-organic intermediate with a Au adatom is favored, which can also play a role in the subsequent dehydrogenation step.[198] This mechanism is similar to the growth process on Cu(111), where a metal-organic diradical intermediate is followed by the activation of the remaining zigzag-site hydrogen atoms to form a second tetraradical species.[185] Au(111) metal-organic intermediates are known to be energetically less favorable compared to Cu(111).[181] In consequence, a tetraradical Au metal-organic coordinate was not detected, and the reaction proceeds directly to the concerted bond formation. However, on Cu(111) no coexistence of the different intermediates was observed, and the resulting aGNRs were shorter and often kinked due to the high reactivity of the surface.[185] This result is in stark contrast to the Au(111) experiments presented here, where despite the temporary presence of a "messy" mixture of molecules due to the coexistence of all reaction species, primarily long, straight aGNRs are formed.

3.4 Conclusions

We provide detailed insight into the growth process of 5- aGNRs from dibromoperylene through a multitechnique approach. Scanning probe microscopy experiments revealed that for a specific temperature window there is a simultaneous presence of pristine

reactants, metal-organic intermediates, and fully cyclodehydrogenated GNRs. A detailed analysis of the carbon and bromine core-level intensity evolution from complementary temperature-dependent XPS experiments provides insight into the GNR growth dynamics and average length. Our experimental results supported with DFT allow us to unambiguously show that the reaction path starting from these planar precursor molecules to ultimately form 5-aGNR does not follow the expected sequence of Ullmann coupling and subsequent cyclodehydrogenation. Here, a concerted mechanism is proposed instead, involving the radical-guided activation of C-H bonds in both reactants, to simultaneously form two C-C bonds that result in a benzenoid ring and a straight intermolecular junction. The insight into this alternative reaction mechanism may help with the understanding of the chemical processes followed by other reactants,[199] as well as predicting the product structures from other rigid and planar halogenated precursors.

CHAPTER 4

Topological end states in 5-armchair Graphene nanoribbons

4.1 Density Functional Theory

After this in depth-study on 5-aGNR growth, we will focus again on their electronic structure. Let's recapitulate. Tight-binding calculations showed a pair of bands matching at the Fermi level. The two bands' wavefunction distribution is shown in Figure 4.1, all the way from the Brillouin zone center (Γ) to its edge (X). If we take a look at the wavefunction of Ψ at Γ we can see how it has a significant weight on the intercell space, while the Φ band has its intercell bonding state at X. From here we can understand why these bands have an opposite dispersion, in words of Hoffmann: "Maximizing bonding in the solid state is connected to lowering the DOS at the Fermi level, moving bonding states to lower energy, antibonding ones to high energy."[55] If we classify the four wavefunctions by their bonding character, we get the following order: $\Phi(X)$ is the most stable one, with two nodes in the wavefunction by unit cell. The next in stability would be both states at Γ: $\Phi(\Gamma)$ and $\Psi(\Gamma)$, with three nodes; and at last $\Psi(X)$ with four. The non-bonding states $\Phi(\Gamma)$ and $\Psi(\Gamma)$ are degenerate for first neighbour hoppings and infinite ribbons (literally with no ends), in which every bond is equivalent.

As we depicted in the introduction, more precise calculations did not corroborate this result.[74] This type of simulation takes into account many other variables such as relaxed bond lengths, electrostatic forces, or the electronegativity of each atom, among others. Their outcome is a more representative version of a free-standing infinite ribbon. For this reason we decided to perform our own calculations to find the causes of this contradiction. The following DFT calculations are the result of a collaboration with Pedro

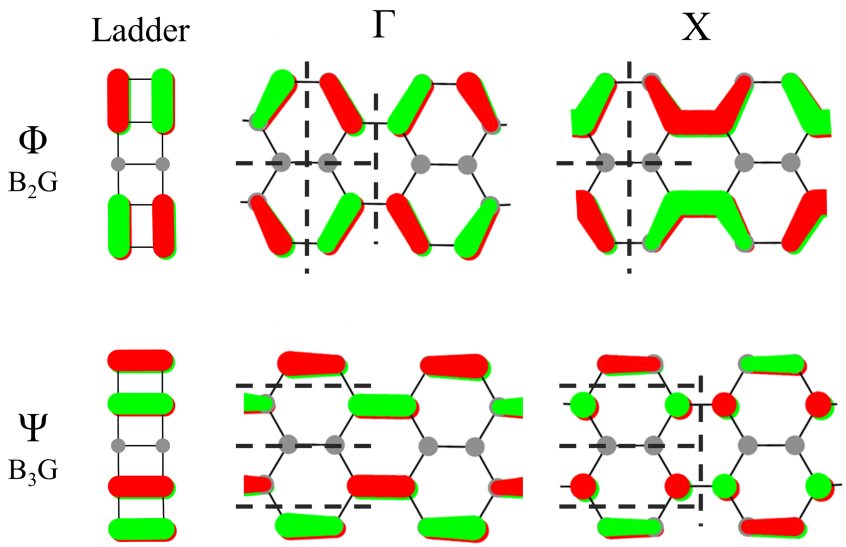

Figure 4.1: Non-bonding states (Φ and Ψ) from 5-aGNR. From left to right: Result of the tight binding on ladder single-unit cell ribbons. Once projected into a periodic ribbon, the wavefunction distributes at phase as (Γ) and at antiphase as (X). Ribbon sketches show two unit cells in order to appreciate the effect of the phase to the nodes, which are marked with dashed lines for the left cell of each ribbon as a guide to the eye.

Brandimarte and Daniel Sánchez Portal, shown in Figure 4.2 (a). 5-aGNR structure has been relaxed to its most stable conformation. It is remarkable to see how the bands, formerly matching at Fermi, now are separated by a gap around 0.4 eV. This matches with the case of polyacetylene.[200, 82] We can see how the valence band (VB) onset (Figure 4.2 (a)) resembles the wavefunction distribution of $\Psi(\Gamma)$ (Figure 4.1). However, the same band at π/a (squared in red), it has $\Phi(X)$ wavefunction distribution. This is a hint of the bands' crossing and posterior bandgap reopening expected for a topologically non-trivial structure.[93, 95, 96] As a counterexample, the unit cell was artificially stretched in order to destabilize inter-cell states ($\Psi(\Gamma)$). Calculations on a strained ribbon with lattice constant a=4.60 Å are shown at Figure 4.2 (b). Resulting of that, the bands now picture a trivial ribbon, with a VB onset similar to $\Phi(\Gamma)$.

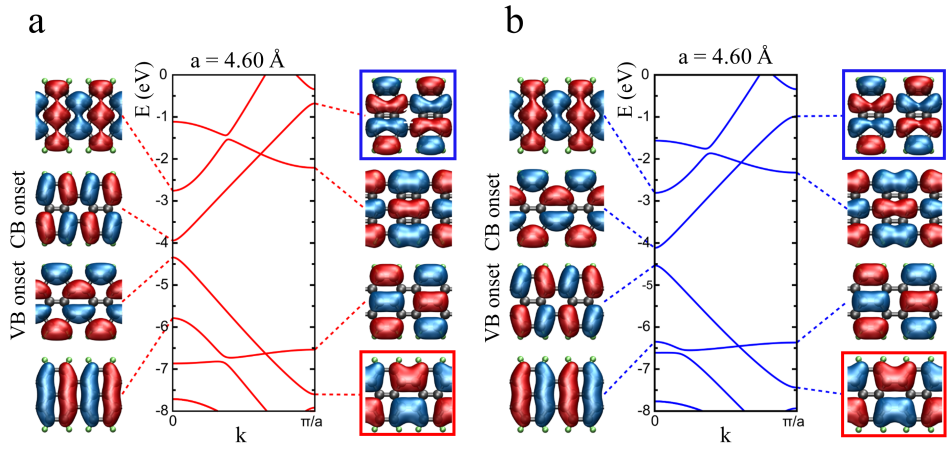

Figure 4.2: Band structures for the periodic ribbon, calculated by unrestricted DFT. 'a' refers to the unit cell length. a) Relaxed structure, topologically non trivial. b) Streched along the periodic direction, trivial. Red boxes mark the valence band at antiphase, that resembles $\Phi(X)$*, while blue boxes mark the conduction band antiphase, similar to* $\Psi(X)$.

The topological hints suggest a more complex electronic structure than expected in the first place. Knowing this, we decided to explore experimentally 5-aGNRs electronic structure.

4.2 Experimental results

After the successful synthesis of the 5-aGNR, we optimized the growth of long ribbons in order to get something closer to the quasi-infinite ribbon. The recipe for the best ribbons confirmed the mechanism proposed previously: Depositing the precursor onto a substrate held at 423K. The hot deposition favours the thermodynamic product over the kinetic byproducts, as well as favours the reaction of the new precursor fed with the already

reacted ribbons. After cooling the sample to 4.2K, we deposited CO in order to obtain BR-STM images.

The resulting ribbons are shown in Figure 4.3(a). When initially recording STM/STS of a 30-unit cell (UC)long ribbon, there are three states close to the Fermi level that are immediately apparent, as shown in the constant-height dI/ dV images in Figure 4.3 (b), along with a high resolution STM (HR-STM) image that reveals the chemical structure of the ribbon. After examining the DFT-calculated band structure of infinite 5-AGNRs (Figure 4.2 (a)), it becomes clear (taking into consideration the p-wave nature of our CO-functionalized probe) that the states observed at -150 and +700 mV are associated with the valence band (VB) and conduction band (CB) onsets of figure 4.3 (c), respectively. The state at 137 mV, notably confined to the GNR end regions, therefore corresponds to an in-gap state that is not predicted by calculations performed on infinite ribbons. Instead, calculations on finite 30-UC ribbons (Figure 4.3) reproduce not only the VB-related and CB-related states but also spin-polarized in-gap states whose superposition nicely resembles the experimental data. From the combination of these experimental and theoretical data, it is thus immediately clear that the actual band gap of a relatively long 5-AGNR on Au(111) is around 0.85 eV, in line with GW calculations in combination with image charge effects.[108]

4.2.1 Topology insights

As we already mentioned, previous tight-binding models predict 5-AGNRs (and the whole family of AGNRs with 3p+2 atoms across their width) non bonding states, but

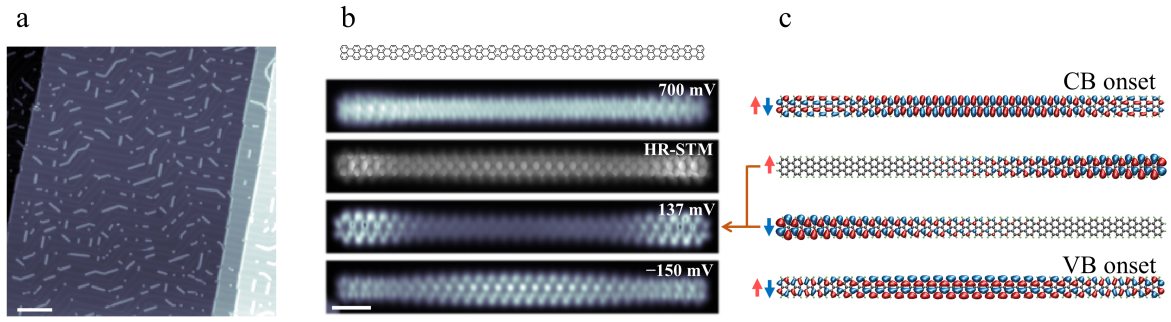

Figure 4.3: a) Sample of 5-aGNR prepared by hot-deposition. Conditions: -0.5 V, 500 pA. Scalebar: 15 nm. b) Closest-to-Fermi states of a 30 unit-cell graphene nanoribbon. c) Unrestricted DFT calculations of it, the two central states are spin-polarized. Their opposite-spin empty counterparts are not shown here.

do not predict their topological phase for different bond lengths (hopping constants). [74] In order to explore anisotropies in the bonds, we decided to include different hopping constants, as suggested by Son.[74] In particular, we use one for the bonds along the longitudinal ribbon axis (t_{par}) and another for the transversal bonds (t_{perp}). The results are displayed in Figure 4.4(a) and show how, starting from a zero band gap ribbon at $t_{par} = t_{perp}$ conditions, its band gap opens as the two hopping constants become increasingly different.

Here we employ a tool introduced previously. Remember that a non-null Zak phase ($\mathbb{Z}_2$=1) denotes a topological phase, while ($\mathbb{Z}_2$=1) represents a trivial phase. [71] In this case, we calculated the Zak phase when the bandgap opens in both directions, and obtained opposite results. Specifically, the ribbons reveal a topological phase $\mathbb{Z}_2 = 1$ when $t_{par} > t_{perp}$ and a trivial $\mathbb{Z}_2 = 0$ for $t_{par} < t_{perp}$, Figure 4.4(a). This case resembles the SSH model explained at section 1.4.

We already referred that it is energetically favorable for materials to open a

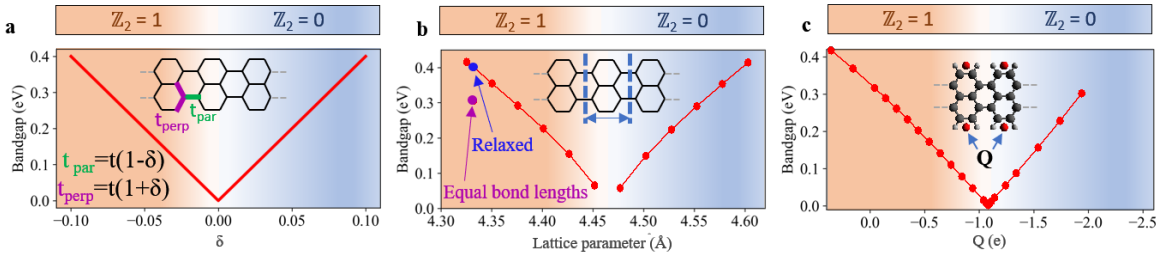

Figure 4.4: Topological class ($\mathbb{Z}_2 = 0$ or $\mathbb{Z}_2 = 1$) and band gap of 5-AGNRs as a function of different parameters: (a) As a function of the varying hopping constants tpar and tperp, marked in the inset, in a simple tight-binding model. (b) As a function of the lattice spacing a in a DFT calculation. The lowest-energy lattice spacing as obtained from DFT is marked with a blue point, whereas the purple data point marks the band gap value at that same lattice spacing but forcing all C-C bonds to be equally long (C-H bond lengths relaxed). (c) As a function of the point charges Q positioned as marked in the inset (calculated for a = 4.36 Å) at the DFT level.

band gap (Section 1.3), and that scenario is thus also expected for 5-AGNRs, however it is not intuitively clear the reason why the topological phase $t_{par} > t_{perp}$ is favoured over $t_{par} < t_{perp}$. To further investigate this question, we have performed more realistic DFT calculations with varying unit cell lattice spacings (Figure 4.4 (b)). The results shows a trend matching what was observed in Figure 4.2. There is a bandgap closing/reopening point at a lattice spacing of 4.46 Å, and the band gap opens toward the trivial or topological class as the lattice spacing increases or decreases from 4.46 Å, respectively. An intuitive analogy can be drawn comparing it to the tight-binding calculations of Figure 4.4(a): As longitudinal stretching affects the parallel bonds more, shorter or larger lattice spacings will promote a stronger or weaker t_{par} coupling relative to that of the transversal bonds t_{perp}, respectively. It goes in line with the already mentioned destabilization of the $\Psi(\Lambda)$ state. We have also performed DFT calculations on finite 30-UC long 5-AGNRs (Figure 4.5), revealing

again the exchanged wave function symmetry between the occupied and unoccupied orbitals near Fermi, as well as the presence or absence of end states depending on the topological class. Note that in the topological case, not one but two pairs of spin-polarized states appear around Fermi. Anderson model for magnetic states on metal substrates[128, 201] predicts these two resonances in the density of states: one below the Fermi level for the singly occupied state (SOMO) and another above the Fermi level (SUMO), separated from the occupied state by the Coulomb repulsion (U). However, for the 30-UC measurements, only one signal is observed, above Fermi. The reason is that the single electrons in both end states are being transferred to the gold substrate due to its high work function. In consequence, both spin polarized pairs are not separated anymore by U and appear as a non-polarized orbital.

Back to the topologic characterization, the lowest-energy configuration corresponds to an equilibrium lattice parameter of 4.33 Å (marked in Figure 4.4(b) with the blue point), which is clearly on the topological side and displays a notable band gap. These calculations thus already provide an answer to the question of the topological class of 5-AGNRs and confirm the topological nature of their experimentally observed in-gap states. However, they do not clarify the causes why the ribbons relax toward the topological regime. A substantial band gap value and the same topological class are obtained from DFT calculations where bond lengths were forced to be equal (purple point in Figure 4.4 (b)). This goes against bond length relaxations as the driving force for the topologic phase.

An alternative we studied is how the band gap opening is driven by the different electrostatic potential felt by valence electrons at different regions of the ribbon due to the

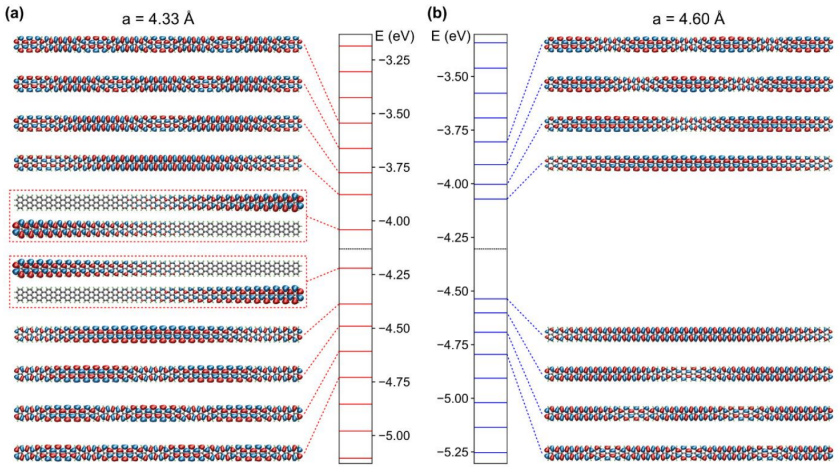

Figure 4.5: A comparison of gas-phase DFT calculations for the topologically (a) non-trivial and (b) trivial 30-UC 5-AGNR. The structures were built by taking the unit cell geometry optimized at a fixed lattice parameter (a = 4.33 Å for the non-trivial case and a = 4.60 Å for the trivial one, see Fig. S2), replicating it and only leaving it to further relax the hydrogen atoms. No spin-split end states can be seen on the trivial ribbon, and the orbital character of the valence and conduction band onsets are noticeably inverted from those seen in the relaxed ribbon (Fig. S2(a) and main paper Fig. 1(d)).

positive partial charge on the hydrogen atoms along the sides of the GNR. The importance of this inductive effect has been tested by performing DFT calculations on 5-AGNRs with additional point charges centered between the two hydrogen atoms of each unit cell on either GNR side (see inset in Figure 4.4 (c)). The point charges are modeled by a Yukawa potential with a decay constant λ = 0.01 Å^{-1} in order to avoid numerical instabilities due to the long range of the unscreened Coulomb interaction. Again, a qualitatively similar behavior is observed as in the calculations shown in Figure 2a,b. A zero band gap and topological inversion point is found for a charge of -1.04 $|e|$ on each Yukawa potential center. More negative charges open a band gap toward the trivial regime, and less negative charges open a band gap toward the topological regime.

An analogy can again be drawn to the tight binding results of Figure 4.2(a). A more negative charge will cause repel on the delocalized -electrons and disfavor their localization at the bonds that are the closest to the Yukawa potential centers, namely, the parallel bonds between the hydrogenated carbon atoms at the edge of the ribbon. This leads to an effectively lower t_{par}. Instead, a positive charge will attract the -electrons toward those parallel bonds, increasing t_{par} with respect to t_{perp}. At Q = 0, the electrostatic potential generated by the positive partial charges of the hydrogen atoms already favors the electrons on those bonds, and the inversion point at -1.04 $|e|$ can be seen as the charge required to compensate for the effect of the hydrogen atoms. This explanation from a physics point of view matches what is defined in chemistry as "inductive effect", a well comprehended phenomenon. This effect depends on the electronegativity of the atoms involved in a bond, and in this case points as well towards a partial negative charge in the

aGNR carbon edges. That is, our numerical experiment suggests that the ultimate reason for why the 5-AGNRs open a gap toward the topological side is the electrostatic potential generated by the partial charges of the hydrogen atoms along the GNR edges. Overall, with strain and the electrostatic potential along the GNR's edges being potentially controllable parameters, this insight may allow the tuning of the topology of GNRs and thus also their associated properties.

There are other explanations for the same phenomena which could reach the same conclusion. One is the bond alternancy proposed by Nakada.[202] Her theory suggested stronger $C_{sp2}H - C_{sp2}H$ bonds in the edges caused by topology, what would resonate to the intercell bonds for the 5-aGNR. From there, we could deduce a stabilization of $\Psi(\Gamma)$ vs the destabilization of $\Phi(\Gamma)$ (Figure 4.1).

Another justification which points in the same direction is the analogy of $\Psi, \Phi(\Gamma)$ with cis-polyacetylene orbitals (Figure 1.13). We mentioned how they are degenerate in first and second order hopping models. However, DFT simulations based on the relaxed structure found a tendency towards a more stable cis-transoid configuration, analogous of our topological configuration. [203, 204] In Yamabe's 1979 tight-binding models, he obtains a similar result even for equal bond lengths, with an HOMO-LUMO gap caused by far-neighbour interactions.[205, 200, 203] Those take part in the axial direction, stabilizing the Ψ-like state. Yamabe also relates the deformation of the lattice in favor of the bonds where the HOMO resides, as a latter consequence. For 5-aGNR, longitudinal long-range interactions could favour $\Psi(\Lambda)$ vs $\Phi(\Lambda)$ in a similar way.

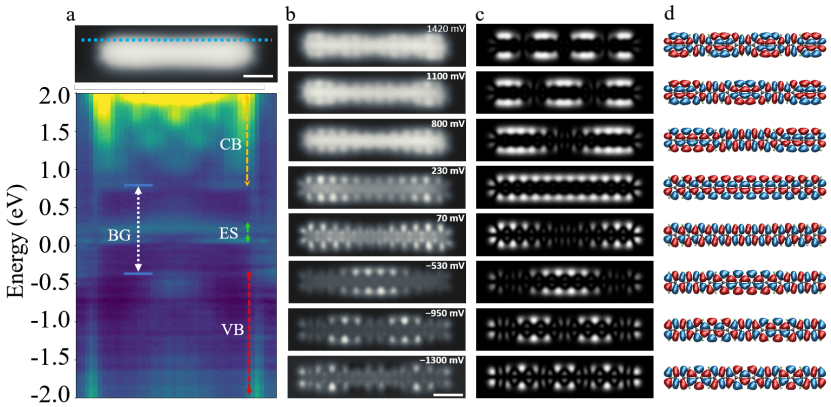

Figure 4.6: Figure 3. (a) Stacked dI/dV point spectra (40 points) along the side of a 12-UC 5-AGNR on Au(111), as marked in the GNR STM image above, recorded with a metallic tip (feedback opened at 303 pA, 500 mV; oscillation: f = 731 Hz, A = 15 mV). The onsets of the valence and conduction bands (VB and CB) are indicated, as are the two in-gap "end states". (b) Corresponding constant-height dI/dV images (Cl tip), with the associated bias voltage of each state. (c) Simulated STM images of the frontier states of a 12-UC 5-AGNR and (d) associated orbitals of free-standing GNRs.

4.3 Characterization of 5-aGNR

In order to fully characterize the electronic structure of the 5-AGNRs, dI/dV point spectra were taken along one longitudinal side of a GNR and stacked into a color-coded map. Such data are displayed in Figure 4.6(a) for a 12-UC 5-AGNR adsorbed on Au(111). A number of discrete states are resolved, with their spatial distribution mapped out in a series of constant-height dI/dV images that are presented in Figure 4.6(b). Simulated constant-height STM images at 4 Å above the molecular plane (to account for the tip-sample distance and the locally different orbital decay into the vacuum[206]) are shown in Figure 4.6(c),[186] and the corresponding wave functions are displayed in Figure 4.6(d). The

excellent agreement between experiment and theory demonstrates that molecule-substrate coupling has little effect on the apparent local density of states on the nanoribbons, which allows for a straightforward assignment of the observed molecular states. They correspond to quantized states of the valence and conduction band, whose number of nodes increases with energy away from the Fermi level. It is important to note the difference in appearance between the onset of the valence and conduction bands in the dI/dV signal, in particular that, whereas the valence band onset is measured with highest intensity over the central region of the ribbon, as normally expected for the lowest-energy quantized mode, the conduction band onset appears with a central node. This relates to the two different orbital symmetries that can be seen in the calculated gas-phase orbitals (Figure 4.6 (d)).

The onsets of the valence and conduction bands have this structure inverted, such that the valence band onset's central features are similar to those seen at the ends of the ribbon in the onset of the conduction band. Phase cancellation effects cause one of these types of orbital structures to extend much more into the vacuum than the other (especially along the sides of the ribbon). As a result, the STM signal, which probes the density of states several angstroms above the molecular plane, is greatly affected by the orbital's symmetry, as clearly supported by the simulated constant-height STM images shown in Figure 4.6(c).

Within the band gap of the 12-UC ribbon, two distinct states are clearly observed in the dI/dV spectra. These can be assigned to the end states of the nanoribbons, of which the lower-energy state is occupied when the ribbon is in the gas phase. However, this is in contrast with the 30-UC case, and our previous reasoning for the presence of only one resonance. For short ribbons, we observe DOS at two different energies, even tough both are

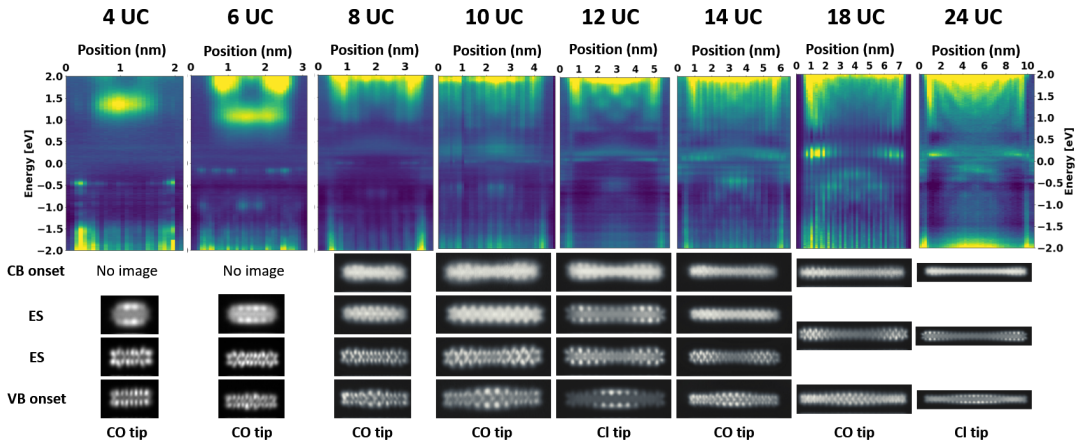

Figure 4.7: A series of dI/dV line scans for ribbons of increasing length, adsorbed on Au(111), accompanied by constant height dI/dV images of their CB onset, end states and VB onset (where possible). The tip used for the images is indicated below. The sharp transition seen in the 10-UC line scan is due to the ribbon moving part way through the experiment. However, all states of interest can still be seen in the region recorded before it shifted.

over Fermi level. To examine the relationship between the length of the 5-AGNRs and the character of these in-gap states, we have measured a series of stacked dI/dV point spectra on ribbons of varying length.

4.3.1 Topological states vs length

A notable length dependence is observed in the ribbon's electronic properties that only tends toward saturation for the longest ribbons that were measured (beyond 20 unit cells, Figure 4.7). Of particular interest is the trend seen in the appearance of the end states of the ribbons as they change in length. Longer 5-AGNRs show a single end state DOS peak that has most of its intensity at the termini. As the length decreases to 14-UC and

below, this splits into two states with an energy gap that increases as the ribbons shorten (Figure 4.7, bottom).

In order to decouple them from the metallic surface, some ribbons of different lengths were transferred to an NaCl monolayer. The salt was deposited at sub-monolayer concentration, in order to form patches. CO required to be deposited again on the cooled sample. The ribbons were transferred to the NaCl by tip manipulation, first lifted from one end, then slowly dragged over a patch of monolayer, differentiable from bilayer due to its amorphous contour. Similar experiments are reported in the literature for 7-AGNRs[7, 207] mixed 7/14-AGNRs,[208] chiral GNRs[207] and zigzag GNRs[11]

The insulating islands act as a decoupling layer that reduces the metal-molecule hybridization, which allows for the acquisition of clearer signals in dI/dV spectra and mapping than the equivalent measurements on the metallic substrate. The effect, however, is not strong enough for long ribbons to recover neutral charge state. Nonetheless, it allows a more precise characterization of the electronic structure of the ribbons, with better-defined peaks in the spectra. For comparison, dI/dV line scans and images of nanoribbons adsorbed on Au(111) are presented in Figure 4.8 at right, comparable to the ones of Figure 4.6 (b).

The transition of the end states with the length is easier to observe in ribbons decoupled from the Au substrate (dashed orange and blue boxes, Figure 4.9 (a)). DFT predicts a transition from degenerate singly occupied, spin-split end states to closed-shell end states as they become closer and hybridize in the shorter ribbons. Simple schematics for this are presented in Figure 4.9 (b,c), showing how 5-AGNRs with 16-UC still have spin-

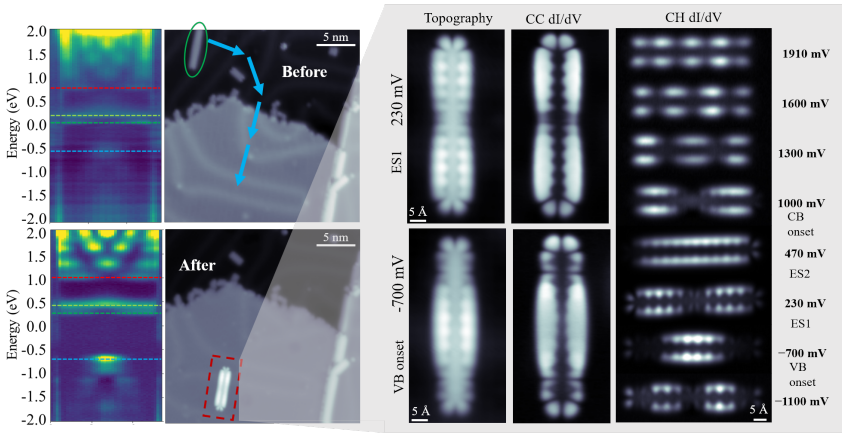

Figure 4.8: Closest states from a 22 unit-cell graphene nanoribbon

polarized end states but those with 14-UC (or fewer) do not. This length threshold matches exactly with experimental data plotted above. An scheme of the energy levels measured and calculated is shown at figure 4.10.

4.3.2 Magnetic characterization of the end states

To further characterize 5-AGNRs and experimentally prove the magnetic nature of their topological end states, we performed transport measurements across GNRs in a two terminal device structure. This is achieved using the STM tip and the substrate as the two contacts, with the GNR bridging the two.[209, 210] This process is depicted in Figure 4.11(a), in which the metallic STM tip is approached to one terminus of the nanoribbon with a low bias voltage (feedback open). As the tip approaches, the tunneling barrier decreases and the associated current increases exponentially. A linear trace is thus obtained in a logarithmic plot of the current. Its slope β, also called the tunneling decay constant, relates to the effective tunneling barrier height and in a first approximation is associated with the average

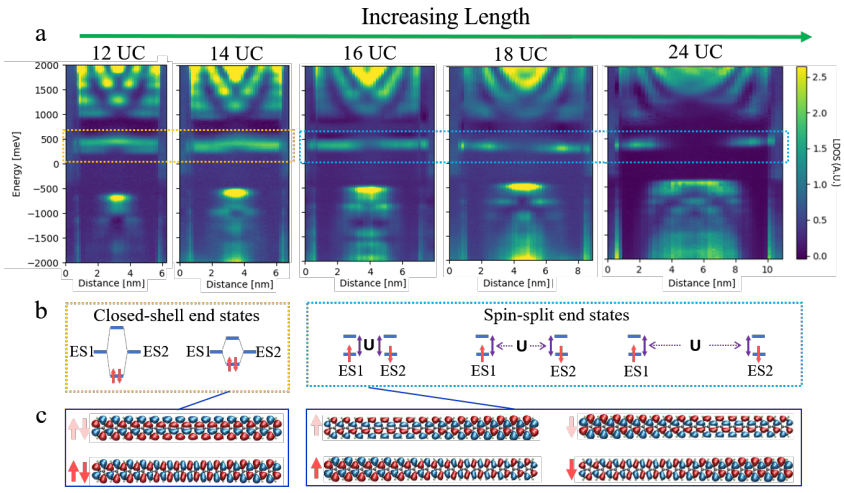

Figure 4.9: (a) Series of dI/dV line scans performed on 5-AGNRs of increasing length, all adsorbed on NaCl/Au(111). The line scans are each scaled to represent the actual length of the ribbons. End states are highlighted with yellow and blue boxes. (b) Simple model for the occupation of the end states (ES1 and ES2) in free-standing ribbons. In ribbons of 14-UC and below, the two end states hybridize into bonding and antibonding orbitals, generating a closed-shell structure. In ribbons of 16-UC and above, the end states are degenerate singly occupied states, separated by the charging energy U from their unoccupied counterparts. (c) Gas-phase molecular orbitals for 14-UC and 16-UC GNRs. Faded red arrows indicate wheter we refer to orbitals (double arrow) or single states (single arrow).

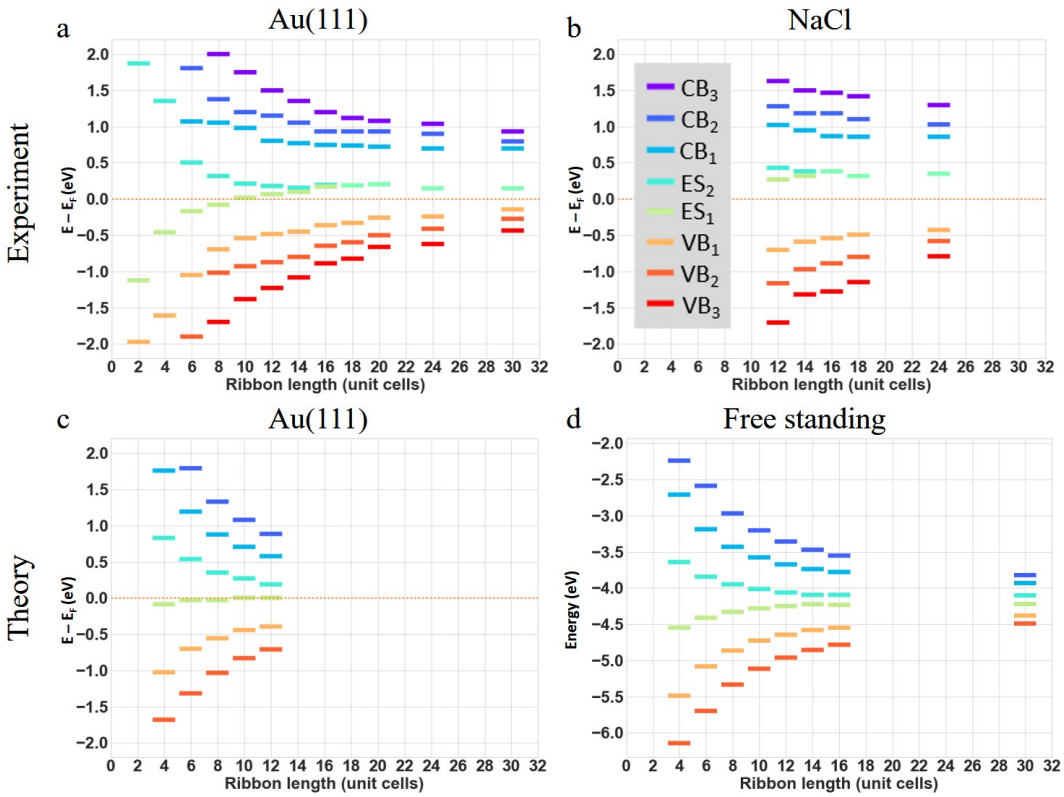

Figure 4.10: Experimental energies for the quantization states as a function of the GNR length on Au(111) (a) and on a NaCl monolayer (b). The energies of those same states from calculations on Au(111)-supported and free-standing GNRs are displayed in (c) and (d), respectively. Comparison of the data on Au(111) and NaCl/Au(111) clearly show the effect of the reduced screening (a larger apparent bandgap) on NaCl for all lengths. Both datasets display a similar strong length dependence that only tends to saturation beyond 20 unit cells. A comparable length dependence is observed in our calculations for both Au(111)-supported and free standing GNRs. In addition, both on Au(111) and NaCl/Au(111) the GNRs get charged by electron donation to the high workfunction substrate for ribbons above a certain length threshold (8-10 UC on Au(111)). This is again confirmed by DFT calculations, which show a similar length threshold (10 UC) at which the GNRs become charged on Au(111).

of the tip and sample work functions. After reaching a sufficiently close distance, a sudden jump in the current signifies the jump to contact of the ribbon to the tip. Thereafter, the tip can be retracted, lifting the ribbon and resulting in the two-terminal device structure. In line with previous results,[211] as the ribbon is lifted, the current decreases with a dramatically reduced β constant ($0.94 \pm 0.1\ nm^{-1}$ at 5 mV bias, Figure 4.11(a)), which is among the lowest values reported for organic materials[212, 213, 214] and underlines the excellent conductive properties of these GNRs. Such a reduced β value can be understood from the low molecular band gap of 5-aGNRs as the tunneling barrier is now determined by the energy difference between E_F and the frontier molecular orbitals, in combination with the renormalized, low effective mass of its charge carriers, which is an additional parameter that also determines β.[209]

Interestingly, at low lifting heights up to around 1 nm, an initial increase in the current is observed. Whereas similar findings have been observed in previous experiments with 5-aGNRs,[211] their explanation has so far remained unclear. To obtain a better understanding, we performed the lifting process in a stepwise manner and took dI/dV spectra at each step. Because of the high conductance displayed by these ribbons, these experiments were performed with ribbons atop a NaCl monolayer. As previously shown in similar experiments with different GNRs,[207] the NaCl layer provides an additional tunneling barrier, which reduces the current flow through the device structure and thus allows the probing of a larger bias window.

A series of dI/dV spectra for the lifting of a 22-UC nanoribbon is presented as a 2D conductance map in Figure 4.11(b). With increasing lifting height, a peak in the dI/dV

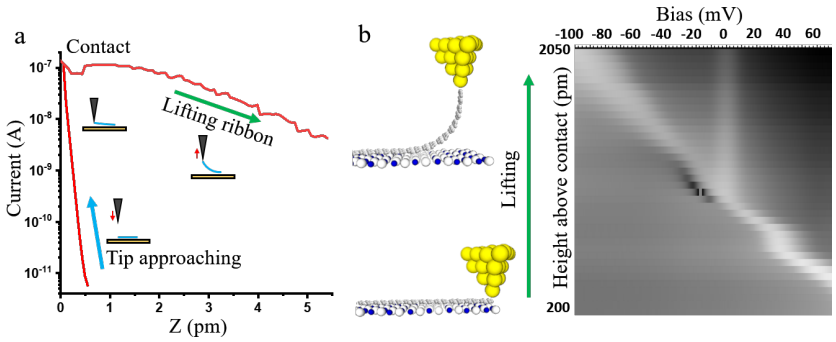

Figure 4.11: Figure 5. 5-AGNR lifting experiments. (a) Logarithmic plot of the current vs relative tip height for the lifting of a 14-UC 5-AGNR on Au(111), showing the sudden change in conductance once the ribbon has been contacted with the STM tip. The zero value of the relative tip height is set as the contact point. Schematics of the different lifting experiment scenarios are added as insets. (b) 2D conductance map of dI/dV spectra recorded during the lifting of a 22-UC 5-AGNR over NaCl. Each spectrum was recorded after moving to the next height value (steps of 50 pm). dI/dV intensity is plotted with a logarithmic scale to enhance the visibility of the zero-bias Kondo feature. Oscillation parameters: 731 Hz, 5 mV.

spectra observed at positive voltages shifts downward in energy. This signal corresponds to the unoccupied end state, which for these 5-aGNRs ribbons extends several nanometers along the ribbon due to its low band gap and can thus contribute to the charge transport at small lifting heights. As the end state approaches E_F, the tunneling barrier is lowered and the current thus increases. Thereafter, it crosses and moves away from E_F again, causing the opposite effect. Ultimately, the end state does not contribute to the charge transport as the lifting height surpasses its extension along the ribbon. This overall scenario explains the non monotonic current dependence on the lifting height.

In addition, a new zero-bias peak is also observed alongside the now-occupied end state that continues to downshift. It has a full-width at half maximum (FWHM) of approximately 14 meV, which, in the absence of a temperature-dependent analysis, is tenuously assigned to a Kondo temperature of around 82 K. To prove the Kondo nature of a zero-bias peak, it needs to be shown that it follows the appropriate behavior as a function of a particular parameter that distinguishes it from all other possible zero-bias resonance sources. The most conventional method consists of sweeping the temperature and analyzing its effect on the peak width or sweeping a magnetic field and monitoring the expected Kondo resonance splitting. The former is unfeasible because of the uncontrollable thermal expansion in the "lifting geometry", whereas, for the latter, our Kondo peak is too broad to reveal conclusive splitting or broadening upon application of magnetic fields typically available in STMs. Instead, we sweep a parameter not generally available in STM experiments, namely, the state occupancy. We sweep across the various occupation regimes described in the Anderson model for magnetic states,[201] from the empty orbital regime at low lifting heights

to the mixed valence regime as the state crosses the Fermi level, finally reaching the Kondo regime as the state becomes populated with a full electron. The appearance of a zero-bias resonance when the end state becomes occupied is unequivocally related with the Kondo effect, in contrast to other possible zero-bias peak sources like tip artifacts. Indeed, similar occupation sweeps have been studied through gating in three-terminal devices,[215, 216] including gateable STM setups.[217] Here, we mimic the gating by the fading electrostatic influence of the high work function substrate on the magnetic end state as it is lifted away from the surface.

The appearance of the Kondo peak upon the occupation of the end states is proof of their magnetism.[218] However, the Kondo peak is also seen in lifting experiments with shorter ribbons that are not expected to have singly occupied end states. This initially unexpected finding actually relates to a change in end state to end state hybridization when the ribbons are in a lifting geometry. The contact to the tip generates an asymmetry in the ribbon that changes the energies of the end states on either side, hindering their hybridization and leading to their open-shell character. This is indeed shown with a simple model in which the asymmetry is introduced by adding a hydrogen atom on one end of a 14-UC long ribbon. The DFT calculations on asymmetrically hydrogenated and pristine GNRs confirm the closed-shell character of the latter and the open-shell character of the former (figure 4.12).

What remains unclear from these experiments is which end state is being probed during the lifting: the state associated with the end of the ribbon in contact with the tip (through a bond of an unknown nature) or the end state of the ribbon terminus that is

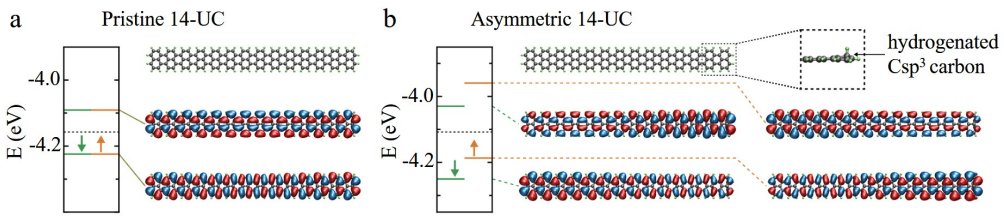

Figure 4.12: a) Structure of a pristine 14-UC 5-AGNR and its associated closed-shell end state orbitals. (b) Structure of an asymmetric 14-UC 5-GNR with a hydrogenated C atom on one end and its associated open-shell end state orbitals. Orange and green lines indicate opposite spin.

still adsorbed on the NaCl layer during lifting. For the former, the Kondo screening would come from the metal tip electrons, whereas, for the latter, it would be from the Au substrate through the NaCl layer. To determine which case it is, and also to further support that these end states are singly occupied and thus reactive π-radicals, we exposed the ribbons at room temperature to molecular oxygen in an ultrahigh vacuum chamber to a pressure of 2×10^{-5} mbar for approximately 2 hours.

4.4 Oxidation of the end states

After the oxygen exposure, many ribbons had a significantly different appearance in the STM imaging, especially at positive bias voltages. Studying these ribbons via BR-STM (Figure 4.13(a,b)) reveals a change in structure at the ends of the ribbon (a comparison is shown in Figure 4.13(c)), with what may be the addition of a new functional group. We tentatively suggest that this is a newly formed ketone group. A stack of dI/dV spectra along a ribbon with this group at both ends (i.e., doubly oxidized) is shown in Figure 4.13(d). In

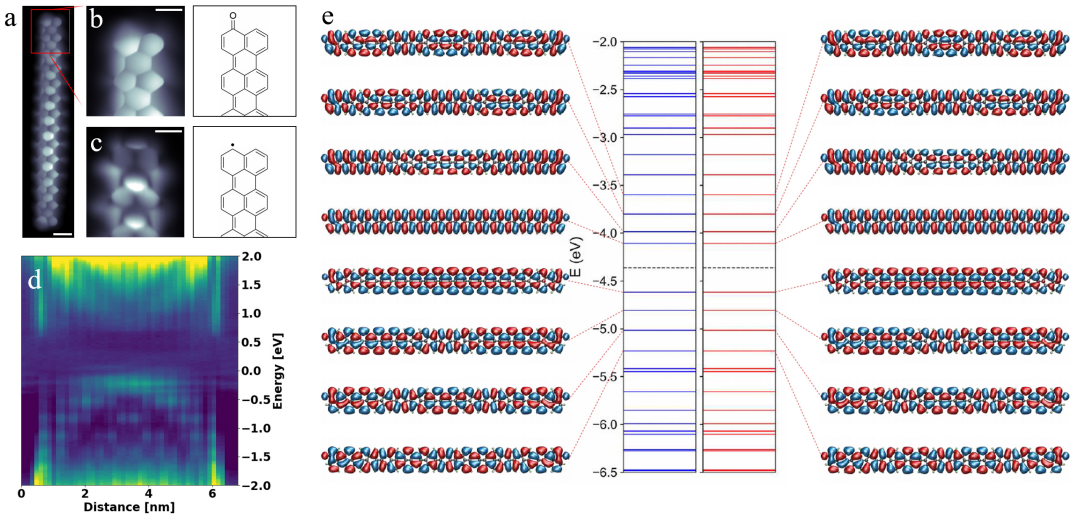

Figure 4.13: a) BR-STM (5 mV, CO tip) of a doubly oxidized 14-UC 5-aGNR on Au(111) (scale bar = 5 Å). b) BR-STM zoomed-in image of the oxidized end of the same nanoribbon showing the change in contrast at the edge of one ring. At side, the suggested chemical structure for the oxidized GNRs. c) Pristine end of a ribbon, for comparison. d) dI/dV line scan (oscillation parameters of 731 Hz, 15 mV) of the same doubly oxidized nanoribbon. Both valence and conduction bands are visible, but there are no longer any in-gap end states. f) Electronic structure and wavefunction of the doubly oxidized 16-UC 5-AGNR. The absence of end states is remarkable.

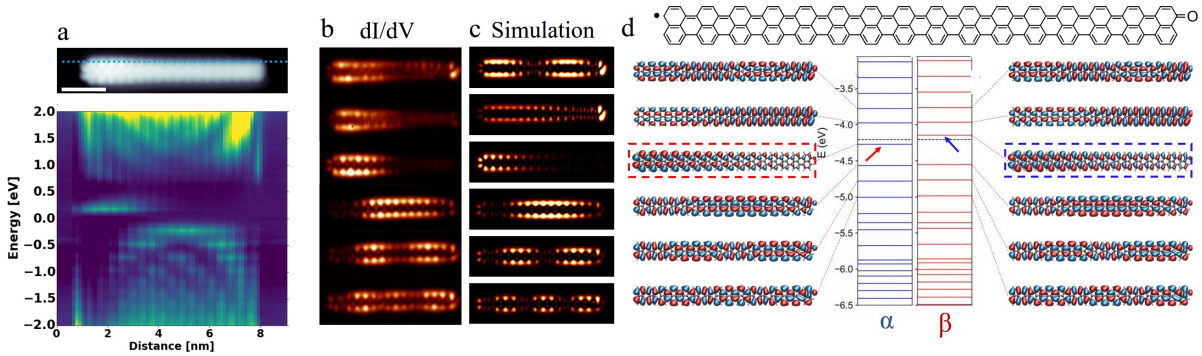

Figure 4.14: a) Half-oxidized 5-AGNR on Au(111), with a stacked dI/dV line scan plot. The end state only appears on the pristine end. Scale bar = 2nm. b) dI/dV C.H. images of of the half-oxidized ribbon over NaCl, corresponding from top to bottom: 1180 mV, 1040 mV, 360 mV (end state), -440 mV, -750 mV, -1080 mV. The results match with the gas-phase simulations (c) for a half-oxidized ribbon electronic structure (d). The arrows mark the presence of a polarized SOMO-SUMO pair at the pristine side.

stark contrast to the pristine ribbon, no in-gap states are found in the doubly oxidized nanoribbon, suggesting that the oxidation reaction results in the destruction of the end states. Both valence and conduction bands are clearly visible, with small changes to their appearances shown in figure Figure 4.13(e). In particular, an increased intensity at the ends of the ribbon is observed throughout both bands.

Some of the nanoribbons were instead only half-oxidized after the exposure, presenting a perfect opportunity for investigating the source of the Kondo feature that is observed when lifting pristine 5-AGNRs. A half-oxidized 5-AGNR electronic structure is presented at figure 4.14. It is clear from the dI/dV imaging at positive bias voltages that the pristine end still retains its end state, while the oxidized side lost its. Notably, the center of the onset states of valence and conduction bands is also spatially shifted relative to the geometrical center of the nanoribbon, with the valence band presenting a higher intensity

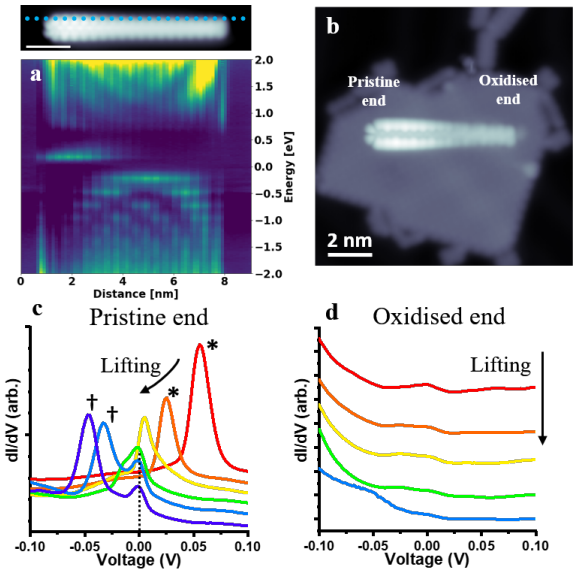

*Figure 4.15: Figure 7. . (a) STM image (0.5 V, 50 pA) of a half-oxidized 16-UC 5-AGNR that has been dragged onto a 1 ML NaCl island via the STM tip, with the pristine and oxidized ends indicated. (b,c) dI/dV lifting experiments of a different (26-UC) half-oxidized 5-AGNR on 1 ML NaCl, each via different ends of the ribbon. The end state shift and corresponding Kondo feature is only observed when lifting from the pristine end of the nanoribbon. Images of the lifted ribbon published in [186] † = 2× scale, * = 0.5× scale (to more clearly show the presence of the Kondo peak, which has a much lower intensity than the molecular state).*

closer to the oxidized end and vice versa for the conduction band. This is supported by DFT calculations of the gas-phase molecular orbitals and simulated dI/dV images of a 16-UC half-oxidized 5-AGNR; these are presented alongside experimental constant-height dI/dV images of the same nanoribbon in Figure 4.14 (b-d), with a high level of agreement between experiment and theory that further confirms the ketone group as the product of the oxidation.

Half-oxidized ribbons can also be manipulated onto a 1 ML NaCl island, as

shown in Figure 4.15. Lifting such nanoribbons provides clear evidence for the origin of the Kondo feature; it is only seen when lifting the pristine end of a half-oxidized ribbon, as shown in Figure 4.15 (b,c). This suggests that the origin of the observed end state that downshifts when lifting the pristine ends of 5-AGNRs is the end of the ribbon in contact with the tip. The increasing decoupling of the end state from the substrate as it is lifted by the tip shifts the state down toward its gas-phase singly occupied state, with Kondo screening coming from the tip itself.

4.5 Reactivity

The high reactivity of unpaired states (radicals) has been widely explored in solution chemistry. However, it is still an unexplored topic in surface science. Our results with the 5-aGNR suggest that the π radicals caused by the topology undergo the same chemical instability as conventional, σ radicals. Our experiments concerning their exposure to O_2 showed how the ribbons' ends oxidized regardless of their predominant phase. The short close-shell 5-aGNR were affected, partially or completely, in a 96% vs a 93% for the longer open-shell ribbons. The minimal difference implies both of them are equally affected by the chemical attack. The result of the oxidation is an electronic structure close to the one of the open-shell ribbon, without the "destabilizing" end states (observe Figure 4.13 vs 4.5). This results suggest that the alternative of a lower energy state through a different topological regime affects the reactivity of the ribbons even for the short 5-aGNR.

This concept is developed in Stuyver's work "Do diradicals behave as radicals?".[97] In it, Stuyver gets a perspective of whether molecules close-to-be open-shell (radicaloids) change their reactivity as their radicals hybridize. He concludes that the reactivity does not get affected about the predominant phase of the system (in terms of the thermodynamic viability of the reaction). The conditioning factor for the reaction is the difference between the initial and final stabilities (a well-known concept). Applying this idea to the 5-aGNR results in an interesting readout: According to periodic calculations (Figure 4.2), the most stable phase is the topological one. These calculations are representative for any ribbon length, with the only difference of the border effects (end state formation) keeping the short, close-shell ribbons from expressing a topological regime. Following that reasoning, the short ribbons must be less stable in thermodynamic terms than the long ribbons, as they lay in a less-stable phase. However, this is contradicted by the air-stability shown by shorter 5-aGNR (2-UC, perylene;3-UC, terrylene; and 4-UC, quaterrylene).[219] The reason for it could lie in two different reasons: First, the enthalpy of the oxidation, as a phase transition, increases by unit cell, so the net stability earned by the oxidation of both ends of a 2-to-4-UC ribbon could be not high enough to justify the oxygen splitting. Second, the hybridization of the end states could mean a higher activation energy for the oxidation of the ribbons. The ribbon may require to transition to the open-shell relaxed structure as the predominant phase before reacting. This could mean a kinetic impediment for the reaction. However, this reactivity limit disappears once the ribbons reach a specific length between 5 and 6 unit cells. For the 6-UC 5-aGNR, the shortest counted in our experiment, we observed an oxidation rate of 85%, in line with the rest of the 5-aGNR. Another factor to consider is the Au(111) catalytic surface. It's presence could have enhaced the reactivity of the shortest members of the 5-

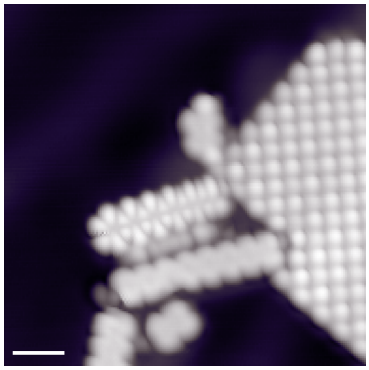

Figure 4.16: Image of the 5-aGNR sample after the O_2 exposure. It shows a NaCl island (right); a half-oxidized 6-UC 5-aGNR (center) and a fully oxidized 8-UC 5-aGNR. The abundance of oxidized ribbons is the same, regardless the phase (96% for close-shell vs 93% for open-shell 5-aGNR.) Scale bar: 1 nm. Scan conditions: 0.5 V, 100 pA.

aGNR family. In any case, further work (both experimental and theoretical) is necessary to test all these reasoning, otherwise just speculative.

What is a sure claim is that the presence of unpaired π states is related with a radical-like reactivity, and this discovery affects a huge fraction of the GNR family. Any magnetically active PAH could suffer from a likely atmospheric degradation. For the 5-aGNR, they only react in the zigzag sections of both ends, leaving the "bulk" of their chemical structure unaffected. However, the effect could be more influential for some zigzag and chiral graphene nanoribbons. Their bulk electronic structure is characterized by the tendency to host singly occupied states. For this reason, their whole integrity is threatened by their potential reactivity versus attacking agents. In the next chapter we will present some of these ribbons as a sample for zigzag edge reactivity, and explore it experimentally.

4.6 Conclusions

We have demonstrated that 5-AGNRs on Au(111) display a semiconducting gap of 0.85 eV. The anisotropic electron potential generated by the partial charges of the hydrogen atoms along the sides of the 5-aGNRs favors the opening of a gap toward the topological (not the trivial) band structure. As a result, the nanoribbonshave topological in-gap states that undergo a transition from singly occupied spin-split states to a closed-shell form at a critical GNR length of 14 unit cells and below. Although the end states are unoccupied when supported on Au(111) or on NaCl monolayers on Au(111), they become filled as the electrostatic influence of the high work function substrate fades when lifting the nanoribbons from the surface via STM tip manipulation. As the states become occupied, a Kondo resonance appears, providing direct proof of their magnetic nature. The end states are no longer observed after GNR oxidation. Lifting experiments with half-oxidized ribbons demonstrate that the source of the observed Kondo feature is the end attached to the STM tip, as it is only observed when lifting a pristine ribbon end and not an oxidized one. We hope that these findings will further advance the understanding of the nature of such narrow AGNRs as well as encourage others to consider and investigate the effects of topological states in other related systems, whereby magnetic functionalities can be integrated into the graphene nanostructures. The results presented here also indicate that such systems can be driven both toward their trivial and nontrivial phases using appropriate degrees of freedom and external parameters. In particular, our calculations point toward strain and inductive effect along the ribbon's edges as two of them.

CHAPTER 5

Reactivity of 3,1,4-chiral graphene nanoribbons

5.1 Introduction

The interaction between ambient reactive agents and hydrocarbon nanostructures is generally assumed to be weak[220, 221, 222, 223, 222, 224, 225, 226] and dominated by London dispersive forces.[220, 222] For this reason, bigger, more polarizable PAH have stronger intermolecular interactions.[220, 222, 223] The utmost example of a conjugated carbon lattice, graphene, was reported to be immune to water's chemical attack.[227] However, those studies go for the bulk of the graphene surface. Those who checked onto edge stability at ambient conditions (specifically for GNRs and mostly oxygen) employed armchair GNRs in their experiments.[171, 228, 229, 186] Their results suggest ominous implications: Whereas the armchair edges remained unaltered, the chemical stability of their zigzag termini is much more limited

Some of the most acclaimed properties of graphene nanostructures rely on the presence of zigzag edge segments.[230] Examples include zigzag (zGNRs) and chiral GNRs (chGNRs), with potential to host spin-split edge states[21, 11, 231, 232, 12] highly valuable in spintronics.[233] Other examples are periodically modulated GNRs featuring short zigzag segments that host closely related topological states and whose appropriate coupling can be used for band-structure engineering. [176, 234, 235] However, the potentially much higher reactivity of their edges could be a downside for their application.[236]

Solution synthesis of GNRs suggests the same: Successful synthesis strategies tipically display armchair-edges at the atomic level,[237, 238] even if the ribbon's net edge-

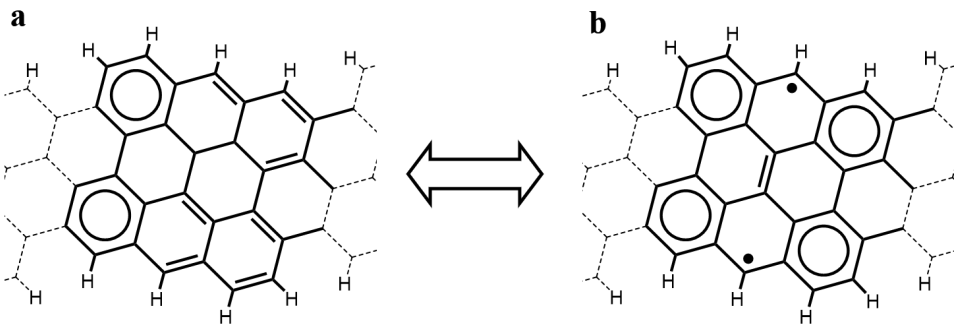

Figure 5.1: The two Clar resonators of 3,1,4-chGNR. The single UC, bisanthene is 12% a) Open-shell structure and 88% b) Close-shell. Decorating edge hydrogen atoms are drawn for clarity. They will be omitted from now on unless chemically affected.

orientation points along zigzag [239] or chiral[240] directions. However, although theoretical studies have examined the potential effects of oxidizing zigzag edges,[241, 242, 243, 6] there is a lack of experimental reports about the chemical and electronic effects of exposing GNRs richer in zigzag edges to water and/or oxygen.

We decided to take the chiral-graphene nanoribbons as a test subject, as they have a significant ratio of zigzag edges in their structure. The narrow 3,1,4-chiral graphene nanoribbons, however, are close-shell structures.[244, 69, 12] They are an exception within the 3,1-chGNR family. While, metallic bands characterize the edges of wider 3,1-chGNR family members. The 3,1,4-chGNR have a 0.65 eV bandgap. The analogy with short 5-aGNR is patent: For this chiral ribbon, its edge states (Figure 5.1 b) hibridize in the armchair direction with the opposite edge state, Figure 5.1 a. It is a unique case of a ribbon with 3-rings-long zigzag segment not hosting measurable radicals (apart from short acenes or non-periodic nanographenes).[245, 66, 62] For that reason, we consider the 3,1,4-chGNR a borderline case to test the reactivity of zigzag edges.

5.2 Ambient exposure

We use bond-resolving scanning probe microscopy (BR-SPM), in combination with theoretical calculations, to study the effects of exposing narrow chiral GNRs to ambient conditions.[244, 69, 69] The sample was prepared as described in earlier works.[244, 69, 244] The ribbons were synthesized on Au(111) and the integrity of their molecular structures was checked by means of bond-resolving scanning tunneling microscopy (BR-STM) using a CO functionalized tip (Figure 5.2 (a,b)). The pristine GNRs were then exposed to ambient conditions for 72 hours. As a result, the Au(111) was covered in a layer of contamination from the atmosphere. The sample was then brought back to ultra-high-vacuum (UHV) conditions, and annealed to 200 ºC for 15 hours in order to desorb the majority of these contaminants and allow a new STM analysis of the integrity of the GNRs. An STM image at an intermediate stage, after 2 hours of annealing is shown in Figure 5.2 c, revealing a much higher amount of coadsorbed contaminants.

Figure 5.2 d shows the sample after the full annealing process. Although the ribbons still appear to be surrounded by dendritic formations that are mostly attributed to remaining contaminants, they can already be unambiguously distinguished. In contrast to the long straight shapes characterizing pristine GNRs,[244, 69, 69] the slightly curved appearance of the ribbons after the exposure already suggests that the molecular structure has been affected (Figure 5.2 a vs d). BR-STM measurements reveal clear signals protruding from many of the C atoms at the GNR edges, as well as modification of the shapes, sizes and brightness of the hexagons that form the carbon backbone (Figure 5.2 (e)). Although

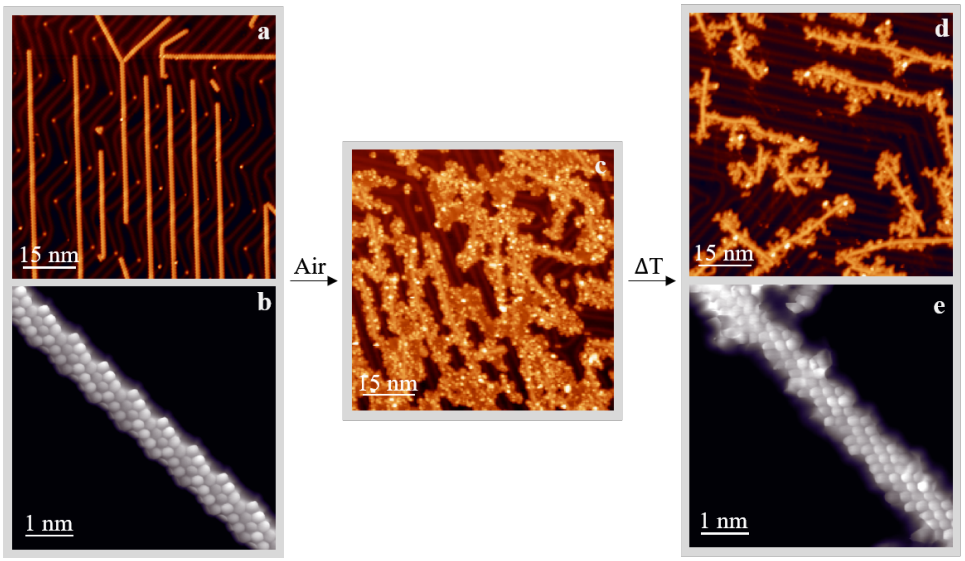

Figure 5.2: Figure 1. Large scale (a,c) and small scale bond-resolving STM images (b,d) of chiral GNRs as grown on Au(111) under UHV (a,b), and after exposure to air for 3 days and then annealed at 200 ºC for 13 hours (c,d). a) V_B = 1 V, I = 100 pA. b) CH, V_B = 8mV, I = 500 pA. c) V_B = 600 mV, I = 30 pA. d) V_B = 300 mV, I = 330 pA. e) CH, V_B = 2mV, I = 60 pA.

the former observation may relate to chemical modifications of the ribbons as well as to coadsorbed molecules, the latter confirms that the chemical structure of the GNRs is dramatically affected by a variety of defects that mostly decorate the edges of the ribbons. At this point, however, many questions remain unclear about the reactive species and the degradation products, as well as whether the oxidation may have already occurred spontaneously at RT or alternatively has been activated during the annealing process in the presence of the unknown ambient atmospheric contaminants.

Thus, we proceeded with more controlled experiments, exposing the sample to a pure gas. Doing so fixes the potentially attacking species as we did with the 5-aGNR, allows the study of edge degradation without the significant levels of contaminants that came with the air-exposed sample and at the same time avoids the need for annealing treatments.

Discarding N_2 and Ar due to their inert nature, two main reagents lie as suspects: H_2O and O_2. We decided to test them independently.

5.3 3,1,4-chGNR vs H_2O

Although the interaction between molecules and water on a metallic surface have been readily studied, [246, 247] there hasn't been a specific study about the interaction between GNRs and water. For that purpose, multiple samples of chiral GNRs were grown following the already published recipe,[244, 68, 69] the quality of which was checked by means of STM/STS/BR-STM with a CO-funcionalized tip, figure 5.3 (a-c). A variety of exposure conditions were performed: going from pressures around 2×10^{-7} mbar to 8×10^{-7} mbar and exposure times from 1 to 2.5 hours, altogether ranging from $\sim$ 540 to $\sim$ 5400 Langmuir.

In a first check it is hard to appreciate the effect of the water, as the ribbons keep their mesoscopic conformation (see Figure 5.3 (d)). A closer look at the topography image shows a series of transversal protrusions in the central part of some unit cells, circled in green in Figure 5.3 (d). Observed with a CO-functionalized tip they appear as a wider, darker central ring of the zigzag segment (marked with yellow arrows in Figure 5.3(f)).

Despite some inorganic reactions,[248, 249] this is the first report of a water-mediated organic reaction directly visualized by STM. Its attack to the central ring of the

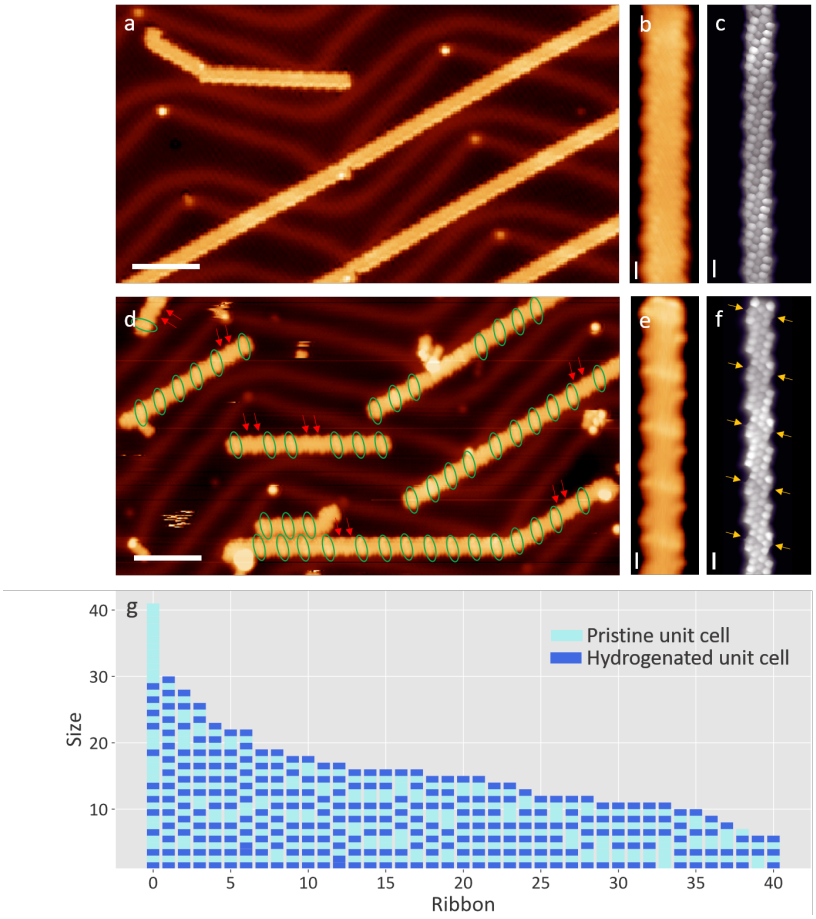

Figure 5.3: a,b,c) Pristine sample of 3,1-chGNR a) Survey at -1.5V, 100pA c) Zoom on the topography c) BR image with a CO funcionalized tip. c,d,e) After being exposed to an H source, the ribbon zigzag edges get doubly hydrogenated in alternating unit cells. d) Survey at -1.5V, 100pA. e)Zoom on the topography of a hydrogenated ribbon. f)BR-Constant height (C.H.) at 5 mV 120pA. g) This is a diagram of representative water-exposed ribbons from a sample exposed to 540 langmuir of water, ordered by size, revealing the general hydrogenation pattern (not a histogram). The hydrogenated and pristine monomers are marked with dark and light blue, respectively, exhibiting their alternating pattern, along with very uncommon exceptions of two hydrogenated neighbors and the more frequently observed exceptions made up by neighboring pristine unit cells. Scale bars: a,d 5nm. b,c,e,f 5 Å

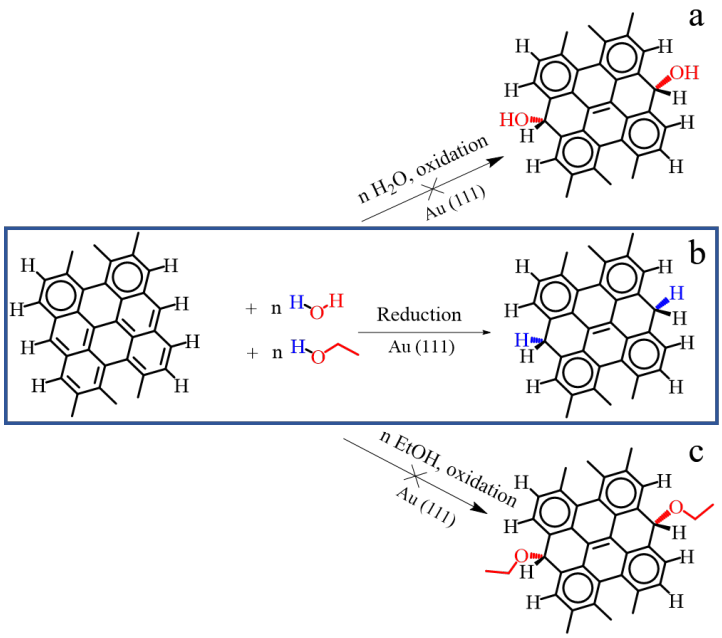

Figure 5.4: Alternative reactivity for 3,1,4-GNR with water (a,b) or ethanol (b,c). The coincident products verify the hydrogenation as the primordial reaction (b). The hypothetical alternative oxidation would have resulted in differentiable hydroxyl/ethoxy functional groups (a,c) .

chGNR goes in line with the two resonating structures idea: An addition from the water to that reactive carbon. Due to the symmetry of the defect, which affects both sides zigzag edges, we expect a double insertion. The result is the stabilization of the four Clar sextets aromatic structure, as in Figure 5.1 (b). However, in this case, the central carbons of the edges do not host radicals but have four σ bonds, in a C sp^3 configuration.

There is another incognita in this experiment: Water is an amphoteric compound. It means, it is capable of reacting both as an acid (when a single incoming hydrogen results in an electrophilic addition) and as a base (when the hydroxile performs a nucleophilic addition). Both the products and the leftovers of these reactions are complementary. The nucleophilic addition of water would result in a C $sp^3 - OH$ which could have been notice-

able to the BR-STM. However, we decided to perform a complimentary counter-experiment to confirm that we have an electrophilic attack. For that, we repeated the experiment using ethanol. Due to the alkyl chain, its nucleophilic addition would be easily identifiable by STM as ethoxy tails attached to the edges of the ribbons. A new pristine sample was exposed to 7×10^{-8} mbar of ethanol for 20 minutes (63 Langmuir). The resulting ribbons displayed defects with an identical appearance as those obtained with water, proving the $H\cdot$ as reducing agent of the ribbons to be more favourable than the $OH\cdot$ or $CH_3CH_2O\cdot$ oxidation in the water and ethanol cases, respectively. Due to the lower exposure, this sample has significantly less reacted rings, which accumulate on the terminal units of the GNRs. This was observed as well in the water-exposed samples.

Interestingly, the reduction of a unit cell prevents their immediate neighbors from hydrogenation, revealing long range effects that affect the overall kinetic or thermodynamic viability of the reaction. Upon saturation, this results in ribbons with a dominating pattern made up by hydrogenated ends and an alternation of pristine and hydrogenated unit cells towards the ribbon's interior, see Figure 5.3 (g).

Exceptions to this pattern are terminal unit cells that are not hydrogenated (accounting for about 5% of the GNR ends, see Figure 5.4), or two neighboring unit cells that are either both hydrogenated or both pristine. Whereas the former only occurs very rarely, the latter is relatively common (marked with red arrows in Figure 5.3 d.

The random distribution of the defects made up by neighboring pristine unit cells hints at the following reaction dynamics: After the terminal cell has reacted, the water

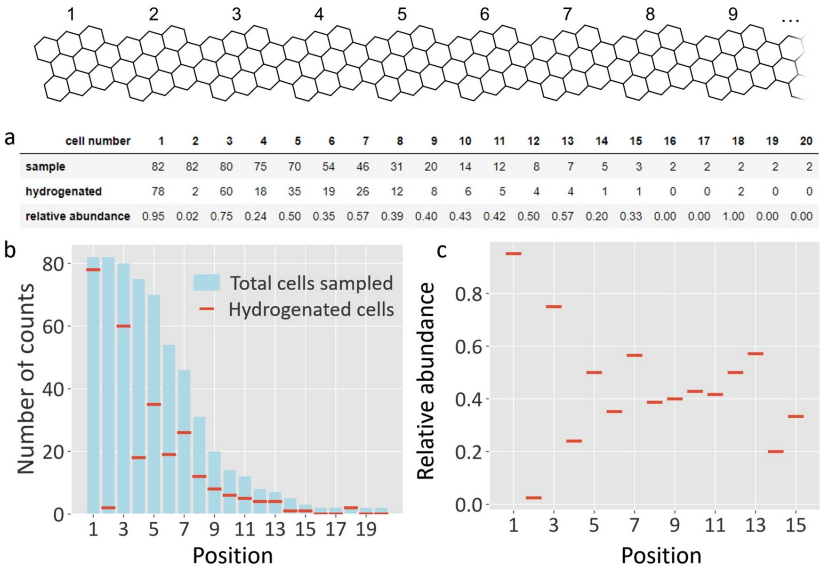

Figure 5.5: Statistics about the position of the hydrogenation relative to the closest termination of the GNR.

attacks randomly any other segment of the GNR that is not next to a hydrogenated unit cell. An exposure to 560 Langmuir of water is close to saturation already, as in figure 5.3(d-g). Once there are no more pristine segments left that include three or more unit cells, the hydrogenation stops.

5.3.1 Theoretical insights

We employed quantum mechanical calculations to probe the possible extent of the water dissociation process on gold adatom, as a way to unveil the impact of entrapped water molecules in gating hydrogenation reactions onto GNRs. This process is analyzed in terms of key thermodynamic variables, such as the relative binding energies of hydrogen and hydroxyl radicals (for computational details see Methods). The calculated bond dissociation energy (O-H bond) of water molecule adsorbed onto gold adatom account for 81 kcal·mol^{-1},

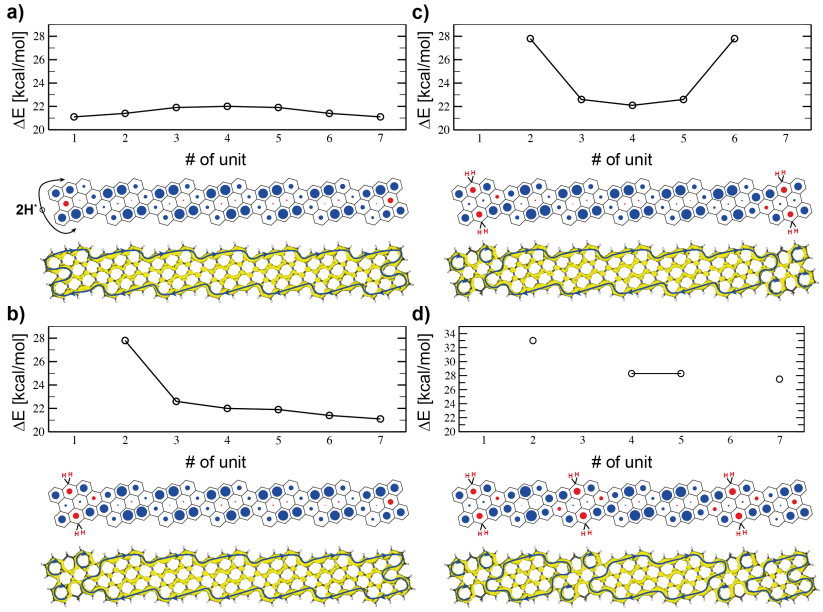

Figure 5.6: Relative energies of hydrogenations of GNRs in different positions and level of reduction. Addition of two H radicals to units in different positions for pristine GNR (a), GNR with one terminal unit reduced (b), GNR with both termini reduced (c) and a heptamer GNR with three reduced units as a possible final product (d). Positions of units correspond with structures below the graphs. NICS and ACID plots for each structure are shown below corresponding graphs. Blue and red circles display aromatic and antiaromatic rings, respectively. ACID isosurfaces are plotted at isovalue of 0.05 a.u.; for high-resolution see SI.

thus it decreases significantly compared to the value calculated for free water (121 kcal·mol^{-1}), and becomes an energetically feasible *in situ* formation of reactive hydrogen radicals. Moreover, theoretical calculations show that both hydrogen and hydroxyl radicals interact with gold adatoms with comparable binding energy (ΔE of 0.5 kcal·mol^{-1}). Nonetheless, the hydrogen radical binds to the zig-zag edge of GNR by 7 kcal·mol^{-1} stronger compared to hydroxyl radical.

The validity of such theoretical description clearly depends on the level of com-

putation and methods used in the study. The ribbons are prone to exhibit a multireference character[12, 65], factor that introduces errors in the DFT calculated energies. Multireference methods, while limited to small size systems, can be used to obtain more accurate results. For this reason, we performed MR-AQCC calculations on dimers and trimer to corroborate the less computationally demanding DFT analysis. The calculated energy trends for both methods are found to correlate well to each other, as shown in the Appendix B. Therefore, we carried out extensive DFT calculations for the relative energies and aromaticity of longer chains, from the dimer to the heptamer. The energetic trends associated to the hydrogenation reaction steps are found similar, irrespective of different chain lengths; the computational results for heptamers are presented herein as the system capable to describe better the variety of possibilities in hydrogenation. Since the hydrogenation process requires two radicals attaching to opposite edges of the carbon framework, this process can be divided into half-steps, leading first to a radical intermediate that becomes later on passivated by interaction with the second hydrogen radical. The results obtained from the computed relative energies of these radicallary intermediates are shown in Figure 5.6. The most stable structure calculated in the first reaction step contains the terminal unit in reduced form; here, H radicals interact with the zig-zag edge, and such process is highlighted in Figure 5.6 a by a black arrow. The relative energies of the products calculated after completion of the first and second step underline the proclivity towards reduction of terminal units versus the inner carbon domains of GNR, Figure 5.6 (a,b). These findings agree well with the experimentally observed products, where the ending portion of the GNRs are found reduced in most cases. Further hydrogenation exhibits a clear opposition to attack subsequent units as seen in Figure 5.6 (b-d). We calculated the diradical character of GNR with increasing length as

a possible mechanism for hydrogenation protection. The calculated values are summarised in Appendix B and show a saturation of diradical character y0 around 18 %, making the studied GNR a relatively weak diradicaloid. It can be seen that diradical character of GNR can be connected to measured bandgap of GNR (see Figure 5.7), i.e., longer GNRs have small bandgap and higher y0 while pristine monomer shows the largest bandgap and almost negligible y0. Although the diradical character on its own its not sufficient to explain the observed protection of consecutive units against hydrogenation, it offers an explanation of the stability of the final quasi-perfect alternation pattern. The diradical character drops for pristine monomer within GNR to value around 4 %, which appears to be below the threshold for successful hydrogenation in presence of water. A deeper study of the reaction mechanism and kinetics is beyond the scope of this work as the number of possible mechanisms renders such study highly convoluted. However, the results from relative total energies of hydrogenated products correlate well with experimentally observed products and thus suggest that the hydrogenation caused by water exposure is thermodynamically driven.

To further investigate the driving force of the observed stability trends, we carried out nucleus-independent chemical shift[250, 251] (NICS) and anisotropy of induced-current density[252] (ACID) calculations in order to analyze the electronic differences between various hydrogenated products. While NICS values characterize each ring by the amount of magnetic shielding (deshielding) due to aromaticity (antiaromaticity) of that ring, another method should always be included in order to characterize the global properties of the system. The π-ACID method offers visualization of conjugation in molecules allowing for global aromaticity description. Plots in Figure 5.6 show ACID and NICS results on

heptamer GNRs in various stages of hydrogenation (for high resolution ACID plots see Appendix B). The results show a globally conjugated circuit along the periphery of the ribbon exhibiting diatropic current, proving global aromatic character of the pristine GNR together with Hückel's 4n+2 rule along the circuit. At the terminal units, the conjugation forms antiaromatic bays, which effectively prolong the conjugated circuit by four more atomic sites. Although this increased conjugation path does not affect Hückel's rule, the presence of this antiaromatic bay may be responsible for the higher local reactivity of the terminal units and must thus be compensated by an otherwise more stable global structure, hinting at an energetic preference for longer conjugation paths. It can be seen that the pristine units extend their conjugation path towards the reduced unit by including one of its formed Clar's sextets (see Figure 5.6 b-d). When the terminus is reduced, there is a globally conjugated periphery of pristine units and three isolated benzene rings in the reduced unit cell. By reducing an internal unit cell, two conjugated paths are formed and only two isolated benzene rings form. By considering reduction of two consecutive unit cells, four extra isolated benzene rings are formed . Both calculations and experiment agree that this scenario, forming less conjugated parts (localized Clar sextets) between two consecutive hydrogenated unit cells, is energetically unfavorable. We thus infer that longer and less fragmented conjugation paths are favored.

5.3.2 Electronic characterization

Hydrogenation of the two edges of a unit cell localizes the aromaticity in the contiguous aromatic rings. The resulting structure has thus a lower conjugation and hence a

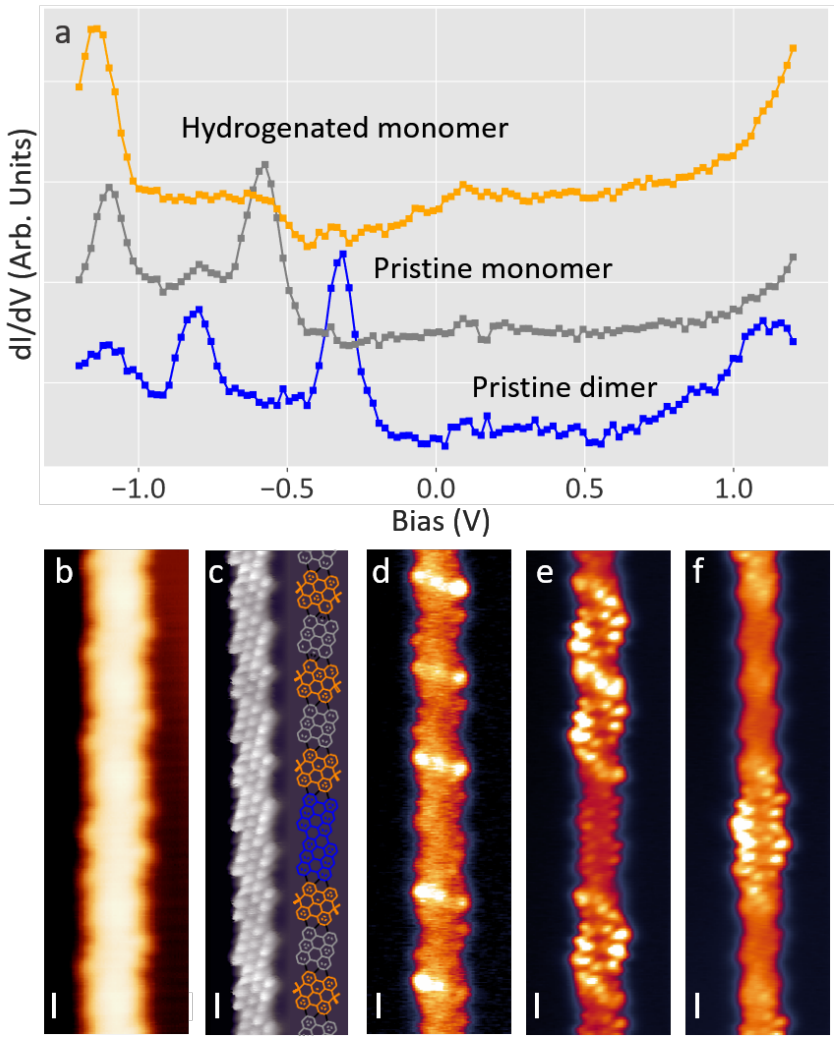

Figure 5.7: Analogous images of a ribbon with alternating hydrogenated cells and a pristine dimer with a CO tip. A) Topography. C.C. -800mV, @50pA. B) BR C.H. 10mV at 260pA. Hydrogenated carbons are visible in the left edge of this backwards scan. C) dI/dV at the HOMO of the hydrogenated segments. -1 V, C.H. D) dI/dV at the HOMO of the pristine monomers. -600 mV, C.H. E)dI/dV at the homo of the pristine dimer. -350mV, C.H. Scale bars 5 Å

wider bandgap. We performed a series of STS measurements to characterize the electronic structure of the hydrogenated graphene nanoribbons shown in figure 5.8 a. From the spectroscopy we can observe how the HOMO of the alternating structure appears at an energy around -0.6 eV, figure 5.7 (d). Compared to the -0.25 eV of the pristine ribbons, this means a large increase of the ribbon's bandgap, specially considering that the LUMO shifted from around 0.5 eV beyond 1.1 eV, the stability threshold of the hydrogenated ribbons (as will be shown below, higher bias dehydrogenates the ribbons back to their pristine form). The bandgap rapidly decreases if larger pristine segments are present. In the case of pristine dimers, we can observe both in the spectroscopy and in the differential conductance images how the HOMO is observed at -0.3 eV in figure 5.7 f, and the LUMO around 0.7 eV, implying a bandgap of around 1 eV.

5.3.3 Radical activation

Further efforts of measuring the LUMO of the hydrogenated ribbons resulted in the tip-induced dehydrogenation of the ribbons. Figure 5.8 (a,b) shows an example of how acquiring a spectrum from 0 to +1.5 eV at the position of the lightning icon causes the dehydrogenation of the C sp^3 under the tip and its associated sp^2 rehybridization. Subsequent bond resolving STM images at low bias display greatly enhanced signal at those positions, Figure 5.8 (b). Conductance spectra show the appearance of a state around the fermi level, Figure 5.8 (e) at this position that was previously absent. This new state is univocally identified as an unpaired electronic state, or in other terms, a radical. The remaining C sp^3 carbon on the opposite side of the unit cell causes an imbalance of p_z electrons between the two

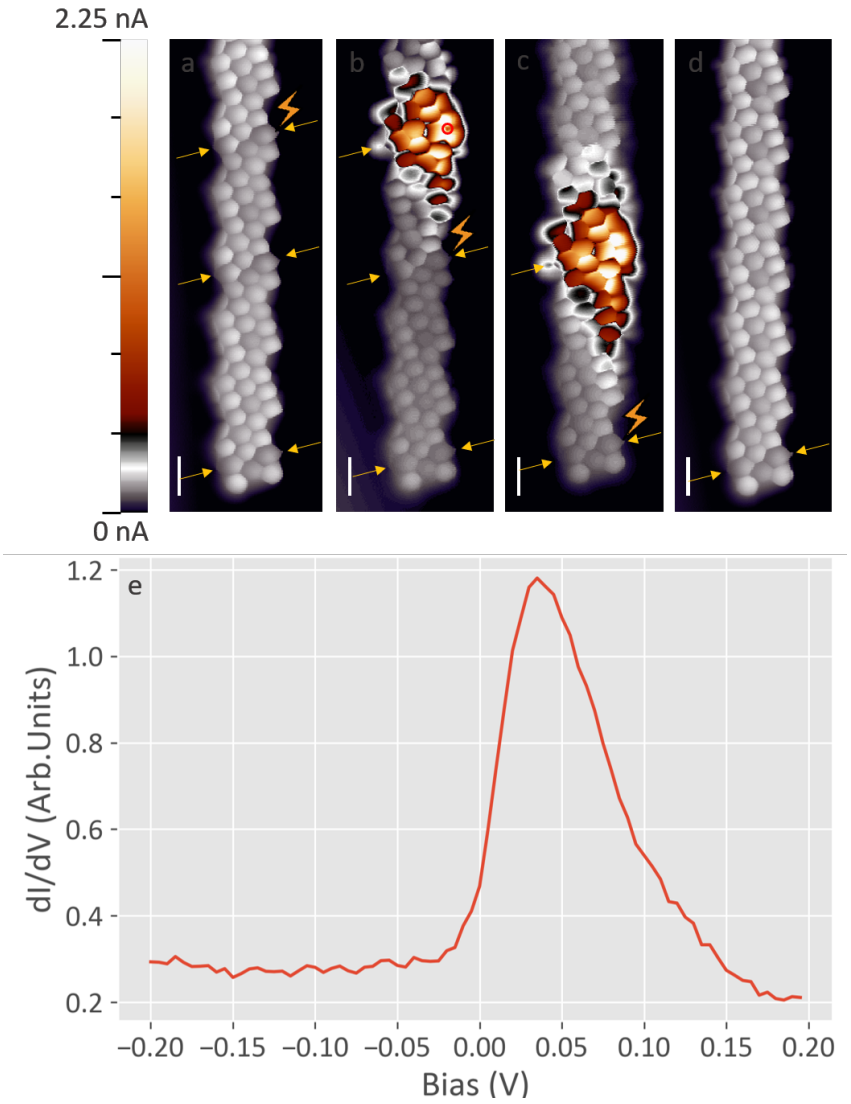

Figure 5.8: Summary of the statistics obtained from the sample, regarding the hydrogenation of ribbons by distance from the edges. Every unit cell has been counter from the closest end. a) Table with the data of the total sample vs ribbon position, being 1 the first unit cell from the end. b) Scheme of the ribbons sampled for this study, ordered by length. Only non-defective ribbons were used for it. d) Relative abundance of hydrogenated unit cells by position, with a clear tendency for end hydrogenation. Scale bars 5 Å

carbon sublattices, as has been reported previously by our group with oxygen funcionalized ribbons.[253, 254] However, whereas with oxygen-functionalized ribbons the radical state remained occupied and resulted in a net spin-moment, in theses pure hydrocarbon ribbons the orbitals lie at higher energies, which causes electron transfer from the ribbon to the underlying Au and thereby depopulates the radical state. Nevertheless, these radical structures reveal a limited stability, and numerous attempts of getting close-by radicals on these ribbons result in the successive full dehydrogenation that regenerate the pristine ribbon, check Figure 5.8 (a-e).

The hydrogenation caused by water is thus a mild modification process of the graphene nanoribbons. Annealing the sample to 150°C results in their complete dehydrogenation, recovering the initial sample. The electronic and molecular integrity of the recovered ribbons was confirmed. The recovery is an analogous process of the original planarization of the GNR, but for two extra factors that help to the recovery: first, the ribbons are now fully planar but for this edge carbons, so the steric hindrance favours the dehydrogenation. Second, the π network environment of this carbon energetically stabilizes the C sp^2 of the product. [255]

We consider that both for the hydrogenation and the regeneration, the presence of the gold surface was influential in the process, as the hydrogenation was favourable thanks to the gold catalyzed water splitting. However, most of the device preparation processes comprehend exposing the metal-supported ribbons to solvents for the transfer process. Not to forget either that these PAH have an almost negligible open shell character (12% for the monomer).[65]

5.4 3,1,4-chGNR vs O_2

For testing the reactivity against oxygen, we employed samples prepared from scratch. The amount of oxygen at the atmosphere is multiple orders of magnitude higher than water's. For that reason, we exposed the pristine chGNRs on Au(111) to 3×10^{-5} mbar of pure O_2 gas, for 2 hours. The exposure was done at room temperature and subsequently cooled back down to 4.3 K for characterization.

Before the oxygen exposure, the STM images reveal the usual CV and VB for a (3,1,4)-chGNRs onsets (-220 mV and 450 mV, respectively) show their characteristic density of states (DOS) modulation along the entirety of the ribbon, Figure 5.9 (a-c).[69] After oxygen exposure, a variety of defects is clearly observed, with a higher concentration found at the position of the central carbon of the zigzag edge segments (Figure 5.10 d). Interestingly, this confirms the high reactivity of such zigzag-oriented edge segments even when they are not the hosts of radicals that are observable by STM, as it was the case with the water.[232, 69]

There is a clear correlation between the presence of defects and the alteration of the electronic structure. Their presence automatically causes the disappearance of the characteristic DOS associated with the pristine GNR bands (Figure 5.9 e,f) and remnants of the VB and CB are only found in defect-free pristine segments like that which is marked by the yellow square in Figure 5.9 d-f (note that the DOS reminiscent of VB and CB is found at energies farther from the Fermi level due to the finite size of these defect-free segments and the associated confinement effect). That is, GNR oxidation severely affects their electronic

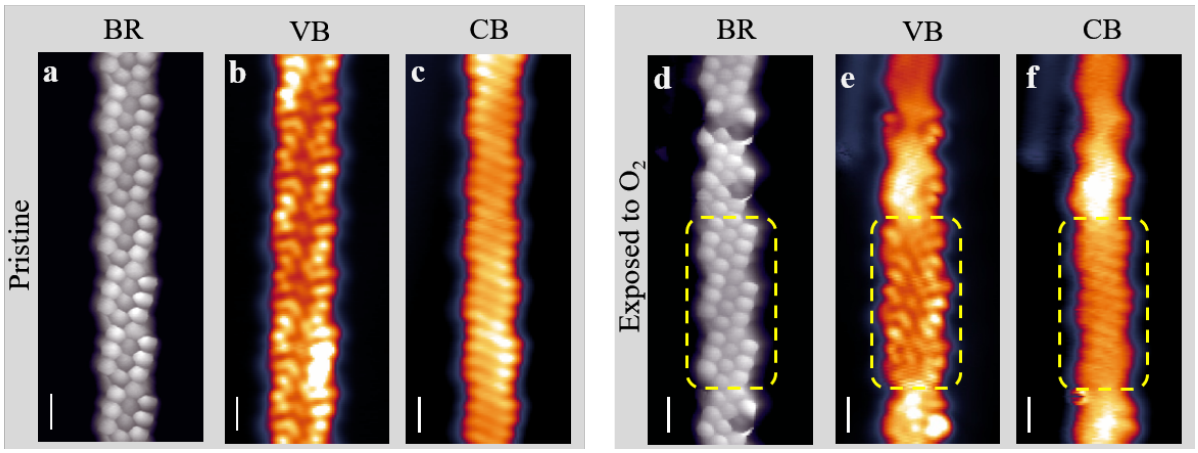

Figure 5.9: Bond resolving images (BR, a ,d) and conductance maps of the valence band (VB, b, e) and conduction band (CB, c, f) of pristine ribbons (a, b, c) and ribbons exposed to 3·10-5 mBar of O2 for two hours (d, e, f). Whereas the valence and conduction band extend over the whole pristine ribbon, it can be seen how the defects of the O2-exposed ribbon severely affect the electronic properties of the ribbon. Remnants of the VB and CB can still be recognized, however, in non-defective segments like that marked by the yellow square. All images have been taken at constant height. Top: BR: 2 mV; VB: -220 mV; CB: 450 mV. Bottom: BR: -2mV; VB: dI/dV -350mV; CB: dI/dV 650 mV. Scalebar 5 Å.

properties, which consequently limits their applicability in optoelectronic devices.

5.4.1 Identification of defects

While there is a strong regioselectivity, with a marked preference for attack on the central ring of the zigzag segment, the oxidation of the (3,1)-chGNRs with molecular oxygen is not chemoselective and results in a variety of products. BR-SPM and NC-AFM images of some of the common oxidation products are collected in figure 5.10, along with images of the pristine ribbons for comparison in Figure 5.10 (a,b). In order to acquire more information about the oxidation defects and facilitate their assignment, the BR-SPM images were acquired both in STM and nc-AFM mode.

The most common defect appears in the BR-STM as a larger ring, (consequently reducing the size of the neighboring rings) terminated in a sharp point and with a fading contrast towards the outer atom (type II). Defects with this contrast are found with (type IIB in figure 5.10 e) or without (type IA in figure 5.10 c) an accompanying metal adatom next to them. Interestingly, the nc-AFM signal differs notably between the two cases. The latter shows a reduced contrast along the outer bonds (figure 5.10 d), whereas for the former a slightly reduced contrast along the outer bonds ends with a very local enhancement at the vertex (figure5.11 f). Type III defects appear in STM as a larger ring with a pointy end (Figure 5.10 e) and in nc-AFM with a substantially enhanced contrast along the outer bonds (Figure 5.10 f). The STM images of type IV defects show a weak signal next to an otherwise unaffected ring in terms of size and brightness (Figure 5.10 g), whereas the nc-AFM images

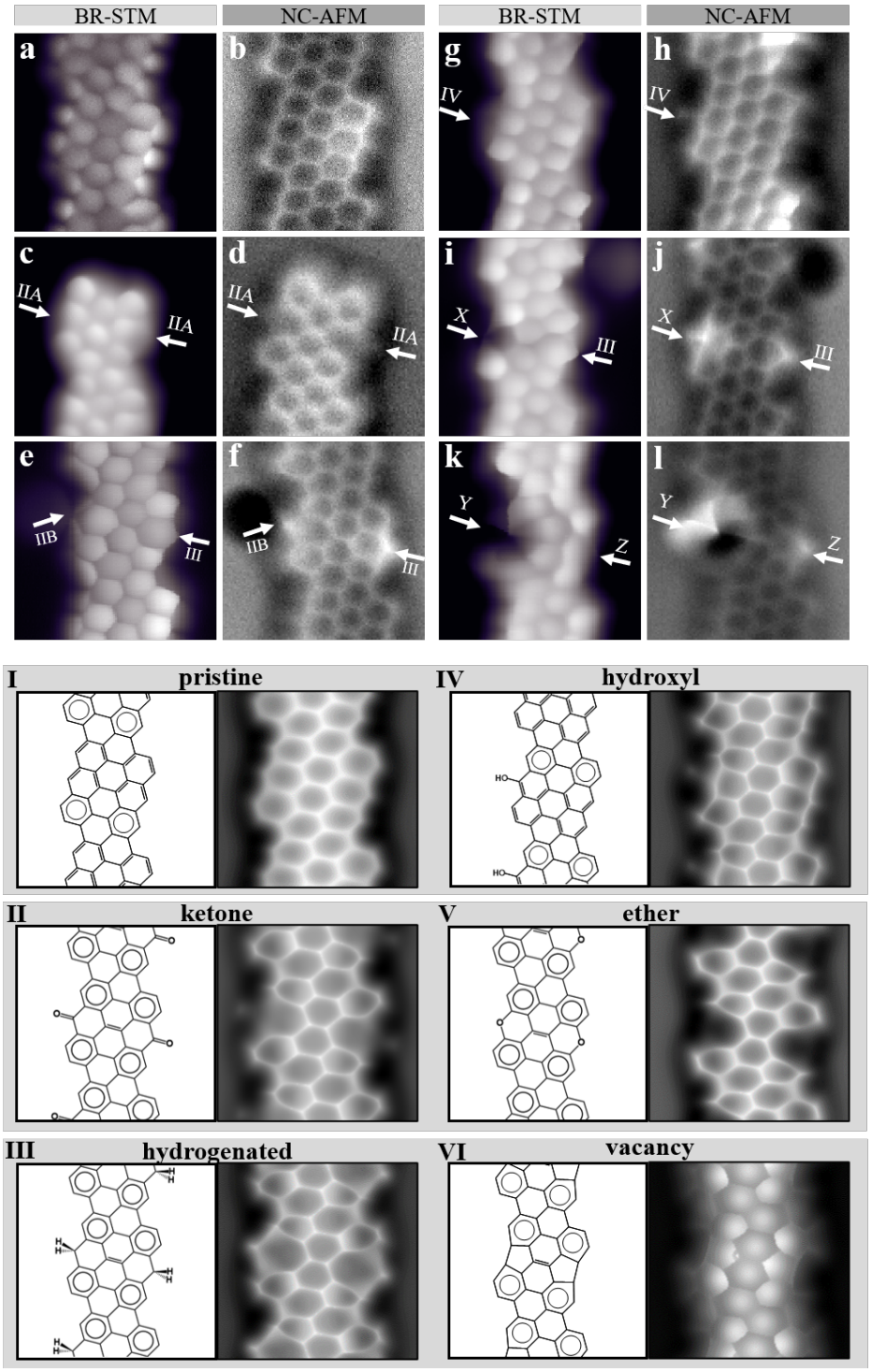

Figure 5.10: Upper part. Large scale (a,c) and small scale bond-resolving STM images (b,d) of chiral GNRs as grown on Au(111) under UHV (a,b), and after exposure to air for 3 days and then annealed at 200 ºC for 13 hours (c,d). a) V_B = 1 V, I = 100 pA. b) CH, V_B = 8mV, I = 500 pA. c) V_B = 600 mV, I = 30 pA. d) V_B = 300 mV, I = 330 pA. e) CH, V_B = 2mV, I = 60 pA. Lower part: BR-STM simulation of different proposed structures with the defects.

display an outgoing long apparent bond with an enhanced contrast at its end (Figure 5.10 h). Type X defects shows up in the STM image as a smaller and darker ring whose neighboring rings consequently deform and "extend" into the defective region (Figure 5.10 i). In contrast to the dark STM signal, the nc-AFM image reveals a greatly enhanced signal alongside extra "apparent bond" lines (Figure 5.10 j), hinting at a pronounced non-planar structure.[184, 256] There are even more disruptive defects (e.g. Figure 5.11) whose STM and nc-AFM contrast increasingly departs from that of the pristine starting product, and suggest a modified carbon backbone topology.

If a unit cell has been affected, it normally displays defects at both of its zigzag sides. The products on either side are often different, in which case one is frequently of type III. In this respect, type IV defects are an exception that are normally not found in pairs but on their own, affecting only one side of a (3,1)-chGNR unit cell as shown in Figure 5.10(g,h).

Particle probe model (PPM) simulations were performed for pristine ribbons as a reference for comparison with our experimental BR-SPM measurements (figure 5.11, I) and for the most plausible defect structures (as relaxed by DFT) that may be generated upon exposure to pure oxygen and could correspond to some of our experimentally observed oxidation products. We considered the following possibilities that could be affecting the central ring of the zigzag segments: a ketone, which matched defect I, a hydroxyl group matching defect IV, the substitution of C by an oxygen heteroatom forming an ether (Figure 5.11 V), or its removal to create a C vacancy (Figure 5.11 VI) that automatically relaxes forming a new 5-membered ring (the passivation of the vacancy by H atoms seems unlikely to occur during the oxidation process and is notably non-planar according to calculations).

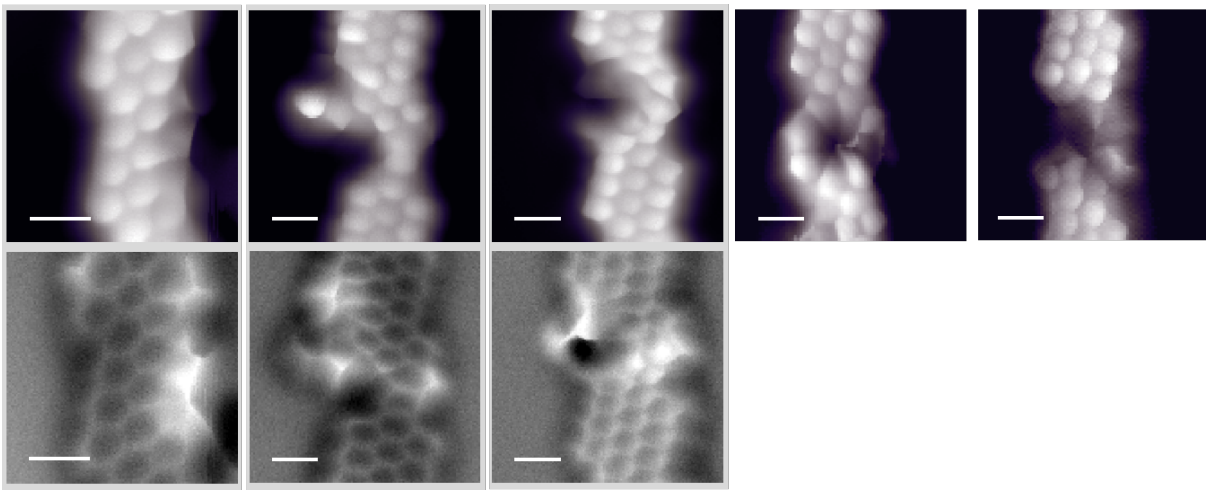

Figure 5.11: Different types of deffects affecting the carbon backbone of the GNR. Top: STM. Bottom: NC-AFM

In addition to all these oxidation products, we also simulated GNRs that are hydrogenated at the central ring (Figure 5.4 III), since some of the defects observed share their appearance with the ones generated by the water exposure. Several of the oxidation products may release their attached H atom, resulting in its displacement that could easily end up bonded to the most reactive C atoms of other zigzag segments.

Beyond the good agreement, a ketone was readily anticipated to be the most common defect for the following reasons: i) it corresponds to a strongly oxidized product; ii) it is expected to be a very stable structure, energetically favored by the creation of new Clar sextets; and iii) it has been demonstrated to be the product structure formed from bisanthene (i.e., the ribbon's unit cell) in oxygen-containing solutions,[257] and notice the similarity with 5-aGNR oxidation defects (Figure 4.12 b).[186] In turn, we assign type-III defects to doubly hydrogenated sp^3 carbon atoms and type-IV defects to hydroxyl groups. Although representing only a minor fraction of the total oxidation products, Y, Z and the

more disruptive defects shown in figure 5.11 remain undetermined (although Z could possibly be another C sp^3-H edge.

5.5 Discussion

We already rationalized why the most affected positions are the central carbon rings of the zigzag edge segments. It is known that an increase in the number of Clar sextets is associated with an energetic stabilization, which depending on the ratio may even be sufficient to compensate for the energetic cost of creating radicals.[258, 62, 259] Figure 5.1 (a) shows the Kekulé structure of a closed-shell (3,1)-chGNR, displaying two Clar sextets per unit cell. A resonant open-shell structure can be drawn as shown in Figure 5.1 (b), with two additional Clar sextets per unit cell at the expense of creating two new radicals at the central C atoms of the zigzag segments. Although both the experiments and theoretical calculations agree on a dominantly closed-shell character for these narrow ribbons,[232, 69] quantum-chemistry calculations of the bisanthene unit cell reveal a 12% contribution of the open-shell structure.[65] This may be sufficient to make the ribbons reactive in spite of their prevailing closed-shell character, as is reported to occur also with bisanthene itself in the presence of oxygen.[257] Importantly, this explains the regioselectivity at the central C atom of the zigzag segment of (3,1)-chGNRs, since it is the atom that dominantly hosts the radical of the open-shell structure (Figure 5.1 b).

In addition, it also explains why the defects preferentially appear in pairs at each

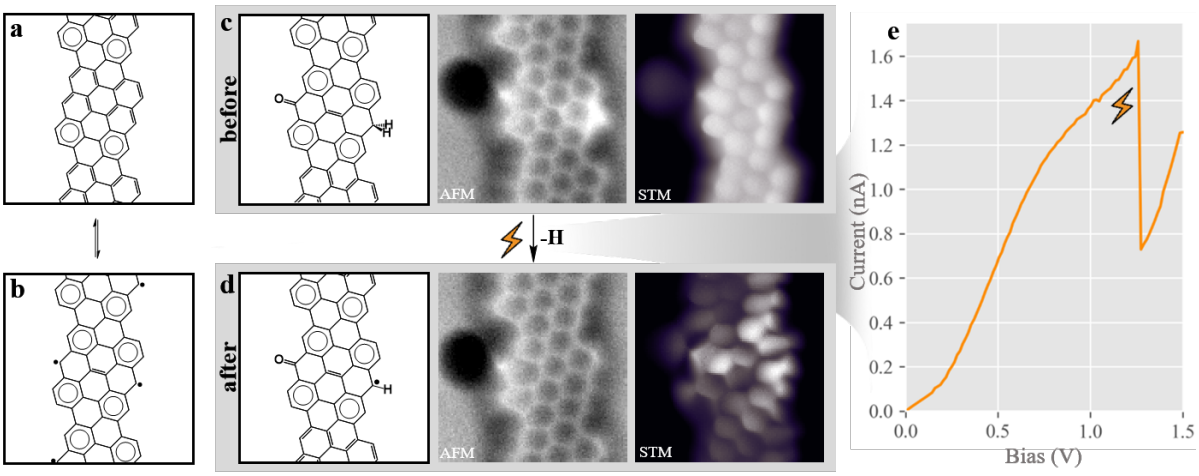

Figure 5.12: (a) BR STM of an oxidized GNR with ketone (left) and hydrogen (right) as scheme (f). BR AFM image of the same area. (e) One of the resonant structures of closed shell GNRs and (f) its associated open-shell analog displaying a larger number of Clar sextets. (g) For some of the defect structures like ketones, its presence on one side only brings along the creation of a radical on the opposite side, which can be quenched as in (h) by a similar or different defect on the opposite side. For the same reason, tip induced dehydrogenation of a defect like that in (f) will cause a radical and the associated zero energy states as in (g).

side of the unit cell. When a first oxygen attacks one side and forms e.g. a ketone, along with the new Clar sextets, it automatically increases the radical character on the opposite side (Figure 5.9). This enhances its reactivity and promotes its reaction with another external agent. In fact, although initially counter intuitive after an O_2 exposure, we find that a notable number of the defects are doubly hydrogenated Csp^3 atoms (type III). Their contrast in BR-STM images happens to be relatively similar to that of the ketones and can be easily mistaken for one another (see e.g. different type III and type II defects in Figure 5.9 (e)). However, the two defects can be clearly discerned from the nc-AFM images, in which they show a more distinct signal, as well as from their response to tip-induced manipulation attempts, in which hydrogenated C sp^3 atoms can be easily dehydrogenated,[218] whereas ketone-linked C cannot be controllably modified. The rationalization for the presence of these doubly hydrogenated C atoms is that oxidation processes can be a close source of hydrogen that migrates after the oxidation on one side of the ribbon to stabilize the facing radical that was just generated, or radicals previously generated on neighbouring ribbons. Although this is argued above with a ketone, it is similarly applicable to other defects, as is indeed found experimentally (Figure 5.11 i). An exception in this respect is the hydroxyl group (type IV defect). If it substitutes the H resulting in a C sp^2-OH, it does not stabilize the opposite side radical on the opposite side, thus it is not observed paired up with other defects (Figure 5.11 g,h).

As mentioned above, doubly hydrogenated C sp^3 atoms (type III defects) can be easily dehydrogenated by means of a scanning probe even under relatively mild tunnelling conditions,[218] bringing about an sp^2 re-hybridization along with the appearance of a low-

energy radical state. An example thereof is shown in Figure 5.13 with a pair of defects consisting of a ketone and a doubly hydrogenated C atom. A bias ramp represented in Figure 5.13 e triggers the dehydrogenation (as proved with subsequent BR-SPM imaging, Figure 5.6 d and causes the appearance of a previously absent low energy density of states. The latter is associated with the Kondo resonance of the newly created radical and shows up in the low-bias BR-STM images, Figure 5.13 d.[176, 218, 260]

At this point it is important to underline that the O_2 exposure experiment may bear little resemblance with an actual air exposure. For the latter, oxygen is present in higher partial pressures, in addition to other potentially reactive materials like water vapour, organic compounds or low amounts of ozone. The controlled low oxygen pressures can thus be considered as a lower limit regarding the harshness of the treatment that the ribbons may be exposed to, if compared to a conventional processing and transfer process during the fabrication of a GNR-based device. We want to remain as well that the studied zigzag edge segments display a limited stability in spite of the closed-shell character of the ribbons. Indeed, the same occurs also with 5-aGNRs, whose zigzag ends become oxidized independently of the ribbon length that determines its varying open- to closed-shell character (Figure 4.last).[261, 65, 186] However, in this case, the defects seem to appear by pairs. This suggests some correlation between the first oxidation and the consecutive neutralization. Another factor as it is the presence of the gold surface has not been considered as a catalyzer of the oxidation. However, the richness of different products generated suggests that there are many routes the ribbon can get oxidized, hence an important tendency towards the oxidation.

5.6 Conclusion.

In conclusion, we have shown that (3,1)-chGNRs are very sensitive to oxygen exposure, and their interesting electronic properties do not survive in oxidizing atmospheres. We have clearly demonstrated that the oxidation is regioselective, with their most vulnerable spots at the central rings of the zigzag segments due to the higher radical character that is expected there when applying the Clar sextet rule. Chiral GNR are an amphoteric structures, with both reducing (vs H_2O/ethanol) and oxidizing (vs O_2) properties. Importantly, the lack of stability is observed in spite of the predominantly closed-shell character of the narrow (3,1)-chGNRs. The same was found for the zigzag ends of short (closed-shell) 5-aGNRs and may thus be applicable to many other graphene nanostructures with zigzag edge segments. The reactivity can be considered to depend on the number of Clar sextets of the product minus the reactive. The open-shell character (or the presence of radicals) may be influential for the reactivity in terms of kinetics, as most of the 3,1,4-chGNR defects were associated in pairs. Our identification of the oxidation and hydrogenation products via BR-STM and nc-AFM and their proposed assignments may be useful to other studies that involve the investigation of similar phenomena at surfaces. These findings point at the urgent need for protection strategies to integrate carbon-based structures in actual devices.

CHAPTER 6

Protection of 3,1,4-chGNR

Edge groups have been often utilized with GNRs to make them soluble[238, 237] or to tune the ribbon's electronic properties.[262, 263, 264] However, although frequently used in solution chemistry with smaller molecules,[95, 265] to date their use for protection purposes on GNRs has remained at a theoretical level.[266, 267, 268] Besides, it remains to be tested whether such chemical protection strategies can also be applied to on-surface synthesis,[269, 270] which is the approach whereby most of the carbon-based nanostructures with peripheral zigzag edges have been synthesized to date.[271, 272] As we have already detailed, such zigzag edges often appear passivated by extra hydrogen atoms, causing a rehybridization of the associated carbon atoms into an sp^3 configuration and increasing the structure's stability. On the other hand, it has been shown that hydrogenation can also be used for edge modification of nanoribbons; in particular, it has been used to remove peripheral chlorine[273] as well as sulfur atoms,[273] with tweaks to the temperature and hydrogen exposure during different stages of the GNR growth also altering their length and termination.[274] This raises the question of whether an intentional hydrogenation of otherwise air-sensitive GNRs, like chiral nanoribbons displaying a regular alternation of three zigzag and one armchair unit along their edges ((3,1)-chGNRs),[254] may act as a protective functionalization that could eventually be controllably removed e.g. by annealing treatments (Figure 6.1). That way, the sp_2 lattice would be reduced, protected from the atmospheric attack. However, a more reducing agent is necessary to assure the protection of every zigzag edge (as water just protected half of them). We chose to employ atomic hydrogen due to its high reactivity and the cleanliness of the reaction.

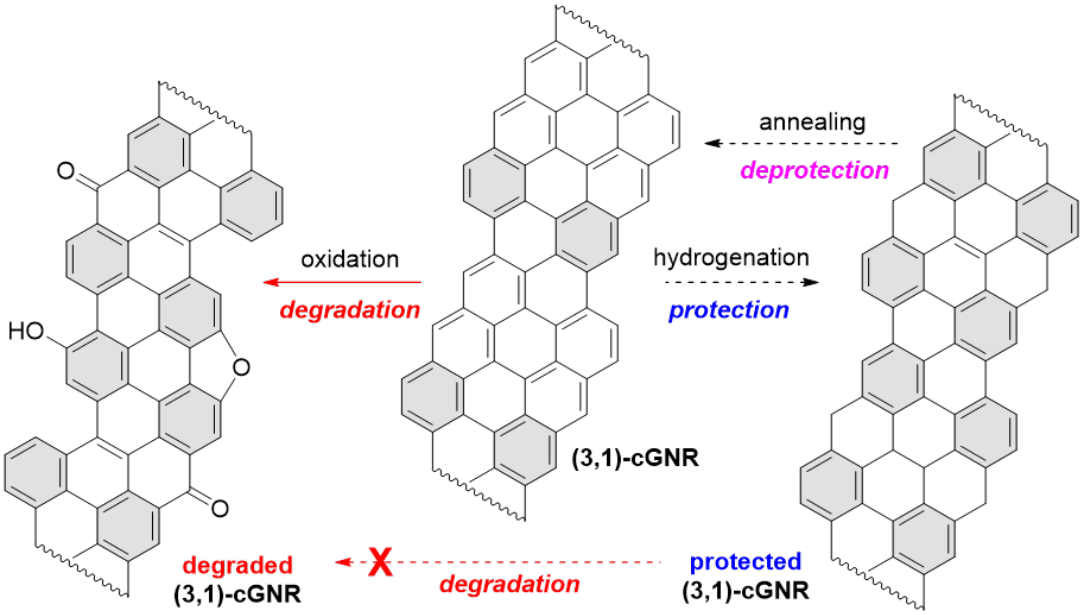

Figure 6.1: Schematic representation of the degradation of (3,1)-chGNRs exposed to air and the prospective protection strategy by controlled hydrogenation. Hydrogenation of the most reactive carbon atoms at the centre of each zigzag segment14 would confer the ribbons two extra Clar sextets (marked in grey) per unit cell, that are normally associated with larger band gaps and increased stabilities.

6.1 Hydrogen protection

We prepared the 3,1,4-chGNR following the same recipe and checked them by means of BR-STM to ensure that they were pristine (denoted henceforth as p-chGNRs). Representative images of the pristine ribbons are shown in figure 6.2(a) and (b). In order to protect the edges, the GNRs were exposed, with the sample held at room temperature, to a flux of atomic hydrogen originated from a molecular H_2 flow through a heated tungsten tube. The H_2 flow is such that the pressure in the preparation chamber increases to 1×10−7mbar, after which the tungsten tube was heated (via electron-beam heating) to around 2,800K with a heating power of 80W (corresponding to an acceleration voltage of 1,000V and 80mA emission current)—this temperature is high enough to split substantial amounts of the molecular hydrogen into atomic hydrogen, but there is no way of measuring the flux of atomic H on the simple hydrogen source used for these experiments. The sample was then placed in front of the source for 2 minutes. Following this treatment, the GNRs were examined again by STM. A representative STM image of the sample after this GNR protection is shown in figure 6.2(c). Notably, substantial changes in the apparent height contrast within the ribbons are observed, as can be seen best in the profiles of figure 6.2(g). The graph shows a comparison between the apparent height profile of pristine and hydrogenated ribbons, with the ribbons approximately doubling their apparent height after hydrogenation. This implies that a significant number of the carbons are converted from sp^2 to sp^3 upon hydrogen exposure, adopting a non-planar conformation to accommodate the change in favoured bond angles. A comparison to previous reports in the literature, in which some of the edge

carbons of chGNRs were shown to be hydrogenated but did not show significant increases in their height profile,[254, 218] leads to the conclusion that several internal double bonds of the GNR backbone have also been hydrogenated, leading to sections of 'graphane' nanoribbon that display extra hydrogen atoms pointing out of the plane of the molecular backbone. Furthermore, this conversion is not uniform, as can be seen from the topographic images in figure 6.2(c) and the aforementioned height profiles.

Whereas such strongly hydrogenated GNRs as those shown in figure 6.2(c) cannot be adequately imaged with bond-resolving power, in order to get an atomistic picture of the hydrogenation we have also characterized ribbons that are only lightly hydrogenated. For that, we backfilled the preparation chamber at a pressure of 1×10^{-6} mbar of H_2, maintaining the sample in proximity to (15cm) and facing the ion gauge for 1 hour. The hot filament splitted the hydrogen into reactive radicals, as control experiments with the ion gauge turned off showed no hydrogenation. A representative nc-AFM image is shown in figure 6.2(d), which reveals the presence of unit cells that remain unaffected, along with others that are subject to different degrees of hydrogenation. It is intuitive to expect the radical positions in the zigzag edges (labelled as "I") to be most reactive spots. DFT calculations indeed confirm that those are the energetically most favourable sites for initial hydrogenation.[179] Thereafter, the inner unit cell atoms (labelled as "II") are the only other carbon atoms whose sp^3 rehybridization does not destroy any of the stabilizing Clar sextets that are marked in grey in Figure 6.2(h).[57] In line with this reasoning, lightly affected unit cells display a clear prevalence for initial hydrogenation at the "radical sites", subsequently at positions II, and only at higher hydrogenation levels at the remaining C atoms (labelled as "I", "I,II", in Figure

6.2 (f), respectively).

It is noteworthy that the pristine chGNRs, which typically appear regularly dispersed over the surface,[68] exhibit a pronounced tendency to aggregate together after the hydrogen exposure. The acquired non-planarity lowers their interaction with the underlying surface[275] and at the same time promotes stacking, increasing the van der Waals interactions between the GNRs, altogether leading to a favoured island formation. Also the interface dipole between the GNRs and the surface may be affected. For low bandgap GNRs like the pristine ones shown here, Fermi level pinning has set in.[70] This is associated to partial charge transfer from ribbon to the Au, which sets up a notable interface dipole and may cause repulsion between adjacent GNRs. As the ribbons hydrogenate, their band gap widens, the charge transfer vanishes and thereby also the repulsive dipole-dipole interactions.

In order to test the air stability of the hydrogenated nanoribbons, the sample was transferred to the fast entry load-lock chamber. Next, that chamber was vented by air at ambient conditions (21 °C, 75% relative humidity). After a 24 minute exposure period, the chamber was pumped. Following this, it was transferred back to UHV (pressure in the low $10^{-}10$ mbar range) and annealed to 300°C for 20 minutes to both dehydrogenate (i.e. "deprotect") the GNRs and remove coadsorbed contaminants from the air. STM images after this treatment are shown in figure 6.2(e) and (f). The vast majority, namely approx. 90% of the chGNR units cells are found to be pristine (561 out of 623 analyzed unit cells), also clearly retaining their electronic properties.[179] A few defects are observed – most commonly, the ketone groups in the central zigzag ring.[254] An example of such defect is circled in Figure 6.2(e), with a pair of ketones on the same GNR unit cell. As the number

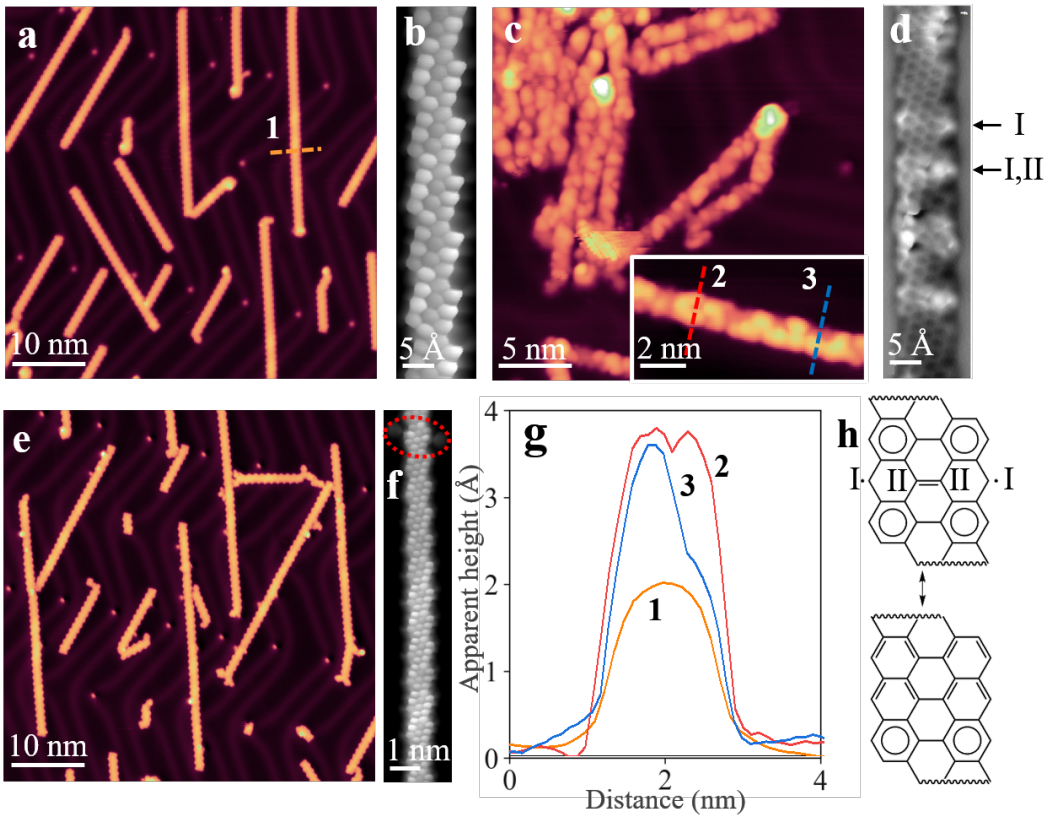

Figure 6.2: SPM analysis of GNRs along the various steps in the cycle of synthesis, hydrogenation (protection), air-exposure and annealing (deprotection). (a) Overview STM image of the sample of pristine (3,1)-chGNRs on Au(111) prior to hydrogenation. I = 1 nA, Vbias = -0.5 V. (b) BR-STM image of a pristine NR. (c) Cluster of hydrogenated ribbons after exposure to atomic hydrogen. Inset: zoom of a hydrogenated nanoribbon. For both images, I = 23 pA, Vbias = -2.0 V. (d) NC-AFM image of a slightly hydrogenated ribbon, where it is possible to observe the initial steps of hydrogenation. (e) Hydrogenated nanoribbons after 24 minutes of air exposure, followed by annealing to 300°C in UHV. I = 20 pA, Vbias = -0.5 V. (f) Nanoribbon after the same treatment, with one defective/oxidized ketone section circled. (g) Topographic profiles on a pristine ribbon (1), partially and totally hydrogenated (2 and 3). (h) Closed shell (bottom) and open shell (top) chGNR, displaying the most ("I") and second most prone ("II") positions to become hydrogenated.

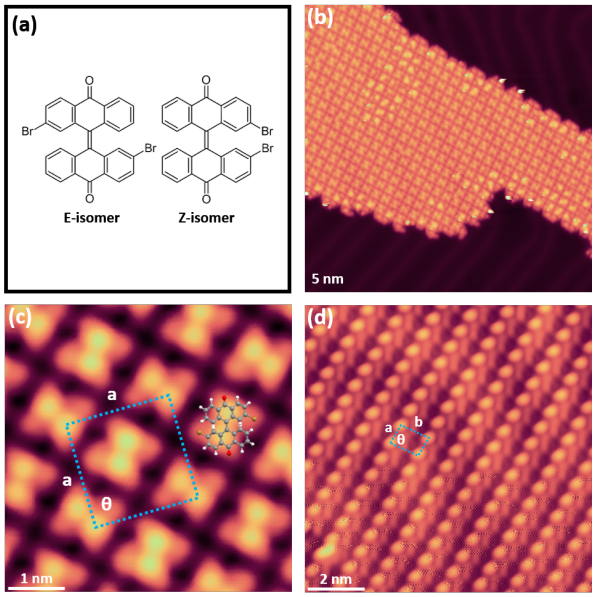

Figure 6.3: (a) Chemical structure of 2,2'-dibromo-10H,10'H-[9,9'-bianthracenylidene]-10,10'-dione ((E/Z)-k-DBBA, (b) Island of (a) at low molecular coverage. (c) Zoom of the same island, showing the regular structure and its unit cell. a = 1.87 ± 0.03 nm. = 90 ± 1°. A scaled gas-phase optimised model of a trans precursor molecule is overlaid in one of its possible conformations for reference. (d) STM image of a packing that was typically observed at higher coverages. a = 0.67 ± 0.02 nm; b = 1.06 ± 0.01 nm; = 85 ± 2°. All four STM images in this figure were recorded with the following parameters: I = 50 pA; Vbias = -0.5 V.

of defects is very low, this result clearly demonstrates the effectiveness of the hydrogenation strategy in protecting the GNRs from the oxidizing effect of the atmosphere; compared to the results presented before in this thesis.[254]

6.2 Ketone-functionalization

To further understand the tendency of chiral GNRs to oxidize at their zigzag edges, we have utilized a different precursor molecule, Figure 6.3(a). This molecule is already

'pre-oxidized' with ketone groups bound at its central zigzag edge positions, which were previously found to be the most reactive sites.

The self-assembly of a mixture of E and Z isomers of k-DBBA is presented in Figure 6.3(b-d). Annealing this precursor mixture on Au(111) to relatively high temperatures (430°C) results in the formation of nanoribbons, henceforth referred to as ketone-chGNRs (k-chGNRs). As shown in Figure 6.4(a), these nanoribbons readily pack together into islands. The chemical structure of the k-chGNRs is shown in Figure 6.4(b). In all experiments, there was a notable issue with anthrone-related molecules. These molecules are often found at the termination of the k-chGNRs, and may be the cause of their relatively short average length when compared to pristine chGNRs that are formed from DBBA. We hypothesize that the Z-isomer, which does not form GNRs, may be the cause of this contamination. It may terminate the polymers and fragment when heated on the surface. Future studies with stereoisomerically pure precursors may clarify this issue and improve the length and quality of the nanoribbons.[68]

An example of a BR-STM image of the 'normal' type of k-chGNRs is shown in Figure 6.4(c). Each unit cell exhibits two sharp features located at the centre of its zigzag edge, corresponding to the positions of the ketones. These features match with previously observed oxidation defects in pristine chGNRs, as well as those described above after exposing the hydrogenated GNRs to air. Crucially, these pre-oxidized chGNRs are no longer susceptible to oxidation under ambient conditions; after exposing a sample of k-chGNRs to air (24 minutes) and post-annealing (200°C) to remove coadsorbed contaminants, the vast majority of the k-chGNR units are unaffected, with only a small minority (10%)

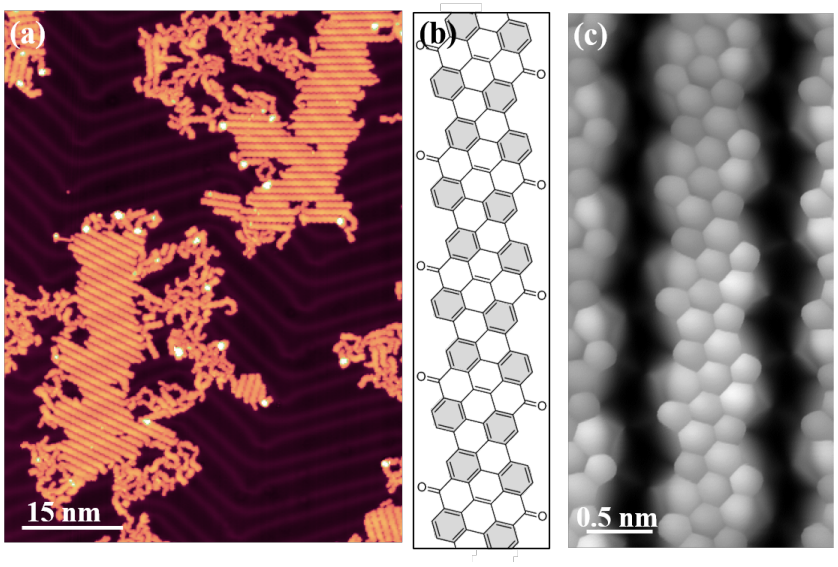

Figure 6.4: Reactant and product structure of pre-oxidized (protected) chiral GNRs. (a) Structures of the two k-DBBA precursor isomers. (b) Overview STM image of self-assembled islands of ketone chiral nanoribbons after annealing the precursors in steps up to 430°C. (scanning parameters: I = 30 pA, U = -0.5 V). (c) Chemical structure of the ketone chiral nanoribbons, with Clar sextets marked by a grey background (d) BR-STM image of a ketone chiral nanoribbon after air exposure and post-annealing to 200°C in UHV conditions. The sharp features at the edge of each central ring correspond to the ketone groups, and these were observed both before and after the air exposure (CO tip, constant height, Vbias = 8 mV).

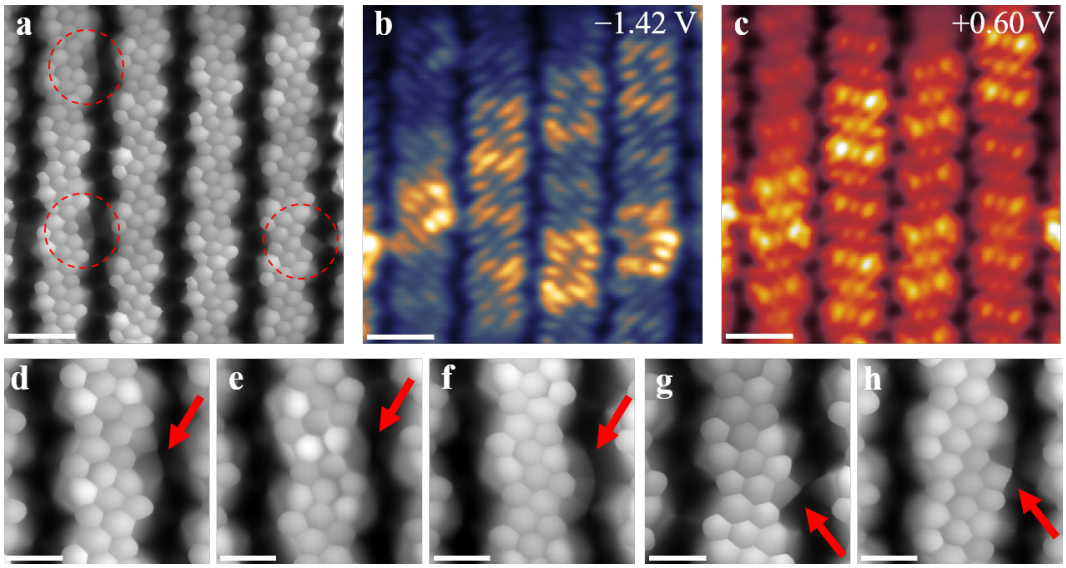

Figure 6.5: (a) Island of ketone-GNRs that were exposed to the atmosphere (24 mins) and post-annealed to 200°C for 1 hour. Defects are highlighted with dashed red circles. (b) and (c) Constant height dI/dV images of the same area (CO tip) at the approximate energies of the valence and conduction bands, respectively. While there are clear changes at the position of the defects, the integrity of the electronic structure remains. Scale bars in (a) – (c) are 1 nm. (d) – (h) BR-STM images of various defects that are found after exposing the ketone-NRs to the air (+ post-annealing). Many oxidation defects may be found in positions that already possessed defects prior to air exposure, e.g. sections in which ketone groups were missing. Scale bars in (d) – (h) are 0.5 nm.

displaying any extra defects that could be ascribed to the air exposure (Figure 6.5(a)). A clear demonstration of the general air stability of the k-chGNRs is the image shown in Figure 6.4(c), which was actually recorded after air exposure followed by annealing and displays no changes from typical BR-STM images recorded prior to the exposure.

The addition of a ketone group significantly changes the conjugation of the chGNRs. As a consequence, the electronic properties are strongly affected. Each unit cell

can be represented with four Clar sextets as in Figure 6.3(c), as opposed to the two Clar sextets that may be drawn for the closed shell representations of the pristine (3,1)-chGNRs (Figure 6.1). Such increase in sextets is normally associated with an enlarged band gap and a concomitantly augmented stability. Figure 6.6(a) displays stacked dI/dV spectra recorded at 45-points along the edge of a 10-unit k-chGNR as shown in Figure 6.6(b). Overlaid is an example of one of the point spectra, recorded at the position marked with a red cross in Figure 6.6(b). The onsets of both the valence and conduction band (VB and CB, respectively) are indicated with dashed lines. Besides conferring the ribbons an n-type semiconducting character, the ketone functionalization endows the ribbons with a much larger band gap (Eg $\approx$ 2.1 eV) than that of the pristine chGNRs (Eg $\approx$ 0.67 eV).[69] As expected, shorter k-chGNRs reveal a wider band gap (e.g. 2.5 eV for a dimer) but it very quickly saturates around 2.05 – 2.10 eV after reaching 4 or 5 units in length.[179] This notably wider band gap supports the assertion of the k-chGNRs' increased stability with respect to the pristine chGNRs. A BR-STM image of the 10-mer, along with four constant height dI/dV maps (CO tip), are presented in Figure 6.6(b-f). These are recorded at the VB and CB onsets, and at two conductance maxima that are found deeper inside the occupied and unoccupied states.

To improve our understanding of the ribbon's electronic properties we have performed complementary DFT calculations. Figure 6.6(g) displays the calculated band structure, along with the integrated density of states (DOS). In qualitative agreement with the experiments, the initial DOS maxima at the VB and CB onsets are followed by stronger maxima, out of which the occupied states are closer to the VB onset than the empty states to the CB onset. These two DOS maxima correspond to van Hove singularities at the Bril-

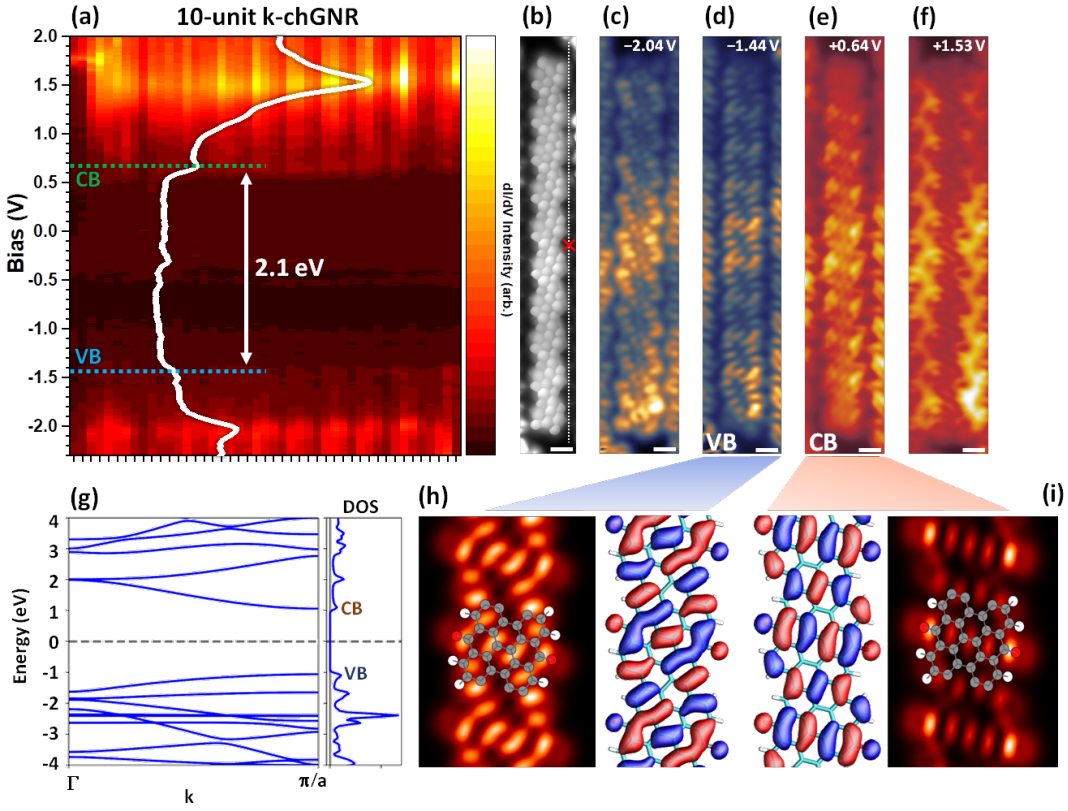

Figure 6.6: Electronic properties of pre-oxidized protected GNRs. (a) Stacked dI/dV point spectra along the edge of a 10-unit ketone nanoribbon. The onsets of the valence and conduction bands are indicated with dashed lines, with a measured band gap of 2.1 eV. One of the spectra is overlaid with a white line. (b) BR-STM image of the same 10-unit nanoribbon, marking with a dashed line the positions along which the spectra were acquired that make up panel (a), and with a red cross the position for the overlaid spectrum (Constant height, CO tip, U = 5 mV). (c)-(f) Constant height dI/dV images of the four strongest resonances observed in the dI/dV spectra (CO tip, indicated scale bars correspond to 500 pm). (g) Band structure calculations for the ketone-functionalized ribbons (aligned with respect to the midgap energy), along with the integrated density of states. (h) Wavefunction and simulated STM image of the orbital at the valence band onset and (i) at the conduction band onset (the simulated images consider tips with 95 % pxpy and 5 % s-wave character and the unit cell structure used for the calculations is superimposed on the images).

louin zone center Γ that contain contributions from the valence and conduction band in combination with following bands (as opposed to the VB and CB onsets at the zone boundary). Focusing on the frontier states, the calculated wavefunctions and the associated STM image simulations show an excellent agreement with the measurements and confirm our assignment, Figure 6.6(h,i).

6.3 Regeneration of chiral GNR

As previously mentioned, the k-chGNRs are found to be particularly stable (in contrast to the pristine chGNRs) due to the presence of carbonyl (C=O) groups in the reactive position that allow the formation of more Clar sextets without the concomitant creation of unpaired radicals. However, disrupting this system with atomic hydrogen may result in the formation of hydroxy derivatives that can in turn be involved in dehydration to afford the pristine chGNRs upon annealing.

Hydrogenation of the k-chGNRs is shown in Figure 6.7(b). Under similar conditions to pristine chGNR hydrogenation, it results in smaller dispersed islands of molecular aggregates, many of which are distorted into small "three-dimensional" objects with little resemblance to nanoribbons. However, annealing this sample to 330°C clearly demonstrates that the ribbons' backbones are not destroyed by the hydrogenation process, as elongated, straight structures are once again formed, shown at Figure 6(c). Examination of these structures via BR-STM, Figure 6(d), reveals that they are now mostly pristine GNRs, with a small

number of ketone defects still remaining. Most of them appear in closed-shell defect pair configurations, that is, either on the same or on neighboring unit cells. These defects have the same appearance as those observed when exposing the hydrogenated pristine GNRs to air. The high level of conversion (approx. 78%, 602 out of 772 unit cells analyzed) may be further improved with tweaks to the hydrogenation process or repeated hydrogenation/annealing cycles. However, this result is remarkable in and of itself. Note that the coverage reduction that may be apparent in Figure 6.7 is spurious and only reflects the disparate tendency of k-chGNRs to assemble into compact islands while p-chGNRs repel each other. Larger area images reveal how the low density of compact islands is comparable in coverage to that of the disperse p-chGNRs.[179]

NC-AFM images cannot be performed with intramolecular bond resolution on heavily hydrogenated structures that become exceedingly non-planar. In order to shed more light onto the whole hydrogenation and annealing process we have performed additional nc-AFM in lightly hydrogenated samples. A reference nc-AFM image of "as grown" k-chGNRs is displayed in Figure 6.7(f), revealing the fading contrast of all the bonds involving the ketone-functionalized carbon atom. A representative image of a hydrogenated sample is shown in Figure 6.7(g). Less reproducible products than for the p-chGNR counterparts point towards more complex or competing reaction processes. Nonetheless, several conclusions can be readily drawn. As for p-chGNRs, also for k-chGNRs the central carbon atom of the zigzag segments (which is the ketone-functionalized atom) is among the most affected.

Indeed, as more clearly shown in the smaller scale image in Figure 6.7(h), the contrast on these atoms displays multiple variations along with that of the starting nanorib-

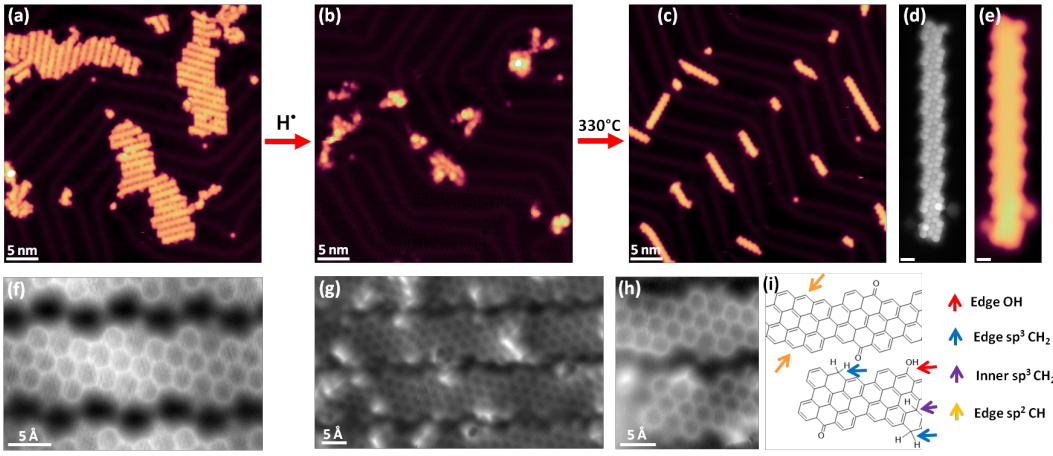

Figure 6.7: STM analysis of GNRs along the various steps in the synthesis process of its pre-oxidized (protected) form, hydrogenation and annealing (deprotection). (a) Overview STM image (I = 100 pA, U = -0.1 V) of mostly metal-organic ketone GNRs after their synthesis on Au(111). (b) Overview STM image (I = 50 pA, U = -1.0 V) of the same GNR sample after exposure to atomic hydrogen. (c) STM image (I = 50 pA, U = -0.5 V) of the same sample after annealing to 330 °C. The GNRs mostly consist of pristine sections, with some remaining ketone defects. (d) BR-STM (Constant height, CO tip, 5 mV) and (e) STM (I = 100 pA, U = -0.5 V) of one of the GNRs from the post-annealed sample (scale bars = 500 pm). Two neighbouring metal-organic ketone defects are observed on the two sections at the lower end of the ribbon. (f) nc-AFM image of as-grown k-chGNRs. (g) nc-AFM image of lightly hydrogenated k-chGNRs. (h) Detail of lightly hydrogenated k-chGNRs, along with (i) the proposed chemical structure.

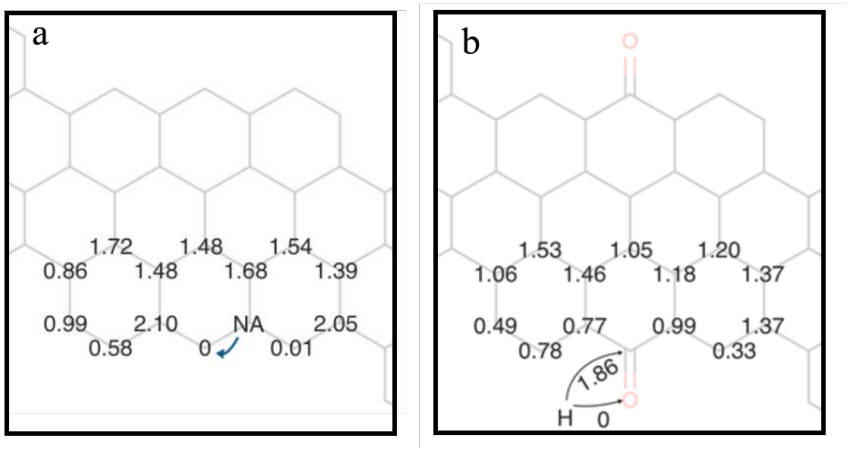

Figure 6.8: Total energy differences between different sites for the initial hydrogenation of ch-GNRs (a) and k-chGNRs (b). Total energy differences (in eV) for addition of atomic H, calculated as the difference from the most stable position.

bon. Our tentatively proposed assignment, based on the comparison with previously characterized defects,[254] is shown in Figure 6.7(i) and includes hydroxyl-functionalized carbon atoms, as well as deoxidized sp^2 and sp^3 atoms. Complementary DFT calculations reveal the oxygen atom as the energetically most favourable initial hydrogenation site, in Figure 6.8. Once the hydroxyl group have been formed on both ketones, the conjugation pattern becomes closer to that of p-chGNRs and the following hydrogenation events can cause either dehydration (affording p-chGNRs) or the hydrogenation of other carbon atoms. These additional options also justify the larger diversity in hydrogenation products observed experimentally when compared to the initial hydrogenation stages of p-chGNRs.

In order to get a deeper insight on the chemical nature of the hydrogenation process, XPS measurements were performed in both chGNR and k-GNR. The spectrum of 'as-grown' p-chGNRs can be decently fitted by one single peak, figure 6.9(a). Our resolution was infered from Fermi edge analysis and resulted in 0.4 eV, therefore we refrain

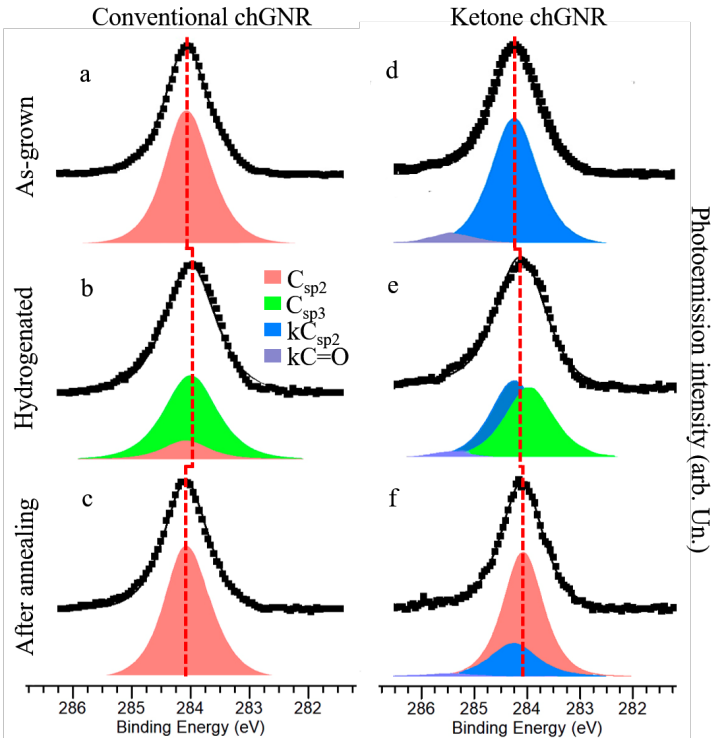

Figure 6.9: XPS analysis monitoring the hydrogenation/dehydrogenation process of pristine and ketone-functionalized ribbons. (a) C_{1s} XPS spectra (symbols) of p-chGNRs "as grown" (top), after hydrogenation (middle) and after subsequent annealing (bottom), along with the fit (solid curve) and its associated components (coloured peaks). The data reveal the successful hydrogenation and its reversibility. (b) C_{1s} XPS spectra (symbols) of k-chGNRs "as grown" (top), after hydrogenation (middle) and after subsequent annealing (bottom), along with the fit (solid curve) and its associated components (coloured peaks). The data reveal the gradual deoxidation upon hydrogenation and the subsequent annealing. Dashed lines act as a guide to the eye to compare the maxima on each of the spectra.

from overfitting with additional components as typically performed with higher-resolution synchrotron-radiation-based XPS spectra[276, 195] and instead assign this peak to C sp^2 atoms. Upon hydrogenation, the energy and full-width at half-maximum of the C sp^2 component is maintained as fixed while leaving the intensity to be fitted, and the spectral broadening towards lower binding energy is accounted for by including a second component that we now associate with hydrogenated C sp^3 atoms, which are indeed expected to appear at lower binding energies,figure 6.9(b).[277] The two fitted components are shifted by only 0.1 eV, much less than the component's full-width at half-maximum (1 eV), and therefore mostly overlap (remember that the C sp^2 component also includes hydrogenated edge atoms). Although this fit can therefore not be considered conclusive, the resulting energy and width for the new sp^3 component coincide with those used for fitting the k-chGNRs, and furthermore, the fit displays a sp^3 to sp^2 ratio of 87:13, in qualitative agreement with estimations based on scanning probe microscopy. Importantly, after annealing the hydrogenated GNRs, the initial spectral shape is recovered, figure 6.9(c), being fitted again only with the sp^2 component and thereby confirming the reversibility of the protection/deprotection process. The k-chGNR case is slightly more complex. To start with, the initial spectrum of 'as-grown' ribbons is less symmetric and is thus fitted with two components in a 1 to 13 intensity ratio for the high and low binding energy signal, respectively, figure 6.9(d). This ratio corresponds to the stoichiometry of the sp^2 carbon atoms bound to the more electronegative oxygen atom (and thus at a higher binding energy; labelled as C=O) and the remaining sp^2 carbon atoms bound only to C or to C and H (and thus at a lower binding energy due to the lower electronegativity of C and H as compared to O; labelled as k-C sp^2). Note that the k-C sp^2 component is at a higher binding energy than the C sp^2 component of the p-chGNRs

due to the electron-withdrawing effect of the ketone. As the ribbons are hydrogenated, there is a notable shift of the spectral weight to lower binding energies. In the fit, we account for this change while maintaining the C=O and k-C sp^2 components unchanged (except for their intensity) and adding a new C sp^3 component for the hydrogenated atoms at the same energy as for the p-chGNR case, figure 6.9(e). With these constraints, we observe that the intensity of both the C=O and k-C sp^2 components is reduced to 56% of the initial values, supporting the deoxidation readily at room temperature during the hydrogenation, as previously concluded from the scanning probe microscopy analysis. After annealing, these two components decrease even further to 32% of their initial value, in qualitative agreement with the 'deprotection' efficiency estimated from the scanning probe microscopy analysis, figure 6.9(f). The remaining intensity is made up by a C sp^2 component that supports the conversion of the k-chGNRs into p-chGNRs. It is important to note that the total intensity during the hydrogenation/annealing cycle remains virtually unchanged, supporting the absence of any important desorption during the treatment. Both of these findings are in qualitative agreement with the scanning probe microscopy analysis.

It should be reminded that, while the GNRs resulting from this process are relatively short in length, this is due not to the hydrogenation process itself, but to the short average length of the k-chGNRs that they began as. Improvements in the synthesis of the k-chGNRs, which may be presumably achieved with a reduced amount of Z-isomer as well as with optimized growth parameters, should also result in longer, higher quality pristine GNRs after the hydrogenation and annealing processes.

6.4 Conclusions

These results demonstrate that chemically protected GNRs can be easily converted back to pristine GNRs, and this method could be applicable to other protecting groups/functionalities that have different properties, as long as the central carbon at the zigzag edge is still present. Reducing the level of hydrogenation may also allow for statistical mixtures of functionalized/pristine GNRs that have different properties.

It is important to note that hydrogenation cannot necessarily be used as a 'cure' for uncontrollably oxidized GNRs, since some of the common defects after exposing chGNRs to air involved modifications of the carbon-backbone structure and even the loss of carbon atoms that cannot be recovered through hydrogenation, as we already saw in chapter 5. However, we have shown that this method allows the application of protection/deprotection strategies, as commonly utilized in conventional organic chemistry, to on-surface synthesis. That is, hydrogenation can be used both to protect chemically labile graphene nanoribbons, as well as to deprotect pre-oxidized nanoribbons that possess a significantly larger band gap and in-built resistance to oxidizing atmospheres, in either case allowing for a reconversion into pristine chiral graphene nanoribbons. Most importantly, this approach may be extrapolated to different graphene nanoribbons and carbon-based nanostructures, as well as to different functional groups that are involved in pre-protected forms, altogether bringing the exploitation of the unique characteristics of zigzag edges in carbon materials a step closer to scalable applications.

CHAPTER 7

Radical coupling in chGNR

The hydrogenation and oxidation strategies succesfully opened the door to GNR protection strategies. However, there are still interesting physics concerning the defective ribbons, on which we haven't focused much yet. During the oxygen and water exposures, we studied how substitutions on one edge could stabilize an unpaired state on the opposite. However, those were uncontrolled oxidations (for the oxygen) or too unstable to work with (for the water case). The combination of the hydrogenation with the k-chGNR opens the door to a higher tunability of the ribbon edge modification with stable - and more importantly radical-stabilizing - functional groups. The different strategies to generate net spins on chGNRs and k-chGNRs are shown in Figure 7.1.

Replacing a CH at the pristine chGNR edge by a C=O (carbonyl) adds one π-electron to the system. As a result, the odd number of total electrons causes the appearance of a π radical following Lieb's theorem.[278] The same is applicable for regularly ketone-functionalized chGNRs[179] if a C=O is replaced by a CH. The introduction of a second radical may either maintain the system's open-shell character or result in their hybridization into a closed-shell structure.[186] On the basis of the above, a variety of radical pairs with different geometries were analyzed in our experiments. Combining scanning tunneling microscopy (STM) with theoretical calculations, we reveal how their relative location, the chemical structure of the units surrounding the two radicals and the chirality itself, all influence the spin interactions. The generation of radical states in chGNRs is schematically displayed in Figure 7.1(a) and starts from the readily described synthesis of pristine (P-) and ketone-functionalized (K-) chGNRs on Au(111).[179, 244] In the case of K-chGNRs, a few defective ribbons with one or more missing oxygen atoms normally coexist with intact

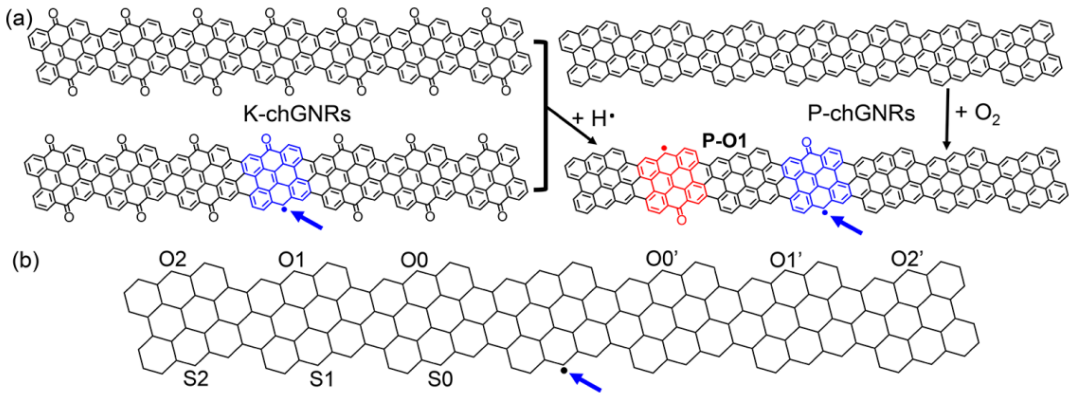

Figure 7.1: Synthesis and nomenclature of radicals and radical pairs. (a) Schematic drawing for the fabrication of magnetic chGNRs. A -radical is introduced into chGNRs by the addition/removal of an oxygen into/from P-/K-chGNRs. (b) Labels for the radical pairs in chGNRs. Taking the radical marked with a blue arrow as the reference, each pair is labeled depending on the position of the second -radical.

ribbons.[179] The substitution of an oxygen by a hydrogen atom makes the total number of p_z electrons an odd number, thus producing an unpaired π radical, as indicated by the blue arrow. In turn, the addition of an oxygen atom to an otherwise P-chGNRs effectively adds one pz electron and equally brings in a radical. This can be achieved either by exposing P-chGNRs to O_2 and postannealing,[254] or removing most of the ketones of K-chGNRs by exposing them to atomic hydrogen and postannealing (as we showed in the previous chapter).[179] Using these procedures, P- and K-chGNRs with single radicals and with radical pairs were produced. Unfortunately, attempts to controllably remove ketone groups by tip manipulation and thereby create radicals at predesigned positions were unsuccessful.

We will use the following nomenclature to refer to different radical pairs. Taking the radical marked with the blue arrow in Figure 7.1(b) as reference, the other labels denote the position of the second radical (Figure 1b). S/O represents the two radicals of

a pair located at the same/opposite sides of a chGNR. The following number shows how many precursor units separate a radical pair. A ' mark is used to distinguish the differing configurations resulting from the ribbon's chirality. Finally, P- denotes P-chGNRs (pristine chGNRs) in which the radicals are caused by additional ketones and K- denotes K-chGNRs (ketone-functionalised chGNRs) with radicals associated with missing ketones. An example P-O1 radical pair is shown in Figure 7.1(a) in red. Figure 7.2(a) presents the BR-STM image of a K-chGNR with a single defect, along with the associated chemical structure. At the low bias value used for BR-STM, the unit cell with a missing ketone exhibits brighter contrast, implying the existence of low-energy states as in chapter 5.

7.1 Single defects

Figure 7.2(b) shows the differential conductance spectrum (dI/dV) taken at the marked position in Figure 7.2(a). Apart from the highest occupied and lowest unoccupied molecular orbitals (HOMO and LUMO) of a K-chGNR at -1.45 and 0.65 V, associated with the reported valence and conduction band onsets,[179] two in-gap states are clearly visible at -0.47 and 0.25 V. The same local density of states (LDOS) distribution at these two energies in dI/dV maps supports their common origin from the singly occupied/unoccupied molecular orbitals (SOMO/SUMO), separated by a 0.72 eV Coulomb gap.[34] In line with the experiments, the spin density calculated for this structure with density functional theory (DFT) with SIESTA[279, 280], Figure 7.2(e), distributes mostly over the "defective" unit cell but extends slightly to the adjacent ones with a clear chirality-driven asymmetry. Evidence of

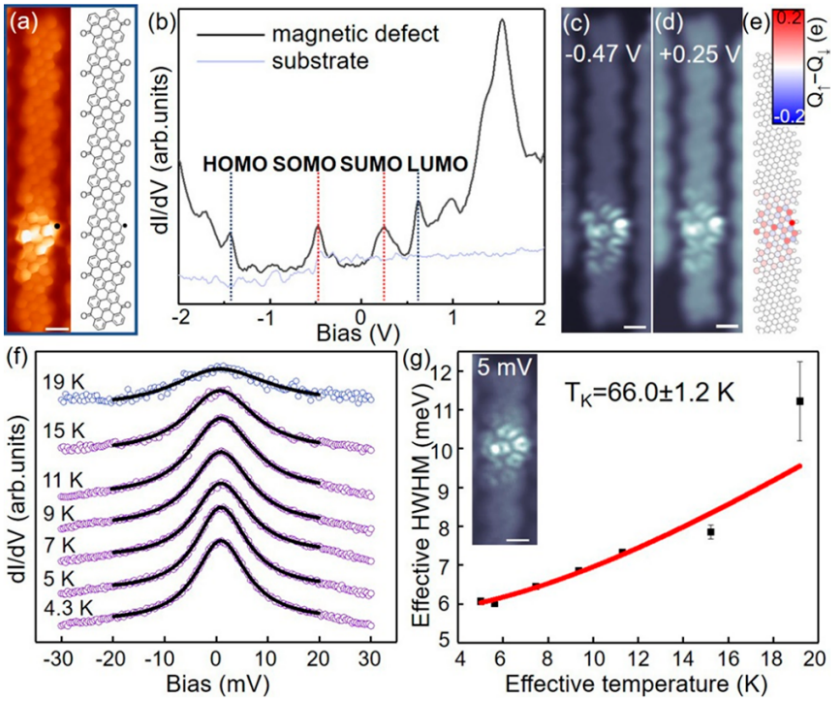

Figure 7.2: Characterization of single radicals. (a) Constant-height BR-STM image of a K-chGNR with single defect (V = 5 mV), together with the corresponding chemical structure. (b) dI/dV spectra at the marked position in (a, black line) and the bare Au(111) substrate (gray line), Vrms = 20 mV. (c,d) Constant-height dI/dV maps recorded at V = -0.47 and 0.25 V, respectively. Vrms = 20 mV. (e) DFT calculated spin density distribution in K-chGNR with single defect. (f) Temperature dependence of the Kondo resonance. All of the spectra are fitted by a Frota function. (g) Extracted HWHM of the Kondo resonances as a function of temperature, fitted by the Fermiliquid model. The inset shows a Kondo map measured at 5 mV. Scale bars: 0.5 nm.

this system's net spin S = 1/2 is detected as a zero-bias peak in the low-energy dI/dV spectra, Figure 7.2(f). It broadens anomalously fast with temperature and can thus be attributed to a Kondo resonance.[271, 126] The half width at half-maximum (HWHM) of the temperature-dependent spectra, as extracted from fits to a Frota function[281], Figure 7.2(f), are further fitted to the Fermi liquid model[129] and result in a Kondo temperature of 66 K, Figure 7.2(g). The identical spin distribution of the Kondo map obtained at 5 mV (Figure 7.2(g) inset) and of the SOMO/SUMO shown at Figure 7.2 (c,d) further corroborates the origin of the spin density in the SOMO.

An equivalent characterization of a single magnetic defect in P-chGNR is presented in Figure 7.3. Compared to the K-chGNR case, the SOMO and the associated spin density in P-chGNR show a much more limited contribution on the ketone and mostly distribute over the pristine side of the defective unit cell. The smaller bandgap of P-chGNR as compared to K-chGNR (∼0.7 vs ∼2.1 eV),[179, 69] causes a stronger hybridization of the radical states with the frontier molecular orbitals, resulting in a notably more extended distribution into neighboring unit cells (though with a similar chirality-driven asymmetry) and consequently a lower Coulomb gap of only 0.35 eV.

7.2 Radical pairs

Next, we focus on chGNRs with radical pairs. Whereas a hybridization of the two radicals may result in a closed-shell ground state with a doubly occupied HOMO, the system

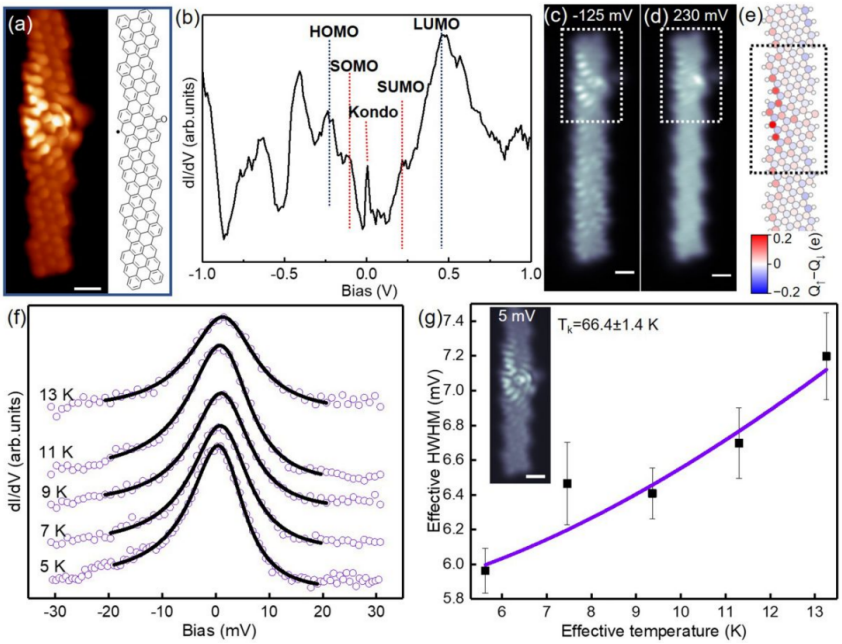

Figure 7.3: (a) Constant-height BR-STM image of P-chGNR with a single magnetic defect, acquired by a CO-functionalized probe, together with the corresponding chemical structure. Bias: 5 mV. (b) dI/dV spectra taken at the marked position in (a), V_{rms} = 20 mV. (c,d) Constant-height dI/dV maps taken with a CO functionalized tip, recorded at the bias of -0.125 and 0.23 V, respectively. Vrms=20mV. The energy of SOMO is close to HOMO thus the signal from HOMO is also visible in (c). (e) DFT calculated spin density distribution in P-chGNR with a single magnetic defect. The dashed frames in (c-e) include same units with high spin density distributions. (f) Temperature dependence of the Kondo resonance between the unpaired radical and conduction electrons on the Au(111) substrate. All the spectra at different temperatures are fitted by a Frota function. (g) Extracted half-width at half-maximum (HWHM) of the Kondo resonances as a function of temperature, fitted by the Fermi-liquid model: $HWHM = 1/2\sqrt{(ak_BT)^2 + (2k_bT_K)^2}$. *The HWHM is corrected to the effective HWHM considering the broadening contributed from the tip temperature to the intrinsic HWHM. The temperature of the sample is also corrected to the effective temperature considering the lock-in oscillation amplitude contribution. A Kondo temperature of 66.4 K is obtained, close to the K-chGNR single defect (66.0 K). A Kondo current map of a P-chGNR with a single magnetic defect is inserted, which was acquired at 5 mV in constant-height mode using relatively far tip-sample distance. Scale = 0.5 nm.*

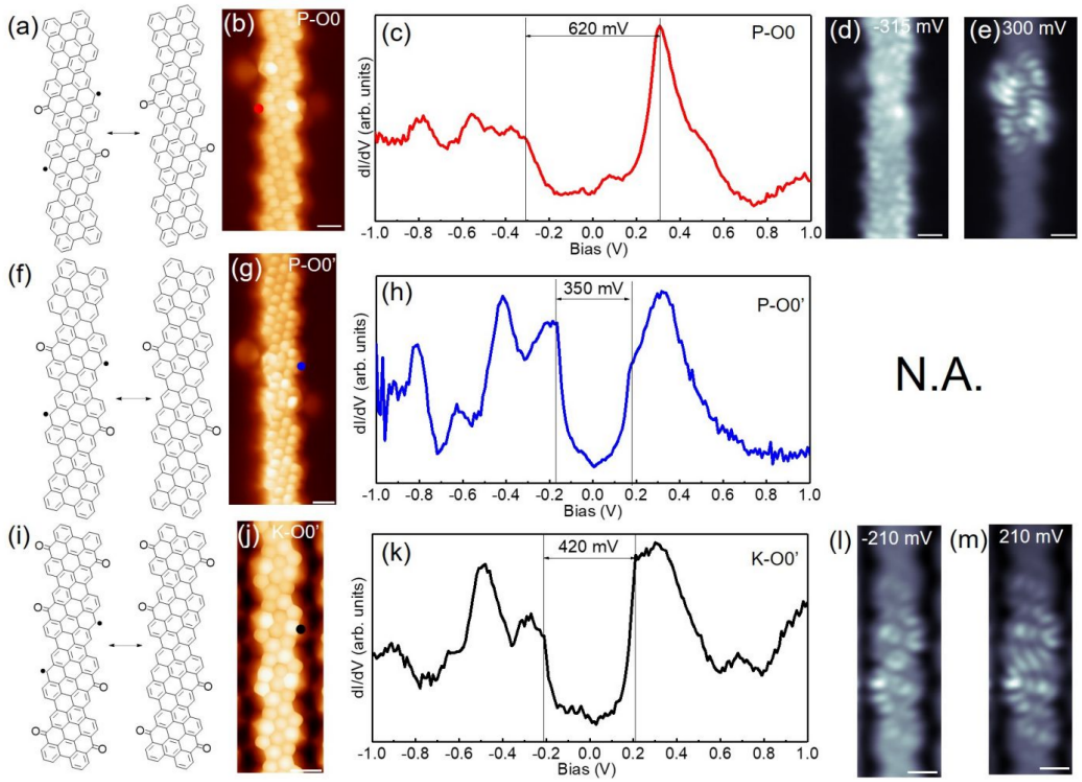

Figure 7.4: Closed-shell defect pairs. (a,f,i) Open-shell and closed-shell resonant structures of P-O0, P-O0', and K-O0'. (b,g,j) Constant-height STM images of P-O0, P-O0', and K-O0' GNRs acquired using CO functionalized probes. V=5 mV. All the scale bars are 0.5 nm. (c,h,k) dI/dV spectra taken at the marked positions in (b,g,j), respectively. (d,e) dI/dV maps acquired at -315 mV and 300 mV for P-O0, respectively. (l,m) dI/dV maps acquired at -210 mV and 210 mV for P-O0, respectively. Lock-in amplitude is 20 mV for all the dI/dV maps. Note that SOMO and SUMO separated by the spin splitting with a Coulomb gap show identical LDOS. The different distributions of occupied and unoccupied orbitals demonstrate they are doubly occupied HOMOs and LUMOs.

can also remain open-shell with the associated SOMOs, if the hybridization energy is lower than the Coulomb repulsion between the corresponding electrons.[186, 36] DFT calcuations predict two radicals in closest proximity but opposite GNR sides (i.e., the O0 and O0 cases in both types of chGNRs) to hybridize into a closed-shell ground state,[253] while all of the other radical combinations show open-shell ground states. The experimentally observed P-O0, P-O0, and K-O0 cases confirm their closed-shell character and are displayed in Figure 7.4 with HOMOs and LUMOs exhibiting distinct LDOS distributions as opposed to the similar appearance expected from SOMO and SUMO.

For the open-shell structures, the exchange interaction between a radical pair can be experimentally accessed from inelastic spin-flip excitations in scanning tunneling spectroscopy.[271] The low-energy dI/dV spectra of radical pairs with a S = 1 triplet ground state may exhibit three features: an underscreened Kondo resonance at Fermi level and two side steps symmetrically positioned around the Fermi level. The latter are associated with inelastic triplet-to-singlet spin-flip excitations,[234, 282] and in contrast to their energetic alignment their intensities may display asymmetries as a result of lacking particle-hole symmetry (that is, the singly occupied orbital is closer to Fermi than the singly unoccupied state or vice versa), spin-polarized tips, and so forth.[283, 284] In contrast, the dI/dV spectra of radical pairs with a S = 0 singlet ground state exhibit only the two singlet-to-triplet side steps.[282, 285, 34]

As the exchange interaction between the radicals becomes sufficiently weak, equaling singlet and triplet energies, the radicals respond independently from one another and may display only a Kondo resonance. The geometries of the experimentally addressed

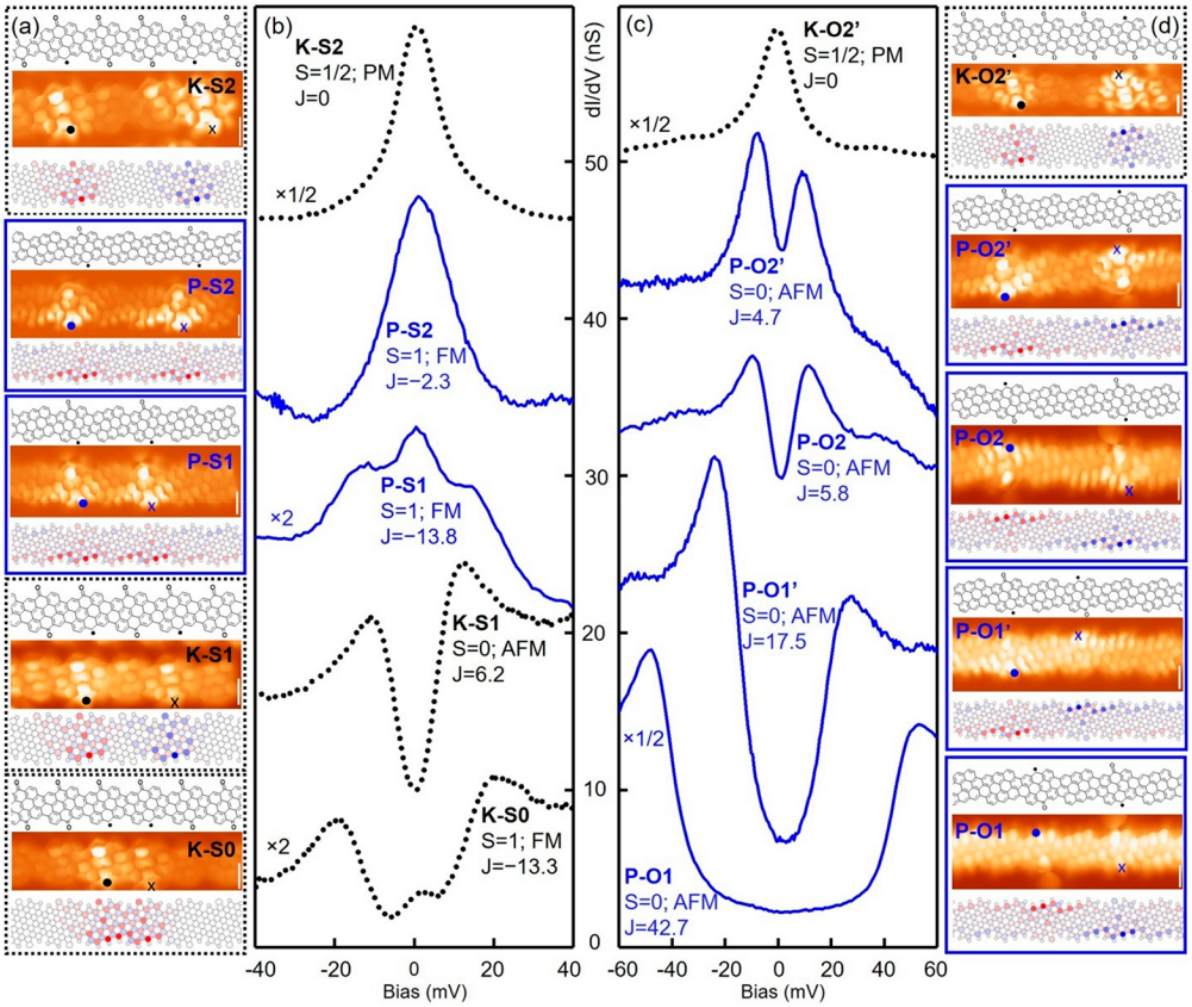

Figure 7.5: Characterizations of radical pairs. (a,d) BR-STM images (V = 5 mV) of experimentally obtained radical pairs at the same (a) and opposite sides (d) on P- and K-chGNRs, together with the chemical structure and DFT calculated spin-polarized LDOS for each case (ground states). (b,c) dI/dV spectra measured at the marked positions in STM images (see comparative spectra at the position of the second radical marked with an x in the Figure S5. The blue solid and black dotted curves refer to radical pairs on P- and K-chGNRs, respectively. P-O1 shows the original signal and other spectra were vertically shifted to match the positions of STM images. Some of the spectra were additionally scaled as marked. Total spin and coupling strength are shown for each case, where PM, FM, and AFM stand for paramagnetic, ferromagnetic and antiferromagnetic coupling, respectively. Lock-in amplitude: 2 mV for P-O1, 1.5 mV for K-S0, 1 mV for other cases. Scale bars: 0.5 nm.

radical pairs are determined from the BR-STM images displayed in Figure 7.5 (a,d), along with their spin densities as calculated with DFT. The associated low-energy dI/dV spectra are shown in Figure 7.3 (b,c). Table 1 includes the values obtained from theoretical calculations by Sofía Sanz and Thomas Frederiksen. The table compares the exchange couplings to the experimental results. Further details of the fitting can be found at Appendix C. The good match of the DFT results with the experiments underlines the predictive power of the calculations on radical pair geometries not accessed experimentally. Focusing on the exchange coupling J, it scales inversely with the spatial separation for both P- and K-chGNRs cases. That is, radical pairs separated by less unit cells show larger J values due to the greater overlap of the radical states' wave functions and the associated spin density (Figure 7.5 (a,d)). Interestingly, J shows a remarkable dependence on the chirality, as observed experimentally with P-O1 and P-O1 and predicted theoretically also for K-O1 and K-O1 (Table 7.6). The chirality-driven asymmetric extension of the SOMO wave function (and of the associated spin density) into neighboring unit-cells strongly affects their overlap. For example, whereas the spin density of radical states in P-O1 mostly extends toward the central unit between the radical pairs, it dominantly extends away from each other in P-O1 (Figure 7.5(d)). As a consequence, the former shows a much stronger exchange coupling than the latter (42.7 vs 17.5 meV). The exchange coupling strength also varies substantially with the nature of the surrounding GNR, as exemplified here with the presence or absence of the edge functionalization by ketones. Radical states in K-chGNRs extend much less than those in P-chGNRs, promoting in the latter a larger overlap and thus larger J for the same radical pair geometry. As for the spin's relative alignment, a generally applicable assumption that relies on the preferred antiferromagnetic alignment of electrons in chemical bonds is that,

type	experiment	DFT	MFH-TB(1)	MFH-TB(2)
P-S0		−31.4	−44	−23.2
P-S1	−13.8	−18.4	−15.5	−12.8
P-S2	−2.3	−11	−7.2	−6.4
P-O0	CS	CS	CS	CS
P-O0′	CS	CS	108	CS
P-O1	42.7	35.8	29	28.8
P-O1′	17.5	28	21.4	20.4
P-O2	5.8	11.3	7.8	6.9
P-O2′	4.7	11.8	7.8	7.1
K-S0	−13.3	−24	−50.9	−19
K-S1	6.2	6.4	−6.6	2.1
K-S2	0	0.4	−0.5	0.1
K-O0		CS	CS	CS
K-O0′	CS	CS	109.1	CS
K-O1		29.1	14.4	20.9
K-O1′		−0.5	2.7	0
K-O2		0.1	0.9	0.5
K-O2′	0	0.7	0.3	0

[a]Positive (negative) J values indicate preferred antiferromagnetic (ferromagnetic) alignment. [b]CS denotes closed-shell structure.

Figure 7.6: Exchange-Interaction Strength J (in meV) Obtained from Experiments and Theoretical Calculations for Multiple Radical Pairs[a,b]

for alternant graphene nanostructures, each of the two sublattices hosts p_z electrons with spin up or down, respectively. Since the ketone group is also sp^2 hybridized, it adds one p_z electron to the system and can to a first approximation be considered as an additional p_z site on its corresponding sublattice. The atoms at same edges of the chGNRs belong to the same sublattice, whereas the atoms at the opposite edge belong to the other sublattice. A radical pair located at the same/opposite side is therefore expected to be ferromagnetically (FM)/antiferromagnetically (AFM) aligned. All experimentally measured radical pairs match this prediction, except K-S1 (AFM ground state; Table 7.6).

For the conductance spectrum of K-S1, one could argue that the Kondo peak expected from a FM alignment is not visible because its intensity is much lower than that of the spin flip steps (as occurs, e.g., in K-S0, Figure 7.5(b)), and its width is comparable to J. In fact, the spectrum can be fitted using Ternes' code[284] assuming an FM alignment. However, to do so, the tip-sample transmission function represented by the T_0^2 parameter required an anomalously large value. Since we did not change the STM tip during the whole

experiment and used comparable tip-sample distances as defined by the STM feedback parameters, it is natural to expect that T_0^2 should be similar for all the spin-coupling scenarios. However, a FM alignment for the K-S1 case required a T_0^2 value an order of magnitude higher and clearly out of the dispersion range, suggesting a preferred AFM alignment of the K-S1 radical pair. FOr more ditails consult Appendix C.3.

7.3 Tuning the tight-binding model

This counterintuitive spin alignment for the K-S1 case is confirmed with DFT calculations, which predict the AFM alignment to be energetically favored. We have additionally performed mean-field Hubbard (MFH) calculations[280] on this same system, given its greater simplicity and successful application to many open-shell carbon nanostructures.[234] As discussed earlier, the extra p_z electron on the sp^2 hybridized ketone was first considered as an additional p_z site taken to be identical to a carbon p_z orbital. Doing so, MFH calculations with the third nearest-neighbor tight-binding model (3NNTB) predict a FM ground state for K-S1, in line with the intuitive expectations for radical states on the same ribbon's side but against DFT and experiments (henceforth we call this model MFH-TB(1)). In a counter-experiment, we performed DFT calculations for another system which is more equivalent to a simulation performed with MFH-TB(1), namely a chGNR with methylidene groups (i.e., C=CH2)[16] instead of carbonyl (C=O). In this case, the DFT results agree with the intuitive expectations and with the MFH-TB(1), predicting a preferred FM alignment and even a comparable J value (CH2-S1 in Figure 7.7 (a)). It follows that the surprising AFM

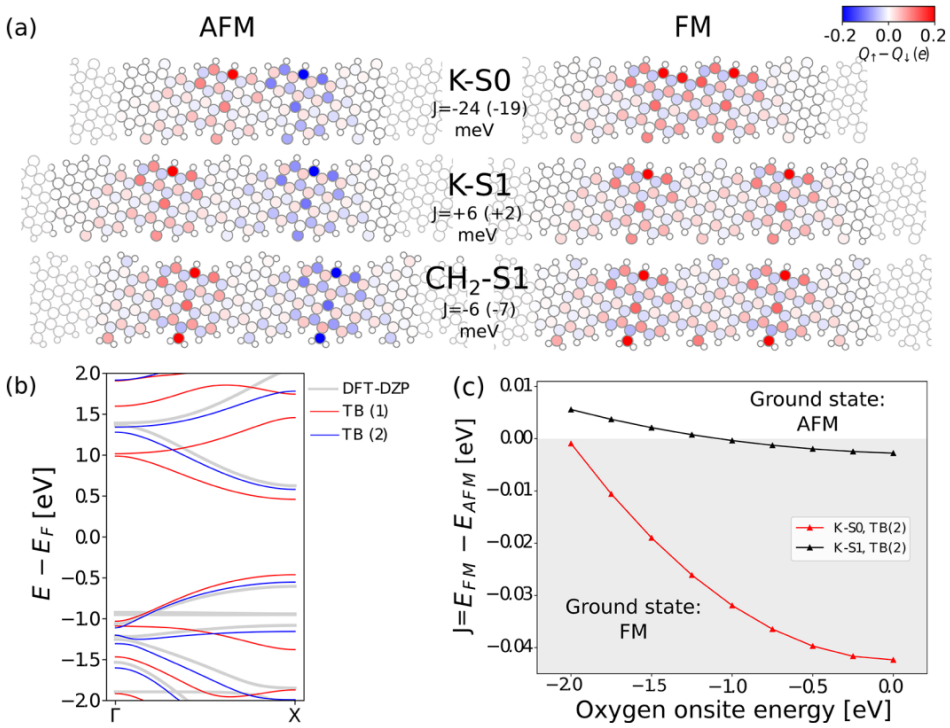

Figure 7.7: Modeling of radical pairs. (a) Spin-polarized LDOS distribution of radical states as calculated by DFT and J (MFH-TB(2) values are shown in parentheses) in K-S0, K-S1, and CH2-S1 (all oxygen atoms are replaced by CH2), respectively. (b) Band structures of intact K-chGNR, acquired from DFT, MFH-TB(1), and MFH-TB(2), respectively. (c) MFH-TB calculated J in K-S0 and K-S1 as a function of oxygen onsite energy in TB(2). The onsite Coulomb repulsion in MFH was set to U = 3 eV

alignment is unequivocally related to the oxygen atom rather than to the mere presence of an extra p_z electron there, exposing insufficient chemical detail in our simple MFH-TB(1) approach.

In an attempt to make the simple MFH calculations also applicable to these more complicated systems including heteroatoms, we have included modified TB parameters (hopping amplitude and on-site energy) for the oxygen heteroatoms in what we call the model MFH-TB(2). To determine the most appropriate parameters, we compare the calculated band

structures obtained from DFT for fully ketone-functionalized chGNRs to those obtained with our MFH-TB models, Figure 7.7 (b). An improvement of the TB model can be obtained with MFH-TB(2) maintaining for carbon atoms the nearest-neighbor hopping amplitude and on-site energies of 2.7 and 0 eV, respectively, but changing the values to 3.8 and -1.5 eV for oxygen atoms bonded to carbon. Qualitatively the increased hopping amplitude on the C=O bonds can be directly related to its shorter length and the nonzero on-site energy to the increased electronegativity of oxygen. The exchange coupling in radical pairs (both strength and sign) is strongly affected by these two parameters, as depicted for the on-site energy in Figure 4c for K-S0 and K-S1. Applying this optimized model now correctly predicts a preferred AFM alignment for K-S1. Furthermore, MFH-TB(2) also corrects the other wrong predictions of the MFH-TB(1) model, as is the open-shell character of the P-O0 and K-O0 radical pairs and provides for all calculated structures J values very similar to DFT calculations (see Table 1). Altogether, we hereby provide a simple yet accurate parametrization to model these more complex systems beyond pure hydrocarbon structures.

It is worth noting that the insight provided in this work about the pairwise interaction between radicals can be extended also to systems with an increasing number of spins and ultimately even to spin chains. By way of example, three P-S2 radical states in a row, Figure 7.8(a) reveal a clearly broader zero-bias resonance at the central radical (blue data, HWHM = 9 meV, Figure 7.8(b)) as compared to the two outer ones (black and red data, HWHM = 7 meV). For this geometry, the three spins are ferromagnetically coupled, leading to a ground state S = 3/2 with two distinct spin-flip excitations to the S = 1/2 manifold. Theoretical simulations of the corresponding inelastic dI/dV features (Figure 5b, dashed

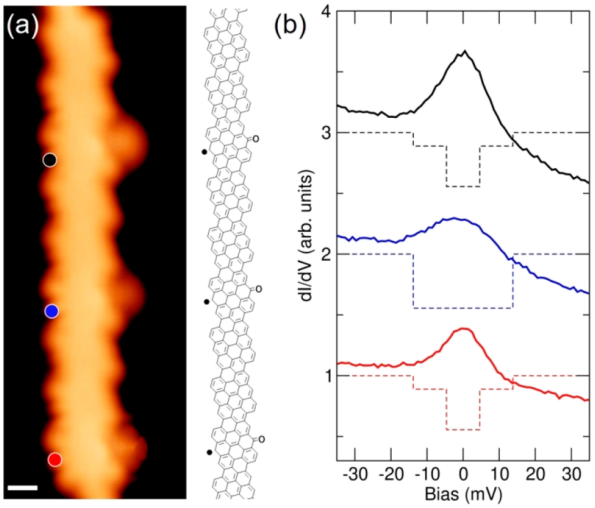

Figure 7.8: (a) STM image (U = -100 mV; I = -1 nA) showing a P-chGNR with three P-S2 radicals in a row, together with the corresponding chemical structure. The scale bar is 5 Å. (b) Vertically offset dI/dV spectra (solid lines) obtained at the marked positions in (a), along with the simulated inelastic electron tunneling spectroscopy (dashed lines) for this three-radical spin system. The exchange energy J = -2.3 meV, as derived from P-S2 in experiments, is used for the simulation.

lines) reveal that only the high-energy excitation contributes at the central radical, whereas the outer sites exhibit predominantly the low-energy steps. Although a clear identification of these inelastic transitions in our spectra is hindered by the low energies involved, along with a relatively broad Kondo signal, these calculations are consistent with the experiment and the broader peak at the central spin in Figure 7.8 (b). This finding is also in line with the previous work from DiLullo et al.,[286] where the central site on a molecular Kondo chain was found to exhibit a larger resonance width than those at the termini. Although the spins in that case were aligned antiferromagnetically, the same argument actually holds.

7.4 Conclusions

In summary, we have characterized the magnetic interactions between radical pairs of diverse geometries hosted by two different types of chGNRs, with and without ketone functionalization at their edges. As confirmed by both experiments and theoretical calculations, the exchange coupling between two radicals shows remarkably large variations depending on their relative location on the same or opposite sides of the GNRs, on the spatial distance between them, on the chiral asymmetry, as well as on the structure of the GNR surrounding the magnetic state. These results thus provide valuable information on the potential use in the design of graphene-based spin chains and networks with tunable magnetic structures. Furthermore, we demonstrated their modeling by the widely used MFH approximation through a minimal extension to these systems of increased complexity including oxygen heteroatoms, which may greatly expedite the understanding and engineering of GNR-based structures in the future.

CHAPTER 8

Conclusions and outlook

This thesis comprehends four years' worth of work on the study of graphene nanoribbons. The lab work has mainly focused on the use of a LT-STM for the sample characterization, occasionally complemented by nc-AFM or XPS for chemical sensitivity. Multiple softwares helped with data analysis: WSXM[287] and Gwyddion[288] for image processing; SPMImage Tycoon[289] and Scan Inspector for file management. XPS data was fitted with CasaXPS.[290] For the general spectroscopic analysis, statistics, and data processing, Python 3.11 was run in a Jupyter lab 3.6 environment. Experimental data were supported with theoretical simulations, mainly DFT, but also tight-binding for modellization and MR-AQCC for more precise open-shell calculations.

This dissertation performed a transversal research, including a study about the chemical synthesis of GNR (chapter 3) and their electronic properties and the presence of magnetic states (chapter 4). It includes an assessment of the reactivity of GNR zigzag edges (chapter 5) and protection strategies towards their applicability (chapter 6), to finalise with a study of the coupling of magnetic states hosted by the ribbons, and how distance, chirality and conjugation affect them (chapter 7). The conclusions are diverse and they have a wide variety of future implications:

Chapter 3: An in-depth study of the 5-aGNR synthesis that provided information about their growth mechanism. STM/AFM data resulted in the identification of an unreported metal-organic intermediate after dehalogenation, a unique mediator for an Au(111) polimerization. Temperature-dependent XPS measurements revealed the coexistence of precursor, metal-organic and ribbons; a unique mixture resulting in surprisingly straight aGNRs. The reason beneath is captivating: An unreported concerted dehydrogenation+CDH, alter-

native to the Ullmann coupling. This pathway is forced by the precursor's planarity and rigidity, that hinder the formation of the polymer. The preference towards a thermodynamically favoured product suggest hot-deposition as a key for a better yield in this reaction.

Chapter 4: We shed some light on the electronic structure of the 5-aGNR. The bandgap was adressed around 0.85 eV on Au(111), matching the most precise predictions.[108] The states observed previously around Fermi have been identified as end states: Hybridize in a bonding-antibonding couple for short ribbons, and spin-split states as they grow longer than 14 unit cells. Their magnetism was probed by gating and transport measurements were performed, obtaining a β=0.94±0.1 nm^{-1}. These results match again the 5-aGNR with the most precise calculations for periodic ribbons. The identification of end states proves the relaxation of the 5-aGNR towards a topological regime, and points towards the rest of the 3p+2 family as unique study cases for solid state physics. Our theoretical study of the effect of different parameters as edge charge and stretching in the bandgap and topology of the ribbons suggests a variety of strategies for modifying their properties.

Chapter 5: Previous hints of the zigzag edges reactivity drive us to experiment with the exposure of chiral GNR to various ambient reagents. The ribbons showed to be reactive against water and oxygen, with different results. Water attacked the zigzag segments in alternating unit cells, to form Csp^3, in a reduction reversible by annealing and tip manipulation. Nevertheless, oxygen oxidizes the ribbons drastically. The consequences of the proven GNR stability affect the whole field of graphene derivatives, and suggest that further protection will be necessary for their application in industry.

Chapter 6: We designed and tested two protection strategies. One based on hydrogenation, another based on the protection of zigzag edges with ketone groups. The latter recovered their pristine structure after hydrogenation + annealing, while the former just required from annealing in order to planarize. Both showed resistance to the atmospheric attack, plus the ketone graphene nanoribbons showed an increased bandgap due to their lower conjugation. Both strategies could be plausible alternatives for graphene derivatives which require from atmospheric transfer during their application in devices or other experiments, as they are transferable to different materials.

Chapter 7: The residual defects, caused by ketones on pristine ribbons/vacants on ketone ribbons, stabilize radicals on the chiral GNR. Those radicals couple when they are close enough. The comparison between them allowed to study the effect of the distance, chirality and ribbon modification. It is the best example of how radicals extend less on a less conjugated ribbon. The radical coupling could be recreated satisfactory by tight-binding. It required from different hopping constants and on-site energy for carbon and oxygen. The values found can be employed on future models of carbon+oxygen conjugated structures. Still, this work is a seminal test for the synthesis of spin chains by punctual addition of chemical derivatives to the precursors.

These experiments are not isolated, but their research lines could progress in different ways: There are still many things to understand from the new reaction mechanism discovered. The chemical substitution of terminal hydrogens by other groups (3,10-difluoro-2,9-dibromoperylene) or the bromines (3,10-difluoroperylene)[291] could affect the required temperature or hinder the formation of an Au intermediate. On the other hand, it would be

interesting to look for other precursors capable of such reactivity. Rigid derivatives of well-known reactives may undergo this mechanism (7,14-dibromobisanthene for 7-aGNR) with interesting metal organic chemistry underneath. However, there are many things to explore in the already synthesized 5-aGNR: We propose the transfer of 5-aGNR to a device capable of doing transport measurements, while mechanically stretching the material in order to force a topological transition, what would place them as valuable strain-sensitive semiconductors for industry. The chemical modification of the armchair edges with charge-withdrawal groups (Fl, OH) may cause the 5-aGNR to become trivial, as our theory suggested. Other strategy would be the synthesis of 5-aGNR from a different precursor with a shifted unit cell and trivial topology. To end with these ribbons, we planned to deposit/transfer them to a semiconductor substrate with a lower workfunction, in order to study their neutral charge state.

On the other hand, the discovery of the 3,1-chGNR reactivity hints a general reactivity for any zigzag edge of a nanographene. Future experiments aim to demonstrate this on other ribbons or graphene flakes, to claim the influence of its reactivity. However, the experiments were done on Au(111). We would like to discard the catalytic effect of the substrate as the reason of the oxidation by transferring ribbons to a different substrate and repeating the exposures. In addition to that, the high reactivity of the ribbons could be exploitable for the design of gas sensors, strategy that is being tested by the group. Other collaborators suggested the potential of the ribbons as catalyzers for water splitting in the energy storage field, what could generate "green hydrogen" with industrial applications. On the other hand, the protection strategies are general for any graphene material, specially

the hydrogenation could be applied in most of the cases. For the case of the ketone, the capacity to reduce them at will is a useful chemical tool that we have already exploited.[130] The radical coupling in ribbons has been an open topic for years.[235] The synthesis of precursors with CH_2/ C=O opposed edges would allow to turn on the metallic states at will by tip manipulation or annealing, what could allow for their ambient transfer before application. These are the short-term applications of our experiments. Nevertheless, their future applications are unpredictable. Paraphrasing Franklin: Who knows the use of an infant?[292]

Other parallel experiments performed during this period are not included for being out of the topic.[293, 245, 194] However, all of them benefited from the experience acquired during GNR experiments.[130] Every experiment included in this dissertation brought light to insights of graphene nanoribbon science. We discovered a new reaction pathway,[195] and unveiled the physics of the 3p+2 GNR family.[186] We found out the relation between reactivity and GNR zigzag segments,[254] and developed strategies to circumvent it,[179] as well as a way of exploiting their punctual defects and magnetism.[253] We have developed in depth our comprehension of the graphene nanoribbon science by answering some questions. Many more have sprouted in the way. All in all, that is a good sign of a satisfactory research.

8.1 Thesis-related publications

-A. Berdonces-Layunta,* F. Schulz,* F. Aguilar-Galindo, J. Lawrence, M. S. G. Mohammed, M. Muntwiler, J. Lobo-Checa, P. Liljeroth, and D. G. de Oteyza, “Order from a Mess: The Growth of 5-Armchair Graphene Nanoribbons,” ACS Nano, vol. 15, no. 10, pp. 16 552–16 561, Oct. 2021. Available: *10.1021/acsnano.1c06226*

-J. Lawrence,* P. Brandimarte,* A. Berdonces-Layunta, M. S. G. Mohammed, A. Grewal, C. C. Leon, D. Sánchez-Portal, and D. G. de Oteyza, “Probing the Magnetism of Topological End States in 5-Armchair Graphene Nanoribbons,” ACS Nano, vol. 14, no. 4, pp. 4499–4508, Apr. 2020. Available: *10.1021/acsnano.9b10191*

-Alejandro Berdonces-Layunta,* Adam Matej,* James Lawrence, Mohammed S. G. Mohammed, Tao Wang, Manuel Vilas-Varela, Reed Nieman, Hans Lischka, Dana Nachtigalova, Diego Peña, Pavel Jelínek, and D. G. de Oteyza, "The Effect of Water on Gold Supported Chiral Graphene Nanoribbons: Rupture of Conjugation by an Alternating Hydrogenation Pattern". Submitted.

-A. Berdonces-Layunta, J. Lawrence, S. Edalatmanesh, J. Castro-Esteban, T. Wang, M. S. G.Mohammed, L. Colazzo, D. Pe na, and P. Jel ınek, “Chemical Stability of (3,1)-Chiral Graphene Nanoribbons,” ACS Nano, p. 8, 2021 *10.1021/acsnano.1c00695*

-J. Lawrence,* A. Berdonces-Layunta,* S. Edalatmanesh, J. Castro-Esteban, T.

Wang, A. Jimenez-Martin, B. de la Torre, R. Castrillo-Bodero, P. Angulo-Portugal, M. S. G. Mohammed, A. Matˇej, M. Vilas-Varela, F. Schiller, M. Corso, P. Jelinek, D. Pe na, and D. G. de Oteyza, “Circumventing the stability problems of graphene nanoribbon zigzag edges,” Nature Chemistry, Sep. 2022. Available: *10.1038/s41557-022-01042-8*

-T. Wang, S. Sanz, J. Castro-Esteban, J. Lawrence, A. Berdonces-Layunta, M. S. G. Mohammed, M. Vilas-Varela, M. Corso, D. Pe na, T. Frederiksen, and D. G. de Oteyza, “Magnetic Interactions Between Radical Pairs in Chiral Graphene Nanoribbons,” Nano Letters, vol. 22, no. 1, pp. 164–171, Jan. 2022. Available: *10.1021/acs.nanolett.1c03578*

8.2 Publications from PhD time but thesis-unrelated

-N. Merino-Díez, A. Pérez Paz, J. Li, M. Vilas-Varela, J. Lawrence, M. S. G. Mohammed, A. Berdonces-Layunta, A. Barragán, J. I. Pascual, J. Lobo-Checa, D. Peña, D. G. de Oteyza, "Hierarchy in the Halogen Activation During Surface-Promoted Ullmann Coupling" ChemPhysChem 2019, 20, 2305. Available: *10.1002/cphc.201900633*

-N. Merino-Díez, M. S. G. Mohammed, J. Castro-Esteban, L. Colazzo, A. Berdonces-Layunta, J. Lawrence, J. I. Pascual, D. G. de Oteyza, and D. Pe na, “Transferring axial molecular chirality through a sequence of on-surface reactions” Chemical Science, vol. 11, no. 21, pp. 5441–5446, 2020. Available: *10.1039/D0SC01653E*

-T. Wang, Y. Pan, W. Zhang, J. Lawrence, M. S. G. Mohammed, J. Huang, L.

Feng, Al. Berdonces-Layunta, D. Han, Q. Xu, X. Wu, S. L. Tait, D. G. de Oteyza, and J. Zhu (2020). "On-Surface Synthesis of a Five-Membered Carbon Ring from a Terminal Alkynyl Bromide: A [4+ 1] Annulation." The Journal of Physical Chemistry Letters, 11(15), 5902-5907. Available: *10.1021/acs.jpclett.0c01483*

-M. S. G. Mohammed, J. Lawrence, F. García, P. Brandimarte, A. Berdonces-Layunta, D. Pérez, D. Sánchez-Portal, D. Peña, D. G de Oteyza. "From starphenes to non-benzenoid linear conjugated polymers by substrate templating" Nanoscale Advances, 3(8), 2351-2358 Available: *10.1039/D1NA00126D*

-T. Wang, J. Lawrence, N. Sumi, R. Robles, J. Castro-Esteban, D. Rey, M.S.G. Mohammed, A. Berdonces-Layunta, N. Lorente, D. Pérez, D. Peña, M. Corso, D. G de Oteyza. "Challenges in the synthesis of corannulene-based non-planar nanographenes on Au (111) surfaces." Phys. Chem. Chem. Phys., 2021,23, 10845-10851. Available: *10.1039/D1CP01212F*

-J. Lawrence, M.S.G. Mohammed, D. Rey, F. Aguilar-Galindo, A. Berdonces-Layunta, D. Peña, and D. G. de Oteyza, “Reassessing Alkyne Coupling Reactions While Studying the Electronic Properties of Diverse Pyrene Linkages at Surfaces,” ACS Nano, vol. 15, no. 3, pp. 4937–4946, Mar. 2021. Available: *10.1021/acsnano.0c09756*

-J. Holec, B. Cogliati, J. Lawrence, A. Berdonces-Layunta, P. Herrero, Y. Nagata, M. Banasiewicz, B. Kozankiewicz, M. Corso, D. G. Oteyza, A. Jancarik, and A. Gourdon, “A Large Starphene Comprising Pentacene Branches,” Angewandte Chemie International Edition, vol. 60, no. 14, pp. 7752–7758, Mar. 2021. Available: *10.1002/anie.202016163*

-T. Wang,* A. Berdonces-Layunta,* N. Friedrich, M. Vilas-Varela, J. P. Calupitan, J. I. Pascual, D. Peña, D. Casanova, M. Corso, and D. G. de Oteyza, “Aza-Triangulene: On-Surface Synthesis and Electronic and Magnetic Properties,” Journal of the American Chemical Society, vol. 144, no. 10, pp. 4522–4529, Mar. 2022. Available: *10.1021/jacs.1c12618*

-P Herrero-Gómez, J. P. Calupitan, M. Ilyn, A. Berdonces-Layunta...K. Woodruff, N. Yahlali. "Ba^{2}+ ion trapping by organic submonolayer: towards an ultra-low background neutrinoless double beta decay detector." Nat Commun 13, 7741 (2022) Available: *10.1038/s41467-022-35153-0*

-J. P. Calupitan, T. Wang, A. Pérez Paz*, B. Álvarez, A. Berdonces-Layunta, P. Angulo-Portugal, R. Castrillo-Bodero, F. Schiller, D. Peña, M. Corso, D. Pérez, and D. G. de Oteyza. "Room-Temperature C–C -Bond Activation of Biphenylene Derivatives on Cu(111)." J. Phys. Chem. Lett. 2023, 14, 4, 947–953 Available: *10.1021/acs.jpclett.2c03346*

*Shared authorship.

APPENDIX A

C1s XPS: analysis and interpretation

The starting considerations include our experimental observation of a metal-organic intermediate within a limited temperature range. However, as readily extracted from our SPM experiments, even within the right temperature window the number of molecules forming the metal-organic intermediate is limited, coexisting with the other molecular species. Since only two atoms per precursor molecule coordinate at most to metal atoms, the stoichiometric ratio of these carbon species is extremely limited throughout the whole growth process. Below we describe the different approaches that have been followed to fit the C 1s spectra.

First approach: Precursor and ribbons.

As a starting point, we have fitted the spectra associated to as-deposited molecules and to the GNRs, as extracted from the first and last spectra during our temperature ramp. For the as-deposited molecules the carbon signal was modelled with three components based on theoretical core level energy calculations. The carbons bonded to hydrogen (C-H) are the lowest in energy. Then, the fully substituted inner Carbons (C-C). The highest binding energy is displayed by those carbons attached to Br (C-Br). The ratio between the components was fixed according to the molecule's stoichiometry (C-H)/(C-C)/(C-Br) = 10/8/2. Parameters like shape, Full-Width Half Minimum (FWHM), relative and absolute position of the peaks were optimized to get the best possible fit. The resulting fit provides notable differences in the FWHM of each of the components, which are in qualitative agreement with the energy spread theoretically predicted for the core levels within each group (see Fig. 4c in main text). For the GNRs the calculations predict two different groups of carbons, one for the external C-H carbons and one for the internal ones. In this case, the ratio C-H/C-C depends on the average length of the fully grown GNRs according to $ratio(\frac{CH}{CC}) = \frac{N+1}{3N-2}$; where N is the number of precursor units. As a result, we can estimate the average ribbon length from the fitted C-H/C-C ratio.

In spite of the highly asymmetric line shape of the spectra, each of the fitting components is maintained symmetric. Although asymmetric peaks have been used in the study of GNRs earlier, we believe that their use is not really justified here, because the bandgap of these GNRs prevents the low energy excitations that are normally imposed to justify the high binding energy "tails" of the core level peaks.

Within our first approach, the fitting of all spectra consisted in a linear com-

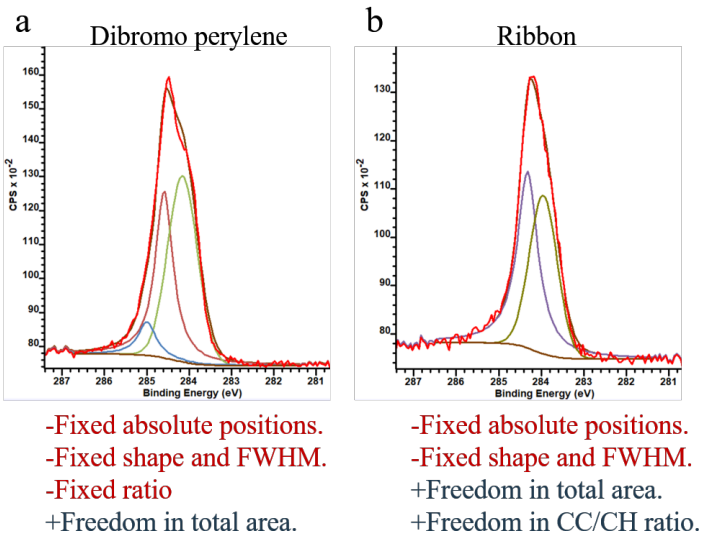

Figure A.1: Sample spectra for the two reference situations, namely as-deposited molecules (a) and fully reacted GNRs (b), along with the reference fits employed for the rest of the spectra.

bination of the components associated to reactants and to GNRs. In the figure A.1 we include sample spectra for the two reference situations, along with a list of the free and fixed parameters that the system could modify.

With these three degrees of freedom, the resulting fit seemed to follow the expected tendency. However, two main problems arise:

-The temperature window of active reactivity is poorly fitted, in particular at the low binding energy side (See Figure A2). -The ratio between the peaks of the ribbon exceeds the limits $f(\frac{CH}{CC}) = 1 \leq r \leq 0.66$

Second approach: Addition of the metal-organic

To overcome the inconsistencies obtained from the previous fitting approach, we

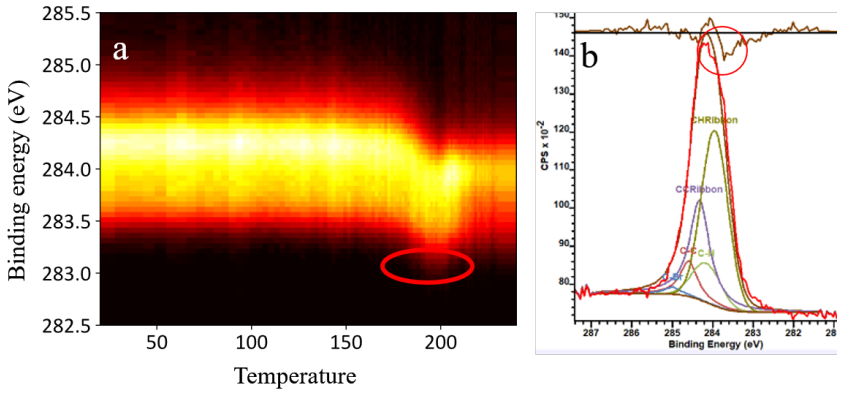

Figure A.2: The first fitting approach failed in addressing the C 1s signal under 284 eV. It caused a systematic error and an impossible CH/CC ratio.

tried adding the metal-organic signal to fill the gaps left by the other two compounds. The signal associated to DBP and ribbons, as fitted in the first and last spectra, is maintained. For the metal-organic, we employed the less reliably fit spectra from the previous approach, which was assumed to contain the largest metal-organic contribution. The relative energies for the C-C/C-H components of the metal-organic molecules have been maintained as in the previous cases. A lower binding energy for a metal-organic may be justified by a significant inductive effect caused by the Au atom. To be consequent, we placed the coordinated carbon peak (C-Au) at lower binding energies, as the literature conventionally does for the other coinage metals (Ag, Cu), although contradicting the core level energies obtained from our DFT calculations, at figure 3.6(c). Representative sample spectra of the three different scenarios during the temperature ramp are displayed in figure A.3, along with the parameters that are fitted or fixed, respectively.

With this new variable, the fitting improves, but the temperature-dependent amount of each component, figure a.4 shows an unreasonable evolution with the (metal-

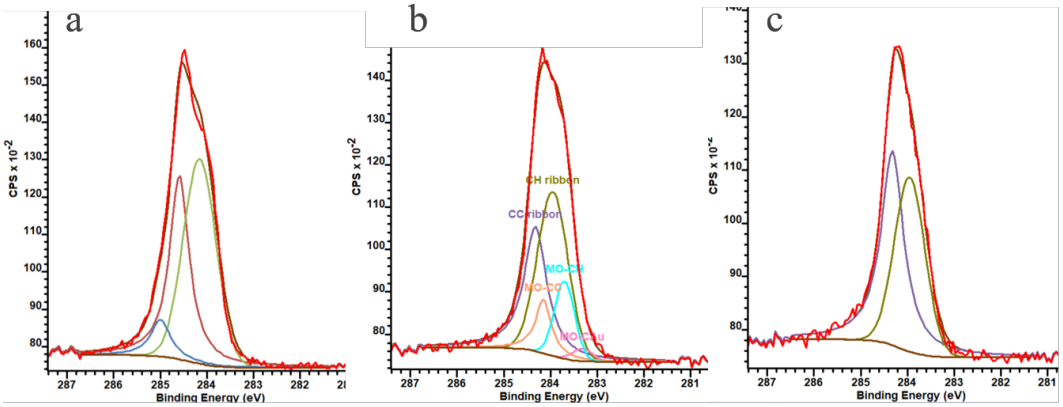

Figure A.3: Degrees of freedom and conditions of the new fitting.

organic) intermediate, since it maximizes with the (GNR) final product, instead of before. We therefore also discarded these fitting results.

Third approach: Addition of the Br-associated work function modulation.

The discrepancies on the low binding energy side obtained with our first fitting approach, figure A.2, may also be an effect of the atomic Br on the local work function. In a new approach, we proceed fitting with a linear combination of as-deposited molecules and GNRs, in combination with a work function modulation that correlates with the concentration of atomic Br on the metal surface. Such optimal fitting result corrected the inconsistencies or deficiencies from the previous two approaches.

We estimate the shift in the local work function analyzing the DBP Br signal, which displays the following advantages: it is associated with unchanged molecules and can

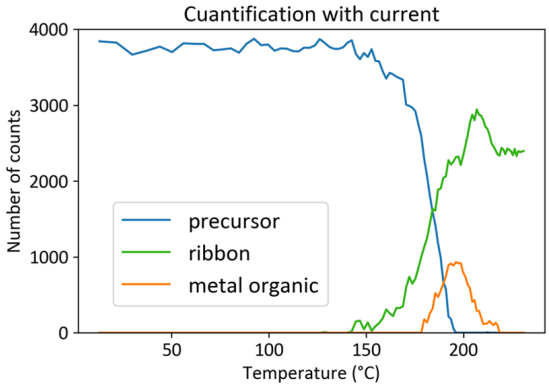

Figure A.4: Temperature-dependent evolution of the relative amounts of as-deposited, metal-organic and GNR molecules, as obtained within this second fitting approach including the metal-organic species.

therefore be associated to work function modifications, it can be followed univocally along the reaction and, being bound to the molecular carbon backbone, the effect on the carbon atoms can be assumed to be similar. Figure S11a shows the rigid shift of the DBP Br doublet during the temperature ramp, whereas figure 3.5(b) shows its linear correlation with the concentration of atomic Br on the surface. With this correlation at hand, we can estimate the associated shift of the carbon core levels throughout the temperature ramp, as plotted in figure 3.5(c), and apply it to the fitting of the temperature-dependent spectra. This fitting satisfies the check conditions offered by the freedom degrees left: The progression of the two species are reasonable, plus the ratio of the GNR peaks grows progressively within realistic ratios ($f(\frac{CH}{CC}) = 1 \leq r \leq 0.66$), figure 3.7(b).

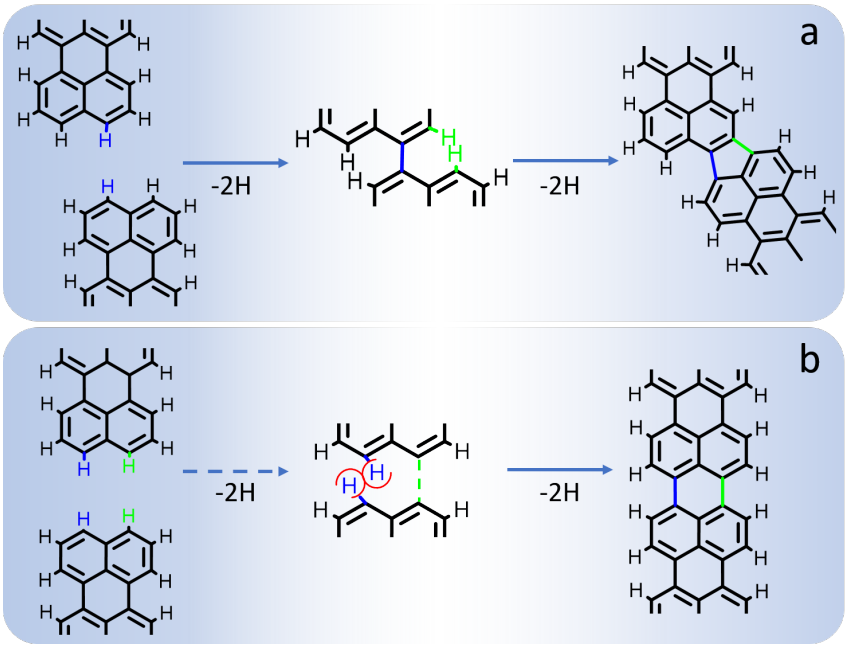

Figure A.5: Proposed mechanism for the halogen-free molecular coupling.[196] There is an expected two-step mediated reaction. With submonolayer coverages, the reaction is regioselective towards their kinked fusion (a), kinetically determined due to the steric hindrance in the straight reaction pathway (b).

APPENDIX B

Chiral graphene nanoribbons

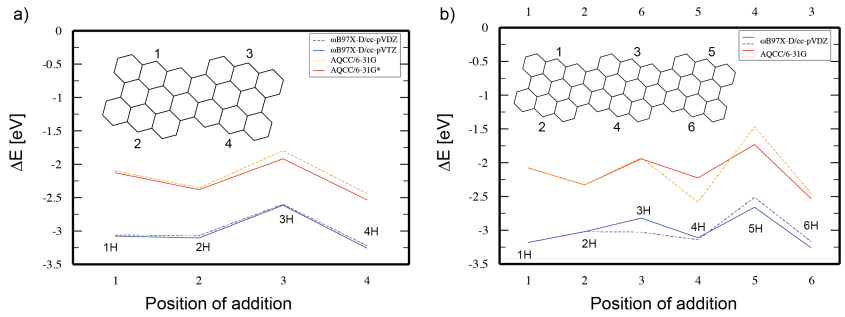

Figure B.1: Comparison between DFT and MR-AQCC methods calculating relative energies of hydrogenation steps on dimer (a) and trimer (b), obtained as energy difference of products and reactants (energy of hydrogen radical included). Overlays illustrate positions of hydrogenation on the ribbons, numbering corresponds to x axes. Steps in panel (a) are consecutive, with 1-4 hydrogens added to dimer, resulting in fully hydrogenated ribbon. In panel (b), two sequences of hydrogenation are illustrated. Bottom x axis (solid lines) illustrates sequential hydrogenation, while top axis (dashed lines) illustrates hydrogenation of termini and subsequent hydrogenation of middle unit. Blue and violet curves represent DFT; red and orange stand for MR-AQCC method. For active spaces used in AQCC calculations see Methods.

		GNR length					
		2	3	4	5	6	7
DFT	HONO	1.63	1.57	1.54	1.53	1.52	1.52
	LUNO	0.37	0.43	0.46	0.47	0.48	0.48
	y_0	0.100	0.143	0.163	0.173	0.180	0.184
MR-AQCC	HONO	1.52	1.54				
	LUNO	0.48	0.47				
	y_0	0.181	0.170				

Table B.1: Natural orbital occupation numbers and calculated diradical character with increasing length of GNR. For computational details see Methods.

APPENDIX C

Spectroscopic details of 3,1-chGNR radicals

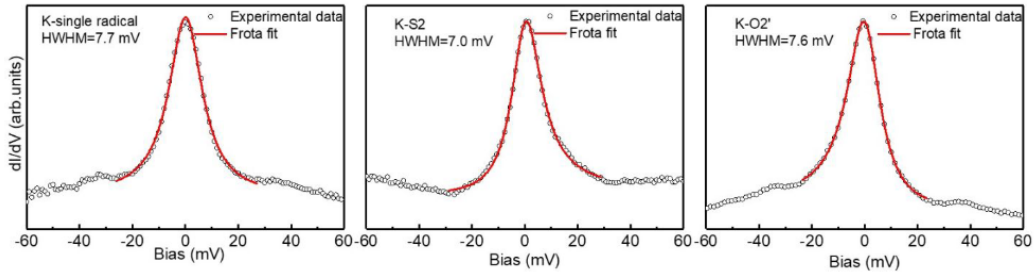

Figure C.1: Comparison between Kondo peaks of K-chGNR with a single radical, K-S2 and K-O2'. Similar HWHMs are obtained by fitting the three peaks with a Frota function. All the spectra were acquired with CO functionalized probes.

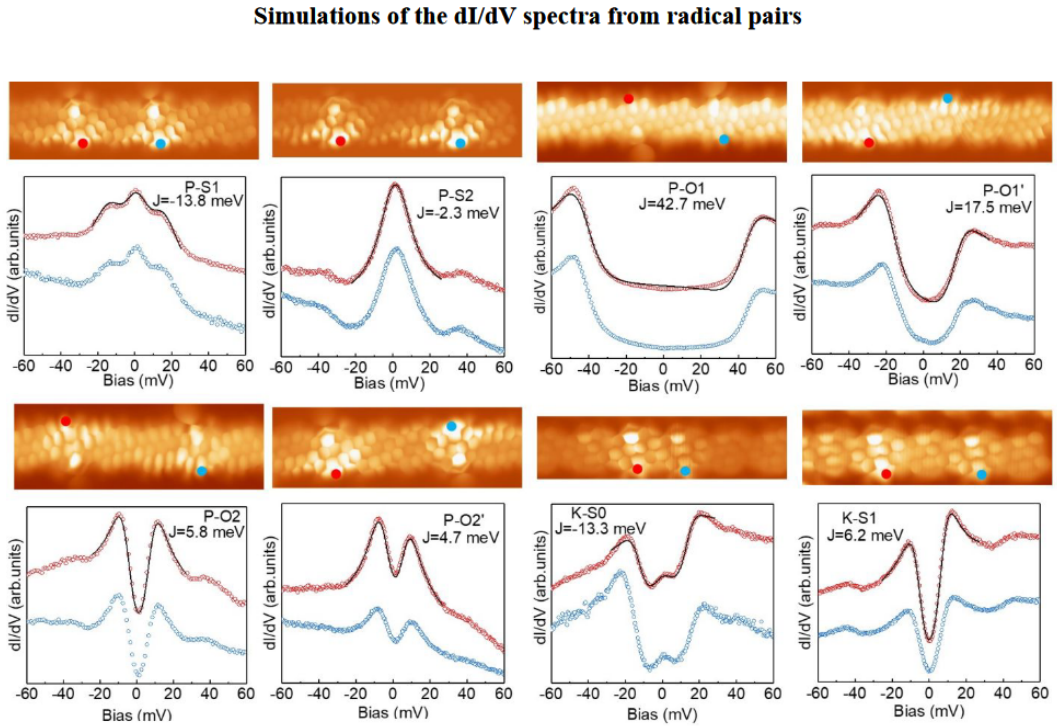

Figure C.2: Comparison between simulated (black) and measured (red and blue) spectra taken for coupled radicals in defective chGNRs. We have chosen the red spectra for the simulation using the code from M. Ternes.[284] The simulated spectra (black lines) are overlaid on the red spectra. In each case the J values obtained from the fitting is written alongside with the radical pair type. All the scale bars in the STM images are 0.5 nm.

Simulation of K-S1 by a FM ground state

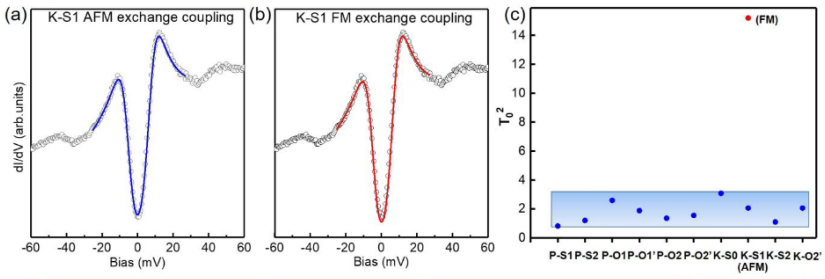

(d)

Coupling type	Bias	Current	T_0^2
P-S1	-60 mV	1.2 nA	0.82
P-S2	-60 mV	1.5 nA	1.20
P-O1	-60 mV	0.8 nA	2.59
P-O1'	-60 mV	1.6 nA	1.88
P-O2	-60 mV	1 nA	1.36
P-O2'	-60 mV	1.9 nA	1.55
K-S0	-60 mV	1 nA (using a same tip as K-S1)	3.08
K-S1 (AFM)	-60 mV	1 nA	2.06
K-S1 (FM)	-60 mV	1 nA	**15.2**
K-S2	-60 mV	1 nA	1.10
K-O2'	-60 mV	1.1 nA	2.06

Figure C.3: (a,b) Simulations of K-S1 by AFM and FM ground states respectively, using the code from Ternes.9[284] (c) Tunnel barrier transmission coefficient T_0^2 values of all the spin coupling cases observed in experiments, including both FM and AFM coupling of K-S1, acquired from the simulations in (a,b). The T_0^2 value FM KS1 obviously exceeds its reasonable range (the blue frame) as obtained from other cases. (d) The correlated bias and current values used for dI/dV measurement as well as T_0^2 values for each case. Since the currents for all the cases are similar, the obtained T02 values should be also similar. However, the T_0^2 value from FM coupled K-S1 is abnormally high, thus the possibility can be excluded.

BIBLIOGRAPHY

[1] G. Binnig and H. Rohrer, "Scanning tunneling microscopy—from birth to adolescence," *Reviews of Modern Physics*, vol. 59, no. 3, pp. 615–625, Jul. 1987. [Online]. Available: https://link.aps.org/doi/10.1103/RevModPhys.59.615

[2] G. Binnig, H. Rohrer, C. Gerber, and E. Weibel, "Surface Studies by Scanning Tunneling Microscopy," *Physical Review Letters*, vol. 49, no. 1, pp. 57–61, Jul. 1982. [Online]. Available: https://link.aps.org/doi/10.1103/PhysRevLett.49.57

[3] R. Young, J. Ward, and F. Scire, "The Topografiner: An Instrument for Measuring Surface Microtopography," *Reviews of Modern Physics*, vol. 43, no. 7, pp. 999–1011, Jul. 1972.

[4] K. S. Novoselov, A. K. Geim, S. V. Morozov, D. Jiang, Y. Zhang, S. V. Dubonos, I. V. Grigorieva, and A. A. Firsov, "Electric Field Effect in Atomically Thin Carbon Films," *Science*, vol. 306, no. 5696, pp. 666–669, Oct. 2004. [Online]. Available: https://www.science.org/doi/10.1126/science.1102896

[5] Y. Yano, N. Mitoma, H. Ito, and K. Itami, "A Quest for Structurally Uniform Graphene Nanoribbons: Synthesis, Properties, and Applications," *The Journal of Organic Chemistry*, vol. 85, no. 1, pp. 4–33, Jan. 2020. [Online]. Available: https://pubs.acs.org/doi/10.1021/acs.joc.9b02814

[6] G. Lee and K. Cho, "Electronic structures of zigzag graphene nanoribbons with edge hydrogenation and oxidation," *Physical Review B*, vol. 79, no. 16, p. 165440, Apr. 2009. [Online]. Available: https://link.aps.org/doi/10.1103/PhysRevB.79.165440

[7] S. Wang, L. Talirz, C. A. Pignedoli, X. Feng, K. Müllen, R. Fasel, and P. Ruffieux, "Giant edge state splitting at atomically precise graphene zigzag edges," *Nature Communications*, vol. 7, no. 1, p. 11507, Sep. 2016. [Online]. Available: http://www.nature.com/articles/ncomms11507

[8] M. Corso, E. Carbonell-Sanromà, and D. G. de Oteyza, "Bottom-Up Fabrication of Atomically Precise Graphene Nanoribbons," in *On-Surface Synthesis II*, D. G. de Oteyza and C. Rogero, Eds. Cham: Springer International Publishing, 2018, pp. 113–152, series Title: Advances in Atom and Single Molecule Machines. [Online]. Available: http://link.springer.com/10.1007/978-3-319-75810-7_6

[9] J. P. Llinas, A. Fairbrother, G. Borin Barin, W. Shi, K. Lee, S. Wu, B. Yong Choi, R. Braganza, J. Lear, N. Kau, W. Choi, C. Chen, Z. Pedramrazi, T. Dumslaff, A. Narita, X. Feng, K. Müllen, F. Fischer, A. Zettl, P. Ruffieux, E. Yablonovitch, M. Crommie, R. Fasel, and J. Bokor, "Short-channel field-effect transistors with 9-atom and 13-atom wide graphene nanoribbons," *Nature Communications*, vol. 8, no. 1, p. 633, Dec. 2017. [Online]. Available: http://www.nature.com/articles/s41467-017-00734-x

[10] P. B. Bennett, Z. Pedramrazi, A. Madani, Y.-C. Chen, D. G. de Oteyza, C. Chen, F. R. Fischer, M. F. Crommie, and J. Bokor, "Bottom-up graphene nanoribbon field-effect transistors," *Applied Physics Letters*, vol. 103, no. 25, p. 253114, Dec. 2013. [Online]. Available: http://aip.scitation.org/doi/10.1063/1.4855116

[11] P. Ruffieux, S. Wang, B. Yang, C. Sánchez-Sánchez, J. Liu, T. Dienel, L. Talirz, P. Shinde, C. A. Pignedoli, D. Passerone, T. Dumslaff, X. Feng, K. Müllen, and R. Fasel, "On-surface synthesis of graphene nanoribbons with zigzag edge topology," *Nature*, vol. 531, no. 7595, pp. 489–492, Mar. 2016. [Online]. Available: http://www.nature.com/articles/nature17151

[12] J. Li, S. Sanz, N. Merino-Díez, M. Vilas-Varela, A. Garcia-Lekue, M. Corso, D. G. de Oteyza, T. Frederiksen, D. Peña, and J. I. Pascual, "Topological phase transition in chiral graphene nanoribbons: from edge bands to end states," *Nature Communications*, vol. 12, no. 1, p. 5538, Dec. 2021. [Online]. Available: https://www.nature.com/articles/s41467-021-25688-z

[13] P. A. Held, H. Fuchs, and A. Studer, "Covalent-Bond Formation via On-Surface Chemistry," *Chemistry – A European Journal*, vol. 23, no. 25, pp. 5874–5892, 2017, _eprint: https://chemistry-europe.onlinelibrary.wiley.com/doi/pdf/10.1002/chem.201604047. [Online]. Available: https://chemistry-europe.onlinelibrary.wiley.com/doi/abs/10.1002/chem.201604047

[14] J. Liu, B.-W. Li, Y.-Z. Tan, A. Giannakopoulos, C. Sanchez-Sanchez, D. Beljonne, P. Ruffieux, R. Fasel, X. Feng, and K. Müllen, "Toward Cove-Edged Low Band Gap

Graphene Nanoribbons," *Journal of the American Chemical Society*, vol. 137, no. 18, pp. 6097–6103, May 2015. [Online]. Available: https://pubs.acs.org/doi/10.1021/jacs.5b03017

[15] B. Yang, "Bottom-up synthesis of graphene nanoribbons and nanographene molecules with new types of periphery," Ph.D. dissertation, Johannes Gutenberg University Mainz, 2016. [Online]. Available: https://openscience.ub.uni-mainz.de/handle/20.500.12030/4551

[16] L. Pisani, J. A. Chan, B. Montanari, and N. M. Harrison, "Electronic structure and magnetic properties of graphitic ribbons," *Physical Review B*, vol. 75, no. 6, p. 064418, Feb. 2007. [Online]. Available: https://link.aps.org/doi/10.1103/PhysRevB.75.064418

[17] A. H. Castro Neto, F. Guinea, N. M. R. Peres, K. S. Novoselov, and A. K. Geim, "The electronic properties of graphene," *Reviews of Modern Physics*, vol. 81, no. 1, pp. 109–162, Jan. 2009. [Online]. Available: https://link.aps.org/doi/10.1103/RevModPhys.81.109

[18] K. Wakabayashi, K.-i. Sasaki, T. Nakanishi, and T. Enoki, "Electronic states of graphene nanoribbons and analytical solutions," *Science and Technology of Advanced Materials*, vol. 11, no. 5, p. 054504, Oct. 2010. [Online]. Available: http://www.tandfonline.com/doi/full/10.1088/1468-6996/11/5/054504

[19] K. Wakabayashi, M. Fujita, H. Ajiki, and M. Sigrist, "Electronic and magnetic properties of nanographite ribbons," *Physical Review B*, vol. 59, no. 12, pp. 8271–8282, Mar. 1999. [Online]. Available: https://link.aps.org/doi/10.1103/PhysRevB.59.8271

[20] J. Wang, S. Deng, Z. Liu, and Z. Liu, "The rare two-dimensional materials with Dirac cones," *National Science Review*, vol. 2, no. 1, pp. 22–39, Mar. 2015. [Online]. Available: https://academic.oup.com/nsr/article/2/1/22/2606199

[21] M. Corso, E. Carbonell-Sanromà, and D. G. de Oteyza, "Bottom-Up Fabrication of Atomically Precise Graphene Nanoribbons," in *On-Surface Synthesis II*, D. G. de Oteyza and C. Rogero, Eds. Cham: Springer International Publishing, 2018, pp. 113–152, series Title: Advances in Atom and Single Molecule Machines. [Online]. Available: http://link.springer.com/10.1007/978-3-319-75810-7_6

[22] K. P. C. Vollhardt and N. E. Schore, *Organic chemistry: structure and function.* Macmillan, 2003.

[23] W. L. Wang, O. V. Yazyev, S. Meng, and E. Kaxiras, "Topological Frustration in Graphene Nanoflakes: Magnetic Order and Spin Logic Devices," *Physical Review Letters*, vol. 102, no. 15, p. 157201, Apr. 2009. [Online]. Available: https://link.aps.org/doi/10.1103/PhysRevLett.102.157201

[24] J. Su, M. Telychko, S. Song, and J. Lu, "Triangulenes: From Precursor Design to On-Surface Synthesis and Characterization," *Angewandte Chemie International Edition*, vol. 59, no. 20, pp. 7658–7668, 2020, _eprint: https://onlinelibrary.wiley.com/doi/pdf/10.1002/anie.201913783. [Online]. Available: https://onlinelibrary.wiley.com/doi/abs/10.1002/anie.201913783

[25] O. Exner, "The inductive effect: theory and quantitative assessment," *Journal of Physical Organic Chemistry*, vol. 12, no. 4, pp. 265–274, Apr. 1999. [Online]. Available: https://onlinelibrary.wiley.com/doi/10.1002/(SICI)1099-1395(199904)12:4<265::AID-POC124>3.0.CO;2-O

[26] G. H. Lewes, *The principles of certitude. From the known to the unknown. Matter and force. Force and cause. The absolute in the correlations of feeling and motion. Appendix:*

Imaginary geometry and the truth of axioms. Lagrange and Hegel: the speculative method. Action at a distance. Trübner & Company, 1875, vol. 2.

[27] P. A. Corning, "The re-emergence of "emergence": A venerable concept in search of a theory," *Complexity*, vol. 7, no. 6, pp. 18–30, 2002, _eprint: https://onlinelibrary.wiley.com/doi/pdf/10.1002/cplx.10043. [Online]. Available: https://onlinelibrary.wiley.com/doi/abs/10.1002/cplx.10043

[28] E. D. Schmid and B. Brosa, "Determination of Conjugation and Angle of Twist in Biphenyls by Raman Intensity," *The Journal of Chemical Physics*, vol. 56, no. 12, pp. 6267–6268, Jun. 1972. [Online]. Available: http://aip.scitation.org/doi/10.1063/1.1677191

[29] A. Bedi and O. Gidron, "The Consequences of Twisting Nanocarbons: Lessons from Tethered Twisted Acenes," *Accounts of Chemical Research*, vol. 52, no. 9, pp. 2482–2490, Sep. 2019. [Online]. Available: https://pubs.acs.org/doi/10.1021/acs.accounts.9b00271

[30] A. Bedi, A. Manor Armon, Y. Diskin-Posner, B. Bogosalvsky, and O. Gidron, "Controlling the helicity of -conjugated oligomers by tuning the aromatic backbone twist," *Nature Communications*, vol. 13, no. 1, p. 451, Dec. 2022. [Online]. Available: https://www.nature.com/articles/s41467-022-28072-7

[31] F. Bloch, "Uber die Quantenmechanik der Elektronen in Kristallgittern." p. 46, 1928.

[32] J. Kovac and M. Weisberg, *Roald Hoffmann on the Philosophy, Art, and Science of Chemistry*. Oxford University Press, Feb. 2012. [Online]. Available: https://doi.org/10.1093/oso/9780199755905.001.0001

[33] K. G. Libbrecht, "Physical Dynamics of Ice Crystal Growth," *Annual Review of Materials Research*, vol. 47, no. 1, pp. 271–295, Jul. 2017. [Online]. Available: https://www.annualreviews.org/doi/10.1146/annurev-matsci-070616-124135

[34] S. Mishra, D. Beyer, K. Eimre, S. Kezilebieke, R. Berger, O. Gröning, C. A. Pignedoli, K. Müllen, P. Liljeroth, P. Ruffieux, X. Feng, and R. Fasel, "Topological frustration induces unconventional magnetism in a nanographene," *Nature Nanotechnology*, vol. 15, no. 1, pp. 22–28, Jan. 2020. [Online]. Available: http://www.nature.com/articles/s41565-019-0577-9

[35] J.-P. Malrieu and G. Trinquier, "Communication: Proper use of broken-symmetry calculations in antiferromagnetic polyradicals," *The Journal of Chemical Physics*, vol. 144, no. 21, p. 211101, Jun. 2016. [Online]. Available: http://aip.scitation.org/doi/10.1063/1.4953040

[36] S. Mishra, D. Beyer, K. Eimre, R. Ortiz, J. Fernández-Rossier, R. Berger, O. Gröning, C. A. Pignedoli, R. Fasel, X. Feng, and P. Ruffieux, "Collective All-Carbon Magnetism in Triangulene Dimers**," *Angewandte Chemie International Edition*, vol. 59, no. 29, pp. 12 041–12 047, 2020, _eprint: https://onlinelibrary.wiley.com/doi/pdf/10.1002/anie.202002687. [Online]. Available: https://onlinelibrary.wiley.com/doi/abs/10.1002/anie.202002687

[37] K. Schofield, "The Historical Development of Aromatic Structures," in *Hetero-Aromatic Nitrogen Compounds*. Boston, MA: Springer US, 1967, pp. 3–9. [Online]. Available: http://link.springer.com/10.1007/978-1-4899-5892-1_1

[38] A. L. Lavoisier, M.-A.-P. Lavoisier, J.-M. Papillon, S. Brown, J.-F.-L. Chardon, and G.-J. Cuchet, *Traité élémentaire de chimie : présenté dans un ordre nouveau et d'après les découvertes modernes : avec figures.* A Paris : Chez Cuchet ..., 1789. [Online]. Available: http://archive.org/details/TraiteYeYleYment1Lavo

[39] B. M. J. F. and S. F. Gilbert, *Developmental biology.* Oxford University Press, 2020.

[40] A. Kekulé, "Ueber die s. g. gepaarten Verbindungen und die Theorie der mehratomigen Radicale," *Annalen der Chemie und Pharmacie*, vol. 104, no. 2, pp. 129–150, 1857. [Online]. Available: https://onlinelibrary.wiley.com/doi/10.1002/jlac.18571040202

[41] R. Anschütz, "XIII.—Life and Chemical Work of Archibald Scott Couper," *Proceedings of the Royal Society of Edinburgh*, vol. 29, pp. 193–273, 1909. [Online]. Available: https://www.cambridge.org/core/product/identifier/S0370164600008907/type/journal_article

[42] L. Dobbin, "The couper quest," *Journal of Chemical Education*, vol. 11, no. 6, p. 331, 1934.

[43] A. Kekulé, 1829-1896 (viaf)69046281, "Sur la Constitution des substances aromatiques," *Published in 1865*, 1865, publisher: 1865. [Online]. Available: http://lib.ugent.be/catalog/rug01:001282677

[44] H. E. Armstrong, "Xxviii.—an explanation of the laws which govern substitution in the case of benzenoid compounds," *Journal of the Chemical Society, Transactions*, vol. 51, pp. 258–268, 1887.

[45] E. Bamberger, "Ueber «alicyclische Homologie»," *Berichte der deutschen chemischen Gesellschaft*, vol. 24, no. 1, pp. 1897–1899, Jan. 1891. [Online]. Available: https://onlinelibrary.wiley.com/doi/10.1002/cber.189102401327

[46] J. W. Armit and R. Robinson, "CCXI.—Polynuclear heterocyclic aromatic types. Part II. Some anhydronium bases," *J. Chem. Soc., Trans.*, vol. 127, no. 0, pp. 1604–1618, 1925. [Online]. Available: http://xlink.rsc.org/?DOI=CT9252701604

[47] L. Pauling and G. W. Wheland, "The Nature of the Chemical Bond. V. The Quantum-Mechanical Calculation of the Resonance Energy of Benzene and Naphthalene and the Hydrocarbon Free Radicals," *The Journal of Chemical Physics*, vol. 1, no. 6, pp. 362–374, Jun. 1933. [Online]. Available: http://aip.scitation.org/doi/10.1063/1.1749304

[48] G. W. Wheland and L. Pauling, "A Quantum Mechanical Discussion of Orientation of Substituents in Aromatic Molecules," *Journal of the American Chemical Society*, vol. 57, no. 11, pp. 2086–2095, Nov. 1935. [Online]. Available: https://pubs.acs.org/doi/abs/10.1021/ja01314a017

[49] E. Hückel, "Quantentheoretische Beiträge zum Benzolproblem," *Zeitschrift für Physik*, vol. 70, no. 3, pp. 204–286, Mar. 1931. [Online]. Available: https://doi.org/10.1007/BF01339530

[50] ——, "Quanstentheoretische Beiträge zum Benzolproblem," *Zeitschrift für Physik*, vol. 72, no. 5, pp. 310–337, May 1931. [Online]. Available: https://doi.org/10.1007/BF01341953

[51] ——, “Quantentheoretische Beiträge zum Problem der aromatischen und ungesättigten Verbindungen. III,” *Zeitschrift für Physik*, vol. 76, no. 9, pp. 628–648, Sep. 1932. [Online]. Available: https://doi.org/10.1007/BF01341936

[52] C. Angeli and J.-P. Malrieu, “Aromaticity: an ab Initio Evaluation of the Properly Cyclic Delocalization Energy and the -Delocalization Energy Distortivity of Benzene,” *The Journal of Physical Chemistry A*, vol. 112, no. 45, pp. 11 481–11 486, Nov. 2008. [Online]. Available: https://pubs.acs.org/doi/10.1021/jp805870r

[53] R. Breslow, J. Brown, and J. J. Gajewski, “Antiaromaticity of cyclopropenyl anions,” *Journal of the American Chemical Society*, vol. 89, no. 17, pp. 4383–4390, Aug. 1967. [Online]. Available: https://pubs.acs.org/doi/abs/10.1021/ja00993a023

[54] R. Breslow, “Antiaromaticity,” *Accounts of Chemical Research*, vol. 6, no. 12, pp. 393–398, Dec. 1973. [Online]. Available: https://pubs.acs.org/doi/abs/10.1021/ar50072a001

[55] R. Hoffmann, “How Chemistry and Physics Meet in the Solid State,” *Angewandte Chemie International Edition in English*, vol. 26, no. 9, pp. 846–878, Sep. 1987. [Online]. Available: https://onlinelibrary.wiley.com/doi/10.1002/anie.198708461

[56] M. Rickhaus, M. Jirasek, L. Tejerina, H. Gotfredsen, M. D. Peeks, R. Haver, H.-W. Jiang, T. D. W. Claridge, and H. L. Anderson, “Global aromaticity at the nanoscale,” *Nature Chemistry*, vol. 12, no. 3, pp. 236–241, Mar. 2020. [Online]. Available: http://www.nature.com/articles/s41557-019-0398-3

[57] E. Clar, *The aromatic sextet.* New York, Wiley, 1972.

[58] Y. Wang, "Quantitative Resonance Theory Based on the Clar Sextet Model," *The Journal of Physical Chemistry A*, vol. 126, no. 1, pp. 164–176, Jan. 2022. [Online]. Available: https://pubs.acs.org/doi/10.1021/acs.jpca.1c08661

[59] T. Wassmann, A. P. Seitsonen, A. M. Saitta, M. Lazzeri, and F. Mauri, "Clar's Theory, -Electron Distribution, and Geometry of Graphene Nanoribbons," *Journal of the American Chemical Society*, vol. 132, no. 10, pp. 3440–3451, Mar. 2010. [Online]. Available: https://pubs.acs.org/doi/10.1021/ja909234y

[60] M. Solà, "Forty years of Clar's aromatic -sextet rule," *Frontiers in Chemistry*, vol. 1, 2013. [Online]. Available: http://journal.frontiersin.org/article/10.3389/fchem.2013.00022/abstract

[61] T. K. Dickens and R. B. Mallion, "Topological Ring-Currents and Clar Sextets in Fully Benzenoid Hydrocarbons. II. Large Structures Containing More than 18 Rings," *The Journal of Physical Chemistry A*, vol. 122, no. 45, pp. 8865–8873, Nov. 2018. [Online]. Available: https://pubs.acs.org/doi/10.1021/acs.jpca.8b08723

[62] G. Trinquier and J.-P. Malrieu, "Predicting the Open-Shell Character of Polycyclic Hydrocarbons in Terms of Clar Sextets," *The Journal of Physical Chemistry A*, vol. 122, no. 4, pp. 1088–1103, Feb. 2018. [Online]. Available: https://pubs.acs.org/doi/10.1021/acs.jpca.7b11095

[63] C.-N. Yeh and J.-D. Chai, "Role of Kekulé and Non-Kekulé Structures in the Radical Character of Alternant Polycyclic Aromatic Hydrocarbons: A TAO-DFT Study," *Scientific Reports*, vol. 6, no. 1, p. 30562, Sep. 2016. [Online]. Available: http://www.nature.com/articles/srep30562

[64] D. G. de Oteyza and T. Frederiksen, "Carbon-based nanostructures as a versatile platform for tunable -magnetism," *Journal of Physics: Condensed Matter*, vol. 34, no. 44, p. 443001, Nov. 2022. [Online]. Available: https://iopscience.iop.org/article/10.1088/1361-648X/ac8a7f

[65] A. Konishi and T. Kubo, "Benzenoid Quinodimethanes," *Topics in Current Chemistry*, vol. 375, no. 6, p. 83, Dec. 2017. [Online]. Available: http://link.springer.com/10.1007/s41061-017-0171-2

[66] J.-P. Malrieu and G. Trinquier, "Can a Topological Approach Predict Spin-Symmetry Breaking in Conjugated Hydrocarbons?" *The Journal of Physical Chemistry A*, vol. 120, no. 48, pp. 9564–9578, Dec. 2016. [Online]. Available: https://pubs.acs.org/doi/10.1021/acs.jpca.6b07597

[67] J. I. Urgel, S. Mishra, H. Hayashi, J. Wilhelm, C. A. Pignedoli, M. Di Giovannantonio, R. Widmer, M. Yamashita, N. Hieda, P. Ruffieux, H. Yamada, and R. Fasel, "On-surface light-induced generation of higher acenes and elucidation of their open-shell character," *Nature Communications*, vol. 10, no. 1, p. 861, Dec. 2019. [Online]. Available: http://www.nature.com/articles/s41467-019-08650-y

[68] N. Merino-Díez, M. S. G. Mohammed, J. Castro-Esteban, L. Colazzo, A. Berdonces-Layunta, J. Lawrence, J. I. Pascual, D. G. de Oteyza, and D. Peña, "Transferring axial molecular chirality through a sequence of on-surface reactions," *Chemical Science*, vol. 11, no. 21, pp. 5441–5446, 2020. [Online]. Available: http://xlink.rsc.org/?DOI=D0SC01653E

[69] N. Merino-Díez, J. Li, A. Garcia-Lekue, G. Vasseur, M. Vilas-Varela, E. Carbonell-Sanromà, M. Corso, J. E. Ortega, D. Peña, J. I. Pascual, and D. G. de Oteyza, "Unraveling the Electronic Structure of Narrow Atomically Precise Chiral Graphene Nanoribbons," *The Journal of Physical Chemistry Letters*, vol. 9, no. 1, pp. 25–30, Jan. 2018. [Online]. Available: https://pubs.acs.org/doi/10.1021/acs.jpclett.7b02767

[70] N. Merino-Díez, A. Garcia-Lekue, E. Carbonell-Sanromà, J. Li, M. Corso, L. Colazzo, F. Sedona, D. Sánchez-Portal, J. I. Pascual, and D. G. de Oteyza, "Width-Dependent Band Gap in Armchair Graphene Nanoribbons Reveals Fermi Level Pinning on Au(111)," *ACS Nano*, vol. 11, no. 11, pp. 11 661–11 668, Nov. 2017. [Online]. Available: https://pubs.acs.org/doi/10.1021/acsnano.7b06765

[71] T. Cao, F. Zhao, and S. G. Louie, "Topological Phases in Graphene Nanoribbons: Junction States, Spin Centers, and Quantum Spin Chains," *Physical Review Letters*, vol. 119, no. 7, p. 076401, Aug. 2017. [Online]. Available: https://link.aps.org/doi/10.1103/PhysRevLett.119.076401

[72] K. Sun, P. Ji, J. Zhang, J. Wang, X. Li, X. Xu, H. Zhang, and L. Chi, "On-Surface Synthesis of 8- and 10-Armchair Graphene Nanoribbons," *Small*, vol. 15, no. 15, p. 1804526, Apr. 2019. [Online]. Available: https://onlinelibrary.wiley.com/doi/10.1002/smll.201804526

[73] N. V. Tepliakov, J. Lischner, E. Kaxiras, A. A. Mostofi, and M. Pizzochero, "Unveiling and Manipulating Hidden Symmetries in Graphene Nanoribbons," *arXiv:2203.02808 [cond-mat]*, Mar. 2022, arXiv: 2203.02808. [Online]. Available: http://arxiv.org/abs/2203.02808

[74] Y.-W. Son, M. L. Cohen, and S. G. Louie, "Energy Gaps in Graphene Nanoribbons," *Physical Review Letters*, vol. 97, no. 21, p. 216803, Nov. 2006. [Online]. Available: https://link.aps.org/doi/10.1103/PhysRevLett.97.216803

[75] M. C. Scharber and N. S. Sariciftci, "Low Band Gap Conjugated Semiconducting Polymers," *Advanced Materials Technologies*, vol. 6, no. 4, p. 2000857, 2021, _eprint: https://onlinelibrary.wiley.com/doi/pdf/10.1002/admt.202000857. [Online]. Available: https://onlinelibrary.wiley.com/doi/abs/10.1002/admt.202000857

[76] R. E. Peierls, *Quantum Theory of Solids*. Clarendon Press, Oxford, 1955. [Online]. Available: https://books.google.com.au/books?id=UrsHbOjiR8QC

[77] J. Rouxel, Ed., *Crystal Chemistry and Properties of Materials with Quasi-One-Dimensional Structures*. Dordrecht: Springer Netherlands, 1986. [Online]. Available: http://link.springer.com/10.1007/978-94-009-4528-9

[78] W. P. Su, J. R. Schrieffer, and A. J. Heeger, "Solitons in Polyacetylene," *Physical Review Letters*, vol. 42, no. 25, pp. 1698–1701, Jun. 1979. [Online]. Available: https://link.aps.org/doi/10.1103/PhysRevLett.42.1698

[79] S.-R. E. Yang, "Soliton Fractional Charges in Graphene Nanoribbon and Polyacetylene: Similarities and Differences," *Nanomaterials*, vol. 9, no. 6, p. 885, Jun. 2019. [Online]. Available: https://www.mdpi.com/2079-4991/9/6/885

[80] A. J. Heeger and A. G. Maciarmid, "Transport, Magnetic and Structural Studies of Polyacetylene," *Molecular Crystals and Liquid Crystals*, vol. 77, no. 1-4, pp. 1–24, Dec. 1981. [Online]. Available: https://www.tandfonline.com/doi/full/10.1080/00268948108075226

[81] F. Zuo, A. Epstein, X.-Q. Yang, D. Tanner, G. Arbuckle, and A. MacDiarmid, "Transport and magnetic studies of segmented polyacetylene," *Synthetic Metals*, vol. 17, no. 1-3, pp. 433–438, Jan. 1987. [Online]. Available: https://linkinghub.elsevier.com/retrieve/pii/0379677987907788

[82] J. Tanaka, C. Tanaka, T. Miyamae, K. Kamiya, M. Shimizu, M. Oku, K. Seki, J. Tsukamoto, S. Hasegawa, and H. Inokuchi, "Spectral characteristic of metallic state of polyacetylene," *Synthetic Metals*, vol. 55, no. 1, pp. 121–126, Mar. 1993. [Online]. Available: https://linkinghub.elsevier.com/retrieve/pii/037967799390920R

[83] S. Willard, *General Topology*, ser. Dover Books on Mathematics. Dover Publications, 2012. [Online]. Available: https://books.google.com.au/books?id=UrsHbOjiR8QC

[84] S. Mashaghi, T. Jadidi, G. Koenderink, and A. Mashaghi, "Lipid Nanotechnology," *International Journal of Molecular Sciences*, vol. 14, no. 2, pp. 4242–4282, Feb. 2013. [Online]. Available: http://www.mdpi.com/1422-0067/14/2/4242

[85] G. Carlsson, "Topology and data," *Bulletin of the American Mathematical Society*, vol. 46, no. 2, pp. 255–308, Jan. 2009. [Online]. Available: http://www.ams.org/journal-getitem?pii=S0273-0979-09-01249-X

[86] J. Wang and S.-C. Zhang, "Topological states of condensed matter," *Nature Materials*, vol. 16, no. 11, pp. 1062–1067, Nov. 2017. [Online]. Available: https://www.nature.com/articles/nmat5012

[87] P. H. Jacobse, Z. Jin, J. Jiang, S. Peurifoy, Z. Yue, Z. Wang, D. J. Rizzo, S. G. Louie, C. Nuckolls, and M. F. Crommie, "Pseudo-atomic orbital behavior in graphene

nanoribbons with four-membered rings," *Science Advances*, vol. 7, no. 52, p. eabl5892, Dec. 2021. [Online]. Available: https://www.science.org/doi/10.1126/sciadv.abl5892

[88] J. Zak, "Berry's phase for energy bands in solids," *Physical Review Letters*, vol. 62, no. 23, pp. 2747–2750, Jun. 1989. [Online]. Available: https://link.aps.org/doi/10.1103/PhysRevLett.62.2747

[89] J.-W. Rhim, J. Behrends, and J. H. Bardarson, "Bulk-boundary correspondence from the intercellular Zak phase," *Physical Review B*, vol. 95, no. 3, p. 035421, Jan. 2017. [Online]. Available: https://link.aps.org/doi/10.1103/PhysRevB.95.035421

[90] O. Gröning, S. Wang, X. Yao, C. A. Pignedoli, G. Borin Barin, C. Daniels, A. Cupo, V. Meunier, X. Feng, A. Narita, K. Müllen, P. Ruffieux, and R. Fasel, "Engineering of robust topological quantum phases in graphene nanoribbons," *Nature*, vol. 560, no. 7717, pp. 209–213, Aug. 2018. [Online]. Available: http://www.nature.com/articles/s41586-018-0375-9

[91] B. Yuan, C. Li, Y. Zhao, O. Gröning, X. Zhou, P. Zhang, D. Guan, Y. Li, H. Zheng, C. Liu, Y. Mai, P. Liu, W. Ji, J. Jia, and S. Wang, "Resolving Quinoid Structure in Poly(*para* -phenylene) Chains," *Journal of the American Chemical Society*, vol. 142, no. 22, pp. 10 034–10 041, Jun. 2020. [Online]. Available: https://pubs.acs.org/doi/10.1021/jacs.0c01930

[92] C. L. Fefferman, J. P. Lee-Thorp, and M. I. Weinstein, "Topologically protected states in one-dimensional continuous systems and Dirac points," *Proceedings of the National Academy of Sciences*, vol. 111, no. 24, pp. 8759–8763, Jun. 2014. [Online]. Available: https://pnas.org/doi/full/10.1073/pnas.1407391111

[93] W. Chen and A. P. Schnyder, "Universality classes of topological phase transitions with higher-order band crossing," *New Journal of Physics*, vol. 21, no. 7, p. 073003, Jul. 2019. [Online]. Available: https://iopscience.iop.org/article/10.1088/1367-2630/ab2a2d

[94] Q. Sun, O. Gröning, J. Overbeck, O. Braun, M. L. Perrin, G. Borin Barin, M. El Abbassi, K. Eimre, E. Ditler, C. Daniels, V. Meunier, C. A. Pignedoli, M. Calame, R. Fasel, and P. Ruffieux, "Massive Dirac Fermion Behavior in a Low Bandgap Graphene Nanoribbon Near a Topological Phase Boundary," *Advanced Materials*, vol. 32, no. 12, p. 1906054, Mar. 2020. [Online]. Available: https://onlinelibrary.wiley.com/doi/10.1002/adma.201906054

[95] F. Eisenhut, T. Kühne, F. García, S. Fernández, E. Guitián, D. Pérez, G. Trinquier, G. Cuniberti, C. Joachim, D. Peña, and F. Moresco, "Dodecacene Generated on Surface: Reopening of the Energy Gap," *ACS Nano*, vol. 14, no. 1, pp. 1011–1017, Jan. 2020. [Online]. Available: https://pubs.acs.org/doi/10.1021/acsnano.9b08456

[96] B. Cirera, A. Sánchez-Grande, B. de la Torre, J. Santos, S. Edalatmanesh, E. Rodríguez-Sánchez, K. Lauwaet, B. Mallada, R. Zbořil, R. Miranda, O. Gröning, P. Jelínek, N. Martín, and D. Ecija, "Tailoring topological order and -conjugation to engineer quasi-metallic polymers," *Nature Nanotechnology*, vol. 15, no. 6, pp. 437–443, Jun. 2020. [Online]. Available: http://www.nature.com/articles/s41565-020-0668-7

[97] T. Stuyver, B. Chen, T. Zeng, P. Geerlings, F. De Proft, and R. Hoffmann, "Do Diradicals Behave Like Radicals?" *Chemical Reviews*, vol. 119, no. 21, pp. 11 291–11 351, Nov. 2019. [Online]. Available: https://pubs.acs.org/doi/10.1021/acs.chemrev.9b00260

[98] A. D. Zdetsis and E. N. Economou, "Topological metal-insulator transition in narrow graphene nanoribbons?" *Carbon*, vol. 176, pp. 548–557, 2021. [Online]. Available: https://www.sciencedirect.com/science/article/pii/S0008622321001846

[99] J. Fernández-Rossier and J. J. Palacios, "Magnetism in Graphene Nanoislands," *Physical Review Letters*, vol. 99, no. 17, p. 177204, Oct. 2007. [Online]. Available: https://link.aps.org/doi/10.1103/PhysRevLett.99.177204

[100] H. Kumazaki and D. S. Hirashima, "Local Magnetic Moment Formation on Edges of Graphene," *Journal of the Physical Society of Japan*, vol. 77, no. 4, p. 044705, Apr. 2008. [Online]. Available: https://journals.jps.jp/doi/10.1143/JPSJ.77.044705

[101] H. González-Herrero, J. M. Gómez-Rodríguez, P. Mallet, M. Moaied, J. J. Palacios, C. Salgado, M. M. Ugeda, J.-Y. Veuillen, F. Yndurain, and I. Brihuega, "Atomic-scale control of graphene magnetism by using hydrogen atoms," *Science*, vol. 352, no. 6284, pp. 437–441, Apr. 2016. [Online]. Available: https://www.science.org/doi/10.1126/science.aad8038

[102] R. Babar and M. Kabir, "Ferromagnetism in nitrogen-doped graphene," *Physical Review B*, vol. 99, no. 11, p. 115442, Mar. 2019. [Online]. Available: https://link.aps.org/doi/10.1103/PhysRevB.99.115442

[103] N. Friedrich, P. Brandimarte, J. Li, S. Saito, S. Yamaguchi, I. Pozo, D. Peña, T. Frederiksen, A. Garcia-Lekue, D. Sánchez-Portal, and J. I. Pascual, "Magnetism of Topological Boundary States Induced by Boron Substitution in Graphene Nanoribbons," *Physical Review Letters*, vol. 125, no. 14, p. 146801, Sep. 2020. [Online]. Available: https://link.aps.org/doi/10.1103/PhysRevLett.125.146801

[104] S. Cheng, Z. Xue, C. Li, Y. Liu, L. Xiang, Y. Ke, K. Yan, S. Wang, and P. Yu, "On-surface synthesis of triangulene trimers via dehydration reaction," *Nature Communications*, vol. 13, no. 1, p. 1705, Dec. 2022. [Online]. Available: https://www.nature.com/articles/s41467-022-29371-9

[105] J. Liu, S. Mishra, C. A. Pignedoli, D. Passerone, J. I. Urgel, A. Fabrizio, T. G. Lohr, J. Ma, H. Komber, M. Baumgarten, C. Corminboeuf, R. Berger, P. Ruffieux, K. Müllen, R. Fasel, and X. Feng, "Open-Shell Nonbenzenoid Nanographenes Containing Two Pairs of Pentagonal and Heptagonal Rings," *Journal of the American Chemical Society*, vol. 141, no. 30, pp. 12 011–12 020, Jul. 2019. [Online]. Available: https://pubs.acs.org/doi/10.1021/jacs.9b04718

[106] H. Zhang, H. Lin, K. Sun, L. Chen, Y. Zagranyarski, N. Aghdassi, S. Duhm, Q. Li, D. Zhong, Y. Li, K. Müllen, H. Fuchs, and L. Chi, "On-Surface Synthesis of Rylene-Type Graphene Nanoribbons," *Journal of the American Chemical Society*, vol. 137, no. 12, pp. 4022–4025, Apr. 2015. [Online]. Available: https://pubs.acs.org/doi/10.1021/ja511995r

[107] A. Kimouche, M. M. Ervasti, R. Drost, S. Halonen, A. Harju, P. M. Joensuu, J. Sainio, and P. Liljeroth, "Ultra-narrow metallic armchair graphene nanoribbons," *Nature Communications*, vol. 6, no. 1, p. 10177, Dec. 2015. [Online]. Available: http://www.nature.com/articles/ncomms10177

[108] L. Yang, C.-H. Park, Y.-W. Son, M. L. Cohen, and S. G. Louie, "Quasiparticle Energies and Band Gaps in Graphene Nanoribbons," *Physical Review Letters*, vol. 99, no. 18, p. 186801, Nov. 2007. [Online]. Available: https://link.aps.org/doi/10.1103/PhysRevLett.99.186801

[109] P. Ruffieux, J. Cai, N. C. Plumb, L. Patthey, D. Prezzi, A. Ferretti, E. Molinari, X. Feng, K. Müllen, C. A. Pignedoli, and R. Fasel, "Electronic Structure of Atomically Precise Graphene Nanoribbons," *ACS Nano*, vol. 6, no. 8, pp. 6930–6935, Aug. 2012. [Online]. Available: https://pubs.acs.org/doi/10.1021/nn3021376

[110] Y.-C. Chen, D. G. de Oteyza, Z. Pedramrazi, C. Chen, F. R. Fischer, and M. F. Crommie, "Tuning the Band Gap of Graphene Nanoribbons Synthesized from Molecular Precursors," *ACS Nano*, vol. 7, no. 7, pp. 6123–6128, Jul. 2013. [Online]. Available: https://pubs.acs.org/doi/10.1021/nn401948e

[111] N. Kharche and V. Meunier, "Width and Crystal Orientation Dependent Band Gap Renormalization in Substrate-Supported Graphene Nanoribbons," *The Journal of Physical Chemistry Letters*, vol. 7, no. 8, pp. 1526–1533, Apr. 2016. [Online]. Available: https://pubs.acs.org/doi/10.1021/acs.jpclett.6b00422

[112] G. Wise, "Science and Technology," *Osiris, 2nd Series*, vol. 1, pp. 229–246, 1985. [Online]. Available: http://www.jstor.org/stable/301734

[113] N. Merino-Díez, "On-surface synthesis and electronic structure characterization of grafphene nanoribbons," This thesis has been carried out at Donostia International Physics Center (DIPC), Centro de Física de Materiales - Materials Physics Center (CFM-MPC), and CIC nanoGUNE: nanoscience cooperative research center., 2019.

[114] A. Enders and G. Nimtz, "Evanescent-mode propagation and quantum tunneling," *Phys. Rev. E*, vol. 48, pp. 632–634, Jul 1993. [Online]. Available: https://link.aps.org/doi/10.1103/PhysRevE.48.632

[115] B. Voigtländer, *Atomic Force Microscopy*, ser. NanoScience and Technology. Cham: Springer International Publishing, 2019. [Online]. Available: http://link.springer.com/10.1007/978-3-030-13654-3

[116] C. J. Chen, *Introduction to Scanning Tunneling Microscopy*. Oxford University Press, 09 2007. [Online]. Available: https://doi.org/10.1093/acprof:oso/9780199211500.001.0001

[117] J. Bardeen, "Tunnelling from a Many-Particle Point of View," *Physical Review Letters*, vol. 6, no. 2, pp. 57–59, Jan. 1961. [Online]. Available: https://link.aps.org/doi/10.1103/PhysRevLett.6.57

[118] A. D. Gottlieb and L. Wesoloski, "Bardeen's tunnelling theory as applied to scanning tunnelling microscopy: a technical guide to the traditional interpretation," *Nanotechnology*, vol. 17, no. 8, pp. R57–R65, Apr. 2006. [Online]. Available: https://iopscience.iop.org/article/10.1088/0957-4484/17/8/R01

[119] J. Orear, E. Fermi, A. Rosenfeld, and R. Schluter, *Nuclear Physics: A Course Given by Enrico Fermi at the University of Chicago*, ser. Midway reprints. University of Chicago Press, 1950. [Online]. Available: https://books.google.es/books?id=WQtkYCWTcicC

[120] J. M. Zhang and Y. Liu, "Fermi's golden rule: its derivation and breakdown by an ideal model," *European Journal of Physics*, vol. 37, no. 6, p. 065406, Nov. 2016. [Online]. Available: https://iopscience.iop.org/article/10.1088/0143-0807/37/6/065406

[121] H. J. Reittu, "Fermi's golden rule and Bardeen's tunneling theory," *American Journal of Physics*, vol. 63, no. 10, pp. 940–944, Oct. 1995. [Online]. Available: http://aapt.scitation.org/doi/10.1119/1.18037

[122] J. Tersoff and D. R. Hamann, "Theory of the scanning tunneling microscope," *Physical Review B*, vol. 31, no. 2, pp. 805–813, Jan. 1985. [Online]. Available: https://link.aps.org/doi/10.1103/PhysRevB.31.805

[123] G. S. Diniz, G. I. Luiz, A. Latgé, and E. Vernek, "From Kondo to local singlet state in graphene nanoribbons with magnetic impurities," *Physical Review B*, vol. 97, no. 11, p. 115444, Mar. 2018. [Online]. Available: https://link.aps.org/doi/10.1103/PhysRevB.97.115444

[124] S. Frank and D. Jacob, "Orbital signatures of Fano-Kondo line shapes in STM adatom spectroscopy," *Physical Review B*, vol. 92, no. 23, p. 235127, Dec. 2015. [Online]. Available: https://link.aps.org/doi/10.1103/PhysRevB.92.235127

[125] M. Moro-Lagares, R. Korytár, M. Piantek, R. Robles, N. Lorente, J. I. Pascual, M. R. Ibarra, and D. Serrate, "Real space manifestations of coherent screening in atomic scale Kondo lattices," *Nature Communications*, vol. 10, no. 1, p. 2211, May 2019. [Online]. Available: https://www.nature.com/articles/s41467-019-10103-5

[126] J. Kondo, "Resistance Minimum in Dilute Magnetic Alloys," *Progress of Theoretical Physics*, vol. 32, no. 1, pp. 37–49, Jul. 1964. [Online]. Available: https://academic.oup.com/ptp/article-lookup/doi/10.1143/PTP.32.37

[127] P. Niu, Y.-L. Shi, Z. Sun, Y.-H. Nie, and H.-G. Luo, "Kondo peak splitting and Kondo dip induced by a local moment," *Scientific Reports*, vol. 5, no. 1, p. 18021, Dec. 2015. [Online]. Available: http://www.nature.com/articles/srep18021

[128] M. Ternes, A. J. Heinrich, and W.-D. Schneider, "Spectroscopic manifestations of the Kondo effect on single adatoms," *Journal of Physics: Condensed*

Matter, vol. 21, no. 5, p. 053001, Feb. 2009. [Online]. Available: https://iopscience.iop.org/article/10.1088/0953-8984/21/5/053001

[129] K. Nagaoka, T. Jamneala, M. Grobis, and M. F. Crommie, "Temperature Dependence of a Single Kondo Impurity," *Physical Review Letters*, vol. 88, no. 7, p. 077205, Feb. 2002. [Online]. Available: https://link.aps.org/doi/10.1103/PhysRevLett.88.077205

[130] T. Wang, A. Berdonces-Layunta, N. Friedrich, M. Vilas-Varela, J. P. Calupitan, J. I. Pascual, D. Peña, D. Casanova, M. Corso, and D. G. de Oteyza, "Aza-Triangulene: On-Surface Synthesis and Electronic and Magnetic Properties," *Journal of the American Chemical Society*, vol. 144, no. 10, pp. 4522–4529, Mar. 2022. [Online]. Available: https://pubs.acs.org/doi/10.1021/jacs.1c12618

[131] Y. Zhao, K. Jiang, C. Li, Y. Liu, G. Zhu, M. Pizzochero, E. Kaxiras, D. Guan, Y. Li, H. Zheng, C. Liu, J. Jia, M. Qin, X. Zhuang, and S. Wang, "Quantum nanomagnets in on-surface metal-free porphyrin chains," *Nature Chemistry*, vol. 15, no. 1, pp. 53–60, Jan. 2023. [Online]. Available: https://www.nature.com/articles/s41557-022-01061-5

[132] X. Su, C. Li, Q. Du, K. Tao, S. Wang, and P. Yu, "Atomically Precise Synthesis and Characterization of Heptauthrene with Triplet Ground State," *Nano Letters*, vol. 20, no. 9, pp. 6859–6864, Sep. 2020. [Online]. Available: https://pubs.acs.org/doi/10.1021/acs.nanolett.0c02939

[133] L. A. Nagahara, T. Thundat, and S. M. Lindsay, "Preparation and characterization of STM tips for electrochemical studies," *Review of Scientific Instruments*, vol. 60, no. 10, pp. 3128–3130, Oct. 1989. [Online]. Available: http://aip.scitation.org/doi/10.1063/1.1140590

[134] M. J. Vasile, D. A. Grigg, J. E. Griffith, E. A. Fitzgerald, and P. E. Russell, "Scanning probe tips formed by focused ion beams," *Review of Scientific Instruments*, vol. 62, no. 9, pp. 2167–2171, Sep. 1991. [Online]. Available: http://aip.scitation.org/doi/10.1063/1.1142334

[135] Z. Zhang, S. Sheng, R. Wang, and M. Sun, "Tip-enhanced raman spectroscopy," 2016.

[136] R. Temirov, S. Soubatch, O. Neucheva, A. C. Lassise, and F. S. Tautz, "A novel method achieving ultra-high geometrical resolution in scanning tunnelling microscopy," *New Journal of Physics*, vol. 10, no. 5, p. 053012, May 2008. [Online]. Available: https://iopscience.iop.org/article/10.1088/1367-2630/10/5/053012

[137] L. Gross, F. Mohn, N. Moll, P. Liljeroth, and G. Meyer, "The Chemical Structure of a Molecule Resolved by Atomic Force Microscopy," *Science*, vol. 325, no. 5944, pp. 1110–1114, Aug. 2009. [Online]. Available: https://www.sciencemag.org/lookup/doi/10.1126/science.1176210

[138] C.-l. Chiang, C. Xu, Z. Han, and W. Ho, "Real-space imaging of molecular structure and chemical bonding by single-molecule inelastic tunneling probe," *Science*, vol. 344, no. 6186, pp. 885–888, May 2014. [Online]. Available: https://www.science.org/doi/10.1126/science.1253405

[139] P. Jelínek, "High resolution SPM imaging of organic molecules with functionalized tips," *Journal of Physics: Condensed Matter*, vol. 29, no. 34, p. 343002, Aug. 2017. [Online]. Available: https://iopscience.iop.org/article/10.1088/1361-648X/aa76c7

[140] L. Gross, N. Moll, F. Mohn, A. Curioni, G. Meyer, F. Hanke, and M. Persson, "High-Resolution Molecular Orbital Imaging Using a p -Wave STM Tip," *Physical*

Review Letters, vol. 107, no. 8, p. 086101, Aug. 2011. [Online]. Available: https://link.aps.org/doi/10.1103/PhysRevLett.107.086101

[141] G. D. Nguyen, H.-Z. Tsai, A. A. Omrani, T. Marangoni, M. Wu, D. J. Rizzo, G. F. Rodgers, R. R. Cloke, R. A. Durr, Y. Sakai, F. Liou, A. S. Aikawa, J. R. Chelikowsky, S. G. Louie, F. R. Fischer, and M. F. Crommie, "Atomically precise graphene nanoribbon heterojunctions from a single molecular precursor," *Nature Nanotechnology*, vol. 12, no. 11, pp. 1077–1082, Nov. 2017. [Online]. Available: http://www.nature.com/articles/nnano.2017.155

[142] P. Hapala, G. Kichin, C. Wagner, F. S. Tautz, R. Temirov, and P. Jelínek, "Mechanism of high-resolution STM/AFM imaging with functionalized tips," *Physical Review B*, vol. 90, no. 8, p. 085421, Aug. 2014. [Online]. Available: https://link.aps.org/doi/10.1103/PhysRevB.90.085421

[143] M. Vilas-Varela, S. Fatayer, Z. Majzik, D. Pérez, E. Guitián, L. Gross, and D. Peña, "[19]Dendriphene: A 19-Ring Dendritic Nanographene," *Chemistry - A European Journal*, vol. 24, no. 67, pp. 17 697–17 700, Dec. 2018. [Online]. Available: http://doi.wiley.com/10.1002/chem.201805140

[144] A. Riss, A. P. Paz, S. Wickenburg, H.-Z. Tsai, D. G. De Oteyza, A. J. Bradley, M. M. Ugeda, P. Gorman, H. S. Jung, M. F. Crommie, A. Rubio, and F. R. Fischer, "Imaging single-molecule reaction intermediates stabilized by surface dissipation and entropy," *Nature Chemistry*, vol. 8, no. 7, pp. 678–683, Jul. 2016. [Online]. Available: http://www.nature.com/articles/nchem.2506

[145] F. Schulz, J. Ritala, O. Krejčí, A. P. Seitsonen, A. S. Foster, and P. Liljeroth, "Elemental Identification by Combining Atomic Force Microscopy and Kelvin Probe Force Microscopy," *ACS Nano*, vol. 12, no. 6, pp. 5274–5283, Jun. 2018. [Online]. Available: https://pubs.acs.org/doi/10.1021/acsnano.7b08997

[146] S. Fatayer, F. Albrecht, Y. Zhang, D. Urbonas, D. Peña, N. Moll, and L. Gross, "Molecular structure elucidation with charge-state control," *Science*, vol. 365, no. 6449, pp. 142–145, Jul. 2019. [Online]. Available: https://www.science.org/doi/10.1126/science.aax5895

[147] J. Lawrence, G. C. Sosso, L. Đorđević, H. Pinfold, D. Bonifazi, and G. Costantini, "Combining high-resolution scanning tunnelling microscopy and first-principles simulations to identify halogen bonding," *Nature Communications*, vol. 11, no. 1, p. 2103, Dec. 2020. [Online]. Available: http://www.nature.com/articles/s41467-020-15898-2

[148] J. Zhang, P. Chen, B. Yuan, W. Ji, Z. Cheng, and X. Qiu, "Real-Space Identification of Intermolecular Bonding with Atomic Force Microscopy," *Science*, vol. 342, no. 6158, pp. 611–614, Nov. 2013. [Online]. Available: https://www.science.org/doi/10.1126/science.1242603

[149] S. K. Hämäläinen, N. van der Heijden, J. van der Lit, S. den Hartog, P. Liljeroth, and I. Swart, "Intermolecular Contrast in Atomic Force Microscopy Images without Intermolecular Bonds," *Physical Review Letters*, vol. 113, no. 18, p. 186102, Oct. 2014. [Online]. Available: https://link.aps.org/doi/10.1103/PhysRevLett.113.186102

[150] G. Binnig, "U.s. patent atomic force microscope and method for imaging surfaces with atomic resolution," U.S. Patent 4.724.318, 1986.

[151] G. Binnig, C. F. Quate, and C. Gerber, "Atomic Force Microscope," *Physical Review Letters*, vol. 56, no. 9, pp. 930–933, Mar. 1986. [Online]. Available: https://link.aps.org/doi/10.1103/PhysRevLett.56.930

[152] T. R. Albrecht and C. F. Quate, "Atomic resolution imaging of a nonconductor by atomic force microscopy," *Journal of Applied Physics*, vol. 62, no. 7, pp. 2599–2602, Oct. 1987. [Online]. Available: http://aip.scitation.org/doi/10.1063/1.339435

[153] G. Binnig, C. Gerber, T. R. Albrecht, and C. F. QuATE, "Atomic Resolution with Atomic Force Microscope." *Europhysics letters*, p. 7, 1987.

[154] Y. Sugimoto, P. Pou, M. Abe, P. Jelinek, R. Pérez, S. Morita, and Custance, "Chemical identification of individual surface atoms by atomic force microscopy," *Nature*, vol. 446, no. 7131, pp. 64–67, Mar. 2007. [Online]. Available: http://www.nature.com/articles/nature05530

[155] T. R. Albrecht, P. Grütter, D. Horne, and D. Rugar, "Frequency modulation detection using high- Q cantilevers for enhanced force microscope sensitivity," *Journal of Applied Physics*, vol. 69, no. 2, pp. 668–673, Jan. 1991. [Online]. Available: http://aip.scitation.org/doi/10.1063/1.347347

[156] "Theory of Amplitude Modulation AFM," in *Amplitude Modulation Atomic Force Microscopy*. Weinheim, Germany: Wiley-VCH Verlag GmbH & Co. KGaA, Oct. 2010, pp. 41–57. [Online]. Available: https://onlinelibrary.wiley.com/doi/10.1002/9783527632183.ch4

[157] F. J. Giessibl, "A direct method to calculate tip–sample forces from frequency shifts in frequency-modulation atomic force microscopy," *Applied Physics Letters*, vol. 78,

no. 1, pp. 123–125, Jan. 2001. [Online]. Available: http://aip.scitation.org/doi/10.1063/1.1335546

[158] G. Binnig and D. P. E. Smith, "Single-tube three-dimensional scanner for scanning tunneling microscopy," *Review of Scientific Instruments*, vol. 57, no. 8, pp. 1688–1689, Aug. 1986. [Online]. Available: http://aip.scitation.org/doi/10.1063/1.1139196

[159] F. J. Giessibl, "High-speed force sensor for force microscopy and profilometry utilizing a quartz tuning fork," *Applied Physics Letters*, vol. 73, no. 26, pp. 3956–3958, Dec. 1998. [Online]. Available: http://aip.scitation.org/doi/10.1063/1.122948

[160] H. Hertz, "Ueber einen Einfluss des ultravioletten Lichtes auf die electrische Entladung," *Annalen der Physik und Chemie*, vol. 267, no. 8, pp. 983–1000, 1887. [Online]. Available: https://onlinelibrary.wiley.com/doi/10.1002/andp.18872670827

[161] W. Hallwachs, "Ueber den Einfluss des Lichtes auf electrostatisch geladene Körper," *Annalen der Physik und Chemie*, vol. 269, no. 2, pp. 301–312, 1888. [Online]. Available: https://onlinelibrary.wiley.com/doi/10.1002/andp.18882690206

[162] A. Einstein, "Über einen die Erzeugung und Verwandlung des Lichtes betreffenden heuristischen Gesichtspunkt," *Annalen der Physik*, vol. 322, no. 6, pp. 132–148, 1905. [Online]. Available: https://onlinelibrary.wiley.com/doi/10.1002/andp.19053220607

[163] H. Shinotsuka, S. Tanuma, C. J. Powell, and D. R. Penn, "Calculations of electron inelastic mean free paths. X. Data for 41 elemental solids over the 50 eV to 200 keV range with the relativistic full Penn algorithm: Calculations of electron inelastic mean free paths. X," *Surface and Interface Analysis*, vol. 47, no. 9, pp. 871–888, Sep. 2015. [Online]. Available: https://onlinelibrary.wiley.com/doi/10.1002/sia.5789

[164] F. Reinert and S. Hüfner, "Photoemission spectroscopy—from early days to recent applications," *New Journal of Physics*, vol. 7, pp. 97–97, Apr. 2005. [Online]. Available: https://iopscience.iop.org/article/10.1088/1367-2630/7/1/097

[165] I. N. Draganic, C. P. Leibman, L. J. Rybarcyk, T. M. Bronson, and K. W. Dudeck, "Hot filament performance in a Freeman ion source," Geneva, Switzerland, 2018, p. 030005. [Online]. Available: http://aip.scitation.org/doi/abs/10.1063/1.5053266

[166] P. Kelly and R. Arnell, "Magnetron sputtering: a review of recent developments and applications," *Vacuum*, vol. 56, no. 3, pp. 159–172, Mar. 2000. [Online]. Available: https://linkinghub.elsevier.com/retrieve/pii/S0042207X9900189X

[167] V. S. Smentkowski, "Trends in sputtering," *Progress in Surface Science*, vol. 64, no. 1-2, pp. 1–58, May 2000. [Online]. Available: https://linkinghub.elsevier.com/retrieve/pii/S0079681699000210

[168] G. Longo, L. Gil-Escrig, M. J. Degen, M. Sessolo, and H. J. Bolink, "Perovskite solar cells prepared by flash evaporation," *Chemical Communications*, vol. 51, no. 34, pp. 7376–7378, 2015. [Online]. Available: http://xlink.rsc.org/?DOI=C5CC01103E

[169] A. W. Warner and C. D. Stockbridge, "Quartz Resonators; Reduction of Transient Frequency Excursion Due to Temperature Change," *Journal of Applied Physics*, vol. 34, no. 2, pp. 437–438, Feb. 1963. [Online]. Available: http://aip.scitation.org/doi/10.1063/1.1702628

[170] L. Grill, M. Dyer, L. Lafferentz, M. Persson, M. V. Peters, and S. Hecht, "Nano-architectures by covalent assembly of molecular building blocks," *Nature*

Nanotechnology, vol. 2, no. 11, pp. 687–691, Nov. 2007. [Online]. Available: http://www.nature.com/articles/nnano.2007.346

[171] J. Cai, P. Ruffieux, R. Jaafar, M. Bieri, T. Braun, S. Blankenburg, M. Muoth, A. P. Seitsonen, M. Saleh, X. Feng, K. Müllen, and R. Fasel, "Atomically precise bottom-up fabrication of graphene nanoribbons," *Nature*, vol. 466, no. 7305, pp. 470–473, Jul. 2010. [Online]. Available: http://www.nature.com/articles/nature09211

[172] L. Lafferentz, V. Eberhardt, C. Dri, C. Africh, G. Comelli, F. Esch, S. Hecht, and L. Grill, "Controlling on-surface polymerization by hierarchical and substrate-directed growth," *Nature Chemistry*, vol. 4, no. 3, pp. 215–220, Mar. 2012. [Online]. Available: http://www.nature.com/articles/nchem.1242

[173] N. Merino-Díez, A. Pérez Paz, J. Li, M. Vilas-Varela, J. Lawrence, M. S. G. Mohammed, A. Berdonces-Layunta, A. Barragán, J. I. Pascual, J. Lobo-Checa, D. Peña, and D. G. Oteyza, "Hierarchy in the Halogen Activation During Surface-Promoted Ullmann Coupling," *ChemPhysChem*, vol. 20, no. 18, pp. 2305–2310, Sep. 2019. [Online]. Available: https://onlinelibrary.wiley.com/doi/abs/10.1002/cphc.201900633

[174] C. Bronner, S. Stremlau, M. Gille, F. Braußе, A. Haase, S. Hecht, and P. Tegeder, "Aligning the Band Gap of Graphene Nanoribbons by Monomer Doping," *Angewandte Chemie International Edition*, vol. 52, no. 16, pp. 4422–4425, Apr. 2013. [Online]. Available: https://onlinelibrary.wiley.com/doi/10.1002/anie.201209735

[175] J. Cai, C. A. Pignedoli, L. Talirz, P. Ruffieux, H. Söde, L. Liang, V. Meunier, R. Berger, R. Li, X. Feng, K. Müllen, and R. Fasel, "Graphene nanoribbon heterojunctions,"

Nature Nanotechnology, vol. 9, no. 11, pp. 896–900, Nov. 2014. [Online]. Available: http://www.nature.com/articles/nnano.2014.184

[176] D. J. Rizzo, G. Veber, T. Cao, C. Bronner, T. Chen, F. Zhao, H. Rodriguez, S. G. Louie, M. F. Crommie, and F. R. Fischer, "Topological band engineering of graphene nanoribbons," *Nature*, vol. 560, no. 7717, pp. 204–208, Aug. 2018. [Online]. Available: http://www.nature.com/articles/s41586-018-0376-8

[177] K. Weiss, G. Beernink, F. Dötz, A. Birkner, K. Müllen, and C. H. Wöll, "Template-Mediated Synthesis of Polycyclic Aromatic Hydrocarbons: Cyclodehydrogenation and Planarization of a Hexaphenylbenzene Derivative at a Copper Surface," *Angewandte Chemie International Edition*, vol. 38, no. 24, pp. 3748–3752, Dec. 1999. [Online]. Available: https://onlinelibrary.wiley.com/doi/10.1002/(SICI)1521-3773(19991216)38:24<3748::AID-ANIE3748>3.0.CO;2-0

[178] D. Zhong, J.-H. Franke, S. K. Podiyanachari, T. Blömker, H. Zhang, G. Kehr, G. Erker, H. Fuchs, and L. Chi, "Linear Alkane Polymerization on a Gold Surface," vol. 334, 2011.

[179] J. Lawrence, A. Berdonces-Layunta, S. Edalatmanesh, J. Castro-Esteban, T. Wang, A. Jimenez-Martin, B. de la Torre, R. Castrillo-Bodero, P. Angulo-Portugal, M. S. G. Mohammed, A. Matěj, M. Vilas-Varela, F. Schiller, M. Corso, P. Jelinek, D. Peña, and D. G. de Oteyza, "Circumventing the stability problems of graphene nanoribbon zigzag edges," *Nature Chemistry*, Sep. 2022. [Online]. Available: https://doi.org/10.1038/s41557-022-01042-8

[180] J. Björk, F. Hanke, and S. Stafström, "Mechanisms of Halogen-Based Covalent Self-Assembly on Metal Surfaces," *Journal of the American Chemical Society*, vol. 135, no. 15, pp. 5768–5775, Apr. 2013. [Online]. Available: https://pubs.acs.org/doi/10.1021/ja400304b

[181] L. Dong, P. N. Liu, and N. Lin, "Surface-Activated Coupling Reactions Confined on a Surface," *Accounts of Chemical Research*, vol. 48, no. 10, pp. 2765–2774, Oct. 2015. [Online]. Available: https://pubs.acs.org/doi/10.1021/acs.accounts.5b00160

[182] J. Björk, S. Stafström, and F. Hanke, "Zipping Up: Cooperativity Drives the Synthesis of Graphene Nanoribbons," *Journal of the American Chemical Society*, vol. 133, no. 38, pp. 14 884–14 887, Sep. 2011. [Online]. Available: https://pubs.acs.org/doi/10.1021/ja205857a

[183] S. Blankenburg, J. Cai, P. Ruffieux, R. Jaafar, D. Passerone, X. Feng, K. Müllen, R. Fasel, and C. A. Pignedoli, "Intraribbon Heterojunction Formation in Ultranarrow Graphene Nanoribbons," *ACS Nano*, vol. 6, no. 3, pp. 2020–2025, Mar. 2012. [Online]. Available: https://pubs.acs.org/doi/10.1021/nn203129a

[184] N. Pavliček, B. Fleury, M. Neu, J. Niedenführ, C. Herranz-Lancho, M. Ruben, and J. Repp, "Atomic Force Microscopy Reveals Bistable Configurations of Dibenzo[a,h]thianthrene and their Interconversion Pathway," *Physical Review Letters*, vol. 108, no. 8, p. 086101, Feb. 2012. [Online]. Available: https://link.aps.org/doi/10.1103/PhysRevLett.108.086101

[185] F. Schulz, P. H. Jacobse, F. F. Canova, J. van der Lit, D. Z. Gao, A. van den Hoogenband, P. Han, R. J. Klein Gebbink, M.-E. Moret, P. M. Joensuu, I. Swart, and P. Liljeroth, "Precursor Geometry Determines the Growth Mechanism in Graphene

Nanoribbons," *The Journal of Physical Chemistry C*, vol. 121, no. 5, pp. 2896–2904, Feb. 2017. [Online]. Available: https://pubs.acs.org/doi/10.1021/acs.jpcc.6b12428

[186] J. Lawrence, P. Brandimarte, A. Berdonces-Layunta, M. S. G. Mohammed, A. Grewal, C. C. Leon, D. Sánchez-Portal, and D. G. de Oteyza, "Probing the Magnetism of Topological End States in 5-Armchair Graphene Nanoribbons," *ACS Nano*, vol. 14, no. 4, pp. 4499–4508, Apr. 2020. [Online]. Available: https://pubs.acs.org/doi/10.1021/acsnano.9b10191

[187] S. Hofmann, *Auger- and X-Ray Photoelectron Spectroscopy in Materials Science*, ser. Springer Series in Surface Sciences. Berlin, Heidelberg: Springer Berlin Heidelberg, 2013, vol. 49. [Online]. Available: http://link.springer.com/10.1007/978-3-642-27381-0

[188] C. Bronner, J. Björk, and P. Tegeder, "Tracking and Removing Br during the On-Surface Synthesis of a Graphene Nanoribbon," *The Journal of Physical Chemistry C*, vol. 119, no. 1, pp. 486–493, Jan. 2015. [Online]. Available: https://pubs.acs.org/doi/10.1021/jp5106218

[189] A. Mairena, M. Baljozovic, M. Kawecki, K. Grenader, M. Wienke, K. Martin, L. Bernard, N. Avarvari, A. Terfort, K.-H. Ernst, and C. Wäckerlin, "The fate of bromine after temperature-induced dehydrogenation of on-surface synthesized bisheptahelicene," *Chemical Science*, vol. 10, no. 10, pp. 2998–3004, 2019. [Online]. Available: http://xlink.rsc.org/?DOI=C8SC04720K

[190] A. Langner, S. L. Tait, N. Lin, C. Rajadurai, M. Ruben, and K. Kern, "Self-recognition and self-selection in multicomponent supramolecular coordination networks on surfaces," *Proceedings of the National Academy of Sciences*, vol.

104, no. 46, pp. 17 927–17 930, Nov. 2007. [Online]. Available: https://pnas.org/doi/full/10.1073/pnas.0704882104

[191] B. Gyurcsik and L. Nagy, "Carbohydrates as ligands: coordination equilibria and structure of the metal complexes," *Coordination Chemistry Reviews*, vol. 203, no. 1, pp. 81–149, Jun. 2000. [Online]. Available: https://linkinghub.elsevier.com/retrieve/pii/S0010854599001836

[192] L. Colazzo, M. S. G. Mohammed, R. Dorel, P. Nita, C. García Fernández, P. Abufager, N. Lorente, A. M. Echavarren, and D. G. de Oteyza, "On-surface synthesis of heptacene on Ag(001) from brominated and non-brominated tetrahydroheptacene precursors," *Chemical Communications*, vol. 54, no. 73, pp. 10 260–10 263, 2018. [Online]. Available: http://xlink.rsc.org/?DOI=C8CC04402C

[193] M. Rano, S. K. Ghosh, and D. Ghosh, "In the quest for a stable triplet state in small polyaromatic hydrocarbons: an *in silico* tool for rational design and prediction," *Chemical Science*, vol. 10, no. 40, pp. 9270–9276, 2019. [Online]. Available: http://xlink.rsc.org/?DOI=C9SC02414J

[194] J. Lawrence, M. S. G. Mohammed, D. Rey, F. Aguilar-Galindo, A. Berdonces-Layunta, D. Peña, and D. G. de Oteyza, "Reassessing Alkyne Coupling Reactions While Studying the Electronic Properties of Diverse Pyrene Linkages at Surfaces," *ACS Nano*, vol. 15, no. 3, pp. 4937–4946, Mar. 2021. [Online]. Available: https://pubs.acs.org/doi/10.1021/acsnano.0c09756

[195] A. Berdonces-Layunta, F. Schulz, F. Aguilar-Galindo, J. Lawrence, M. S. G. Mohammed, M. Muntwiler, J. Lobo-Checa, P. Liljeroth, and D. G. de Oteyza,

"Order from a Mess: The Growth of 5-Armchair Graphene Nanoribbons," *ACS Nano*, vol. 15, no. 10, pp. 16 552–16 561, Oct. 2021. [Online]. Available: https://pubs.acs.org/doi/10.1021/acsnano.1c06226

[196] Z. Cai, L. She, Y. He, L. Wu, L. Cai, and D. Zhong, "Halogen-Free On-Surface Synthesis of Rylene-Type Graphene Nanoribbons," *Macromolecular Chemistry and Physics*, vol. 218, no. 17, p. 1700155, Sep. 2017. [Online]. Available: http://doi.wiley.com/10.1002/macp.201700155

[197] L. Ferrighi, I. Píš, T. H. Nguyen, M. Cattelan, S. Nappini, A. Basagni, M. Parravicini, A. Papagni, F. Sedona, E. Magnano, F. Bondino, C. DiValentin, and S. Agnoli, "Control of the Intermolecular Coupling of Dibromotetracene on Cu(110) by the Sequential Activation of CBr and CH Bonds," *Chemistry - A European Journal*, vol. 21, no. 15, pp. 5826–5835, Apr. 2015. [Online]. Available: http://doi.wiley.com/10.1002/chem.201405817

[198] J. Björk, C. Sánchez-Sánchez, Q. Chen, C. A. Pignedoli, J. Rosen, P. Ruffieux, X. Feng, A. Narita, K. Müllen, and R. Fasel, "The Role of Metal Adatoms in a Surface-Assisted Cyclodehydrogenation Reaction on a Gold Surface," *Angewandte Chemie International Edition*, vol. 61, no. 49, Dec. 2022. [Online]. Available: https://onlinelibrary.wiley.com/doi/10.1002/anie.202212354

[199] T. A. Pham, B. V. Tran, M.-T. Nguyen, and M. Stöhr, "Chiral-Selective Formation of 1D Polymers Based on Ullmann-Type Coupling: The Role of the Metallic Substrate," *Small*, vol. 13, no. 13, p. 1603675, Apr. 2017. [Online]. Available: http://doi.wiley.com/10.1002/smll.201603675

[200] "THE ELECTRONIC STRUCTURES OF CIS—POLYACETYLENE," *Solid State Communications*, vol. 29, 1979.

[201] P. W. Anderson, "Localized Magnetic States in Metals," *Physical Review*, vol. 124, no. 1, pp. 41–53, Oct. 1961. [Online]. Available: https://link.aps.org/doi/10.1103/PhysRev.124.41

[202] K. Nakada, M. Igami, and M. Fujita, "Electron-Electron Interaction in Nanographite Ribbons," *Journal of the Physical Society of Japan*, vol. 67, no. 7, pp. 2388–2394, 1998, _eprint: https://doi.org/10.1143/JPSJ.67.2388. [Online]. Available: https://doi.org/10.1143/JPSJ.67.2388

[203] C. Q. Wu, J. Miao, J.-Z. Yu, and Y. Kawazoe, "Lack of a ***trans-cisoid*** phase in *cis* -polyacetylene," *Physical Review B*, vol. 57, no. 1, pp. 6–9, Jan. 1998. [Online]. Available: https://link.aps.org/doi/10.1103/PhysRevB.57.6

[204] T. Yumura, D. Nozaki, K. Hirahara, S. Bandow, S. Iijima, and K. Yoshizawa, "Quantum-size effects in capped and uncapped carbon nanotubes," *Annual Reports Section "C" (Physical Chemistry)*, vol. 102, p. 71, 2006. [Online]. Available: http://xlink.rsc.org/?DOI=b419102c

[205] K. Fukui and K. Tanaka, "A Theoretical Study on Biradicals. I. Theoretical Characteristics of Biradicals," *Bulletin of the Chemical Society of Japan*, vol. 50, no. 6, pp. 1391–1398, 1977, _eprint: https://doi.org/10.1246/bcsj.50.1391. [Online]. Available: https://doi.org/10.1246/bcsj.50.1391

[206] H. Söde, L. Talirz, O. Gröning, C. A. Pignedoli, R. Berger, X. Feng, K. Müllen, R. Fasel, and P. Ruffieux, "Electronic band dispersion of graphene

nanoribbons via Fourier-transformed scanning tunneling spectroscopy," *Physical Review B*, vol. 91, no. 4, p. 045429, Jan. 2015. [Online]. Available: https://link.aps.org/doi/10.1103/PhysRevB.91.045429

[207] P. H. Jacobse, M. J. J. Mangnus, S. J. M. Zevenhuizen, and I. Swart, "Mapping the Conductance of Electronically Decoupled Graphene Nanoribbons," *ACS Nano*, vol. 12, no. 7, pp. 7048–7056, Jul. 2018. [Online]. Available: https://pubs.acs.org/doi/10.1021/acsnano.8b02770

[208] S. Wang, N. Kharche, E. C. Girão, X. Feng, K. Müllen, V. Meunier, R. Fasel, and P. Ruffieux, "Quantum Dots in Graphene Nanoribbons," *Nano Letters*, p. 24, 2017.

[209] M. Koch, F. Ample, C. Joachim, and L. Grill, "Voltage-dependent conductance of a single graphene nanoribbon," *Nature Nanotechnology*, vol. 7, no. 11, pp. 713–717, Nov. 2012. [Online]. Available: http://www.nature.com/articles/nnano.2012.169

[210] L. Lafferentz, F. Ample, H. Yu, S. Hecht, C. Joachim, and L. Grill, "Conductance of a Single Conjugated Polymer as a Continuous Function of Its Length," *Science*, vol. 323, no. 5918, pp. 1193–1197, Feb. 2009. [Online]. Available: https://www.science.org/doi/10.1126/science.1168255

[211] P. H. Jacobse, A. Kimouche, T. Gebraad, M. M. Ervasti, J. M. Thijssen, P. Liljeroth, and I. Swart, "Electronic components embedded in a single graphene nanoribbon," *Nature Communications*, vol. 8, no. 1, p. 119, Dec. 2017. [Online]. Available: http://www.nature.com/articles/s41467-017-00195-2

[212] D. Xiang, X. Wang, C. Jia, T. Lee, and X. Guo, "Molecular-Scale Electronics: From Concept to Function," *Chemical Reviews*, vol. 116, no. 7, pp. 4318–4440, Apr. 2016. [Online]. Available: https://pubs.acs.org/doi/10.1021/acs.chemrev.5b00680

[213] T. A. Su, M. Neupane, M. L. Steigerwald, L. Venkataraman, and C. Nuckolls, "Chemical principles of single-molecule electronics," *Nature Reviews Materials*, vol. 1, no. 3, p. 16002, Mar. 2016. [Online]. Available: http://www.nature.com/articles/natrevmats20162

[214] C. Nacci, F. Ample, D. Bleger, S. Hecht, C. Joachim, and L. Grill, "Conductance of a single flexible molecular wire composed of alternating donor and acceptor units," *Nature Communications*, vol. 6, no. 1, p. 7397, Nov. 2015. [Online]. Available: http://www.nature.com/articles/ncomms8397

[215] D. Goldhaber-Gordon, J. Göres, M. A. Kastner, H. Shtrikman, D. Mahalu, and U. Meirav, "From the Kondo Regime to the Mixed-Valence Regime in a Single-Electron Transistor," *Physical Review Letters*, vol. 81, no. 23, pp. 5225–5228, Dec. 1998. [Online]. Available: https://link.aps.org/doi/10.1103/PhysRevLett.81.5225

[216] G. D. Scott and T.-C. Hu, "Gate-controlled Kondo effect in a single-molecule transistor with elliptical ferromagnetic leads," *Physical Review B*, vol. 96, no. 14, p. 144416, Oct. 2017. [Online]. Available: https://link.aps.org/doi/10.1103/PhysRevB.96.144416

[217] Y. Jiang, P.-W. Lo, D. May, G. Li, G.-Y. Guo, F. B. Anders, T. Taniguchi, K. Watanabe, J. Mao, and E. Y. Andrei, "Inducing Kondo screening of vacancy magnetic moments in graphene with gating and local curvature," *Nature Communications*, vol. 9, no. 1, p. 2349, Dec. 2018. [Online]. Available: http://www.nature.com/articles/s41467-018-04812-6

[218] J. Li, S. Sanz, M. Corso, D. J. Choi, D. Peña, T. Frederiksen, and J. I. Pascual, "Single spin localization and manipulation in graphene open-shell nanostructures," *Nature Communications*, vol. 10, no. 1, p. 200, Dec. 2019. [Online]. Available: http://www.nature.com/articles/s41467-018-08060-6

[219] E. Clar, *Polycyclic Hydrocarbons*. Berlin, Heidelberg: Springer Berlin Heidelberg, 1964. [Online]. Available: http://link.springer.com/10.1007/978-3-662-01668-8

[220] E. M. Cabaleiro-Lago, J. A. Carrazana-García, and J. Rodríguez-Otero, "Study of the interaction between water and hydrogen sulfide with polycyclic aromatic hydrocarbons," *The Journal of Chemical Physics*, vol. 130, no. 23, p. 234307, 2009. [Online]. Available: http://aip.scitation.org/doi/10.1063/1.3152577

[221] S. Tsuzuki and T. Uchimaru, "Magnitude and physical origin of intermolecular interactions of aromatic molecules: Recent progress of computational studies," *Current Organic Chemistry*, vol. 10, no. 7, pp. 745–762, 2006.

[222] D. Feller and K. D. Jordan, "Estimating the strength of the water/single-layer graphite interaction," *The Journal of Physical Chemistry A*, vol. 104, no. 44, pp. 9971–9975, 2000. [Online]. Available: https://pubs.acs.org/doi/10.1021/jp001766o

[223] C. S. Lin, R. Q. Zhang, S. T. Lee, M. Elstner, T. Frauenheim, and L. J. Wan, "Simulation of water cluster assembly on a graphite surface," *The Journal of Physical Chemistry B*, vol. 109, no. 29, pp. 14 183–14 188, 2005. [Online]. Available: https://pubs.acs.org/doi/10.1021/jp050459l

[224] H. Li and X. C. Zeng, "Wetting and interfacial properties of water nanodroplets in contact with graphene and monolayer boron–nitride sheets," *ACS Nano*, vol. 6, no. 3, pp. 2401–2409, 2012. [Online]. Available: https://pubs.acs.org/doi/10.1021/nn204661d

[225] O. Leenaerts, B. Partoens, and F. M. Peeters, "Water on graphene: Hydrophobicity and dipole moment using density functional theory," *Physical Review B*, vol. 79, no. 23, p. 235440, 2009. [Online]. Available: https://link.aps.org/doi/10.1103/PhysRevB.79.235440

[226] G. Hong, Y. Han, T. M. Schutzius, Y. Wang, Y. Pan, M. Hu, J. Jie, C. S. Sharma, U. Müller, and D. Poulikakos, "On the mechanism of hydrophilicity of graphene," *Nano Letters*, vol. 16, no. 7, pp. 4447–4453, 2016. [Online]. Available: https://pubs.acs.org/doi/10.1021/acs.nanolett.6b01594

[227] A. H. Holm, R. Møller, K. H. Vase, M. Dong, K. Norrman, F. Besenbacher, S. U. Pedersen, and K. Daasbjerg, "Nucleophilic and electrophilic displacements on covalently modified carbon: introducing 4,4-bipyridinium on grafted glassy carbon electrodes," *New Journal of Chemistry*, vol. 29, no. 5, p. 659, 2005. [Online]. Available: http://xlink.rsc.org/?DOI=b415623d

[228] A. Fairbrother, J.-R. Sanchez-Valencia, B. Lauber, I. Shorubalko, P. Ruffieux, T. Hintermann, and R. Fasel, "High vacuum synthesis and ambient stability of bottom-up graphene nanoribbons," *Nanoscale*, vol. 9, no. 8, pp. 2785–2792, 2017. [Online]. Available: http://xlink.rsc.org/?DOI=C6NR08975E

[229] C. Ma, Z. Xiao, A. A. Puretzky, A. P. Baddorf, W. Lu, K. Hong, J. Bernholc, and A.-P. Li, "Oxidization stability of atomically precise graphene nanoribbons,"

Physical Review Materials, vol. 2, no. 1, p. 014006, Jan. 2018. [Online]. Available: https://link.aps.org/doi/10.1103/PhysRevMaterials.2.014006

[230] O. V. Yazyev, "Emergence of magnetism in graphene materials and nanostructures," *Reports on Progress in Physics*, vol. 73, no. 5, p. 056501, May 2010. [Online]. Available: https://iopscience.iop.org/article/10.1088/0034-4885/73/5/056501

[231] O. V. Yazyev, R. B. Capaz, and S. G. Louie, "Theory of magnetic edge states in chiral graphene nanoribbons," *Physical Review B*, vol. 84, no. 11, p. 115406, Sep. 2011. [Online]. Available: https://link.aps.org/doi/10.1103/PhysRevB.84.115406

[232] S. Suda and A. Oshiyama, "Energetics, Electron States, and Magnetization in Nearly Zigzag-Edged Graphene Nano-Ribbons," *Journal of the Physical Society of Japan*, vol. 84, no. 2, p. 024704, Feb. 2015. [Online]. Available: http://journals.jps.jp/doi/10.7566/JPSJ.84.024704

[233] W. Han, R. K. Kawakami, M. Gmitra, and J. Fabian, "Graphene spintronics," *Nature Nanotechnology*, vol. 9, no. 10, pp. 794–807, Oct. 2014. [Online]. Available: http://www.nature.com/articles/nnano.2014.214

[234] Q. Sun, X. Yao, O. Gröning, K. Eimre, C. A. Pignedoli, K. Müllen, A. Narita, R. Fasel, and P. Ruffieux, "Coupled Spin States in Armchair Graphene Nanoribbons with Asymmetric Zigzag Edge Extensions," *Nano Letters*, vol. 20, no. 9, pp. 6429–6436, Sep. 2020. [Online]. Available: https://pubs.acs.org/doi/10.1021/acs.nanolett.0c02077

[235] D. J. Rizzo, G. Veber, J. Jiang, R. McCurdy, T. Cao, T. Chen, S. G. Louie, F. R. Fischer, and M. F. Crommie, "Inducing Metallicity in Graphene Nanoribbons via Zero-Mode Superlattices," *Science*, p. 23, 2020.

[236] A. Bellunato, H. ArjmandiTash, Y. Cesa, and G. F. Schneider, "Chemistry at the Edge of Graphene," *ChemPhysChem*, vol. 17, no. 6, pp. 785–801, Mar. 2016. [Online]. Available: http://doi.wiley.com/10.1002/cphc.201500926

[237] A. Narita, X.-Y. Wang, X. Feng, and K. Müllen, "New advances in nanographene chemistry," *Chemical Society Reviews*, vol. 44, no. 18, pp. 6616–6643, 2015. [Online]. Available: http://xlink.rsc.org/?DOI=C5CS00183H

[238] K.-Y. Yoon and G. Dong, "Liquid-phase bottom-up synthesis of graphene nanoribbons," *Materials Chemistry Frontiers*, vol. 4, no. 1, pp. 29–45, 2020. [Online]. Available: http://xlink.rsc.org/?DOI=C9QM00519F

[239] M. Slota, A. Keerthi, W. K. Myers, E. Tretyakov, M. Baumgarten, A. Ardavan, H. Sadeghi, C. J. Lambert, A. Narita, K. Müllen, and L. Bogani, "Magnetic edge states and coherent manipulation of graphene nanoribbons," *Nature*, vol. 557, no. 7707, pp. 691–695, May 2018. [Online]. Available: http://www.nature.com/articles/s41586-018-0154-7

[240] M. G. Schwab, A. Narita, Y. Hernandez, T. Balandina, K. S. Mali, S. De Feyter, X. Feng, and K. Müllen, "Structurally Defined Graphene Nanoribbons with High Lateral Extension," *Journal of the American Chemical Society*, vol. 134, no. 44, pp. 18 169–18 172, Nov. 2012. [Online]. Available: https://pubs.acs.org/doi/10.1021/ja307697j

[241] Shan Sheng Yu, Wei Tao Zheng, and Qing Jiang, "Oxidation of Graphene Nanoribbon by Molecular Oxygen," *IEEE Transactions on Nanotechnology*, vol. 7, no. 5, pp. 628–635, Sep. 2008. [Online]. Available: http://ieeexplore.ieee.org/document/4581650/

[242] K. Xu and P. D. Ye, "Theoretical Study on the Oxidation Mechanism and Dynamics of the Zigzag Graphene Nanoribbon Edge by Oxygen and Ozone," *The Journal of Physical Chemistry C*, vol. 118, no. 19, pp. 10 400–10 407, May 2014. [Online]. Available: https://pubs.acs.org/doi/10.1021/jp500633w

[243] O. Hod, V. Barone, J. E. Peralta, and G. E. Scuseria, "Enhanced Half-Metallicity in Edge-Oxidized Zigzag Graphene Nanoribbons," *Nano Letters*, vol. 7, no. 8, pp. 2295–2299, Aug. 2007. [Online]. Available: https://pubs.acs.org/doi/10.1021/nl0708922

[244] D. G. de Oteyza, A. García-Lekue, M. Vilas-Varela, N. Merino-Díez, E. Carbonell-Sanromà, M. Corso, G. Vasseur, C. Rogero, E. Guitián, J. I. Pascual, J. E. Ortega, Y. Wakayama, and D. Peña, "Substrate-Independent Growth of Atomically Precise Chiral Graphene Nanoribbons," *ACS Nano*, vol. 10, no. 9, pp. 9000–9008, Sep. 2016. [Online]. Available: https://pubs.acs.org/doi/10.1021/acsnano.6b05269

[245] J. Holec, B. Cogliati, J. Lawrence, A. Berdonces-Layunta, P. Herrero, Y. Nagata, M. Banasiewicz, B. Kozankiewicz, M. Corso, D. G. Oteyza, A. Jancarik, and A. Gourdon, "A Large Starphene Comprising Pentacene Branches," *Angewandte Chemie International Edition*, vol. 60, no. 14, pp. 7752–7758, Mar. 2021. [Online]. Available: https://onlinelibrary.wiley.com/doi/10.1002/anie.202016163

[246] K. Lucht, D. Loose, M. Ruschmeier, V. Strotkötter, G. Dyker, and K. Morgenstern, "Hydrophilicity and Microsolvation of an Organic Molecule Resolved on the Sub-molecular Level by Scanning Tunneling Microscopy," *Angewandte Chemie International Edition*, vol. 57, no. 5, pp. 1266–1270, Jan. 2018. [Online]. Available: https://onlinelibrary.wiley.com/doi/10.1002/anie.201711062

[247] K. Lucht, I. Trosien, W. Sander, and K. Morgenstern, "Imaging the Solvation of a One-Dimensional Solid on the Molecular Scale," *Angewandte Chemie International Edition*, vol. 57, no. 50, pp. 16 334–16 338, Dec. 2018. [Online]. Available: https://onlinelibrary.wiley.com/doi/10.1002/anie.201808579

[248] H. Shi, H. Yuan, Y. Sun, X. Ma, Z. Li, D. Zhou, Z. Li, and X. Shao, "Single Molecular Reaction of Water on a ZnO Surface," *Nano Letters*, vol. 21, no. 22, pp. 9567–9572, Nov. 2021. [Online]. Available: https://pubs.acs.org/doi/10.1021/acs.nanolett.1c03218

[249] O. Bikondoa, C. L. Pang, R. Ithnin, C. A. Muryn, H. Onishi, and G. Thornton, "Direct visualization of defect-mediated dissociation of water on TiO2(110)," *Nature Materials*, vol. 5, no. 3, pp. 189–192, Mar. 2006. [Online]. Available: http://www.nature.com/articles/nmat1592

[250] P. v. R. Schleyer, C. Maerker, A. Dransfeld, H. Jiao, and N. J. R. van Eikema Hommes, "Nucleus-Independent Chemical Shifts: A Simple and Efficient Aromaticity Probe," *Journal of the American Chemical Society*, vol. 118, no. 26, pp. 6317–6318, Jan. 1996. [Online]. Available: https://pubs.acs.org/doi/10.1021/ja960582d

[251] D. Geuenich, K. Hess, F. Köhler, and R. Herges, "Anisotropy of the Induced Current Density (ACID), a General Method To Quantify and Visualize Electronic Delocalization," *Chemical Reviews*, vol. 105, no. 10, pp. 3758–3772, Oct. 2005. [Online]. Available: https://pubs.acs.org/doi/10.1021/cr0300901

[252] R. Herges and D. Geuenich, "Delocalization of Electrons in Molecules," *The Journal of Physical Chemistry A*, vol. 105, no. 13, pp. 3214–3220, Apr. 2001. [Online]. Available: https://pubs.acs.org/doi/10.1021/jp0034426

[253] T. Wang, S. Sanz, J. Castro-Esteban, J. Lawrence, A. Berdonces-Layunta, M. S. G. Mohammed, M. Vilas-Varela, M. Corso, D. Peña, T. Frederiksen, and D. G. de Oteyza, "Magnetic Interactions Between Radical Pairs in Chiral Graphene Nanoribbons," *Nano Letters*, vol. 22, no. 1, pp. 164–171, Jan. 2022. [Online]. Available: https://pubs.acs.org/doi/10.1021/acs.nanolett.1c03578

[254] A. Berdonces-Layunta, J. Lawrence, S. Edalatmanesh, J. Castro-Esteban, T. Wang, M. S. G. Mohammed, L. Colazzo, D. Peña, and P. Jelínek, "Chemical Stability of (3,1)-Chiral Graphene Nanoribbons," *ACS Nano*, p. 8, 2021.

[255] D.-e. Jiang, B. G. Sumpter, and S. Dai, "Unique chemical reactivity of a graphene nanoribbon's zigzag edge," *The Journal of Chemical Physics*, vol. 126, no. 13, p. 134701, Apr. 2007. [Online]. Available: http://aip.scitation.org/doi/10.1063/1.2715558

[256] F. Albrecht, N. Pavliček, C. Herranz-Lancho, M. Ruben, and J. Repp, "Characterization of a Surface Reaction by Means of Atomic Force Microscopy," *Journal of the American Chemical Society*, vol. 137, no. 23, pp. 7424–7428, Jun. 2015. [Online]. Available: https://pubs.acs.org/doi/10.1021/jacs.5b03114

[257] S. M. Arabei and T. A. Pavich, "Spectral-luminescent properties and photoinduced transformations of bisanthene and bisanthenequinone," *Journal of Applied Spectroscopy*, vol. 67, no. 2, pp. 236–244, Mar. 2000. [Online]. Available: http://link.springer.com/10.1007/BF02681841

[258] D. Wu, X. Gao, Z. Zhou, and Z. Chen, "Understanding Aromaticity of Graphene and Graphene Nanoribbons by the Clar Sextet Rule," in *Graphene Chemistry*, D.-E. Jiang

and Z. Chen, Eds. Chichester, UK: John Wiley & Sons, Ltd, Aug. 2013, pp. 29–49. [Online]. Available: http://doi.wiley.com/10.1002/9781118691281.ch3

[259] S. W. Slayden, "The Energetics of Aromatic Hydrocarbons: An Experimental Thermochemical Perspective," *Chemical Reviews*, p. 26, 2001.

[260] R. Vranik, V. Stetsovych, S. Feigl, and S. Müllegger, "Stable -radical 2,2-diphenyl-1-picrylhydrazyl (DPPH) adsorbed at the elbows of 22 × 3 reconstructed Au(111)," *Surface Science*, vol. 700, p. 121676, Oct. 2020. [Online]. Available: https://linkinghub.elsevier.com/retrieve/pii/S003960282030114X

[261] A. Konishi, Y. Hirao, K. Matsumoto, H. Kurata, R. Kishi, Y. Shigeta, M. Nakano, K. Tokunaga, K. Kamada, and T. Kubo, "Synthesis and Characterization of Quarteranthene: Elucidating the Characteristics of the Edge State of Graphene Nanoribbons at the Molecular Level," *Journal of the American Chemical Society*, vol. 135, no. 4, pp. 1430–1437, Jan. 2013. [Online]. Available: https://pubs.acs.org/doi/10.1021/ja309599m

[262] E.-j. Kan, Z. Li, J. Yang, and J. G. Hou, "Half-Metallicity in Edge-Modified Zigzag Graphene Nanoribbons," *Journal of the American Chemical Society*, vol. 130, no. 13, pp. 4224–4225, Apr. 2008. [Online]. Available: https://pubs.acs.org/doi/10.1021/ja710407t

[263] E. Carbonell-Sanromà, J. Hieulle, M. Vilas-Varela, P. Brandimarte, M. Iraola, A. Barragán, J. Li, M. Abadia, M. Corso, D. Sánchez-Portal, D. Peña, and J. I. Pascual, "Doping of Graphene Nanoribbons *via* Functional Group Edge Modification," *ACS Nano*, vol. 11, no. 7, pp. 7355–7361, Jul. 2017. [Online]. Available: https://pubs.acs.org/doi/10.1021/acsnano.7b03522

[264] J. Li, P. Brandimarte, M. Vilas-Varela, N. Merino-Díez, C. Moreno, A. Mugarza, J. S. Mollejo, D. Sánchez-Portal, D. Garcia de Oteyza, M. Corso, A. Garcia-Lekue, D. Peña, and J. I. Pascual, "Band Depopulation of Graphene Nanoribbons Induced by Chemical Gating with Amino Groups," *ACS Nano*, vol. 14, no. 2, pp. 1895–1901, Feb. 2020. [Online]. Available: https://pubs.acs.org/doi/10.1021/acsnano.9b08162

[265] T. W. Greene, "Greene's protective groups in organic synthesis | wiley online books," 2006. [Online]. Available: https://onlinelibrary.wiley.com/doi/book/10.1002/0470053488

[266] C.-I. Chia and V. H. Crespi, "Stabilizing the Zigzag Edge: Graphene Nanoribbons with Sterically Constrained Terminations," *Physical Review Letters*, vol. 109, no. 7, p. 076802, Aug. 2012. [Online]. Available: https://link.aps.org/doi/10.1103/PhysRevLett.109.076802

[267] Y. Li, Z. Zhou, C. R. Cabrera, and Z. Chen, "Preserving the Edge Magnetism of Zigzag Graphene Nanoribbons by Ethylene Termination: Insight by Clar's Rule," *Scientific Reports*, vol. 3, no. 1, p. 2030, Dec. 2013. [Online]. Available: http://www.nature.com/articles/srep02030

[268] Z. Sun, S. Lee, K. H. Park, X. Zhu, W. Zhang, B. Zheng, P. Hu, Z. Zeng, S. Das, Y. Li, C. Chi, R.-W. Li, K.-W. Huang, J. Ding, D. Kim, and J. Wu, "Dibenzoheptazethrene Isomers with Different Biradical Characters: An Exercise of Clar's Aromatic Sextet Rule in Singlet Biradicaloids," *Journal of the American Chemical Society*, vol. 135, no. 48, pp. 18 229–18 236, Dec. 2013. [Online]. Available: https://pubs.acs.org/doi/10.1021/ja410279j

[269] S. Clair and D. G. de Oteyza, "Controlling a Chemical Coupling Reaction on a Surface: Tools and Strategies for On-Surface Synthesis," *Chemical Reviews*, vol. 119, no. 7, pp. 4717–4776, Apr. 2019. [Online]. Available: https://pubs.acs.org/doi/10.1021/acs.chemrev.8b00601

[270] T. Wang and J. Zhu, "Confined on-surface organic synthesis: Strategies and mechanisms," *Surface Science Reports*, vol. 74, no. 2, pp. 97–140, May 2019. [Online]. Available: https://linkinghub.elsevier.com/retrieve/pii/S016757291930010X

[271] S. Song, J. Su, M. Telychko, J. Li, G. Li, Y. Li, C. Su, J. Wu, and J. Lu, "On-surface synthesis of graphene nanostructures with -magnetism," *Chemical Society Reviews*, vol. 50, no. 5, pp. 3238–3262, 2021. [Online]. Available: http://xlink.rsc.org/?DOI=D0CS01060J

[272] J. Liu and X. Feng, "Synthetic Tailoring of Graphene Nanostructures with Zigzag-Edged Topologies: Progress and Perspectives," *Angewandte Chemie International Edition*, vol. 59, no. 52, pp. 23 386–23 401, 2020, _eprint: https://onlinelibrary.wiley.com/doi/pdf/10.1002/anie.202008838. [Online]. Available: https://onlinelibrary.wiley.com/doi/abs/10.1002/anie.202008838

[273] R. Zuzak, P. Brandimarte, P. Olszowski, I. Izydorczyk, M. Markoulides, B. Such, M. Kolmer, M. Szymonski, A. Garcia-Lekue, D. Sánchez-Portal, A. Gourdon, and S. Godlewski, "On-Surface Synthesis of Chlorinated Narrow Graphene Nanoribbon Organometallic Hybrids," *The Journal of Physical Chemistry Letters*, vol. 11, no. 24, pp. 10 290–10 297, Dec. 2020. [Online]. Available: https://pubs.acs.org/doi/10.1021/acs.jpclett.0c03134

[274] R. Zuzak, A. Jančařík, A. Gourdon, M. Szymonski, and S. Godlewski, "On-Surface Synthesis with Atomic Hydrogen," *ACS Nano*, vol. 14, no. 10, pp. 13 316–13 323, Oct. 2020. [Online]. Available: https://pubs.acs.org/doi/10.1021/acsnano.0c05160

[275] M. S. G. Mohammed, L. Colazzo, R. Robles, R. Dorel, A. M. Echavarren, N. Lorente, and D. G. de Oteyza, "Electronic decoupling of polyacenes from the underlying metal substrate by sp3 carbon atoms," *Communications Physics*, vol. 3, no. 1, p. 159, Dec. 2020. [Online]. Available: https://www.nature.com/articles/s42005-020-00425-y

[276] M. Di Giovannantonio, O. Deniz, J. I. Urgel, R. Widmer, T. Dienel, S. Stolz, C. Sánchez-Sánchez, M. Muntwiler, T. Dumslaff, R. Berger, A. Narita, X. Feng, K. Müllen, P. Ruffieux, and R. Fasel, "On-Surface Growth Dynamics of Graphene Nanoribbons: The Role of Halogen Functionalization," *ACS Nano*, vol. 12, no. 1, pp. 74–81, Jan. 2018. [Online]. Available: https://pubs.acs.org/doi/10.1021/acsnano.7b07077

[277] O. Endo, M. Nakamura, K. Amemiya, and H. Ozaki, "Graphene nanoribbons formed from n-alkane by thermal dehydrogenation on Au(111) surface," *Surface Science*, vol. 635, pp. 44–48, May 2015. [Online]. Available: https://linkinghub.elsevier.com/retrieve/pii/S0039602814003793

[278] E. H. Lieb, "Two theorems on the Hubbard model," *Physical Review Letters*, vol. 62, no. 10, pp. 1201–1204, Mar. 1989. [Online]. Available: https://link.aps.org/doi/10.1103/PhysRevLett.62.1201

[279] J. M. Soler, E. Artacho, J. D. Gale, A. García, J. Junquera, P. Ordejón, and D. Sánchez-Portal, "The SIESTA method for *ab initio* order- *N* materials simulation,"

Journal of Physics: Condensed Matter, vol. 14, no. 11, pp. 2745–2779, Mar. 2002. [Online]. Available: https://iopscience.iop.org/article/10.1088/0953-8984/14/11/302

[280]

[281] H. O. Frota, "Shape of the Kondo resonance," *Physical Review B*, vol. 45, no. 3, pp. 1096–1099, Jan. 1992. [Online]. Available: https://link.aps.org/doi/10.1103/PhysRevB.45.1096

[282] Y. Zheng, C. Li, C. Xu, D. Beyer, X. Yue, Y. Zhao, G. Wang, D. Guan, Y. Li, H. Zheng, C. Liu, J. Liu, X. Wang, W. Luo, X. Feng, S. Wang, and J. Jia, "Designer spin order in diradical nanographenes," *Nature Communications*, vol. 11, no. 1, p. 6076, Dec. 2020. [Online]. Available: http://www.nature.com/articles/s41467-020-19834-2

[283] J. Li, N. Friedrich, N. Merino, D. G. de Oteyza, D. Peña, D. Jacob, and J. I. Pascual, "Electrically Addressing the Spin of a Magnetic Porphyrin through Covalently Connected Graphene Electrodes," *Nano Letters*, vol. 19, no. 5, pp. 3288–3294, May 2019. [Online]. Available: https://pubs.acs.org/doi/10.1021/acs.nanolett.9b00883

[284] M. Ternes, "Spin excitations and correlations in scanning tunneling spectroscopy," *New Journal of Physics*, vol. 17, no. 6, p. 063016, Jun. 2015. [Online]. Available: https://iopscience.iop.org/article/10.1088/1367-2630/17/6/063016

[285] Y. Zheng, C. Li, Y. Zhao, D. Beyer, G. Wang, C. Xu, X. Yue, Y. Chen, D.-D. Guan, Y.-Y. Li, H. Zheng, C. Liu, W. Luo, X. Feng, S. Wang, and J. Jia, "Engineering of Magnetic Coupling in Nanographene," *Physical Review Letters*, vol. 124, no. 14, p. 147206, Apr. 2020. [Online]. Available: https://link.aps.org/doi/10.1103/PhysRevLett.124.147206

[286] A. DiLullo, S.-H. Chang, N. Baadji, K. Clark, J.-P. Klöckner, M.-H. Prosenc, S. Sanvito, R. Wiesendanger, G. Hoffmann, and S.-W. Hla, "Molecular Kondo Chain," *Nano Letters*, vol. 12, no. 6, pp. 3174–3179, Jun. 2012. [Online]. Available: https://pubs.acs.org/doi/10.1021/nl301149d

[287] I. Horcas, R. Fernández, J. M. Gómez-Rodríguez, J. Colchero, J. Gómez-Herrero, and A. M. Baro, "WSXM : A software for scanning probe microscopy and a tool for nanotechnology," *Review of Scientific Instruments*, vol. 78, no. 1, p. 013705, Jan. 2007. [Online]. Available: http://aip.scitation.org/doi/10.1063/1.2432410

[288] D. Nečas and P. Klapetek, "Gwyddion: an open-source software for SPM data analysis," *Open Physics*, vol. 10, no. 1, Jan. 2012. [Online]. Available: https://www.degruyter.com/document/doi/10.2478/s11534-011-0096-2/html

[289] A. Riss, "SpmImage Tycoon: Organize and analyze scanning probemicroscopy data," *Journal of Open Source Software*, vol. 7, no. 77, p. 4644, Sep. 2022. [Online]. Available: https://joss.theoj.org/papers/10.21105/joss.04644

[290] J. Walton, P. Wincott, N. Fairley, and A. Carrick, *Peak Fitting with CasaXPS: A Casa Pocket Book*. United Kingdom: Accolyte Science, 2010.

[291] M. T. Stephenson and H. J. Shine, "Cation radicals. 47. Reaction of perylene cation radical with fluoride ion and of perylene with xenon difluoride. Formation of 1-fluoro-, 3-fluoro-, and a difluoroperylene. Complications with chloride ion impurity," *The Journal of Organic Chemistry*, vol. 46, no. 15, pp. 3139–3141, Jul. 1981, publisher: American Chemical Society. [Online]. Available: https://doi.org/10.1021/jo00328a035

[292] I. B. Cohen, “Faraday and franklin’s "newborn baby"," *Proceedings of the American Philosophical Society*, vol. 131, no. 2, pp. 177–182, 1987. [Online]. Available: http://www.jstor.org/stable/986790

[293] T. Wang, J. Lawrence, N. Sumi, R. Robles, J. Castro-Esteban, D. Rey, M. S. G. Mohammed, A. Berdonces-Layunta, N. Lorente, D. Pérez, D. Peña, M. Corso, and D. G. de Oteyza, “Challenges in the synthesis of corannulene-based non-planar nanographenes on Au(111) surfaces,” *Physical Chemistry Chemical Physics*, vol. 23, no. 18, pp. 10 845–10 851, 2021. [Online]. Available: http://xlink.rsc.org/?DOI=D1CP01212F